University of Strathclyde

Strathclyde Institute of Pharmacy and Biomedical Sciences

Measurements in Optical Microscopy

Alison McDonald

A thesis presented in partial fulfilment of the requirements for the degree of Doctor of Philosophy

2013

Author Declaration

I declare that the work presented in this thesis is my own apart from the following elements:

- Preparation of aluminised coverslips used in Chapter 3 was carried out by Dr William Amos, MRC Laboratory of Molecular Biology, Cambridge.
- Test SEM imaging of gold coated pre-ablated coverslips were performed by Dr William Amos and Dr Jeremy Skepper at the University of Cambridge.
- The smooth muscle cells used in Chapter 4 were prepared by Drs Debbi MacMillan, Marnie Olson and Susan Chalmers in Prof. John McCarron's laboratory at the University of Strathclyde.
- In Chapter 5 the numerical simulations of the optical focusing capabilities of a 20μm diameter parabolic mirror were performed by Dr Paul Griffin at the University of Strathclyde.

The thesis has been composed by the author and has not been previously submitted for examination which has led to the award of a degree.

Signed:

Date:

Abstract

Optical microscopy is a powerful technique that allows visualisation of structures that are invisible with the naked eye. With innovations in computer technology, detectors, optics and photochemistry, the field of microscopy has developed significantly in recent years with highly sophisticated systems commercially available as a matter of routine. With the advent of new microscopes new challenges arise, particularly in the quantification of data so that the end-user may better understand the images obtained. For accurate quantification, the microscope has to be accurately aligned and calibrated, and one must be aware of the tolerances of use. Some of these parameters, such as resolution, are well-documented but other properties of the microscope, such as the effect of the dose of light on the specimen or the size of the optical focus and its repeatability over time, are less well understood.

The aim of this thesis is to identify areas which are generally not tested or calibrated by the vendor or end user of an optical microscope, and provide methods that can inform on the performance.

Following the introduction, the second and third chapters describe improved techniques for assessing the alignment and performance of a laser scanning microscope.

The second part of this thesis, Chapters 4 and 5, describe the implications of accurate measurements in microscopy to measurements in both a life sciences application and a physical sciences application.

Chapter 6 concludes the thesis and includes a discussion of future opportunities that may follow.

Publications

Peer-reviewed journal articles

A McDonald, W.B. Amos and G McConnell, “Electron microscopic measurement of the size of the optical focus in laser scanning microscopy” Microscopy and Microanalysis, vol 18 (3), pp596- 602 (2012).

A McDonald, J Harris, D MacMillan, J Dempster and G McConnell, "Light-induced Ca^{2+} transients observed in widefield epi-fluorescence microscopy of excitable cells". Biomedical Optics Express, vol 3 (6), pp 1266-1273 (2012)

W Zhang, A McDonald, T Ackemann, E Riis and G McConnell “Femtosecond synchronously in-well pumped vertical-external-cavity surface-emitting laser” Optics Express, Vol. 18 (1), pp.187-192 (2010)

Conference contributions

Oral presentations:

A McDonald, W.B Amos and G McConnell “Accurate measurement of the optical focus in laser scanning microscopy” European Microscopy Congress 2012, Manchester, September 2012.

A McDonald, “Light-induced Ca^{2+} transients observed in widefield epi-fluorescence microscopy of excitable cells” SU2P 3rd annual symposium, Heriot Watt University, April 2012.

Poster presentations:

A McDonald, W.B. Amos and G McConnell "Direct measurement of the optical focus in laser scanning microscopy" Focus on Microscopy, Singapore, April 2012

A McDonald, W.B. Amos and G McConnell "Direct measurement of mirror scanning jitter in laser scanning microscopy" Focus on Microscopy, Singapore, April 2012

A McDonald, W Zhang, T Ackemann, E Riis and G McConnell "Femtosecond pulsed synchronously in-well pumped VECSEL" Photon 10, Southampton, September 2010

A McDonald, J Harris and G McConnell "Non-invasive electromagnetic micro-stirring device" Focus on Microscopy, Shanghai, March 2010

Acknowledgements

Over the course of my PhD research I have had the opportunity to work with many wonderful people without whom I am sure the past three years would have been a less enjoyable experience. First I thank my supervisor Prof. Gail McConnell for her encouragement since the days of my summer placement as an undergraduate to the completion of this thesis. I would never have thought back then that I would have reached this stage, and this is undoubtedly due to the support and opportunities that Gail has given me. It has been a privilege to work in this group and I have learned so much over my time here. I also thank my second supervisor (and my favourite biologist) Dr Owain Millington who has always been there to give advice and encouragement.

I thank Dr Brad Amos for all of his help and suggestions for the experiments. I have also very much enjoyed hearing the stories from the early days of the confocal and his excellent impressions. In particular, thank you for all of your help with the ablation experiments and for kindly preparing the aluminium coated coverslips.

Now to the many past and present members of the Centre for Biophotonics who have made it such a great place to work. To the two guys that have been there from start to finish, Greg and Rumelo. It has been a pleasure working with you both, thanks for all of the advice and help you have given me. Most of all thanks for making the past three years a lot of fun, the epic Singapore and Philippines trip will never be forgotten. Additional thanks go to David Blatchford for all of his help over the years and for the many interesting facts he has taught me. Thanks also go to Sarah for her advice, friendship and laughs over the year she spent in the group.

Special thanks go to the ‘old’ team: Dr Wei Zhang, Dr John Harris and Dr Elric Esposito for their help and advice at the start of my PhD. In particular to John for his help with the Ca^{2+} experiments. Further thanks go to Dr Debbi MacMillan for her suggestions when writing the Ca^{2+} paper.

I also thank Dr Paul Griffin and Prof. Erling Riis from the Photonics group for their help with the micro mirror experiments.

Further thanks go to all of the people in the office for putting up with me when I was writing up. Thanks to Jenny, Rhona, Nicola, Felicity, Ava, Tam, Dave, Walid and Asia. Special thanks go to Debbie for her excellent chat and friendship over the years. Additional thanks go to SB Imerb for all of the sweets, cakes and haw flakes that would appear on my desk when I was writing (+55).

Lastly I thank all of my friends and family for their support and encouragement. Without them I wouldn't have been able to do this.

Table of Contents

Abbreviations

AFM- Atomic force microscopy

BFP- Back focal plane

CCD- Charge coupled device

CLSM- Confocal laser scanning microscopy

CW- Continuous wave

EOM- Electro-optic modulator

FIBM- Focussed ion beam milling

HAZ- Heat affected zone

IR- Infrared

LED- Light emitting diode

LSM- Laser scanning microscopy

MPLSM- Multi-photon laser scanning microscopy

PMT- Photomultiplier tube

PSF- Point spread function

ROI- Region of interest

SEM- Scanning electron microscopy

TPA- Two-photon absorption

TPE-Two-photon excitation

UV- Ultra-violet

Table of Figures

Chapter 1: Introduction

1.1 General Introduction

First pioneered by Leeuwenhoek and later improved by Hooke in the late 1600's, optical microscopy continues to be a useful tool in many scientific fields to this day. The original optical microscopes of the type used by Robert Hooke comprised a single lens element and, although simple, the elegant drawings of biological specimens published in "Micrographia" [1] prove that even very detailed structures were visible using the first systems. Since this early work, optical microscopy has developed significantly, in particular after the invention of the laser in 1960's, computer technology becoming widespread in the 1980s, improved photo-detectors and continued advances in photochemistry. This new technology has created a number of new imaging modalities including fast widefield fluorescence recording [2–6] and confocal and multi-photon laser scanning microscopy (CLSM and MPLSM) [7–10]. However, for all optical microscopy techniques, old and new, it remains critical to understand the limitations of the instrumentation, particularly where quantitative measurements rather than a qualitative assessment is required. These limitations can be mechanical or electronic in origin, e.g. jitter of scanning mirrors, spatio-temporal, e.g. in the resolution of data from the specimen, or may even depend on the amount of light provided to the specimen. Microscopes are used by scientists from many different backgrounds to visualise and quantify physical properties of materials with high accuracy in both the lateral and axial domains. This is often successful, however due to the diverse nature of disciplines this can lead to misinterpretation of data and inaccuracies arising from misalignment of the instrument. There are few guides on calibrating and maintaining microscope systems in order to make the accurate measurements required, and the commercial suppliers rarely provide this information, instead leaving measurements to the microscope owner.

To achieve the most information about the sample of interest from imaging with any microscopy system, the alignment and stability of the platform is crucial. In order to

ensure the images are calibrated such to allow quantitative measurements to be made post-acquisition, it is necessary to regularly measure the stability and resolution of the system. This is the subject of several review articles and book chapters (examples include [11–14]), and usually these techniques involve the repeat imaging of standardised fixed test specimens, such as fluorescent beads in mountant, to calibrate the system. However, these measurement techniques do not isolate the scanning system from the stage stability, nor do they include the effect of the light on the specimen.

The aim of this thesis is to report new measurement techniques in optical microscopy. This includes new methods which can be used to monitor the performance of a laser scanning microscope with sub-diffraction limited accuracy, a study of how titrating the dose of light to a specimen may alter the very behaviour one wishes to investigate, and the application of a quasi-confocal microscope to measure the profile of micro-mirror structures. Details of these experiments will be described in subsequent chapters but first, this introductory chapter provides background on the range of optical microscopy modalities included in this thesis and an overview of frequently used quantification methods.

1.2 Imaging methods

1.2.1 Brightfield microscopy

Since the development of the early compound microscopes by Antonie van Leeuwenhoek and Robert Hooke in the 17th Century [1], [15], standard brightfield microscopes have been used to characterise intricate microscopic structures. However, brightfield microscopes are best suited to imaging relatively thin sections of transparent specimens. The basic design of a brightfield microscope is shown in the schematic in Figure 1.1, where a lens is used to magnify a sample which can then be viewed using an eyepiece. These microscopes are now designed around the ISO standard which requires the real image to be formed by the objective lens at a tube length of 160mm (shown as ‘m’ in Figure 1.1). Although some Zeiss microscopes

have a tube lens of 170mm, such that objective lenses used for these systems are not suitable for use in the standard 160mm tube length systems, due to ineffective spherical aberration correction.

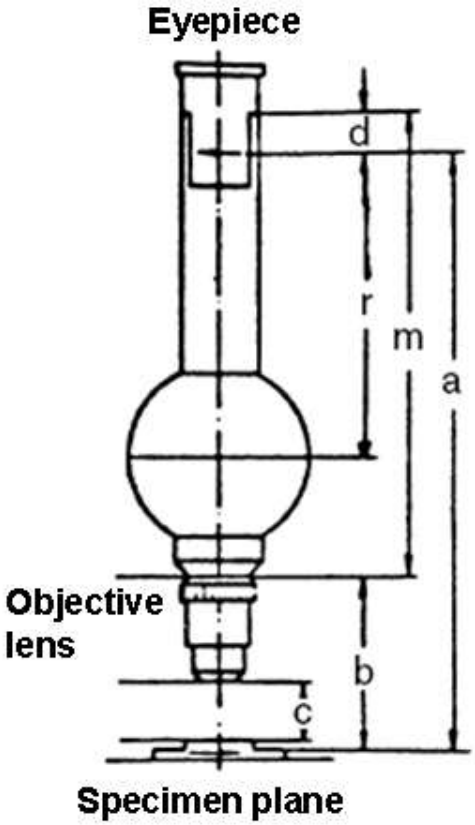

Figure 1.1- Compound microscope where m is the mechanical tube length, a is the object to image distance, b is the parfocal distance of the objective lens, d is the intermediate image distance of eyepiece, c is the working distance of the objective lens and r is the distance from the mounting shoulder of the monocular to the intermediate image plane [16]**.**

In order to achieve the highest spatial resolution, the best possible alignment of the optical components is advised, and the aberrations in the system should be minimised [17]. Therefore, the important starting point in setting up an imaging system is providing sufficient and uniform illumination conditions. Prior to the 1890's, critical illumination, where the light source was directly focused on the focal plane of the specimen, was used routinely [18]. This was the most efficient way to provide light at the specimen plane. However, this resulted in an inhomogeneous illumination across the sample arising from irregularities in the light source (typically a flame or filament in modern tungsten lamps). This resulted in regions of higher intensity in

the image plane which adversely affected the image quality. To overcome this effect, August Köhler, working with Carl Zeiss, developed a new alignment protocol which used the addition of condensers and field apertures to the microscope instrumentation [18]. This was subsequently defined as Köhler illumination and is still the method of transmission microscope illumination to date.

Schematic representations of Köhler illumination and image formation are shown in Figure 1.2. The key improvement of Köhler illumination is that the illuminating light path (Figure 1.2(a)) and the image forming light path (Figure 1.2(b)) are not in conjugate planes. Therefore, the field can be uniformly illuminated without the light source being imaged in the focal plane of the objective lens. However, one disadvantage of the planes not being conjugate is that the collection efficiency is lower than for the critical illumination case. This is generally not a limiting factor in modern microscope systems as the light sources are generally of high power, which easily provide sufficient illumination intensity.

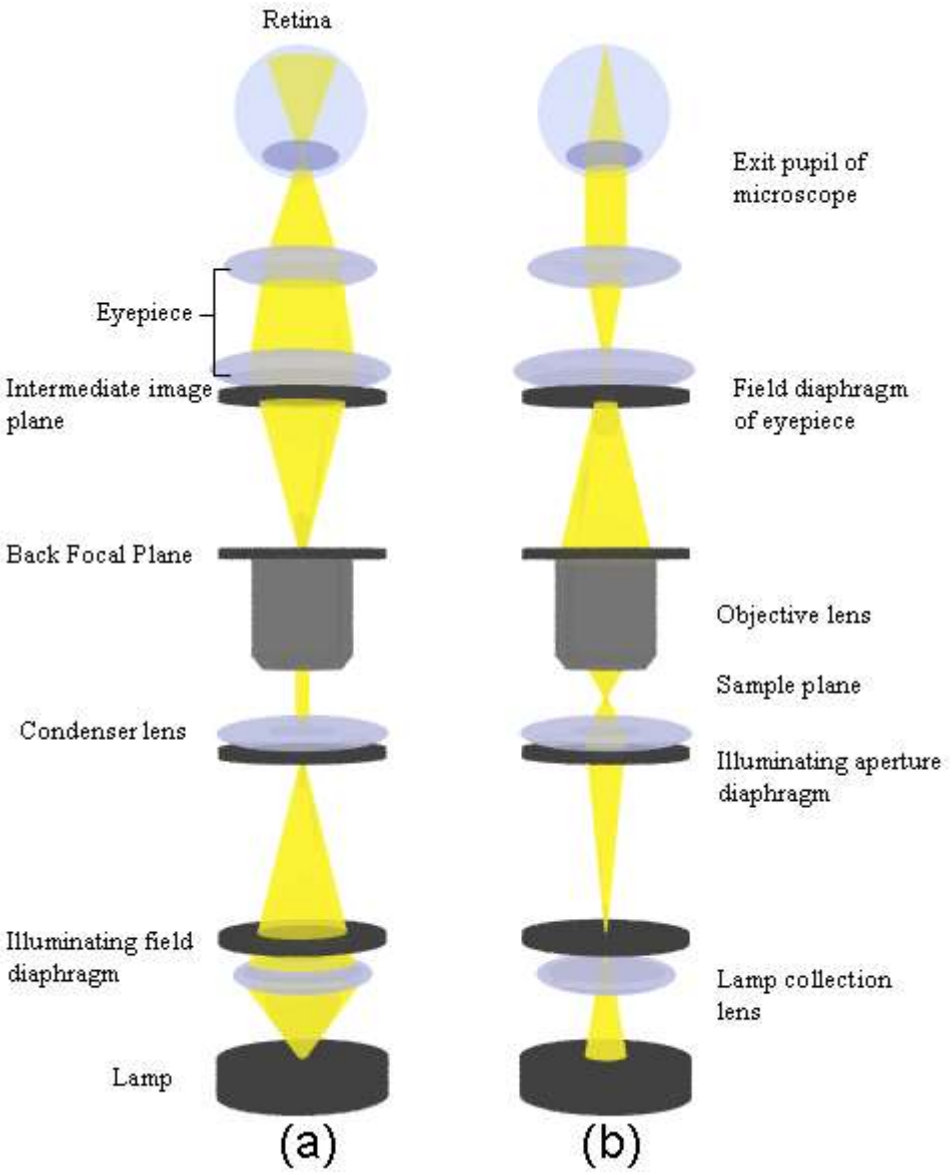

Figure 1.2- (a) shows the illumination path and (b) shows the image formation path under the conditions of Köhler illumination[18], [19]**.**

1.2.2 Epi-fluorescence microscopy

The principles of fluorescence were first described by G. G. Stokes in 1853, where he reported in the transactions of the Royal Society an observation of the change of the 'refrangibility' of light from the incident rays that entered a sample [20], [21]. He observed that upon illuminating fluorescent compounds such as quinine with a given wavelength of light, the compound generated light at a longer wavelength. This change in wavelength is known as the Stokes shift. As an example, the excitation and

emission spectrum of Green Fluorescent Protein (GFP) is shown in Figure 1.3, with the Stokes shift visible.

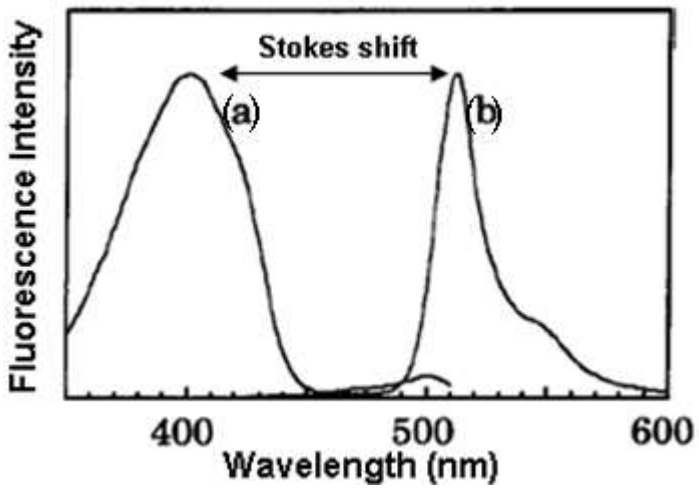

Figure 1.3- (a) Fluorescence excitation and (b) emission spectra of Aequorea GFP mutant reproduced from [22]**.**

However, it was not until the 1930's when the mechanisms of molecular photophysics were described in more detail by Perrin and Jablonski independently [23–25]. The principles of fluorescence can be understood in terms of a simple energy level diagram known as the Jablonski diagram as shown in Figure 1.4. The atom or molecule absorbs light at a wavelength specific to the medium and emits light at a longer wavelength and thus lower energy. This process is known as the Stokes shift. During excitation, a photon is absorbed promoting an electron from the ground state S to the excited state S*. The molecule can then relax back to the ground state via a number of mechanisms, i.e. either radiatively, such as in the case of fluorescence, or non-radiatively, where the energy is dissipated as heat and a longer-wavelength photon is not emitted. In the radiative case, the photon emitted is of lower energy than the excitation photon, where the remaining energy is lost in the thermal relaxation.

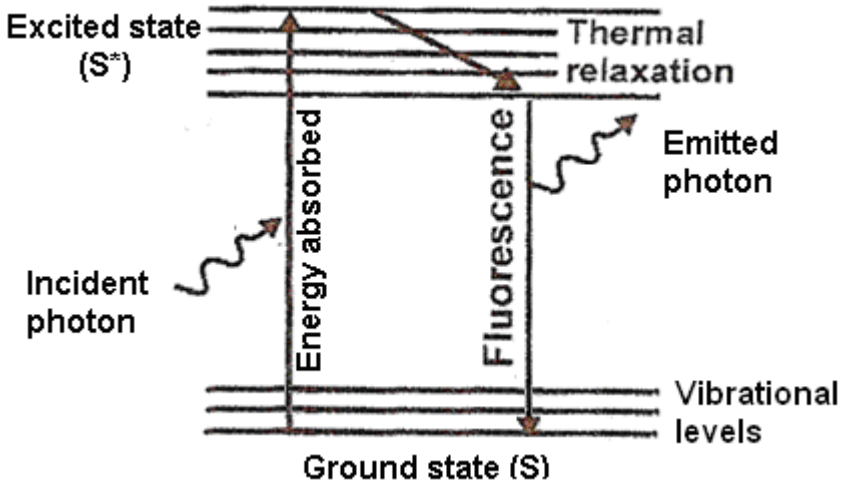

Figure 1.4- Jablonski energy level diagram illustrating the process of fluorescence [26]**.**

This Stokes shift is critical in making fluorescence such a sensitive technique as the low number of emitted photons can be separated from the high number of excitation photons using spectral filters [27]. The efficiency of this process is known as the quantum yield, which is the ratio of the number of photons absorbed by the molecule to the number of photons emitted. The maximum is therefore 1.0, when 100% of the photons absorbed result in an emitted photon. This would not be achieved in reality due to the energy lost as thermal energy corresponding to the Stokes shift [28]. However, fluorophores with a quantum yield of 10% are still efficient enough for most applications. As an example, one of the most common fluorophores used in confocal microscopy is fluorescien which has a high quantum yield of 0.95, whereas a commonly used Ca^{2+} fluorescent indicator, Fluo-3AM, has a quantum yield of 0.183 [29]. It is worth noting that the fluorescent properties of most fluorophores can be temperature and pH dependent.

The earliest demonstration of fluorescence microscopy was in the early 1900's where autofluorescence was observed as a result of UV irradiation on a bacteria sample [30–33]. The process of autofluorescence occurs for a number of endogenous compounds such as NAD(P)H and flavins, which are naturally fluorescent under certain excitation conditions [29]. This can be problematic in cases where synthetic fluorescent probes are used which excite and emit at the similar wavelengths as the

autofluorescence wavelength, where it can be challenging to eliminate autofluorescence from the resultant image.

The first demonstration of fluorescence labelling was in 1941 by Coons et al, who demonstrated labelling of an antibody with a fluorescent dye [34], [35]. This technique provided a means to study the interaction of the antibody with antigen in the cell. What followed this first report was an explosion in the development of new fluorescent probes. In 1962 Simomura first extracted Green Fluorescent Protein (GFP) from the jelly fish *Aequorea victoria* [36]. In 1994, the first demonstration of GFP as a useful research tool in biology was reported by Chalfie et al [37]. This was the turning point for fluorescent microscopy techniques and the development of this protein into various mutations by Roger Tsien and others occurred throughout the 1990s and continues now [29], [38–41]. This has led to a 'tool box' of fluorescent probes with excitation and emission wavelengths covering the near-UV to near-infrared spectral range [41]. This is particularly advantageous in applications which require multiple stains for different parts of the cell. These developments improved the number of applications of fluorescence microscopy, which is an invaluable tool in biological applications. In addition to labelling different components of the cell including the nuclei, golgi bodies etc, the development of probes which change their properties under environmental changes were also developed [42].

1.2.3 Laser scanning microscopy

1.2.3.1 Confocal laser scanning microscopy (CLSM)

The first form of a scanning microscope was the flying spot microscope developed by Young and Roberts [43]. This early development used a cathode ray tube to scan an oscilloscope trace across a sample producing an image. However, limitations in the technology, which was adapted from the television industry, resulted in low light levels and the poor images did not generate much scientific interest [8]. The first confocal microscope was invented by Minsky in 1955, who was motivated to develop a technique that reduced the effect of out of focus scattered light from the specimen. His approach was to block the scattered rays from entering the detector, where an ideal microscope would observe each point of a sample individually [44].

The Minsky design is shown in Figure 1.5, where there are two pinholes (14 and 24 on diagram) to create a point source of light from an arc light source (13) and to detect only light from the plane of focus another pinhole (24) was placed before the detector. The focal planes of both pinholes are the same, i.e. confocal. This approach combined with scanning the sample allowed for imaging of improved axial resolution, compared with epi-fluorescence microscopy, negating out of focus light. However, Minsky was limited by the technology available at the time and as a result the application of confocal microscopy to biology and materials science did not occur until later developments from the late 70s to early 80s which demonstrated the true power of CLSM [7], [45], [46]. In particular, the invention and development of the laser in the 1960's provided new avenues of research in CLSM.

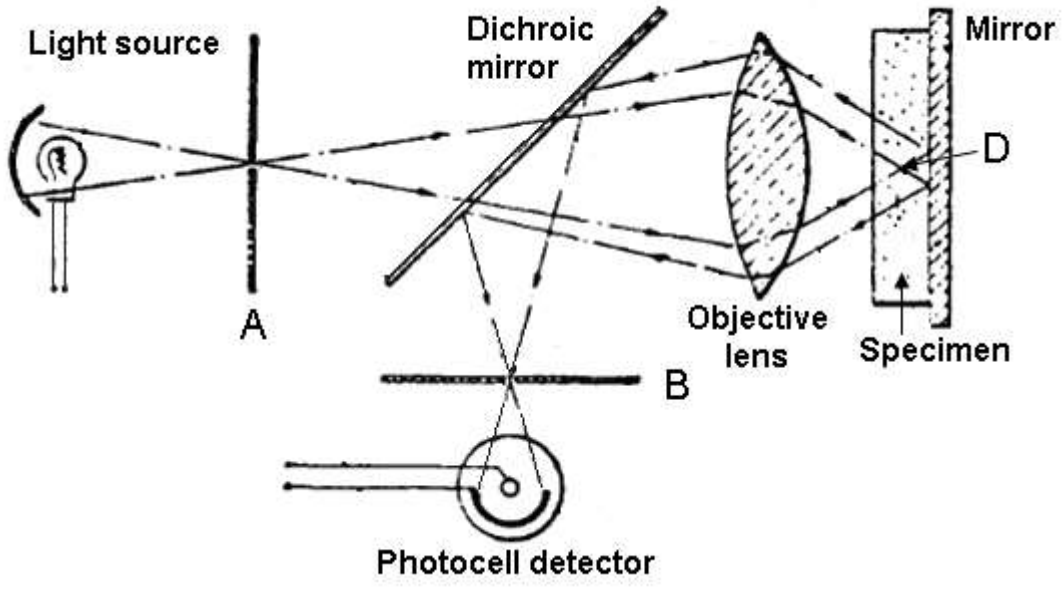

Figure 1.5- Marvin Minsky's confocal microscope. The schematic shows the epi-illumination confocal geometry. The pinholes A and B (illumination and emission respectively) are in the same focal plane (confocal) as point D in the specimen. The dichroic mirror transmits light from the light source towards the sample and reflects the light from the specimen to the detector. The illumination light is focused on to the specimen by the objective lens. In this case the light that passes through point D is reflected by the mirror below the specimen back towards the dichroic Only light from the point D passes through pinhole B to the photocell detector (reproduced from [44] **with edited labelling for clarity).**

The work of Sheppard, Cox, Wilson and Brankenhoff developed this field further [13], [47], [48] to develop the first laser scanning microscopes (LSMs). However, these developments were primarily for optical microscopy of physical samples such

as semiconductor characterisation and therefore a moving sample scanning system, as with Minsky's confocal microscope, was used. This posed obvious limitations to the extension of confocal microscopy to biological applications where samples in various media were of interest: physically moving the sample would perturb the biological specimen, resulting in damage and modifications of the structure. This sparked further investigations into beam scanning methods such as scanning polygon and galvanometer scanning mirrors. This was first achieved by Amos and White in 1987 [46] and their design was subsequently commercialised by Bio-Rad.

1.2.3.2 Modern confocal microscopy systems

A simplified diagram of a standard CLSM system is shown in Figure 1.6. The light source, which for confocal microscopy would be a continuous wave (CW) laser, enters from the RHS of the schematic. The beam is then adjusted by the beam expander, to match the beam diameter to the back focal plane (BFP) of the objective lens. A dichroic filter then directs the excitation light to the scanning galvonometer mirrors and the angles of the scanning mirrors are varied over time to produce a raster scanning pattern of the beam at the sample plane. The fluorescence emission from the focal plane then passes back through the system and by selecting the correct dichroic filter for the fluorescent probe of interest, the fluorescence light will reach the PMT detector. The confocal pinhole at the detector will reject out focus light, providing optical sectioning.

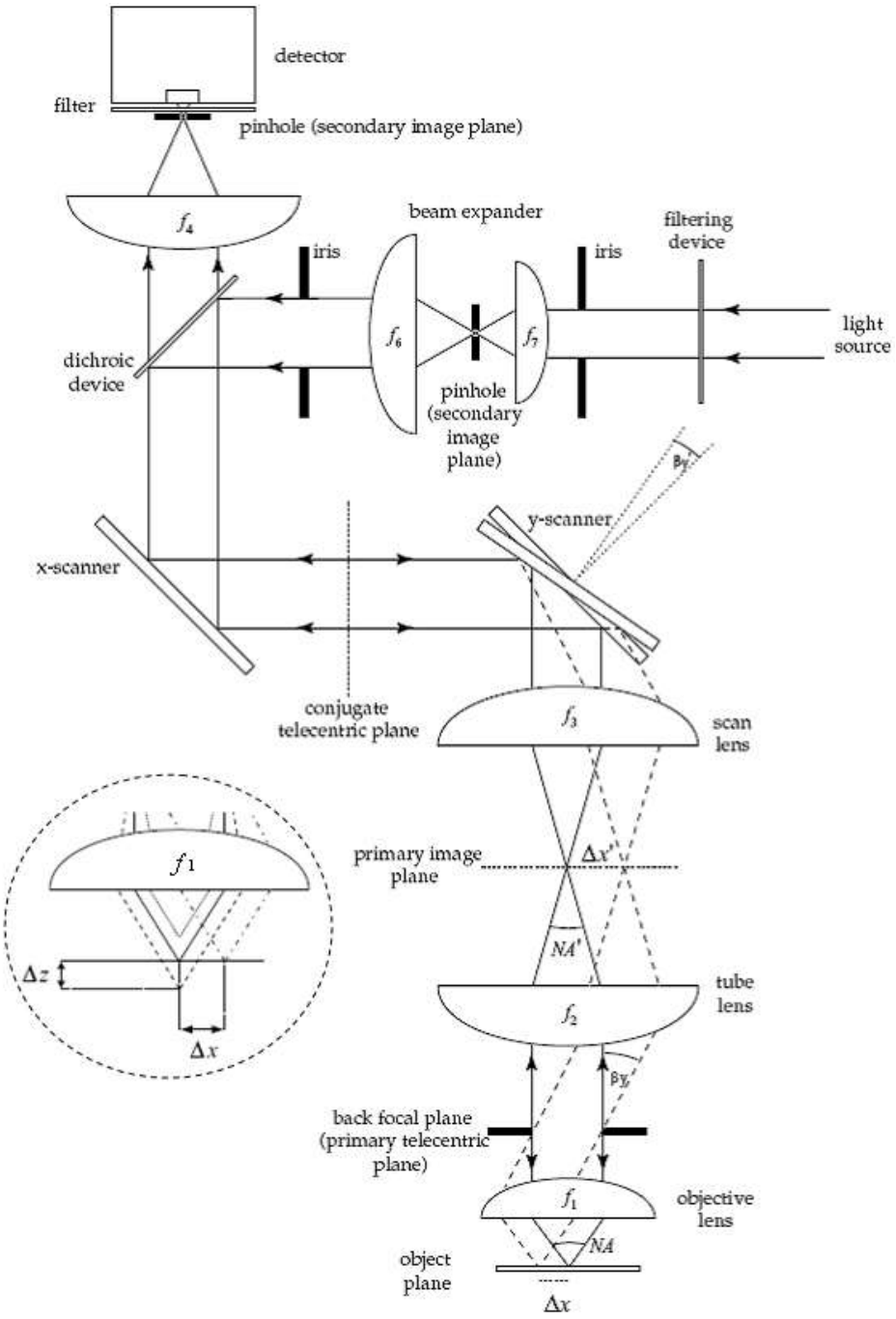

Figure 1.6-Schematic of a confocal scanning microscope reproduced from [49]**. Schematic of the focal position over x scan and varying z position (to create a z stack or xz scan, for example) is shown inset.**

1.2.3.2 Multi-photon laser scanning microscopy (MPLSM)

The process of multi-photon excitation was first theoretically described by the work of Maria Göppert-Mayer in her doctoral thesis in 1931 [50]. For simplicity, the case of two-photon excitation (TPE) is considered here.

Two-photon excitation is the simultaneous absorption of two photons of long wavelengths that combine their energies to generate molecular excitation that would otherwise require a single photon of shorter wavelength [51]. The simplified Jablonski diagram for two-photon excitation is shown in Figure 1.7.

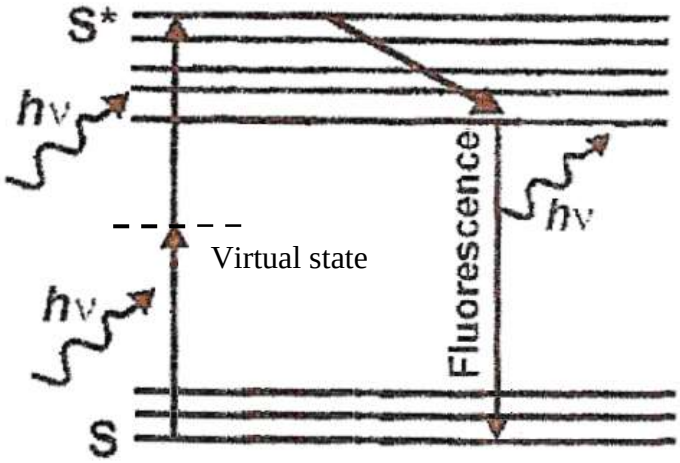

Figure 1.7-Two photon absorption Jablonski diagram [14]

The probability of two-photon absorption (TPA) depends on the square of the intensity of the excitation source [51]. As a result, two-photon microscope systems require a pulsed laser source which has high peak intensities, but with a modest average power [52], [53]. It was reported by Squirrell et al that damaging effects on developing embryos after CLSM at shorter wavelengths was significantly higher than under IR irradiation during MPLSM [53]. Studies on isolated cells have shown significant damage, leading to apoptosis, that was strongly dependent on average power [54] as well as pulse duration [55]. These studies reported laser induced damage for average powers exceeding 7mW. In MPLSM, fluorophore excitation is limited to the plane of focus and as a result this method does not require a confocal pinhole. The inherent optical sectioning in the z axis is due to the quadratic dependence of the probability of TPA on the intensity of the incident radiation. This means that the probability of excitation in the z axis outside of the focal region, varies with z^{-4} for two photon absorption [51]. The dependence on intensity on the

probability of TPA, results in confinement of excitation to the focus this also confines the effects of photo-bleaching and photo-damage to the focal plane [51].

However, TPE was not realised experimentally for many years after the initial theoretical predictions of its existence because no light source was sufficiently intense. It was not until 30 years later after the invention of the ruby laser by Maiman in 1960 [56] that it was possible to achieve the intensity required to absorb two photons, this was first experimentally realised and reported by Denk et al in 1990 [52].

The comparison between TPE and single-photon excitation is shown in the photograph in Figure 1.8. To directly visualise the excitation volumes, the fluorescence emission of the dye Nile red, within a cuvette, was observed for linear excitation (top) and non-linear excitation (bottom/arrow). For linear excitation, a CW laser at 532nm was used, whereas for TPE, an ultra-short pulsed Nd:YLF laser with an emission wavelength of 1047nm was used. This clearly shows the generation of fluorescence beyond the plane of focus for the single photon and the localised excitation at the focus for multi-photon. Therefore, the requirement for a pinhole in the detection path in CLSM and not in MPLSM can be realised.

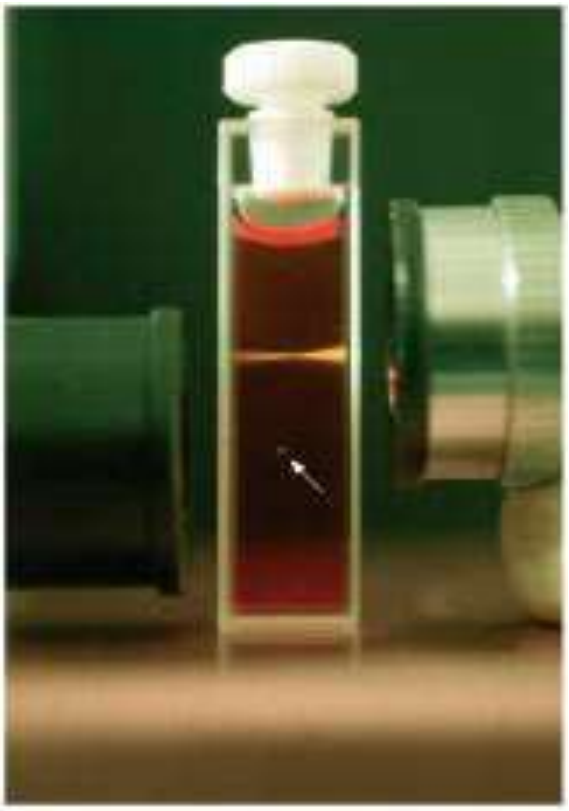

Figure 1.8- Photograph showing the difference in excitation volume for single photon (confocal) and multi-photon imaging. Photograph taken by Brad Amos MRC Lab of Molecular Biology, Cambridge (1994) and used with permission.

The use of longer wavelengths in MPLSM results in reduced scattering, and therefore deeper imaging, because of the λ^{-4} dependence of Rayleigh scattering [57]. The Rayleigh scattering approach is a reasonable approximation in the case where the scattering objects are much smaller than the wavelength of light incident upon the material. However, this is merely an approximation as in biological imaging the components scattering the light will be of a similar dimension to the wavelength of light being scattered. Therefore, scattering under these conditions needs to be considered using Mie theory. However, this becomes difficult to compute for scattering particles that are not spherical in shape.

In 1991, the first demonstration of multi-photon laser scanning microscopy (MPLSM) was reported by Denk et al [52]. This opened new routes in biological microscopy. The pulsed nature of the excitation was proven to be less damaging to the sample and the use of longer wavelengths provided improved imaging depth

from reduced scattering, as well as reduced auto fluorescence and toxicity from that at shorter wavelengths [53]. In addition the nature of multi-photon absorption limits the irradiation to the plane of focus, thus limiting the photo induced damage and phototoxicity to a small volume of the sample. There is also a significant improvement in the signal to noise ratio as the losses induced using a confocal pinhole are not incurred in MPLSM. This study was shortly followed by the application of the Kerr lens mode-locked Ti:Sapphire laser to biological microscopy [10], [58]. This excitation source will be covered in more detail in Chapter 3.

1.2.4 Super resolution microscopy

The development of new microscopy techniques is still on-going, but one of the greatest recent advances has been in breaking the diffraction limit to provide improved spatial resolution. Many techniques now exist that overcome the diffraction limit [59], but the technique that sparked this revolution is stimulated emission depletion microscopy (STED), where two beams are used instead of one scanned beam. The first beam is the same excitation beam as in standard techniques, whereas the second beam is used to de-excite the fluorophores surrounding the centre in a doughnut mode: both beams are raster scanned as with CLSM or MPLSM. This leaves a sub-diffraction limited effective focal volume as shown schematically in Figure 1.9. This technique was first proposed in 1994 by Stefan Hell and experimentally observed in 1999 [60], [61]. The technique has been shown to improve the resolution 10-12 fold, compared with standard linear excitation techniques [60].

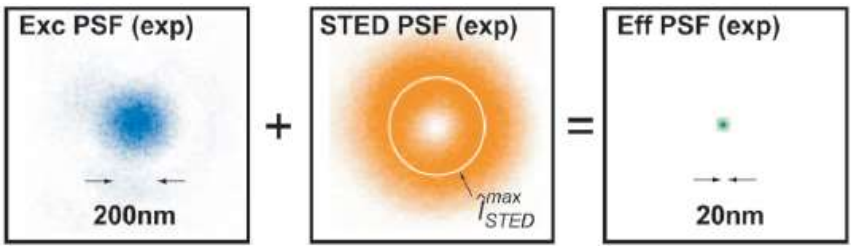

Figure 1.9- Schematic of the mechanism of improved resolution in STED microscopy reproduced from [62]**.**

In recent years the advantages of improved resolution have been demonstrated in biological applications using these systems. A recent article has shown the impact of using STED imaging for immuno-detection within the nucleus, where structures were observed in the nuclear membrane that were not observable in conventional CLSM and MPLSM techniques [63]. In addition to this, STED microscopy has shown promising results in the field of neuroscience, where mouse brain imaging has been performed in-vivo [64].

1.3 Measurements in optical microscopy

1.3.1Role of quantitative measurements in optical microscopy

The ability to visualise microscopic objects with a high magnification and high resolution is only part of the reason why microscopes have impacted upon many areas of science. The ability to quantify, with high precision, many properties of the sample is where microscopy has been able to develop our understanding of the absolute properties and therefore the characteristics of the sample. This is all carried out with minimal perturbation to the subject of investigation: the specimen is visualised intact and thus can be preserved.

In order to obtain highly accurate measurements using an optical microscope, the alignment and calibration of the system is required to be of a very high standard to minimise (or at least understand the effect of) systematic measurement errors . Thus, there are a number of properties of the system which need to be measured and calibrated prior to imaging experiments. This section will outline the main properties of the microscope platform to consider, in order to achieve the most precise and accurate quantitative data.

1.3.2 Measurements: accuracy and precision

The most fundamental measurement in microscopy is the quantification of dimensions. In order to do this accurately, the dimensions of the image formed by a

microscope have to be accurately calibrated with a specimen of already known dimensions.

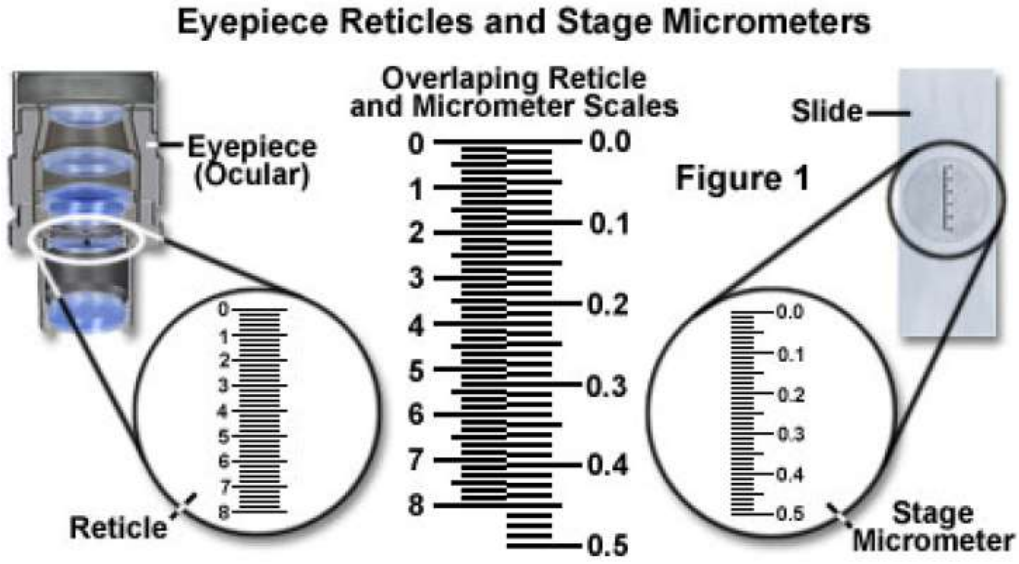

Figure 1.10- Figure showing the alignment of the eyepiece reticule and the stage micrometer scale to calibrate image dimensions reproduced from [65]**.**

In compound microscopes, micrometer scales on the stage as well as in the eyepiece reticules can be employed to calibrate the image dimensions, as shown in Figure 1.10. The eyepiece reticule is aligned with the standardised stage micrometer slide, in order to define the conversion factor between the known dimension in the sample plane and the dimension observed in the image plane. The eyepiece reticule can then be used to measure dimensions of the sample directly, by viewing and aligning the eyepiece reticule with the sample. However, this technique is not appropriate for all measurements of dimensions in microscopy: in particular for imaging with a detector or camera another calibration step is required, and there is no specific information about the z-dimension.

With the measurements that can be performed post calibration there remain several issues and sources of error to consider. For techniques that image both a reticule as well as the sample, alignment of the rulings of the reticule with the edges of the object can be subjective, resulting in reduced precision in the linear dimension being recorded. This is also true for image analysis techniques often applied to acquired images. In addition measurements done in this way will be significantly impaired by

optical aberrations, contrast and non-uniform illumination which will reduce the image quality and image sharpness, which in turn will limit the true measurement of the objects dimensions.

1.3.3 Resolution

The most important feature of a microscopic measurement is the spatial resolution. The resolving power of the microscope is illustrated schematically in Figure 1.11, where A and B are the two objects and A' and B' are the image of these objects respectively and there is a minimum distance where the objects A and B can be resolved as separate This distance prescribes the resolution of the image.

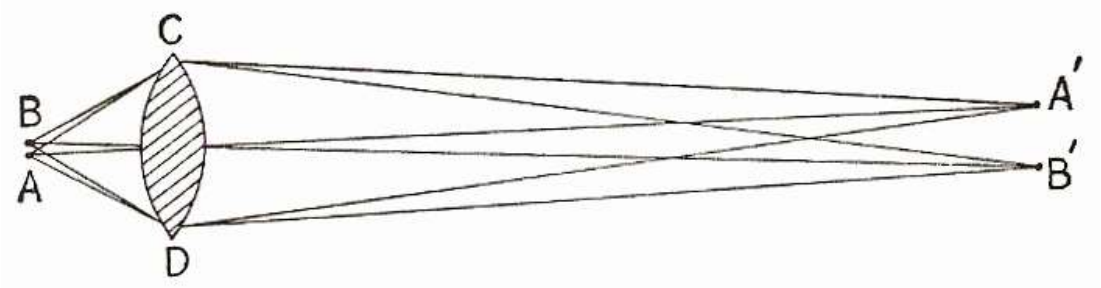

Figure 1.11- Resolving power of a microscope reproduced from [66]**.**

The resolution of the microscope was first theoretically described by Ernst Abbe in 1881, where he defined the amount of light collected by the objective lens and its effect on the resolution of the system [67]. He defined the numerical aperture, *NA* of the lens which is given by

$$NA = n\sin\theta, \tag{1.1}$$

where n represents the refractive index of the medium (air or an immersion material) and θ is the half-angle of the maximum cone of light which may enter the lens.

The image formation of a point object that is free from aberration is a diffraction pattern. The case of diffraction by a circular aperture was mathematically explained by Airy (and is therefore known as the Airy disk). It comprises a central maximum surrounded by a series of rings, as shown in Figure 1.12(a). When the separation of

two points is sufficiently large, the diffraction patterns from each point do not overlap and they can be resolved as separate objects. However, when the central disks of the image of each object are so close as to overlap they cannot be distinguished as separate objects. In practice the boundary between resolved and unresolved is not always clear, and so a criterion was required. Rayleigh defined the boundary between resolved and not resolved as the condition where the central maximum in the diffraction pattern from one object must coincide with the first minimum in the diffraction pattern of the other object. This is shown in Figure 1.12(b).

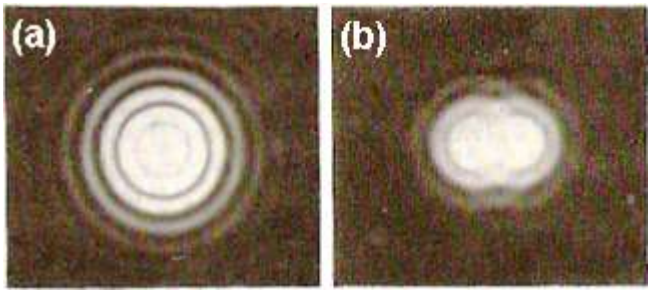

Figure 1.12- (a) Airy disk, (b) Rayleigh criterion reproduced from [66]**.**

The radius r_{min}, of the disk's central ring limits the smallest point to which a beam may be focused. This is known as the diffraction limit, and is given by

$$r_{\min} = \frac{0.61\lambda}{NA}, \tag{1.2}$$

where λ is the wavelength of irradiating light and *NA* is the numerical aperture of the lens, as defined by equation (1.1).

Using the Airy disk diffraction pattern described for the Rayleigh criterion in three dimensions, the minimum distance that two points can be resolved in the z direction, axial resolution is defined as,

$$z_{\min} = \frac{2\lambda n_s}{(NA)^2}, \tag{1.3}$$

where n_s is the refractive index of the sample.

Airy's diffraction theory describes the case of a perfect optical instrument, free from aberration, and therefore is the diffraction limit of the system. The point spread function (PSF), describes the response of an imaging system to a point source or object. If the point source is unresolved by the system it appears stretched in the lateral and axial dimensions of the image. In microscopy, a fluorescent bead of dimensions below the diffraction limit given by equation (1.2), acts as a point source from which the PSF of the system can be determined.

1.3.4 Factors influencing resolution

From equations (1.2) and (1.3) it is clear that the resolution in microscopy is a function of the *NA* and the wavelength of light irradiating the sample. However, the resolution can be further limited by the detection part of the system. These factors include contrast, signal to noise ratio, and how the image is sampled.

1.3.4.1 Contrast

1.3.4.1.1 Contrast mechanisms

In order to correctly image a complex and heterogeneous microscopic structure, differences in contrast between components of varying properties within the sample is required. The number of photons detected determines the contrast, such that the variation in image intensity relative to the background intensity defines the amount of detail we can observe and therefore measurement of the specimen [68]. In a real optical system the resolution will be limited by the number of photons detected from the sample [69]. This is described mathematically in equation (1.4)

$$\gamma = \frac{\Delta I}{I_B} \tag{1.4}$$

where γ is the contrast, ΔI is the variation in intensity between two points on the specimen and I_B is the background intensity level.

Image contrast arises from interaction of the incident light with the sample, which can occur through a number of mechanisms [68]. The most common method of contrast enhancement in microscopy is fluorescence which was described previously. However, methods such as phase contrast microscopy and differential interference contrast (DIC) use the inherent refractive index differences within the specimen to discriminate between different structures instead of adding synthetic contrast agents to the specimen. Phase contrast uses the phase variation of light transmitted through regions of the specimen which have different refractive index properties. This phase change can be seen as variations from dark to light which enhance the contrast, particularly in samples with very little absorption changes across the compartments of the specimen and can distinguish features that are invisible with standard brightfield microscopy [70]. DIC also makes use of the refractive index variation across the sample using polarised light and interferometry to detect variations in the optical path length. These techniques require additional optical components to the conventional microscopes described previously.

1.3.4.1 Signal to noise ratio

It is important to consider the signal to noise ratio for all types of imaging. The Rose criterion states that a feature of a single pixel in size must differ in intensity by 5 times the intensity of the background noise to be considered visible [71]. However, for instances where the object being imaged has a repeating and well defined structure, such as straight edges and grids, the factor can be lower than 5 for the object still to be discernable [72]. The visibility is not solely based on this rule, where the effects on the resolution of the system and the contrast function will also play an important role. Therefore, the visibility as well as image quality should consider all of these effects together. In conditions where the noise levels are high, Kalman averaging is applied. Kalman averaging or filtering is a weighted average such that the later frames have a greater effect on the final image [73]. This is an option given on most commercial LSM systems for image acquisition.

1.3.4.2 Nyquist criterion

When obtaining a digital image, a continuous (analogue) signal is converted into a series of digital points. The image is sampled by measuring intensity at these regular intervals, known as pixels. Due to the digitisation of the analogue signal, the sampling rate is crucial in order to record all the possible variations in the signal accurately. In imaging systems it is therefore necessary to consider the size of the pixels on the detector relative to the smallest variations detectable with a given wavelength and *NA* used for imaging. As described previously this is the theoretical resolution of the system. The Nyquist criterion states that the sampling frequency should be a factor of 2.4x higher than the highest spatial frequency being investigated [72]. There is therefore only one sample size for a given wavelength and *NA*. This is important to note in LSM, where there will only be one digital zoom setting which satisfies the Nyquist sampling criterion. Over-sampling of the data is a wasteful process, with an increased time to take an image compared to a correctly sampled image. In addition this results in excessive light doses on the sample which can generate bleaching effects. On the other hand, under sampling where the pixel size is larger than set by the Nyquist criterion, small features of the image will be lost. This may also present other artefacts in the image such as aliasing [74].

1.3.5 Optical power measurements

The power applied to the sample, which is a factor of both the light source and the lens transmission, is an important parameter in all types of optical microscopy. In particular for techniques involving light matter interaction such as optical trapping [75], [76] and nano-surgery [77], the power at the sample has to be controlled accurately. Unfortunately objective lens manufacturers do not always provide transmission spectra for their lenses. It is often the case that theoretical transmission curves will be provided, which would rely on the lens design being perfect, but this rarely occurs in practice. In addition, any experimental measurements provided may be made using different measurement techniques, making it difficult to then compare

the transmission of lenses from different manufacturers [78]. Therefore, it is necessary to accurately measure the transmission of any objective lens used.

1.3.4 Methods to test and calibrate microscope systems

It was explained at the beginning of this chapter that there are few guides available which cover techniques suitable for quantitative microscopy techniques. However, in the guides that do exist there are a number of techniques which can be subjective and thus limit the accuracy of quantitative measurements taken with a given system. Examples of common measurement techniques in microscopy are outlined in this section, which is by no means an exhaustive list.

1.3.5.1 Assessing the alignment of an optical microscope

The first step when performing imaging using any microscope system is ensuring the alignment is correct such that the system will operate at the full capabilities. This is often intuitive to the user, such that any illumination irregularities would be quickly noticed from the images obtained of test specimens. Following the protocol for Kohler illumination (section 1.1.1) correctly should be effective. However, to further test the alignment of a microscope system a method was outlined by Centonze et al [79], where the alignment of the beam on the back aperture (BFP) of the lens and the consequent excitation path at the sample plan was tested using a uranium doped glass at the focal plane of the microscope and a 45° prism is placed at the BFP of the objective lens such that the circular target and alignment can be viewed simultaneously. The resulting fluorescent excitation of the uranium doped glass was then visible on an external camera. The excitation volume relative to the alignment at the BFP is shown in Figure 1.13. It can be seen clearly that when the beam is off axis at the BFP the beam output of the objective lens is attenuated significantly. This case shows an extreme misalignment of the system, which would be apparent from the images taken with a system misaligned to this extent. However, this technique provides an indication of the magnitude of the effects of beam mis-alignment, which could be a useful test mechanism prior to imaging experiments.

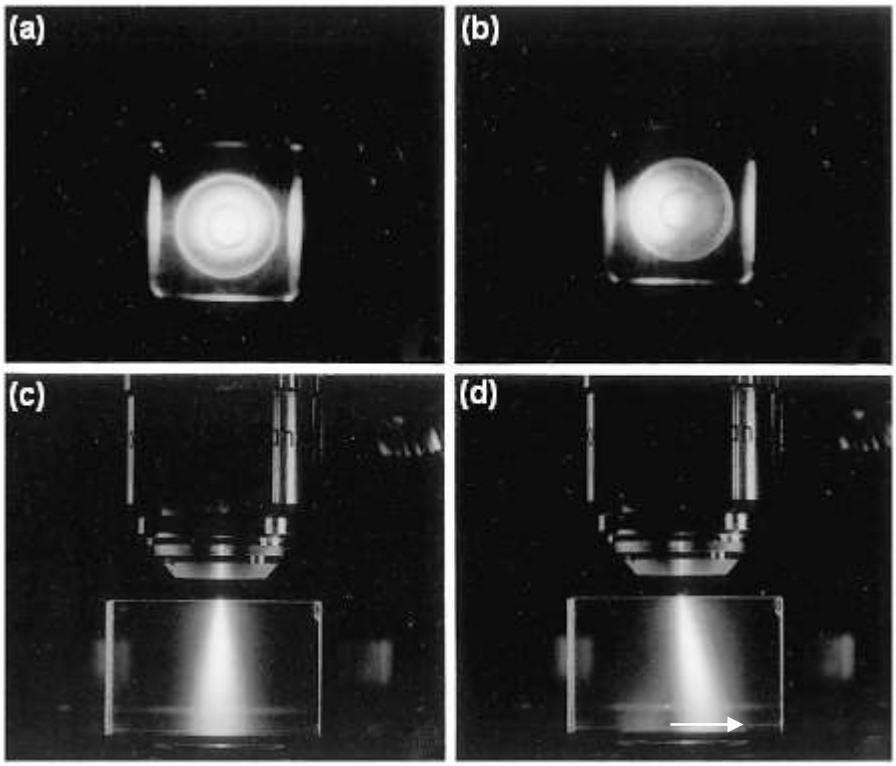

Figure 1.13-Photographs of microscope alignment test showing the on axis alignment at the back focal plane of the objective lens (a) and the corresponding excitation beam at the output of the objective lens (c). The off axis beam at the back focal plane (b) and the corresponding excitation beam (d) clearly show the effects of alignment on the excitation beam. Images reproduced from [79].

The importance on uniform illumination has been discussed in detail throughout this chapter but alignment of the detector position is also required. An effective technique to assess these properties was described by Zucker et al to fully assess the alignment of a system prior to fluorescence imaging [80]. These techniques require the use of a uniform test slide to assess intensity variations across the field of view. Test slides suitable for these measurements can include highly concentrated suspensions of fluorescent beads on a glass slide, or stained tissue paper with a fluorescent dye, which provide a uniform fluorescent surface. However, Zucker et al found that plastic fluorescent slides (e.g. Applied Precision, Spherotech) provided the most consistent results. This technique allows assessment of the alignment of the system as well as the quality of the objective lens *in situ*. Representative field illumination profiles for varying objective lenses using this technique are shown in Figure 1.14.

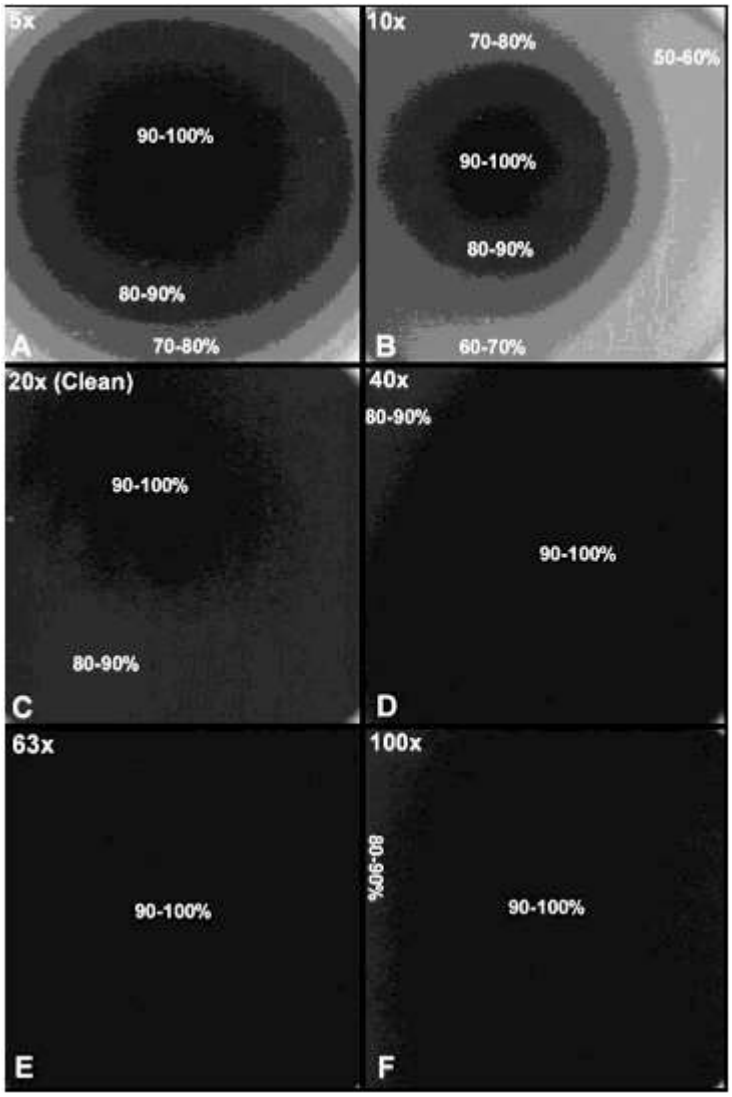

Figure 1.14-Testing field illumination of objective lenses with varying magnification and numerical apertures (A) 6.2x/0.25*NA*, (B) 10x/0.3*NA*, (C) 20x/0.6*NA*, (D) 40x/ 0.5-1*NA*, (E) 63x/1.2*NA* and (F) 100x/1.4*NA*.Illumination pattern determined by imaging a fluorescent plastic slide, where the darkest regions shown are of highest intensity. The most uniform illumination is shown in panel F, with panels A and B showing cases of inhomogeneous illumination(reproduced from [80]**)**

The illumination across the field of view should be uniform for lenses at all magnifications; any inconsistencies for a given lens would be shown as contours in the plot with a central intensity maximum. This effect would then have to be counter acted by selecting a higher digital zoom such that the imaged region only corresponds to a uniform illumination. However, this would not be recommended as this would then limit the capability of the lens in terms of the *NA*.

1.3.5.2 Measuring the lateral and axial resolution

As described briefly earlier, the most common method to test the resolving power of an optical microscope uses a test specimen comprising of sub-resolution fluorescent polystyrene beads in mountant. The beads are selected of a diameter slightly less than the theoretical resolution for the chosen lens and excitation wavelength, with reference to equation (1.2). The lateral resolution of the point spread function (PSF) is then taken as the FWHM of the intensity profile of the imaged bead.

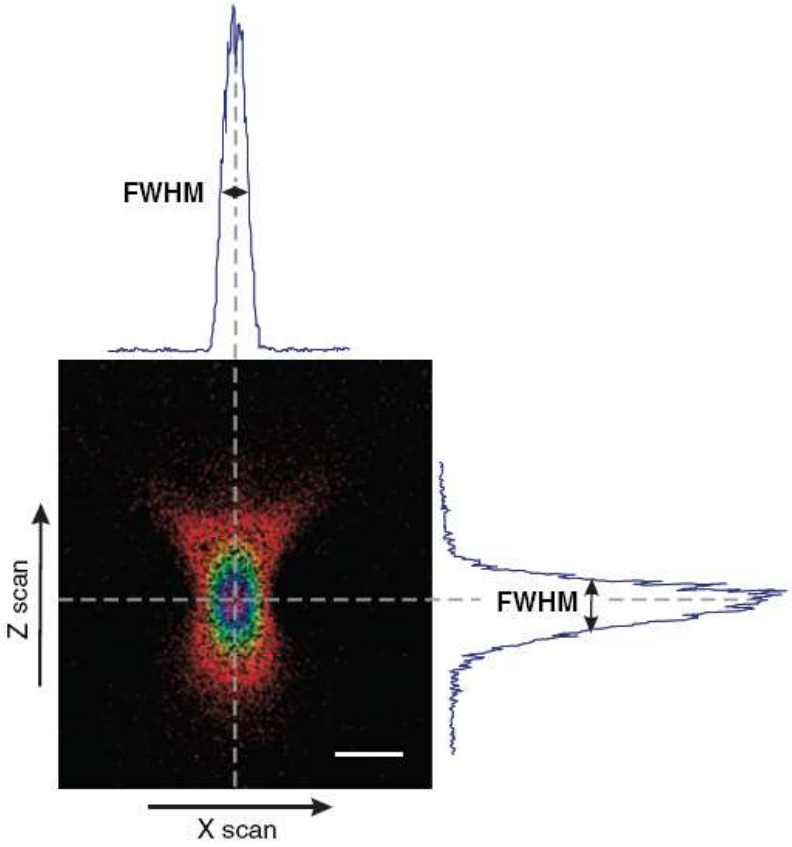

Figure 1.15- PSF, measuring the lateral and axial resolution using the fluorescence bead measurement technique. Image reproduced from [12]**.**

There are several sources of error in measuring the lateral and axial resolution of a microscope system with fluorescent beads. Any noise in the image of the bead will make the measurement subjective, and vibration and instability of the microscope system can make it challenging to obtain an accurate image of the point source. These effects can in part be counteracted by selecting a slow scan as well as using

Kalman averaging. However, the beads can often undergo photo bleaching and laser induced damage effects, which further reduce the accuracy of the final measurement.

In addition to resolution measurements made by beads, it is also possible to image an accurately prepared test slide with gratings produced at known dimensions using ion beam machining. The line width at which the image contrast is insufficient to resolve the lines is taken as the resolution limit of the system. A scanning electron microscopy (SEM) image of a typical test slide is shown in Figure 1.16.

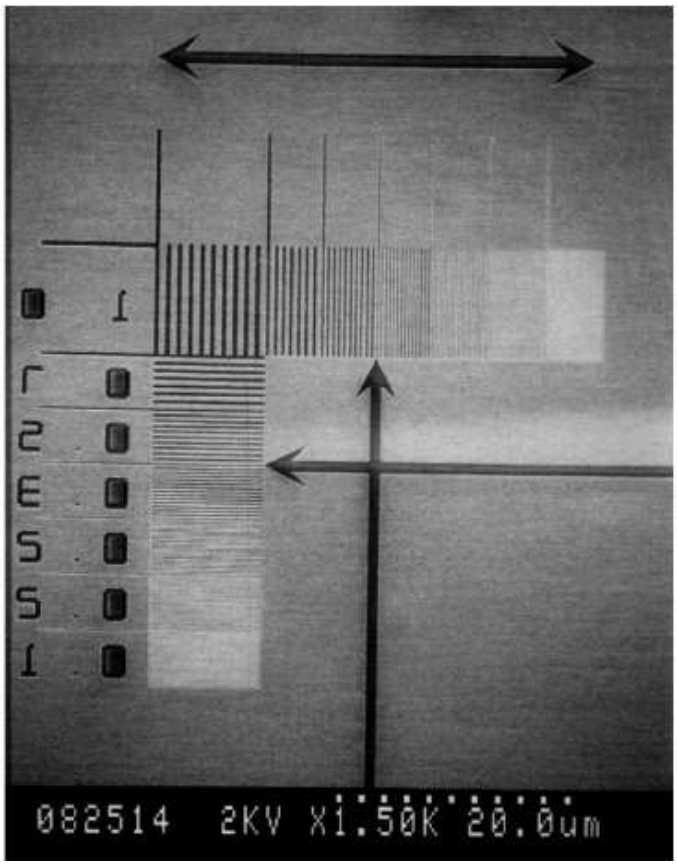

Figure 1.16- SEM image of a test slide produced using ion beam lithography to produce markings below the resolution limit of optical microscopes reproduced from[79]**.**

1.3.5.3 Measuring laser scanning stability using a test slide

Measurements of the stability of the microscope system are also useful for quantitative microscopy applications. It is possible by repeat imaging of a standard test slide, with a uniform and repeating structure, to identify any instability in the

system. By producing an overlay of images taken in the system at varying time points it is possible to observe any irregularities over the field of view of the image. This needs to be tested at varying scan speeds, zoom levels and for varying objective lenses, as errors can arise from a large number of sources. Therefore, a test slide which is suitable for high and low magnification imaging is required. This technique can then be used to quantify any drifts and errors, which can be accounted for in post image processing. A typical test slide comprising a reflective square grid imaged over time is shown in Figure 1.17a. The image at time point 1 is in green and the image taken at a later time point is shown in red, with scan irregularities visible at low zoom. Another test standard was used to test the effect more clearly at high zoom Figure 1.17b. It can be seen that the regions appear to be rectangular with varying dimensions across the x axis of the image, indicating poor calibration of the x scanning galvanometer mirror. The high magnification image (b) shows wavering of the scan, resulting in distortion effects across the image.

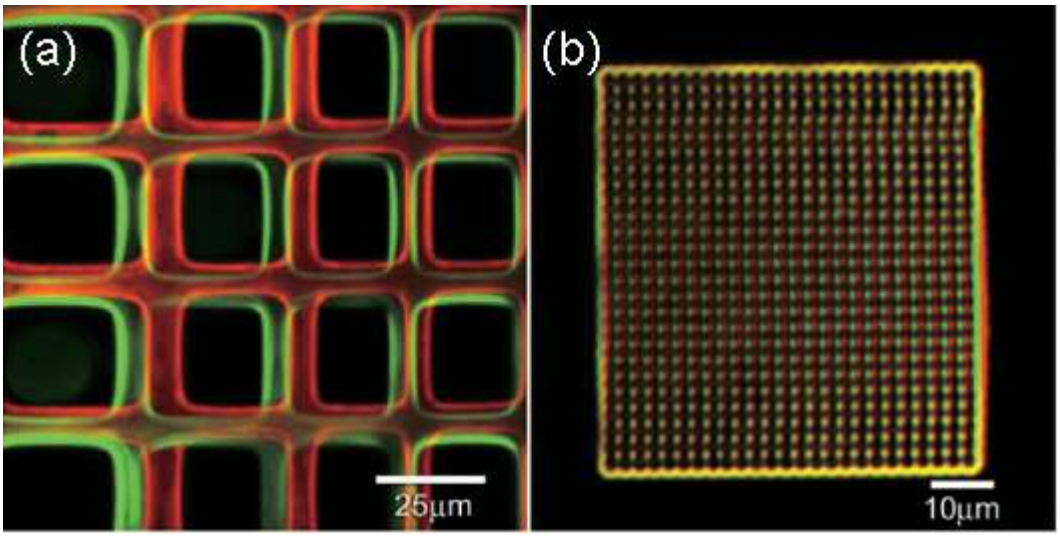

Figure 1.17-Imaging a malfunctioning system using a two standardised test slides with reproducible features of known dimensions to a higher accuracy than optical microscopy a) low magnification imaging of a grid test slide at varying time overlay (red-green) and b) high magnification images of another test slide showing scan irregularities such as wavering across the image [12]**.**

1.4 Summary

This chapter has outlined the development of optical microscopy from the brightfield techniques pioneered in the 17th century to the super resolution techniques developed in the past decade. This field has been revolutionised at several points along this timeline by advances in the manufacture of optical components, to the development of specialised fluorescent probes as well as developments in laser technology. However, despite the capabilities of the instruments and methods described, it is also imperative that the microscope system is aligned and tested to ensure maximum performance. Therefore, it is crucial to quantify external vibrations or internal errors which could compromise the image acquisition and thus the measurements obtained thereafter.

This thesis identifies areas which are generally not tested or calibrated by users of all optical microscopes, in particular laser scanning systems, which have important implications on quantitative microscopy. This is highlighted by the development of two techniques for assessing the stability of the laser scanning mechanism in situ as well as accurately measuring the quality and size of the optical focus at the sample plane. The implications of accurate measurements in microscopy are then applied to measurements in a life science application as well as a physical science application.

1.5 Thesis outline

Chapter 2 describes the development of a technique to assess the scanhead stability over the course of a typical time lapse imaging experiment. The theoretical operation of galvanometer scanning mirror systems is presented and a method to assess scanning mechanism in situ, with minimal modifications to the system, is described. Results are presented on the efficacy of this measurement technique to the quantification of scanning jitter and drift over the course of image acquisition.

Chapter 3 outlines a correlative microscopy technique to provide an accurate measurement of the optical focus after the objective lens in a laser scanning microscope. The process of laser ablation is described, and the use of an electron

microscope to visualise the resultant raster scan trace of the excitation beam in a thin aluminium film. Results are presented and described in relation to how this might be used to quantify the optical focus at the specimen plane of a MPLSM system.

Chapter 4 outlines the effects of excitation power on biological samples. The case of physiology experiments which rely upon optical recording of processes in excitable cells is explained. A method to accurately control the excitation dose at the sample is described and tested in the specific case of Ca^{2+} imaging of live cells. Results on the recommended light levels for these types of experiments to avoid unwanted effects are presented and discussed.

Chapter 5 describes a modified reflection confocal microscopy technique used to accurately measure the focal length of miniaturised mirror arrays. The fabrication and design of these devices is outlined. The advantages of this modified confocal technique are discussed in comparison to measurements using free space bench mounted optics. Results are presented of three designs of micro mirrors of varying dimensions, structures and focal lengths. The application of the measurement technique to these features is discussed.

Chapter 6 concludes the thesis and gives an overview of possible future work arising from the work presented here.

Chapter 2: Direct measurement of scanning mirror induced error in laser scanning microscopy

2.1 Introduction

As described in Chapter 1, LSMs are complex systems comprising of a large number of optical components, electronics and lasers [81]. However, to date there are few comprehensive tests to analyse the performance of the system and this limits the ability to easily understand the tolerances of the system, or compare the capability of systems from different manufacturers. In particular, biomedical applications and characterisation of materials require a high degree of precision in measurement, as well as reliability which can only be achieved if the instrumentation is functioning effectively.

In recent years, optical microscopy methods have been developed that overcome the diffraction limit and, as such, the resolution of images is no longer limited by the traditional Abbe-Rayleigh relation. As an elegant example, the instrumentation for STED microscopy is driven to the limits of precision to achieve super-resolution imaging [60], [61], [82]. However, with increasing resolution comes an increase in the effect of mechanical and electrical noise and instabilities that may be tolerated in conventional laser scanning microscopy. This includes engineering the microscope platform to reduce jitter and instability. The limitations and sources of instability are rarely investigated by microscope users and or developers in this field. With few publications or guides available which provide good descriptions of how one may assess microscope performance, instabilities such as those found in scanning mirrors are largely not considered [80], [83], [84]. Some of the current test methods were outlined in detail in Chapter 1.

This Chapter describes a method of measuring the stability of the laser scanning galvanometer mechanism *in situ*, by taking macroscopic, far-field images of the laser raster scan pattern after the condenser lens in an optical microscope. Images were acquired using a cooled camera at 10 second intervals of a continually scanning

system and these images were analysed using ImageJ to measure the displacement and linearity of the raster scan over time. Measurements of scan drift in the y axis galvanometer scanner mechanism were obtained, as well as measurements of scan jitter and 'wobble' in the x galvanometer mechanism.

2.2 Theory

2.2.1 Scanning galvanometer mirrors

Galvanometers are used in laser scanning microscope systems to precisely raster scan a collimated incident laser beam into the objective lens. In standard LSMs, this provides a near-diffraction limited spot that is raster scanned over the field of view of the specimen. Accurate imaging requires the scanning mechanism to scan the laser beam over the sample upon each round trip, such that the path of the beam matches with the data locations in the image memory. Any errors in the precision of the scanned pattern would clearly result in the data being displaced to a different pixel in the image, leading to displacement effects [72]. The stability and reproducibility of the scanning position is monitored and controlled using closed-loop feedback. The feedback approach requires the use of position sensors to accurately monitor the position of the mirror and this is then fed back into the circuitry controlling the scanning mirrors. Galvanometer scanning systems are the most favourable for laser scanning microscopy in the life sciences as they provide highly versatile scan settings opposed to acousto-optic deflectors (AODs). Galvonometer scanning systems are capable of scanning a laser beam in the range of 500Hz to 1000Hz, with the ability to control the scan speed and number of lines scanned, whereas AODs have the ability to scan much faster (100kHz) due to having no moving parts. However, the suitability of AODs is limited for many applications due to their wavelength dependence, because the scan angle depends on the wavelength of the beam [85].

LSM is an important tool for many measurements, in particular quantifying dimensions of a given cellular component. However, complex time course analysis

of moving objects is also frequently measured via tracking software. In addition to this the co-localization of proteins at certain regions of the cell can provide insights into disease progression [86], [87]. Reproducibility of scanning path over time is essential for quantifying these processes often over long-term imaging experiments. For all of these applications accurate position measurements are required and it is possible to measure changes in the centre position of an object to sub resolution precision from the image itself. These types of measurements are not limited to laser scanning techniques: early widefield microscopy techniques have shown measurements of object motion to 1nm [88]. Although dimensions of that scale can not be resolved, the localisation of the object can be determined accurately by measuring the motion of a bead relative to a fiducial marker, a point of reference placed in the sample and visible in the image, provided that the drifts caused by sample and or sample stage movement have been accurately determined. However, the stability of the widefield microscope is better than for laser scanning instruments which require moving parts (galvanometer scanners). Therefore, the accuracy of controlling the scanning mirrors position is the limiting factor in the capability of the LSM to verify position [72].

One manufacturer states explicitly that the life-cycle of their devices is of the order of billions of cycles of operation (Cambridge Technology [89]), but the data sheets provided with such galvanometer systems from all manufacturers give little information on the stability and repeatability of the scan in terms relative to the image acquired as a function of scanning parameters. Therefore, the galvanometer mechanisms are generally not tested *in situ* by the end user and the degradation in scanning stability over time often not considered. However, scanning error could affect the resolution of the images captured: measurements of the lateral and axial resolution are meaningless unless the accuracy and precision of the pixel to pixel spacing in three dimensions is known to be exactly reproducible [12]. Although scanning mirrors have been engineered to provide extremely fast and reliable scanning, secondary measurements of scanning stability should be measured in situ. The use of post image acquisition correction of position measurements would therefore be possible, thus improving the accuracy of measurements using LSM.

2.2.2 Laser scanning microscopy systems

The most effective method of scanning the beam uses galvanometer scanners with attached mirrors, as shown in Figure 2.1.

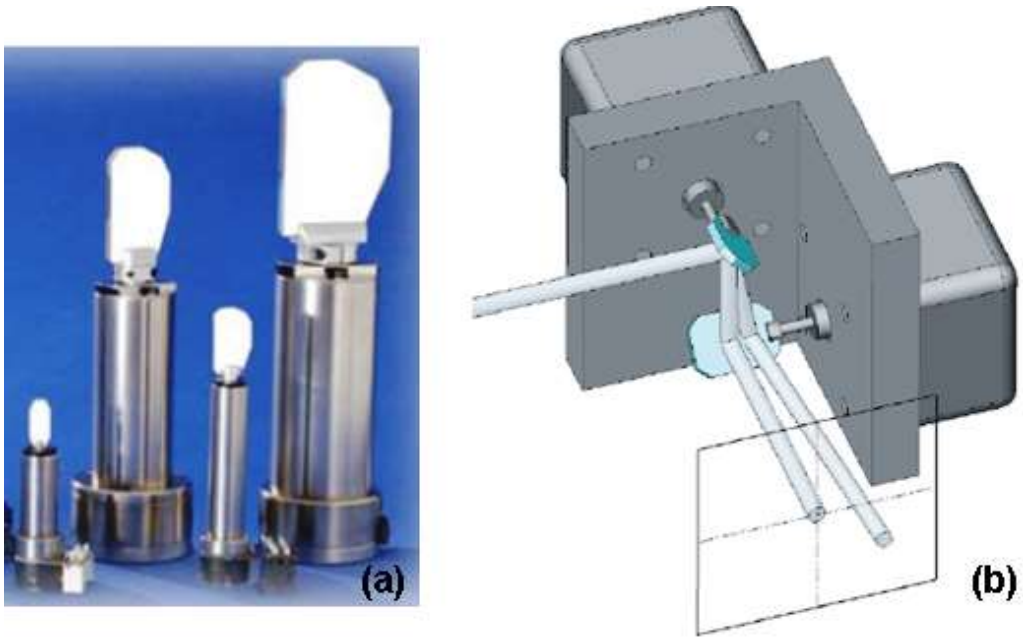

Figure 2.1- (a) Cambridge Technology mirrors of varying dimensions mounted on the scanning mechanism and (b) standard set-up of x and y galvos in a LSM scanhead reproduced from [49], [90] **respectively.**

If the rotational axis of the scan mirrors coincides with both its own surface and the optical axis at a telecentric plane (any plane that is a conjugate of the back focal plane (BFP) of the objective), rotation of the angle of the mirror moves the focal spot across the focal plane in a straight line. This is shown schematically in Figure 2.2.

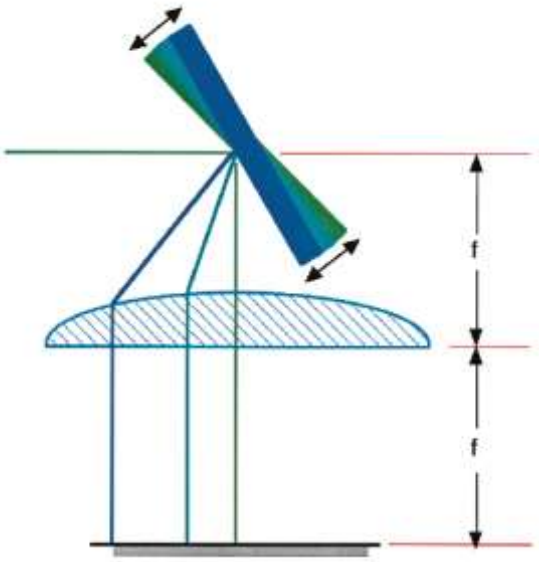

Figure 2.2- Schematic of single galvanometer scanning mirror and resultant position at the specimen plane. Reproduced from [72]**. The green line shows the beam position at the sample plane when the mirror is in the neutral position. The dark blue line shows the outermost region the scan mirrors can rotate to position the beam at the corresponding point on the sample. The light blue line shows the approximate half way point between neutral scan position and maximum deflection. The focal length, f, shows the distance to the focus at the sample plane and the distance from the lens to the BFP of the objective. The scanning mirrors can not be placed at the BFP under normal circumstances therefore the scan lens is placed at the BFP.**

2.2.3 Types of galvanometer mechanisms

Galvanometers are a type of ammeter, whereby upon the application of a current they produce a rotation in the position of a moving part [91]. This works by the conversion of electrical energy into mechanical energy. When a current flows in a magnetic field it experiences a magnetic torque. It is then possible to rotate a moving part through an angle proportional to the current flowing through it. Galvanometer mirrors combine this mechanism with a mirror used to deflect a laser beam with high precision [49]. There are two common types of galvanometer mechanisms, as shown in Figure 2.3. The first to be developed was the moving coil galvanometer, which consists of a wire coil inside a magnet, when there is a current applied to the wire coil it creates an electromagnet [89]. With the addition of a permanent magnet placed close to the coil they will repel and attract depending on the polarity, with the magnetic field being proportional to the current applied to the coil. This in turn will generate forces required to rotate and control the position of the moving part. In the

moving magnet case a magnet instead of a wire coil is used. Moving coil actuators generally have better accuracy than the moving magnet type. However, moving magnet actuators are more rigid and smaller than the previous type, making them more suitable for certain applications [85].

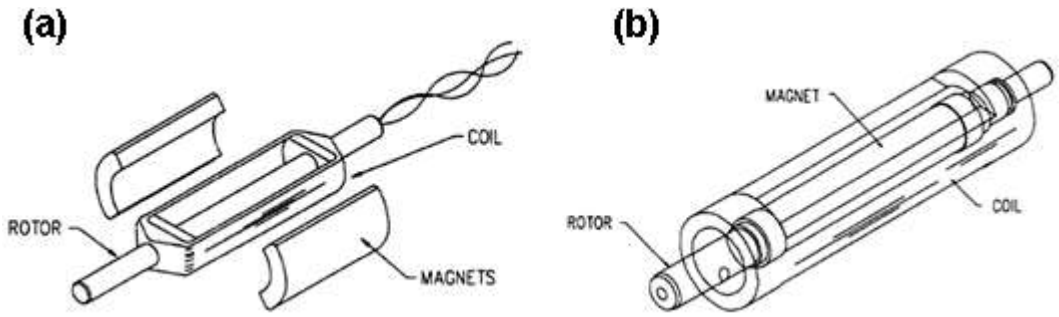

Figure 2.3- (a) moving coil actuator and (b) moving magnet actuator. Reproduced from [89]**.**

Modern galvanometer systems are also categorised as open or closed loop systems. In closed loop systems, the output is fed back into the control mechanism, providing a method of improving accuracy and repeatability of the scan pattern. Open looped systems are mainly found in barcode scanners and in space flight applications; the reduction in the need to use oil in the mechanism makes these devices well suited to applications requiring high vacuum. LSM systems use closed looped systems.

2.2.4 Scanning patterns

Although raster scanning is widely used in commercial scanning microscopes, other scan patterns are possible, such as Lissajous pattern and tornado scanning [92], [93]. Various types of scanning patterns are shown in Figure 2.4.

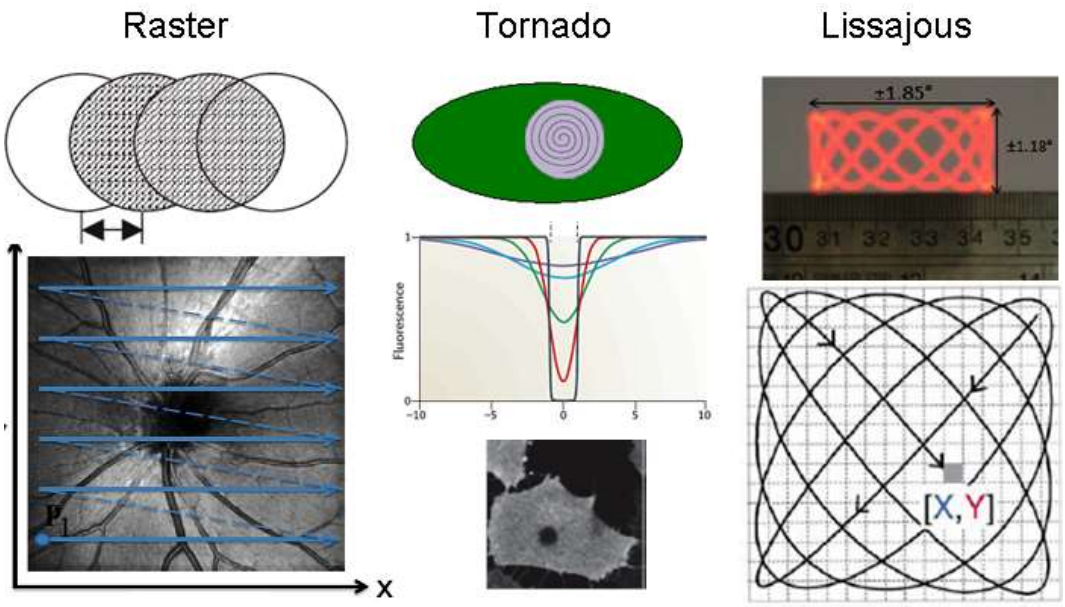

Figure 2.4- Scanning patterns used in LSM applications. The most common scan pattern is the raster scan, where the beam is scanned across a line in the x dimension of the image using a fast mirror, then the beam is scanned to another line using the slow y axis mirror. Image reproduced from [94]**. Tornado scanning is typically used in photo-bleaching studies where the beam is scanned over a small region of the cell in order to bleach the fluorescence from that region, reproduced from** [95]**. Lissajous scanning is commonly used in endoscope based scanners where the fibre is scanned in this pattern, reproduced from** [96], [97]**.**

In modern LSMs it is common to find overscan of the imaged region. During overscan, the scan line sweeps beyond the region corresponding to the image during the flyback portion of the scan. This is a requirement of the raster scanning pattern and for the mirrors to sweep back to the start position. The time spent over scanning has direct implications: the frame acquisition rate is limited by the overscanned region, and the application of light beyond the region presented in the image may contribute towards photo-damage of the specimen, and may increase the probability of bystander effects [98]. It could be potentially unknown to the user that some of the surrounding area around the field of view has undergone interaction with the scanned laser beam. The implications of this will therefore increase in techniques requiring high power laser sources. The fly back line is also a wasteful process relating to the duty cycle, with the fraction of time scanning the image against the time taken to reposition to the next scan line.

2.2.5 Bidirectional scanning

To increase the image acquisition rate it is possible in modern LSMs to collect data during the backward scan as well as the forward scan of the mirror (which would usually be blocked using the electro-optic modulator (EOM))[85]. This provides the ability to double the data acquisition speed with, for example, 4000 lines per second systems being able to capture 8000 lines per second in a bidirectional scan. However, the changing direction of the scan means the pixels are read out in the reverse order from the previous line of the image. A software correction is applied such that the pixels correspond to the correct space in the image. However, the alignment is generally not exact, resulting in a lateral displacement of the object in each subsequent line scanned. Modern LSMs allow for this to be corrected by observing the image and varying the off set to minimise this displacement [99].

2.2.6 Sources of error in scanning galvanometer systems

Significant errors can be introduced by the electro mechanical properties of the scanning mechanism, where a significantly large and diverse range of properties need to be considered. This list would vary significantly depending on the exact type of scanner, mirrors and servo chosen for the LSM. Image irregularities are often less noticeable in samples that have few straight edges or a repeating structure than a uniform sample such as a square grids [100].

Producing accurate, stable and reproducible images whilst achieving high spatial and temporal resolution in laser scanning microscopy is a major challenge, where it is generally not possible to achieve all aspects simultaneously. This is predominantly a limitation in the scanning speeds achievable, where the scan speed cannot be increased without affecting image resolution. Therefore scanning error will vary with scan speed. However, suitable scanning setting will depend upon the application. For biological applications where changes are occurring on a fast time scale, slow scan rates would be unsuitable but for static or fixed samples a slow scan could provide more accurate images.

2.2.7 Defining jitter and instability

The term jitter is generally associated with temporal fluctuations in the performance of a system [101–103]. Galvanometer scanning mirrors are accepted as providing stable and reproducible scanning, however beam scanning can be affected in a number of different ways arising from temperature effects and mechanical breakdown.

2.2.8 Vibrational error

The effects of vibrations can severely hinder the imaging quality of a system. It is often assumed that isolating the microscope system from external vibrations via an isolation table would then eliminate sources of vibrational error. However, other components of the optical system such as laser cooling fans and the scanning galvanometer mirrors can introduce vibrational noise into the isolated system: these effects, if above a level of tolerance, could reduce the resolution of the system. It is advised that the levels of noise are minimised to less than 10% to the resolution limit for the objective [104].

2.2.9 Measuring instabilities in galvanometers

Present measurement techniques generally utilise a test specimen from which images taken over time can be analysed to determine if scanning inconsistencies are present. For instance, it is possible to compare images of a knife edge at high zoom to measure drifts and scanning error. Also imaging known fixed samples over time can provide insight into scanning drift. However, both techniques require accurate preparation of the sample to ensure it is adequately fixed and immovable and in these methods, errors and drift in the image caused by the sample stage cannot be ruled out [72]. The technique developed in this chapter has the advantage that the sample stage

will not affect the measurement, therefore it can be assumed that the measurements taken only correspond to the scanning mirrors.

Modern galvanometer scanners are quoted by manufacturers as having a short term stability of better than 1 microradian and position sensor nonlinearity of the order of several parts per million [105]. There are very few instances where the performance of the scanning mechanism in a LSM is assessed *in situ* [106], [107]. This is due to the high reliability of scanning devices as quoted by the manufacturers. However, this does not account for degradation in the scanning actuator over time or the effects of external vibrations.

This chapter presents a method which can be easily performed on all LSM systems to accurately determine the stability of laser scanning galvanometers in LSM. The method described requires an externally mounted camera to capture images of the scan pattern over time. Standard image analysis is performed to measure the scanning errors across the raster scan. The effects of digital zoom levels and the subsequent variation in scanning reproducibility and error will be fully investigated using simple image analysis techniques. It is likely that the quantitative measurements obtained could then be used to correct any systematic inconsistencies during post image capture processing.

2.3 Methodology

2.3.1 Microscope Configuration

To measure the scanning stability of an LSM the scan lines were re-imaged in transmission. The experimental setup is shown schematically in Figure 2.5. This method can easily be modified for inverted microscopes, however to demonstrate the protocol an upright microscope platform (Eclipse E600FN, Nikon) was investigated. The microscope platform was coupled to a scan head suitable for CLSM and MPLSM (Radiance 2000MP, Bio-Rad). This system had an Argon-ion fibre coupled laser for confocal imaging as well as a femtosecond-pulsed Ti:Sapphire laser for multi-photon imaging (Chameleon, Coherent). The 488nm Argon ion laser line was used in this study.

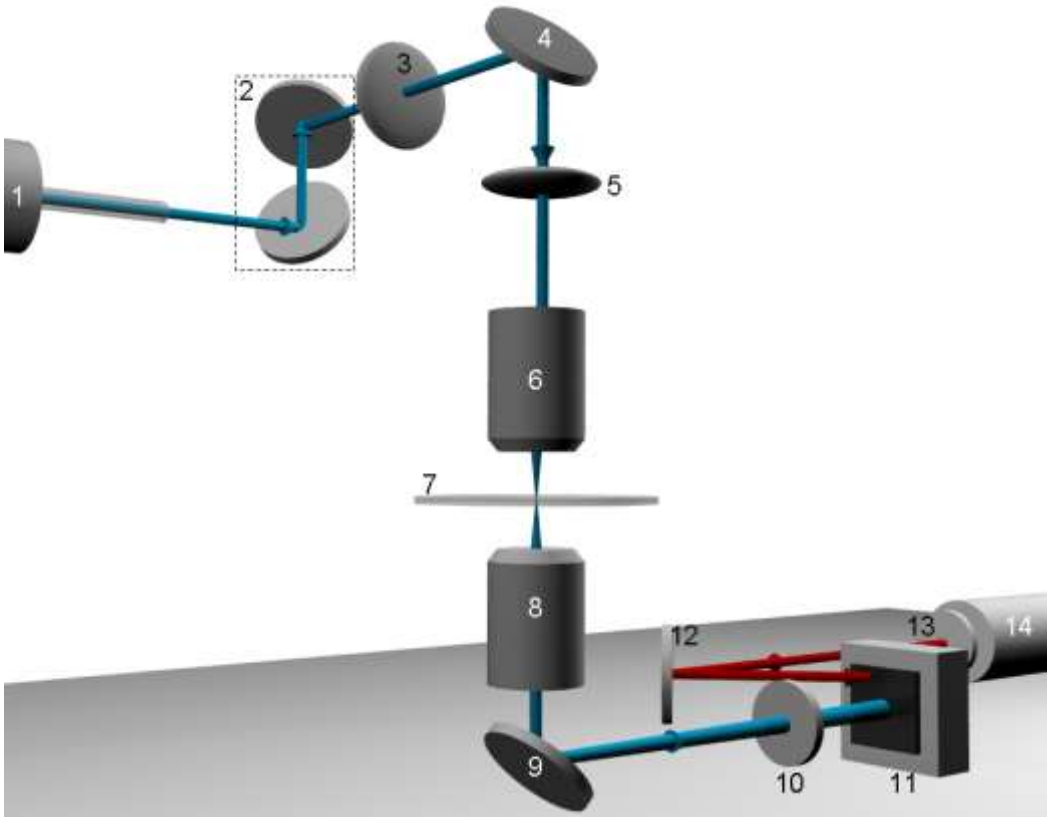

Figure 2.5- Schematic of set-up to measure line scan properties of LSM. The fibre coupled Argon Ion laser (1) was coupled to the Bio-Rad 2000 scanhead (2). The beam was subsequently directed to the back aperture of the first 20x/0.75N.A air objective lens via mirror 4. The laser beam was able to overfill the back aperture of the objective via scan lens 3 and the tube lens 5. There was no

sample on the sample stage (7). Another 20x/0.75N.A objective lens was secured in the condenser mount using a custom made adapter (8). The collected laser light was then directed towards the monochrome CCD camera (Nikon) (11) via another high reflectance mirror (9) to provide snapshots of the scan. In order to avoid saturating the camera an ND=6 filter (10) was mounted in front of the CCD camera. To monitor external stability a Helium-Neon laser with an emission wavelength of 633nm (14) was directed to the camera using mirror 12 and ND=4 filter (13) to ensure the image was not saturated, the beam spot is visible on all images captured with the CCD camera and the beam spot is used as a stability marker.

To re-image the scan lines a 20x/0.75 N.A. objective lens was placed in the position of a condenser lens. The condenser lens was removed to improve the sharpness of the imaged raster scan. This collection objective lens was aligned with the microscope objective lens using the centralising controls on the condenser mount. Below the collector lens an aluminium mirror suitable for use at visible wavelengths was mounted at 45° to reflect the scan pattern to the side of the microscope. A monochrome camera (Ds-Qi1Mc, Nikon) mounted at the side of the microscope platform on a highly stable camera tripod was used to take images of the beam scanning. This method of mounting the camera was found to be more stable than mounting with off the shelf optical posts and mounts; alternatively a bespoke ultra-stable mount could be made for this application. To avoid saturation of the camera detector a neutral density filter (ND=4) was mounted in the beam path. A bench mounted Helium-Neon laser (Melles Griot) was aligned on the camera detector using two high reflecting aluminium mirrors. This source provided a laser output of 5mW at λ=633nm.This external laser source was used to monitor environmental vibrations on the optical bench and the camera, acting as a stability marker. Again to avoid saturation by the Helium-Neon beam an ND filter was placed at the output of the laser (ND=6).

The scan imaging settings were controlled using the Lasersharp 2000 (Bio-Rad) software where the average laser power, number of scan lines and scan speed could be modulated. To test this method, images of scanning at 1x zoom and at 5.5x zoom were tested at constant scan speed of 500 lines per second and 64 x 64 lines. The 5.5x zoom was selected to show the full scan in the image, whereas the 1x scan

overfilled the camera detector such that only 25% of the scan was imaged. The camera was first aligned using high zoom such that the scan pattern was centred on the detector. The zoom was then reduced to 1x, such that it can be assumed the imaged region of the 1x scan is the central part of the full raster scan. To correctly capture the full scan on the camera, the exposure time on the external Nikon camera was approximately matched to the frame rate of the LSM. In the experimental results presented in this chapter were taken with 166 lines per second (lps) scan with 64x64 lines corresponding to a frame rate of 2.59Hz, and a pixel dwell time of 83.71μs. The camera images were recorded with an exposure time of 1/10 s. This setting was chosen to achieve images with high signal to noise ratio, whilst containing most of the scan in a single frame. The frame acquisition rate of the camera was programmable and therefore this technique is not limited to the scan rates for which results are presented in this chapter.

2.3.2 Image analysis and co-ordinate system

In order to effectively sample the full scan region on the external camera system, the images obtained were segmented as shown in Figure 2.6 and Figure 2.7 for 1x and 5.5x zoom scans respectively, where intensity line profiles were obtained from ImageJ and separated into image coordinates in the x and y planes of the image. Only a sample of the data was selected, which best described the scanning properties over time. The images were analysed at 20s intervals corresponding to every second image from t=0s to t=490s.

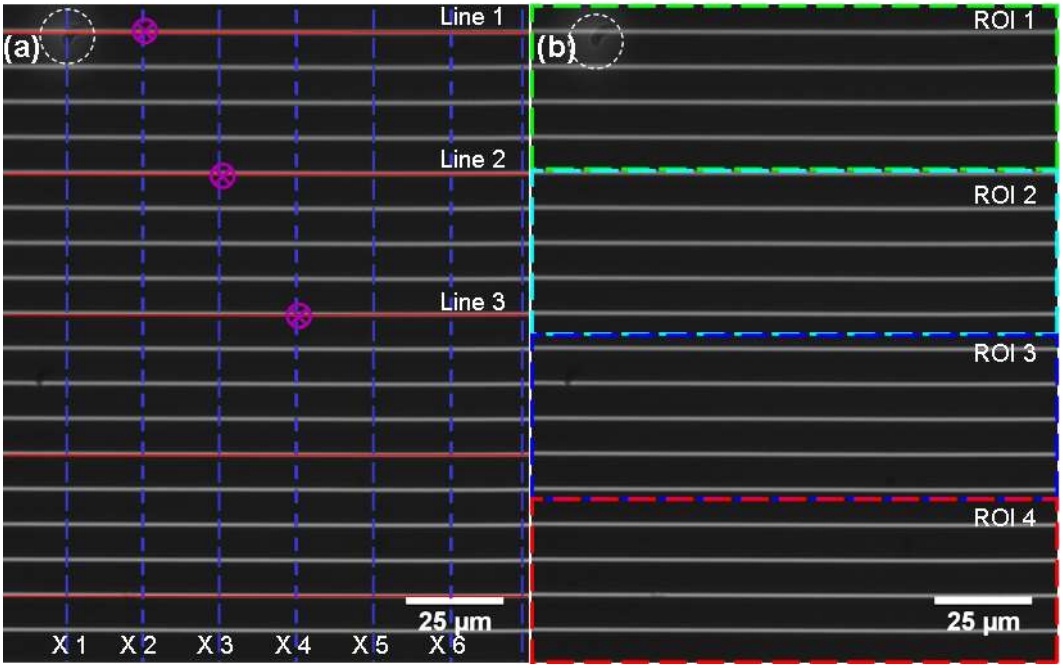

Figure 2.6-(a) line number and x scan position grid used to measure the scan shift at each point, (b) Segmentation of 1x images for surface plot image analysis showing regions of interest (ROI) 1-4. These are shown over the image taken at time t=0s. The grey lines are the scanned beam measured by the monochrome camera in the far-field.

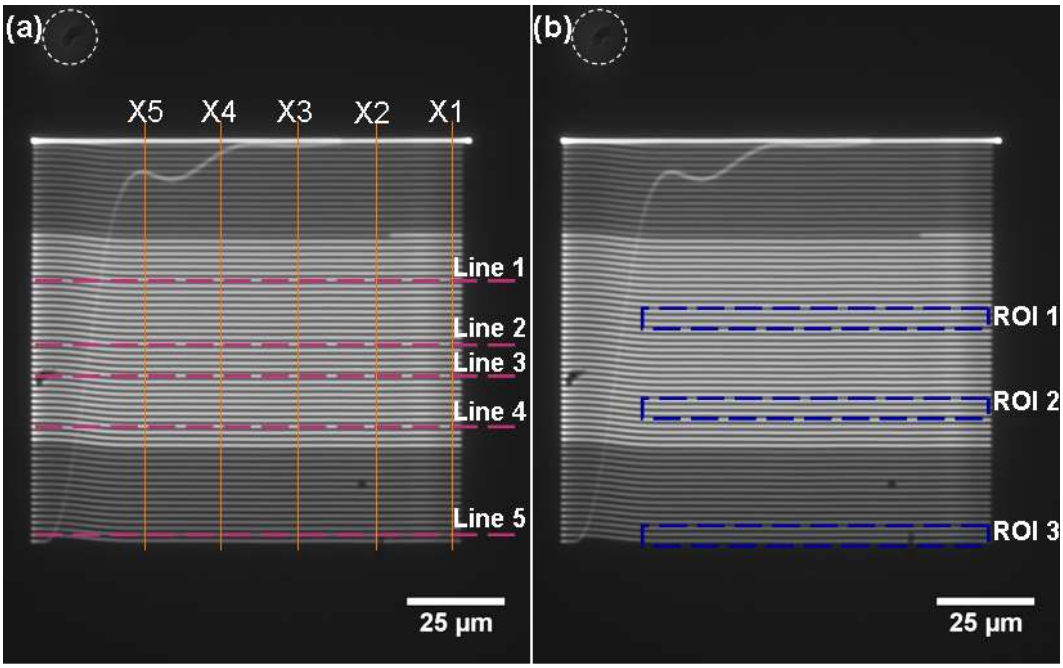

Figure 2.7- (a) line number and x scan position grid used to measure the scan shift at each point, (b) Segmentation for surface plot image analysis showing ROI 1-3 for 5.5x zoom scanning. The images presented are an overlay over two time points to show the complete raster pattern, where some lines of the scan are not captured in a single frame by the CCD.

The image sequence over time for each zoom level were then analysed using ImageJ using two methods. The first method was used to get a qualitative representation of the scanning shifts over time, to do so the image difference was calculated using the inbuilt image calculator function in ImageJ. The image difference calculation subtracts one image from the other and then represents the magnitude of the difference in terms of the intensity in a new image. This is explained in terms of a single intensity line profile showing a representative displacement in position in Figure 2.8. The subtraction of the intensity profiles and the magnitude of this difference are plotted on the same x-axis.

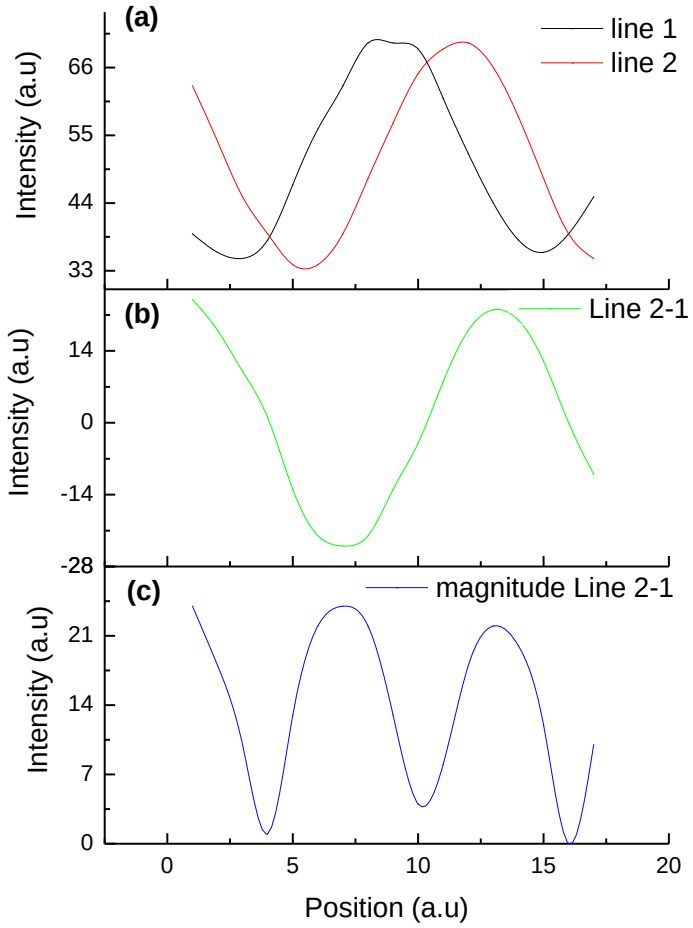

Figure 2.8- ImageJ difference calculation shown in three steps (a) Intensity profiles from image, (b) Subtraction between intensity profile line 1 and line 2 and (c) the magnitude of the difference between line 2 and line 1 (equivalent to ImageJ difference calculation).

The calculated difference was plotted using the surface plot option, providing a 3D representation of the variation in intensity, and the position variation shown by the image difference, across the x and y dimensions of the image. This was carried out for the four regions marked in Figure 2.6(b) and the three regions shown in Figure 2.7(b).

The second image analysis technique provided quantitative data on the magnitude of the scanning drifts, this method used the intensity line profiles at the cross over points in y scan line position and x scan position as indicated Figure 2.6(a) and Figure 2.7(a). The shift at these coordinates was measured as the position variation between the maximum intensity points on the intensity line profile. This provided a measure of the y scan variations over time and over x by selecting different points on along the x direction of the image.

2.3.3 Camera Calibration

To calibrate the camera detection system the image dimensions of the field of view (FOV) given for the 20x/0.75 lens by the Lasersharp software at these image acquisition settings were used. The quoted dimensions are used for quantification via image analysis by measuring the size of the raster scanned pattern on the CCD and making this equivalent to the FOV dimensions. The image taken for calibration is shown in Figure 2.9.

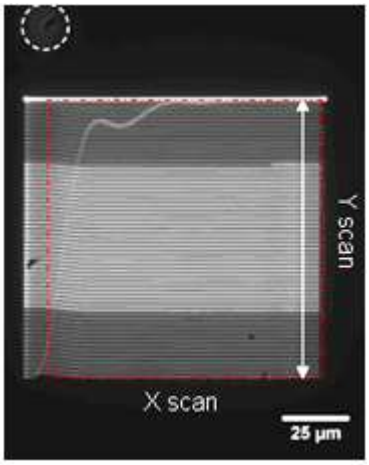

Figure 2.9- photograph of scanning pattern at 5.5x zoom used for image calibration. The y dimension of the scan denoted by the white arrowed line was used to calibrate the image with the given dimensions for a 5.5x zoom scan by the Lasersharp software. The region corresponding to the image is shown by the red box, indicating the portion of overscan in the x scanning mirror. The circle in the top LHS of the image corresponds to the stability marker.

It can be seen that the x and y dimensions are not equal with overscan in the x galvo mirror. The region corresponding to the imaged region in the LSM is shown by the marked red region in Figure 2.9. This was then used with the stated 5.5x zoom dimensions to calibrate the pixel size on the camera by measuring the dimension of the y scan in pixels on the detector and calibrating with the dimensions given by the software. At 1x zoom the raster scan pattern over filled the 2/3 inch active region of the camera. The raster scan pattern is therefore significantly larger at the camera detector than at the sample plane. The shifts in scan lines are therefore more pronounced. Measurements of position variation over time were made in terms of pixels on the external camera and then the corresponding dimension at the sample plane calculated using the calibration.

2.3.4 Stability test

To monitor the external sources of vibration which may affect the camera stability the external bench mounted Helium-Neon laser was used as a marker as shown in Figure 2.5. To test this stability measurement external vibration was applied whilst the camera was acquiring images, by tapping the optical bench. It was then possible to observe any variation in the external beam position on the detector over time, for the case of applied external vibration as well as for normal operation conditions.

2.4 Results

2.4.1 Calibration

The images were calibrated using the 5.5x zoom images acquired by the external camera system. The stated dimension of the image for the 20x/0.75 N.A objective lens at 5.5x optical zoom was 103μm, this correspond to a calibrate pixel dimension of 7.753 pixels/micron. This calibration was applied to all images used to test this method.

2.4.2 Stability testing

To test the action of the stability marker over time the intensity over the region was monitored to view any shifts in position. In addition to this the difference in images from time t=0s to each later time point was calculated using ImageJ, providing an indicator of any beam shifts, i.e. with no shift the image difference would be equal to zero and therefore the image over the selected region would cancel out completely. In the instance where the position has shifted, the images do not completely cancel, and the difference in intensity between the images is visible. Figure 2.10 shows the stable beam and the induced vibration shifting the marker, showing that this technique is an effective monitor to test the stability of the external camera system.

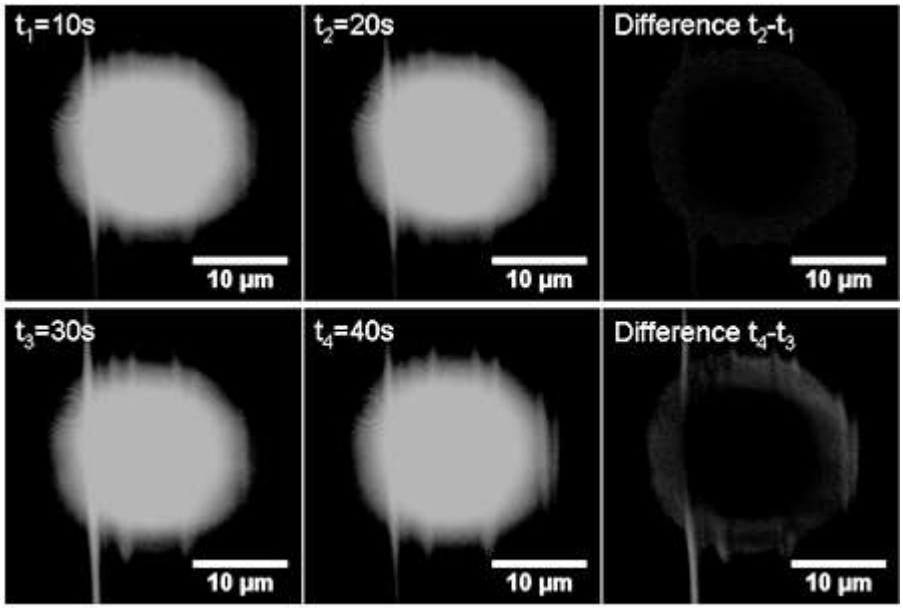

Figure 2.10- Selected images showing the external marker for stability. The top row shows the case before external vibration was applied and the bottom row shows the case where external vibration was applied. The difference of the images calculated (ImageJ) before and after external vibrations are also shown.

The images used to test the scanning stability of the beam over time for both 1x zoom and 5.5x zoom did not show any shift in the external beam position marker.

2.4.3 Testing scanning mirrors at 1x optical zoom: y-drift

A series of transmission images were taken of the raster scan at 1x zoom over a period of 5 minutes. Selected frames are shown in Figure 2.11, with images taken at t=0s, t=250s and t=490s.

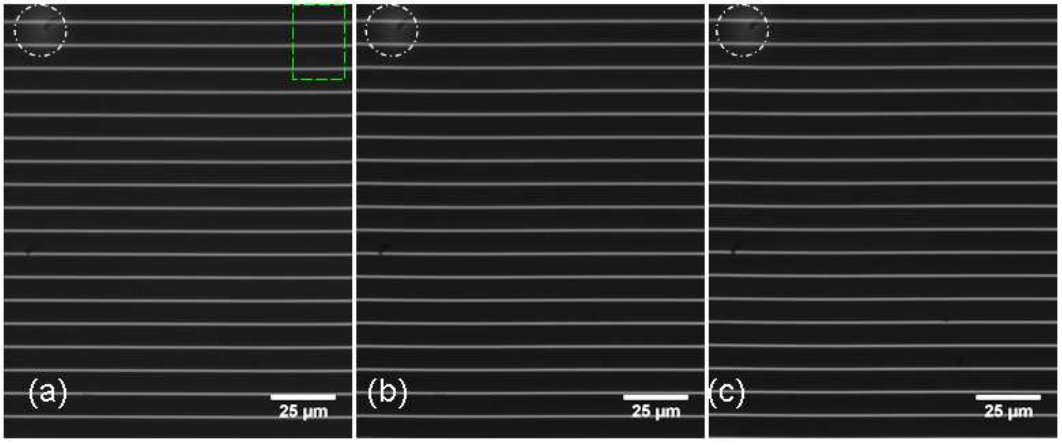

Figure 2.11- Images taken of 1x zoom scan at 166 lines per second (lps), 64x64 line scan at time (a) t=0s, 9b) t=250s and 9c) t=490s. The circle region shows the beam stability marker, the green rectangle shows the cropped region for further image comparison.

The images in Figure 2.11 (a-c) show 25% of the full scan at 1x zoom. From alignment on to the external camera, the imaged region is approximately at the centre of the full scan. The images also show the stability marker used to rule out any external vibrations. To show the variation in scan line position from the start position at t=0s the final position at t=490s a cropped and digitally magnified region of the images in Figure 2.11 are shown in Figure 2.12.

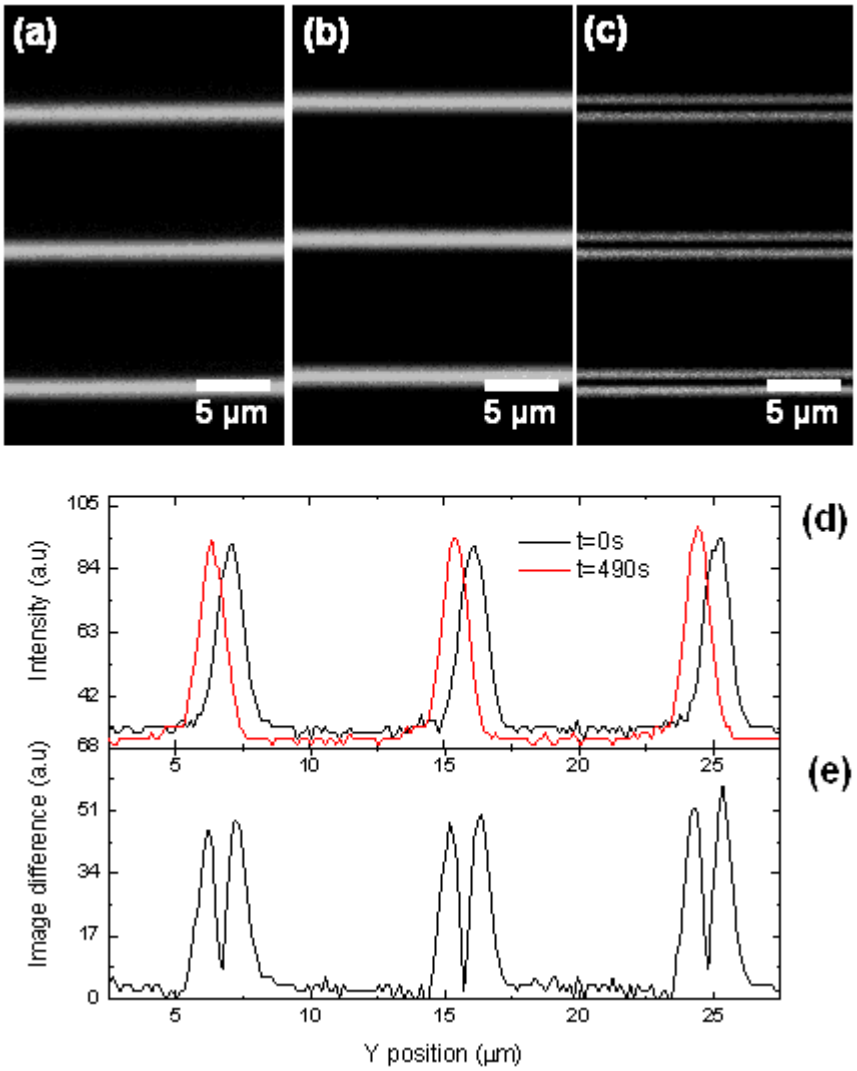

Figure 2.12- Cropped regions of Figure 2.11 (a) and (c), showing drift in y scan lines from start position at (a) t=0s to the end position at (b) t=490s. The image difference calculated using ImageJ is shown in part (c). Intensity profiles across the three y scan lines are shown in (d) with the plot of the image difference plotted in (e). The region is cropped as indicated in Figure 2.11.

It is clear from Figure 2.12 that the position of the y scan lines drifts over time with the end position at t=490 s higher than the initial scan line position at t=0 s. The image difference plotted in Figure 2.12c shows the regions of overlap correspond to a minimum in intensity as they cancel out in the subtraction, as shown in Figure 2.12e. The two regions of higher intensity occur due to the image difference being equal to the magnitude of the intensity difference. To investigate this observation further, surface plots of the images at each time point were produced to show the changes in position over time over the regions of the image defined previously. The images were divided into 4 regions such that only 4 scan lines were in each surface plot as shown in Figure 2.6, but the full x scan across the line is shown in the surface plot. Surface plots are shown in Figure 2.13 at the start position of t=0 s and at the end position of t= 490 s for regions 1 and region 3. Region one corresponds to the top of the image, where the stability marker is observed. This marker is shown clearly in the surface plots at both time points. The orientation of the images has been changed from the image direction shown in Figure 2.11 and Figure 2.12, with the x position on the y axis and y position on the x-axis, because the shifts in position are clearer in this format on a surface plot. Region 1 and 3 were selected to give a representation in variations across the full image.

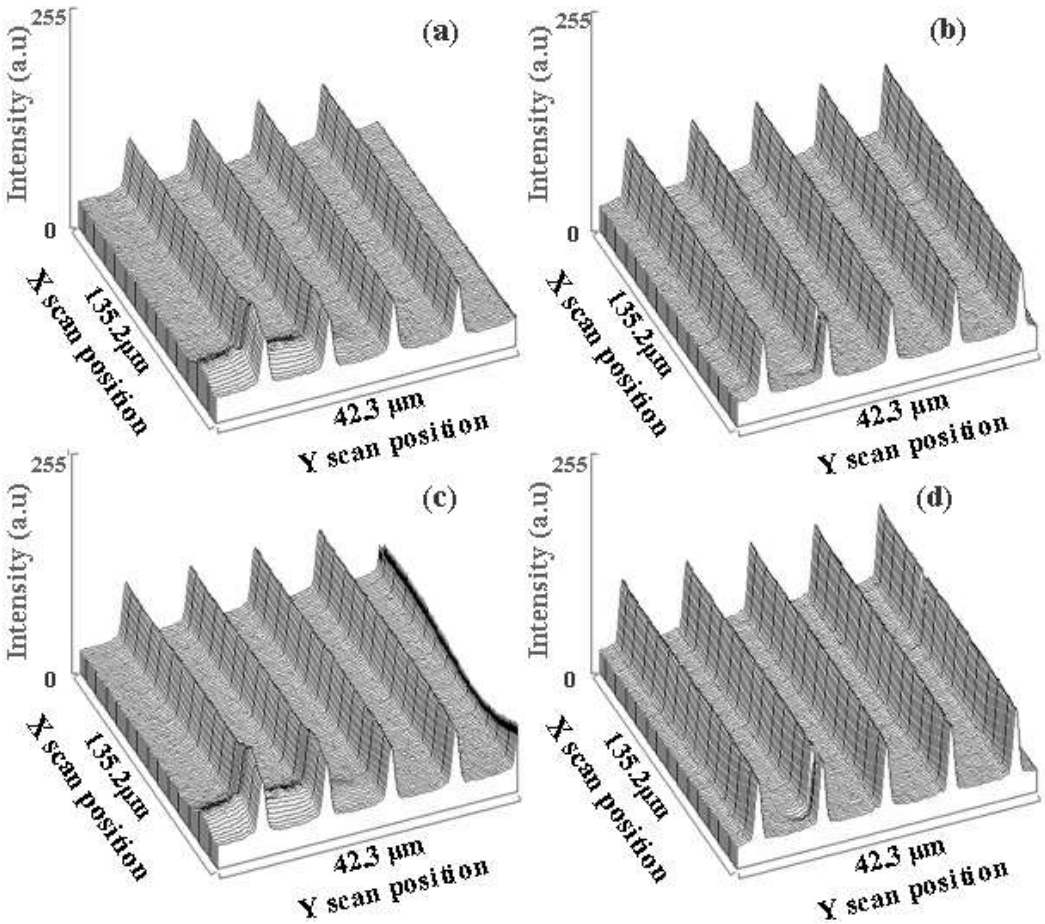

Figure 2.13- Surface plot of scanned lines over a 39.5 micron region of the image (a) region 1 at t=0s, (b) region 3 at t=0s, (c) region 1 at t=490s and (d) region 3 at t=490s. Note that axes are reversed from the images shown previously denoted by x and y label. As these are 8-bit images, the z axis is image intensity, and ranges from 0-255. Regions previously defined in Figure 2.6b.

2.4.4 Testing scanning mirrors at 1x optical zoom: y-drift relative to x-position

However, analysing the images in this way does not account for changes in x scan positioning as in the 1x zoom case the scan over fills the active region of the camera detector. Thus, measuring shifts in the start and end x positions of the scan are not possible. However, to assess changes in the y scan shift with x scan position the difference between the images at each later time point and the initial image are computed using ImageJ. Surface plots of the difference are shown in Figure 2.14 and Figure 2.15, for region 1 and region 3 respectively showing the x and y position changes over time.

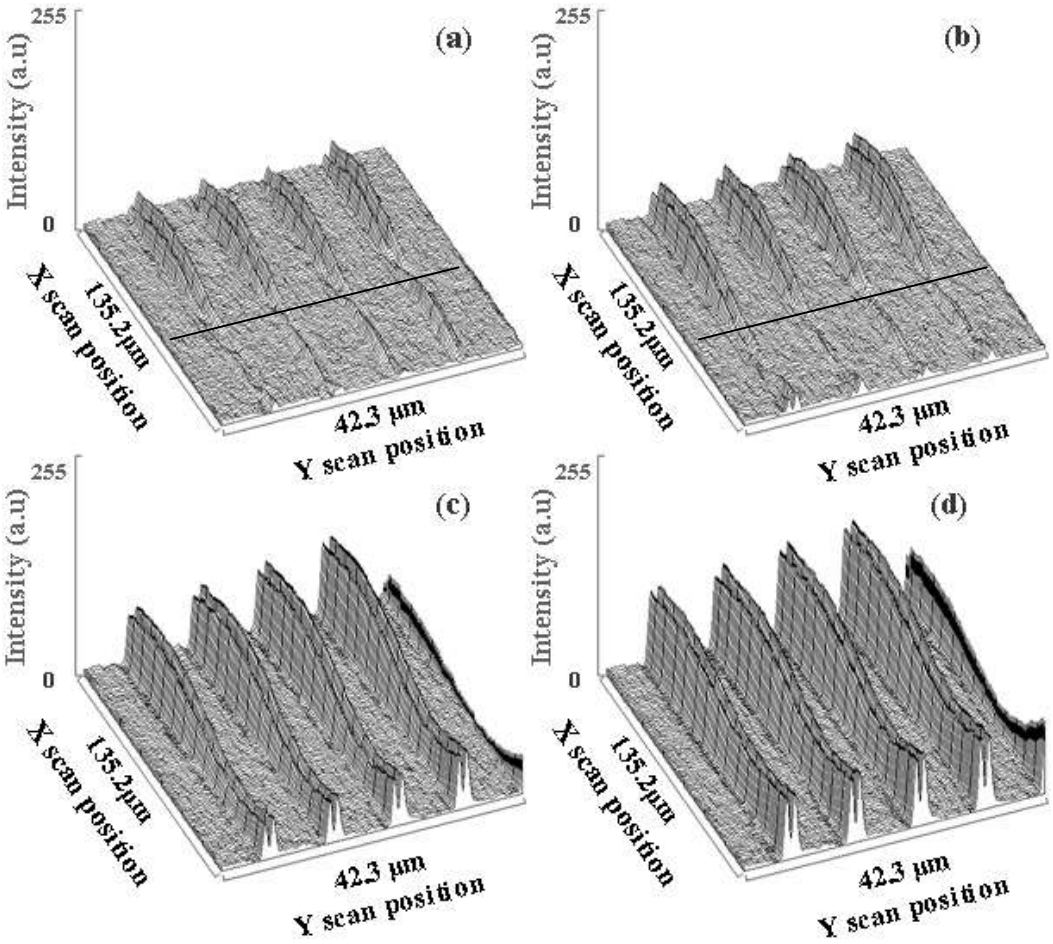

Figure 2.14-Three-dimensional surface plots of the image difference from the start position at t=0s for scanning time (a) t=40s, (b) 160s, (c) 250s and (d) 490s, data from region 1 as defined in Figure 2.6b.

In Figure 2.14 the image differences over time are shown in region 1, it can be seen in early time points (a and b) there are positions across the x direction of the scan where there was no shift in the y position of the scan line these are highlighted with the blue lines in Figure 2.14. This effect is consistent with the effect of 'wobble' in the x galvanometer mirror [105], whereas, at later time points (c) and (d), the scan line shift in the y direction was found to be more consistent across the x direction. The increase in the amplitude of the calculated image difference over time corresponds to an increase in the magnitude of the drift of the y scan position, therefore the difference in position of the scan line from t=0s is greater at time points (d) and (e) with an approximately linear increase over time.

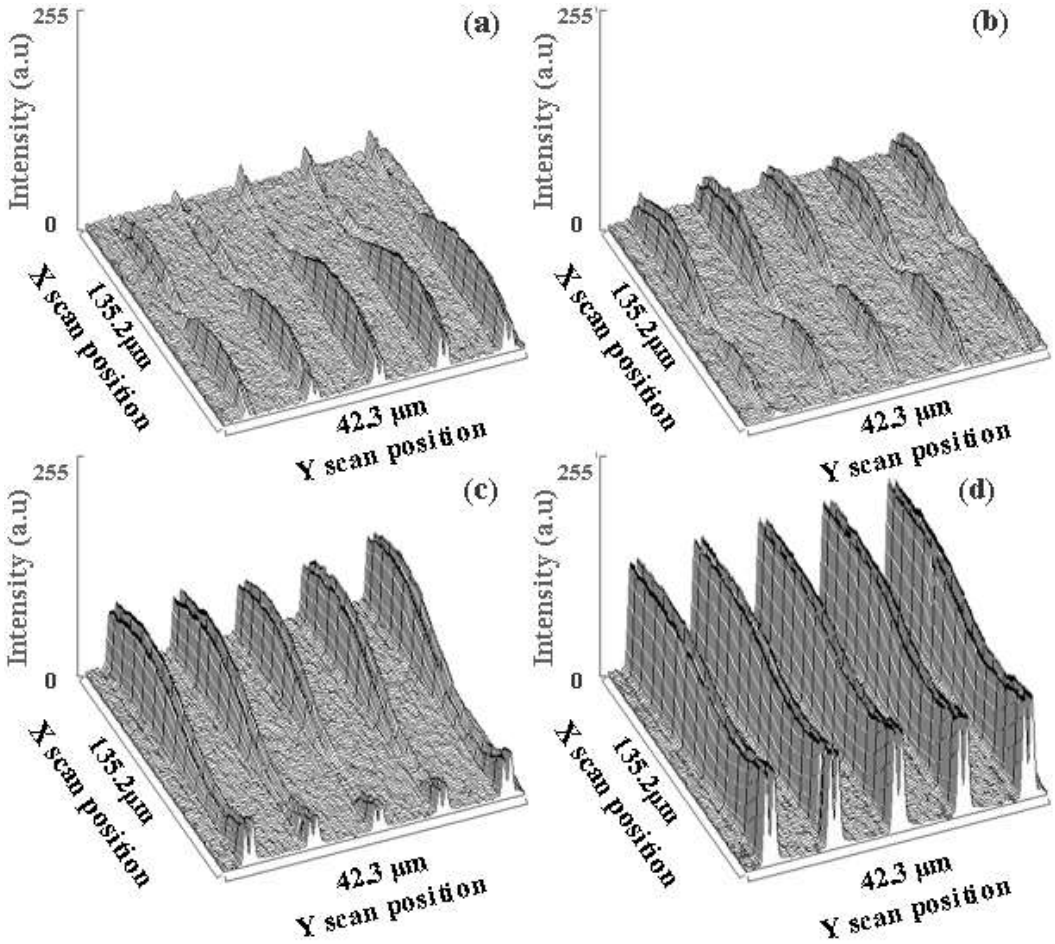

Figure 2.15- Surface plots of the image difference from the start position for scanning time (a) t=40s, (b) 160s, (c) 250s and (d) 490s in region 3 of the scan as defined previously.

The surface plots taken for region 3 are shown in Figure 2.15 as for region 1 it can be seen that at the early time points (a-c) the position of the lines are more irregular over the x direction than the later time points. However, the top of the surface plot, corresponding to the LHS of the x scan, is more irregular. The opposite was shown in Figure 2.14. Therefore, the variation in scan drift with the x direction was found to be nonlinear across the whole image over time. A reproducing pattern over the time course investigated was not observed.

2.4.5 Testing scanning mirrors at 1x optical zoom: x-position over time

The intensity profile of scan line 1, as indicated in Figure 2.6, at x scan position 1 is shown in Figure 2.16 for varying time points. It can be seen that the there is a significant spread in position of the line over time, where the end position is 0.55 μm from the start position. Whereas, theoretically if the scanner was functioning as designed and stated by manufacturers the intensity profiles in Figure 2.16 should overlap spatially over time.

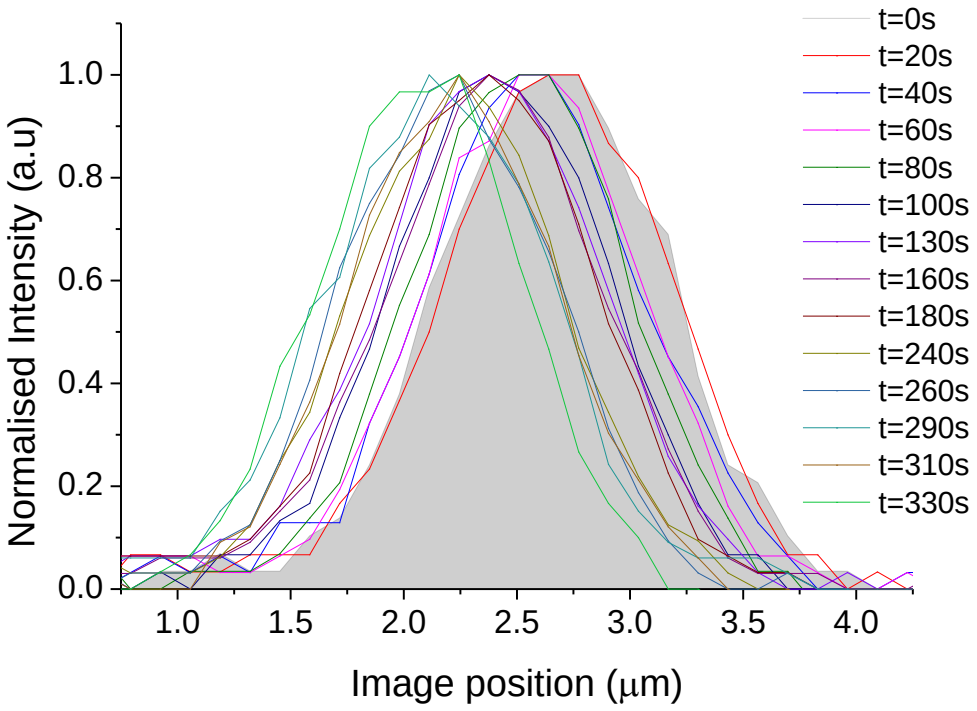

Figure 2.16- Line intensity profiles over line 1 at position y=0 from time 0s to t=330s. The intensity profile of the line at t=0s is denoted by the shaded region under the curve.

The scan shift over time, from the start position, measured from Figure 2.16 is shown in Figure 2.17. The legend corresponds to line 1, x position=0 which was defined previously in Figure 2.6. It can be seen that the shift in line position increases linearly over time. The scan drift is taken as the gradient of the best fit line which was found to be 1.63 ± 0.1 nm/s where the error is the calculated error in the gradient of the best fit line. Note that this technique is not measuring below the diffraction limit and the shifts at the sample plane are inferred using the calibration of the image on the camera with the known dimensions of the scan pattern at the sample.

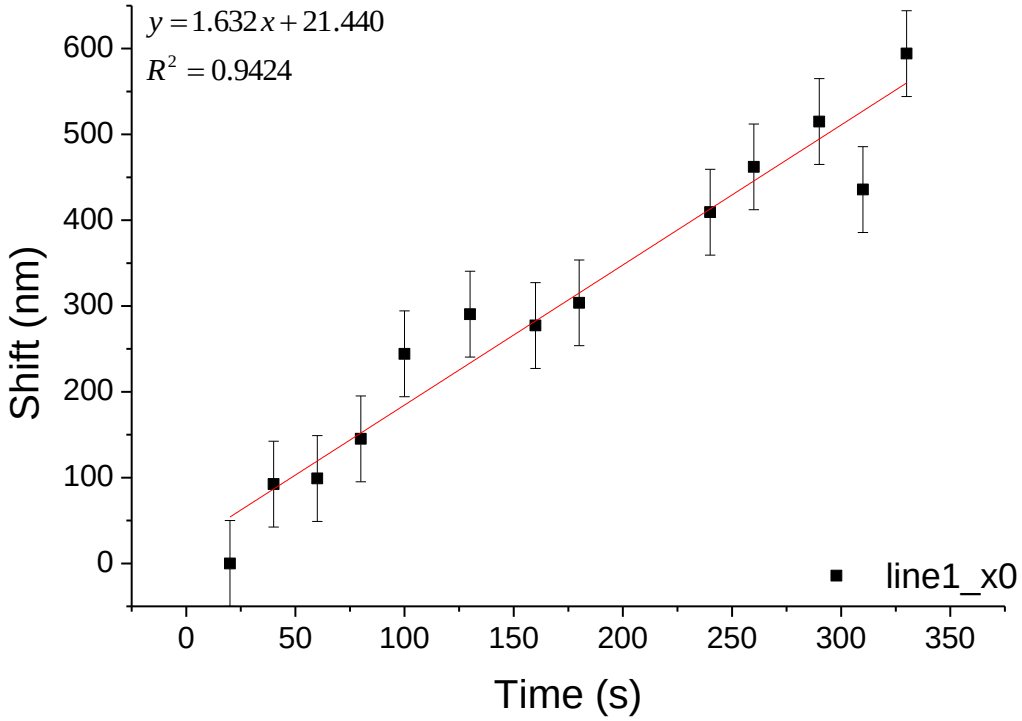

Figure 2.17-Measured shift in scan position of line 1 at x=0 over time.

The determined scan drifts for two other scan lines, line 2 and line 3 defined in Figure 2.6, at the same x scan position (x=0 as defined previously) on the image are plotted in Figure 2.18. The gradients for line 2 and 3 were found to be 1.93 ± 0.1 nm/s and 1.95 ± 0.1 nm/s respectively. This indicates an increase in scan drifts from the top of the raster scan to the bottom. However, to build the fullest picture of the variation in scan drift, a line by line analysis would be required over time across the full image.

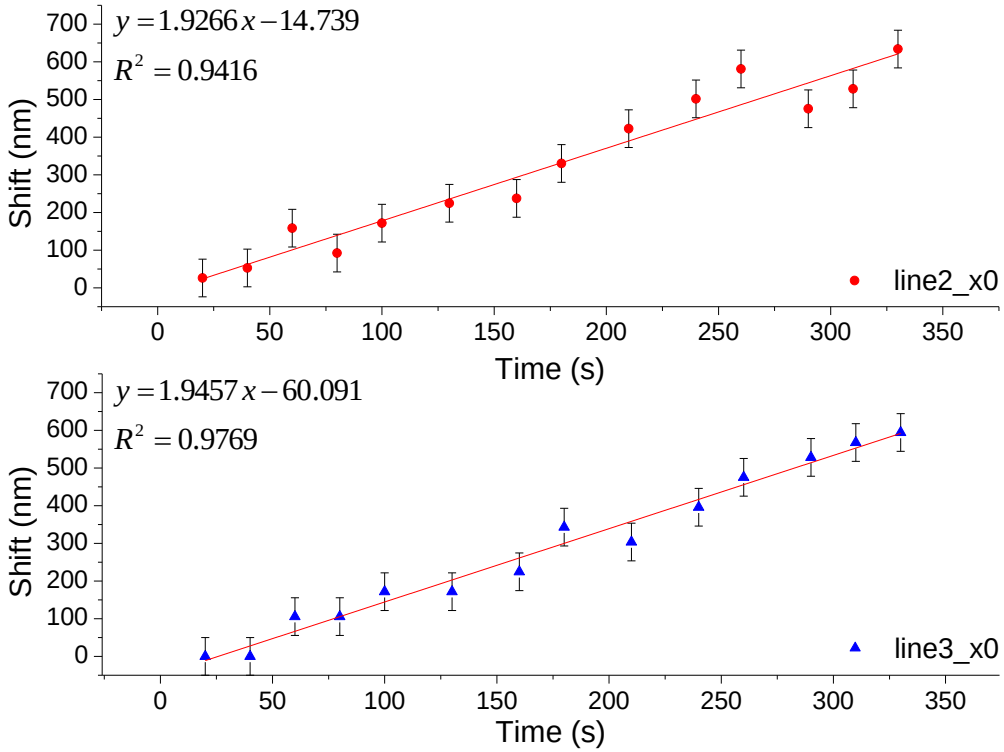

Figure 2.18- Measured scan position shift of line 2 and line 3 at x=0.

The plots shown in Figure 2.17 and Figure 2.18 were repeated for varying points along the x scan direction. The scan drifts as a function of x position are shown in Figure 2.19.

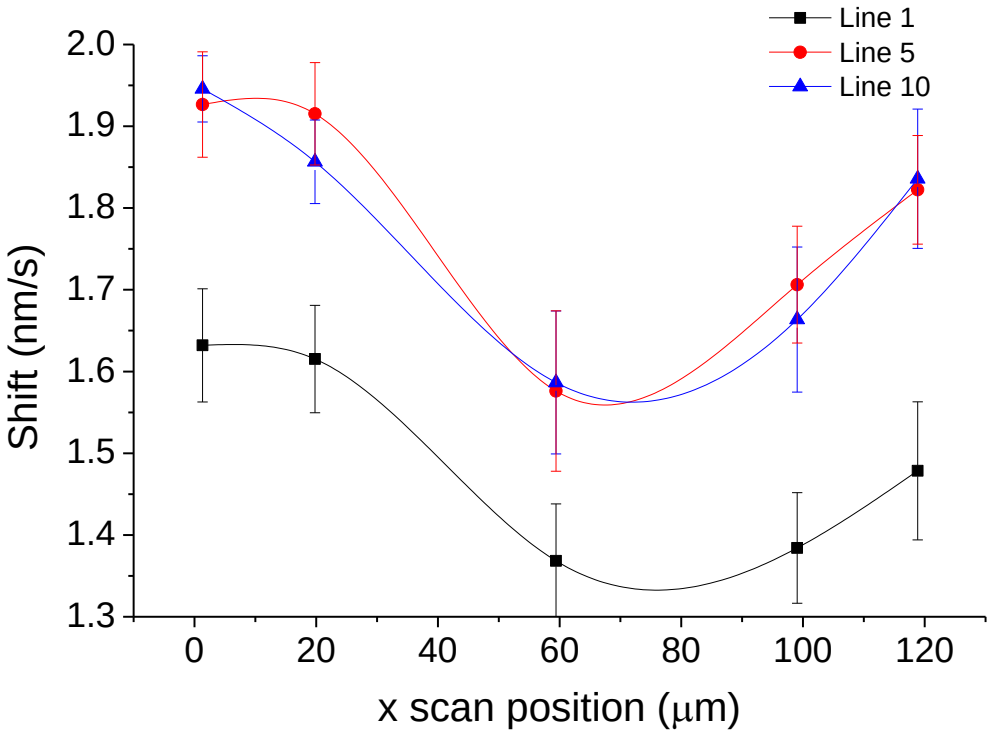

Figure 2.19- Measured scan drift across the x scan positions. Corresponding to the scan drift as a function of the fast scanning (x) galvanometer mirror. Error is standard deviation in the mean measured scan position shift.

It can be seen that the drift is not constant over the x scan of the mirror, indicating wobble in the mirror mechanism. The images at 1x zoom correspond to 25% of the full x scan, thus the relationship shown in Figure 2.19 could be periodic over the areas either side of the region imaged. Therefore, the results presented for the zoom=1x are only representative of the central portion of the scan.

2.4.6 Testing scanning mirrors at increased (5.5x) optical zoom

To further apply this measurement technique a series of images at 5.5x zoom were acquired at 10 second intervals as described previously. The advantage of this zoom level is that the full scan shift can be measured applying the same image analysis techniques outlined previously for 1x zoom. Surface plots over two regions of the scan are shown in Figure 2.20. This shows the position of 3 scan lines from start time t=0s to a late time point after t=450s of scanning. The shift in scan position is clear over both regions.

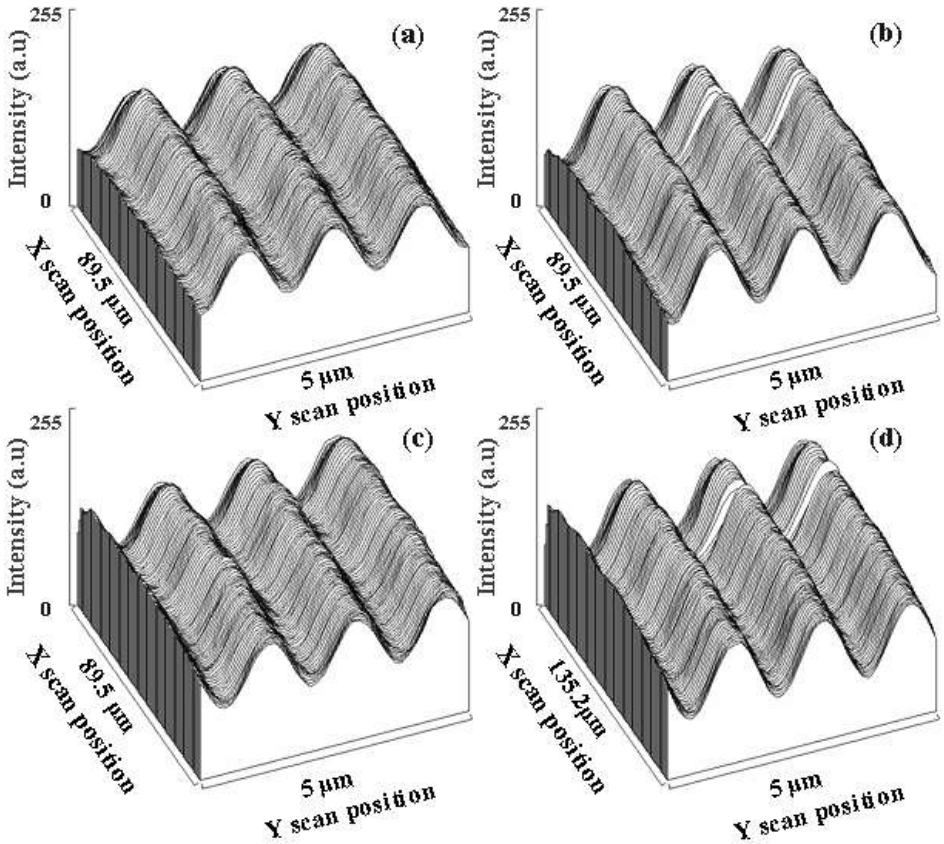

Figure 2.20- Surface plots over region 1 at time (a) t=0s and (b) t=450s. Surface plots of region 3 are shown at time (c) t=0s and (d) t=450s.

The calculated image differences in position across three regions are shown in Figure 2.21, where the first row shows the shift in the earliest time point t=0s. The magnitude of the difference is lowest at this time point, which is shown by the reduced intensity in the difference of the images. As well as being lowest the shift is most non-linear at the initial frames of the scan, which is shown by the irregular regions of overlap, in particular over region 2.

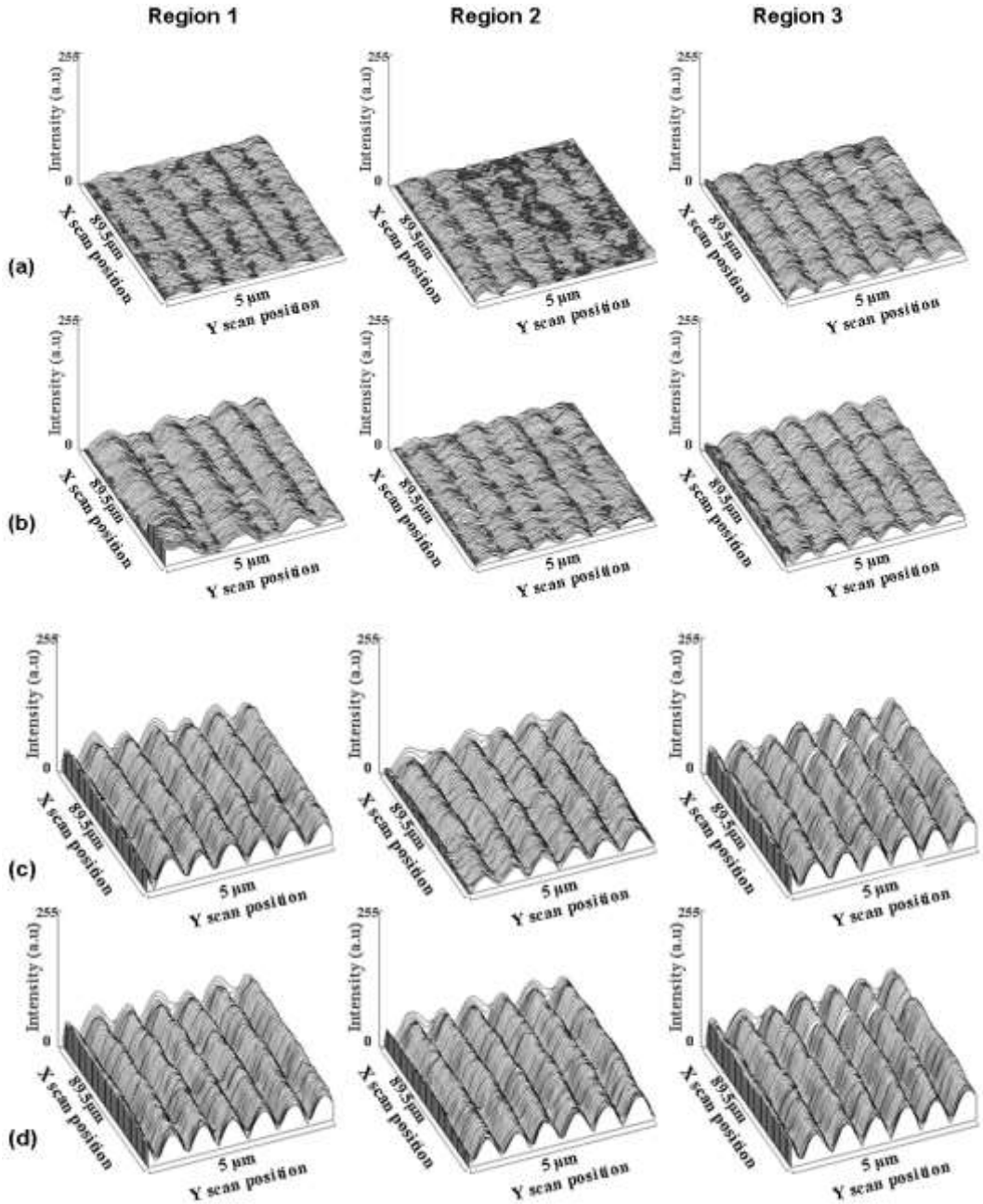

Figure 2.21- Surface plots of the difference between the image of the scan at (a) t1= 100s, (b) t2=200s, (c) t3=360s, (d) t4=450s and the image at t0=0s. The columns are arranged for regions 1-3 from left to right.

To investigate both x and y scan drift a higher zoom scan was required such that the full scan fits within the detector dimensions. The plot of line intensity over the same x, y coordinates is shown in Figure 2.22 for one line of the 5.5x zoom scan. As for the 1x zoom case a significant shift in the line position over time was observed.

However, the shifts were in the opposite direction. Despite an initial drift in the same direction as the 1x case the scan lines drift in the opposite direction; this is defined as a negative shift. The shifts are plotted against time in Figure 2.23.

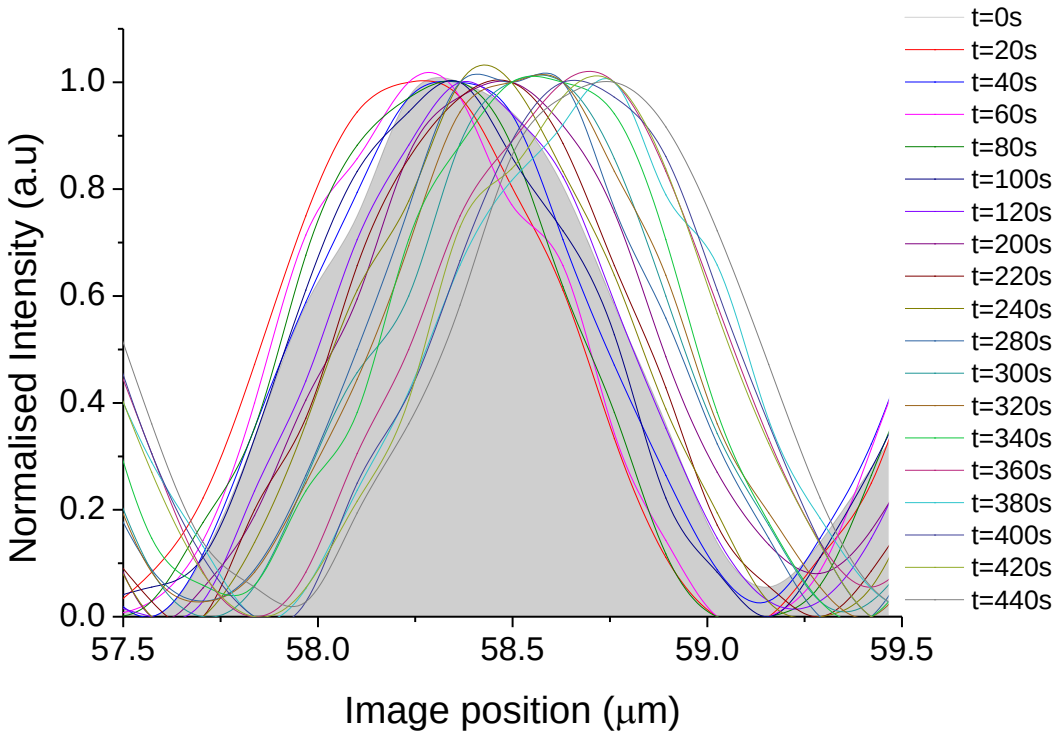

Figure 2.22- Intensity profile of scan line 2 at y=0 at time t=0 seconds to t=440 seconds the intensity profile corresponding to the start position is shaded.

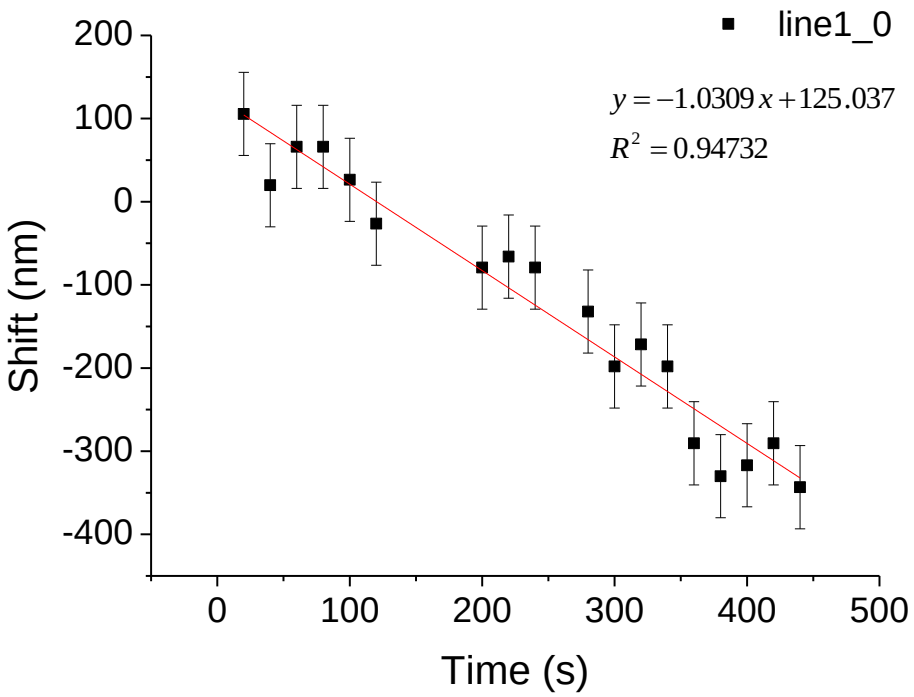

Figure 2.23- Measured shift in scan line position over time period of continual scanning.

The measured shift over time for 3 other y scan lines are shown in Figure 2.24, where the drifts were measured to vary from 1.03 to 1.27 nm/s. Thus the expected scan drift would be approximately 2μm after continuous scanning for 30minutes. The scan drifts plotted for different y scan lines, on the raster pattern, show a variation of 0.25nm/s in the measured drifts. This would be significant when correcting the images post acquisition to account for scan line position shifts at varying x and y scan coordinates.

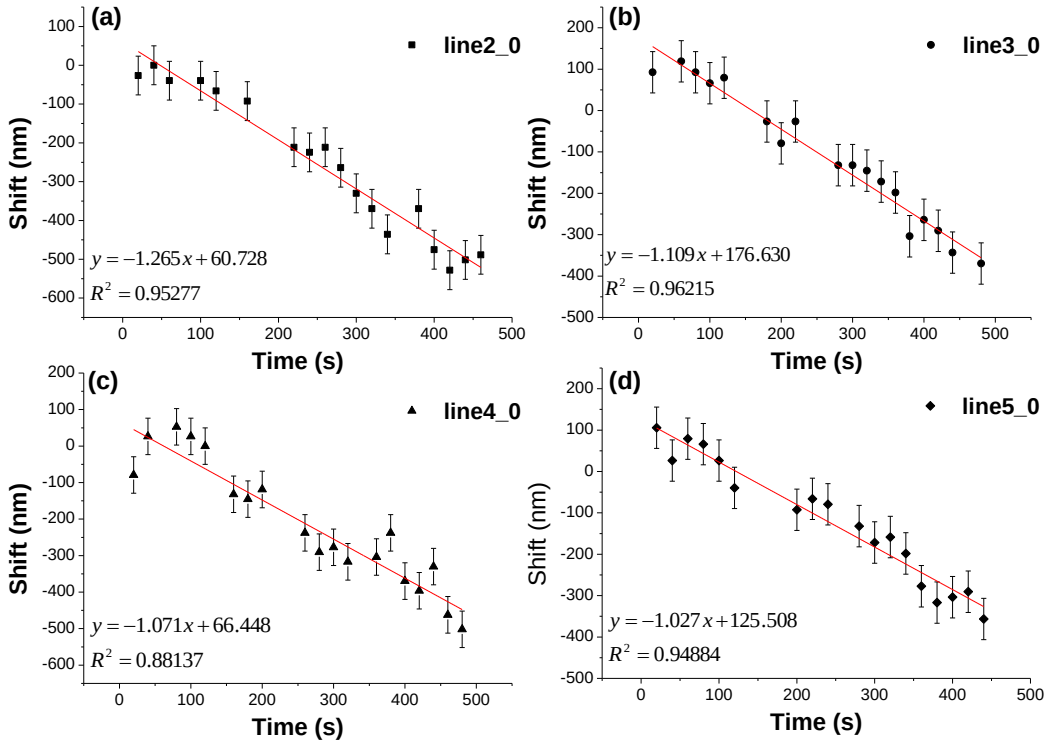

Figure 2.24- Measured shift in scan line position over time period of continual scanning for (a) line 2, (b) line 3, (c) line 4 and (d) line 5 as indicated in Figure2.7.

The measured scan line drifts obtained from the analysis shown in Figure 2.23 Figure 2.24 as well as the corresponding plots for each line for every x coordinate, defined in Figure 2.7 are shown in Figure 2.25. This shows the variation in y scan line position as a function of the x scan galvanometer stability. These types of drifts should be minimised using feedback, suggesting that there is a fault in the feedback position sensors.

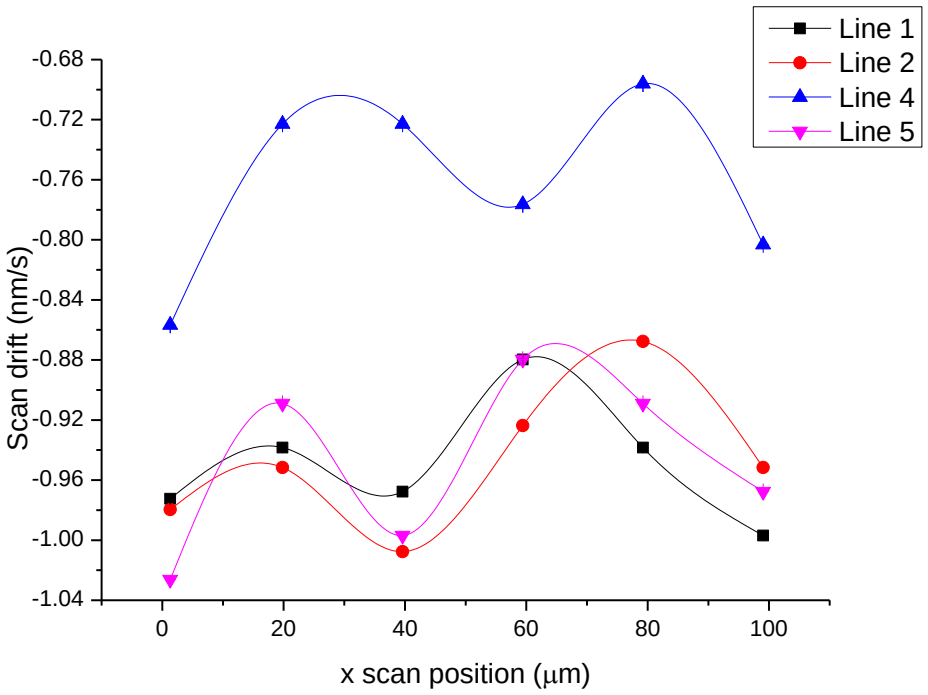

Figure 2.25-Scan drift obtained from Figure 2.24, at varying x scan position for each scan line indicated in Figure 2.7. Error is standard deviation in the mean measured scan position shift.

From Figure 2.25 it can be seen that the magnitude of the measured y scan drift varies periodically across the x position on the image. This shows a non-linearity in the scanning mechanism across the x dimension of the raster pattern. However, for scan line 4 the magnitude of the drift is lower than for the other lines sampled. This suggests that the effects of scan irregularities are not consistent across the full raster scan. This study only presents data for 5 out of 64 lines scanned, thus a full analysis across each scan line would be required to fully quantify positioning accuracy.

As described previously the advantage to using the high zoom scan to analyse scan shift is that the full scan region is viewed in one image. These images therefore provide a means to investigate any shift in the x scan position. This provides additional information to the y scan shift as a function of x position shown in the previous figure. This is shown in Figure 2.26, where the calculated image difference at t=450s to t=0s shows inconsistencies in the start and end position of the scan line over time.

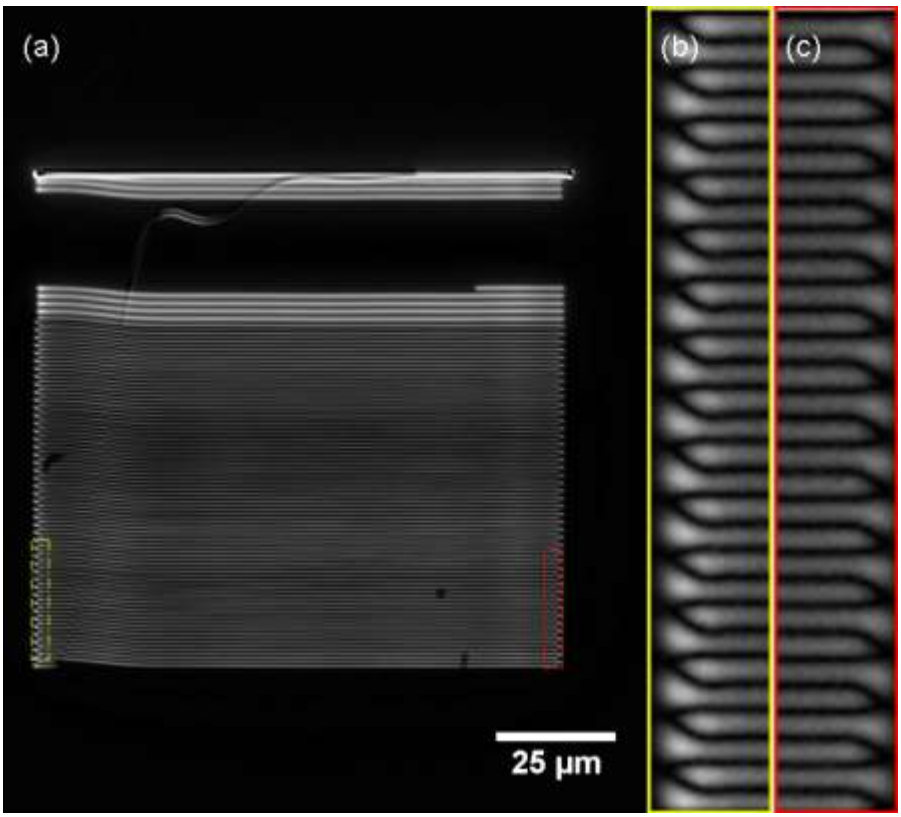

Figure 2.26-(a) image difference calculated using ImageJ between scan at t=450s and t=0s, (b) shows the yellow marked region at the LHS of the scan and (c) shows the red region at the RHS of the scan. These regions correspond to scan shifts in the x scan position from t=0s to t=450s.

Surface plots at the LHS and RHS of the image, corresponding to the edges of the x scan are shown in Figure 2.27. Surface plots were taken of the images at t=0s and t=450s separately prior to the calculated image difference. A region of 5µm was selected within the ROI outlined in the previous figure. The image difference of these regions over time is shown in the surface plots presented in Figure 2.28. This clearly shows the shift in the x scan start and end positions. It is clear that the shift in x position is less than 0.5µm. This is approximately equal to the average shift in the y scan position over time.

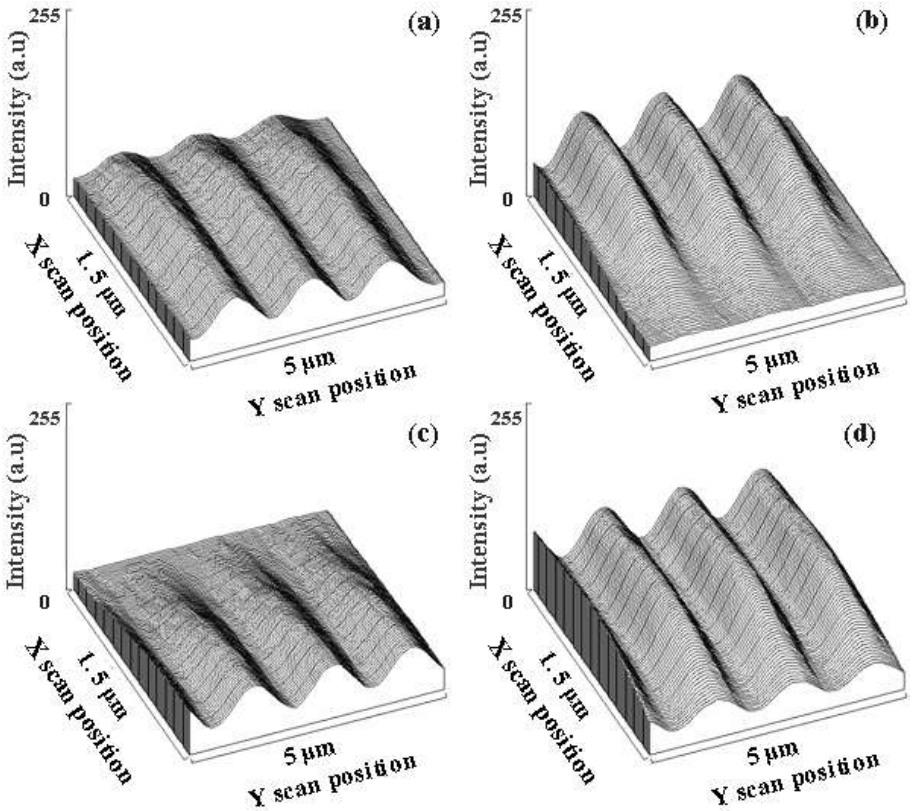

Figure 2.27- (a) shows the surface plot at the LHS at time t=0s, (b) shows the surface plot at the RHS at time t=0s, (c) is the surface plot at the LHS at t=450s and (d) is the plot of the RHS at t=450s.

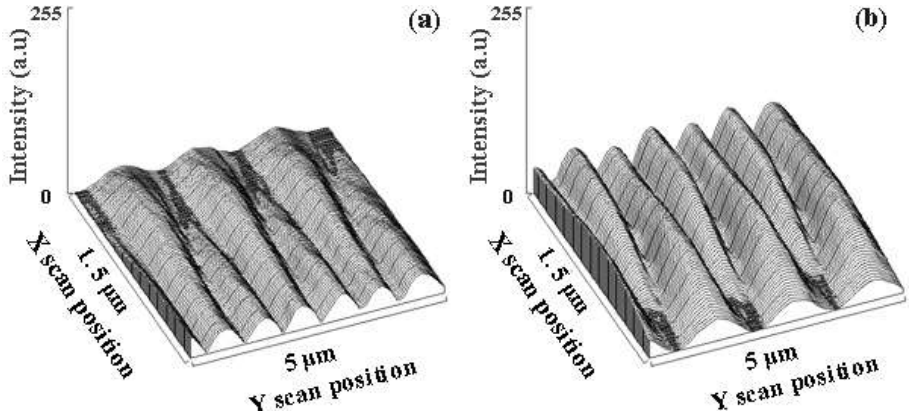

Figure 2.28- surface plots of (a) LHS and (b) RHS of the same regions as for Figure 2.27 for the calculated image difference from t=0s to t=450s.

2.5 Discussion

Measurements using this technique were taken for low zoom (1x) and high zoom (5.5x), it was found that the y scanning drift reduced with increasing zoom. The average scan drift decreased from 1.8nm/s at 1x scanning to 1.10nm/s at 5.5x scanning. This was expected as the rotation angle required to scan a reduced field is smaller, thus reducing scanning error. Therefore, scanning errors are more prominent at low zoom. However, there is no comparison for the scan drift in the x direction as a 1x the edges of the scan lines are not included in the image as only the central 25% of the raster scan pattern was sampled. For these reasons it would be advantageous to also repeat the image sequence at an edge/ corner of the scan to allow for x drift to be measured accurately. Although this has not been carried out, this could be easily implemented into the current method, by either aligning the camera to capture the edge of the scan or by mounting the camera on a translation stage to adjust the position accordingly. The second option would allow for all regions of the zoom=1 scan to be imaged such that the full scan drift and jitter can be measured instead of the small field imaged in this case.

This technique requires substantial image analysis, which can be very time consuming. However, it is possible that a plug-in for ImageJ, the programme used to generate intensity line plots, could be developed to analyse the images in the same way as reported in this chapter. This could potentially reduce the time required to perform complete analysis over the full scanned region, and not only a selected number of regions as presented here. However, the surface plot of the image difference analysis method reported requires less time and provides qualitative information on the behaviour of the scanning mechanism in x and y simultaneously. This would provide sufficient information to identify any scanning errors prior to completing a full quantitative analysis of the scanning system.

As well as the level of zoom having a measurable effect on the scanning error, the scan speed is also important. Using this method a full array of imaging settings can easily be tested to measure the scan drift and jitter at varying zoom and scan speed.

However, one limitation is the exposure and capture rate of the detector being used as it is necessary to match to the frame rate of the scan. This is evident in the case of 5.5x zoom data presented in this chapter, where the full scan was not captured in a single frame by the external camera. This was not completely detrimental as there were enough points of overlap to measure the scanning drifts line by line effectively. As well as the temporal properties of the scan, it is difficult to distinguish scanning error if a high number of lines are used in the scan such as a 512x 512 scan. The measurements in this Chapter were made at 64 x 64 lines. This limitation in the number of lines which can be resolved is more important for high zoom scans than at low zoom. Therefore, there are a number of limitations on the scan parameters that can be tested in this way.

This technique was used to detect small variations, corresponding to sub μm at the sample plane, of scan line position shifts over time course imaging, for applications requiring substantially longer imaging times on the order of hours these effects would be more prominent. The quantitative measurements obtained were of sufficiently small magnitude, of a similar size to the diffraction limited resolution and are unlikely to affect images taken using this system with the scan settings described. However, for scanning super resolution systems, such as STED, scan errors on the dimensions described could potentially have a much more significant impact on the images obtained.

2.6 Conclusion

This chapter presented a new method to test the performance of the x and y scanning galvanometers *in situ* within a standard LSM. Although demonstrated here with an upright microscope, this method could be easily adapted for an inverted microscope, providing accurate measurements of scan stability over time.

The results presented for the Radiance 2000 scanhead using this method show that scan irregularities and drifts are present over time course scanning. This would be of particular importance in quantitative microscopy measurements such as tracking or

visualising moving objects over long time periods, hereby, the overall image could shift in the x and y directions over the recording period, reducing the accuracy of position measurements. The galvanometer scanning instrumentation should incorporate effective feedback mechanisms which should reduce the effects observed. In the case of this experiment the laser scanning microscope was a commercial system, which did not allow for independent monitoring or control of the feedback mechanism. In home built systems or where interfacing is carried out using custom made software it would be possible to control and monitor the feedback to correct for the errors measured using this technique.

Chapter 3: - Microscopic measurement of the size of the optical focus in laser scanning microscopy with resolution below the diffraction limit.

3.1 Introduction

As discussed previously, the resolving power of a microscope is the most important feature of the optical system and influences the ability to distinguish between fine details of a specimen. This lateral resolution is particularly important in life and materials science research where sub-micron scale objects are frequently visualised using methods such as CLSM and MPLSM [7], [17], [45], [52].

The current gold-standard method for measuring the resolution of a standard laser scanning microscope consists of imaging fluorescently labelled beads or pre-fabricated etched gratings on a slide and then analysing the optical image [13], [83], [108]. Clearly, the accuracy of this technique can never exceed the resolution of the objective lens used and hence precise measurement of the lateral spatial resolution of a confocal or multi-photon laser scanning microscope is limited to a few hundreds of nanometres, at best.

One of the key problems in using fluorescent beads for resolution measurements of multi-photon laser scanning microscopes arises from the use of high peak intensity lasers: even at very modest applied powers, the peak intensity of the radiation used for excitation exceeds the low damage threshold of the small diameter beads, and thus a resolution measurement can be difficult to perform accurately. In super-resolution optical microscopy, methods including stimulated emission depletion [61], stochastic processes [109], and sequential photo-bleaching [110], can be used to increase spatial resolution. However, these methods depend heavily on specialised photochemistry, software and instrumentation, and cannot be used easily to measure the lateral spot size or resolution of standard multi-photon microscopes.

Away from microscopy, measurement of laser beam radii is usually performed using knife-edge methods [111], but here the minimum resolvable radius is typically >5 μm, simply because of the mechanical tolerances of the instrumentation used. To overcome this, to some extent, Liu [112] reported a technique for more accurate measurement of stationary beam radii from a frequency-doubled and frequency-quadrupled 20 picosecond-pulsed Nd:YAG laser at wavelengths of 532 nm and 266 nm. The laser source was focused onto single-crystal silicon surfaces, resulting in a micro-ablation process, and a direct image of the distribution of the laser-energy density could be made using an optical microscope. From this image, and with simple Gaussian-beam analysis, the beam radius could be measured. However, although compatible with high repetition rate, ultra-short pulsed lasers [113], [114], this method is limited to beam radii that are larger than the resolving power of the objective lens used to analyse the micro-ablated spot. As such, this method has not been applied to measuring beams of sub-micron radius, such as those routinely used in laser scanning microscopy.

Clearly, the weakness of these beam radius measurement techniques is the optical microscope as the measuring device, and a higher resolution technique is needed for more accurate quantification. This method is likely to prove useful for assessing laser focus quality, since an optimised diffraction-limited focus is an essential prerequisite for STED [60] and other methods which depend on a focussed and scanned laser beam as described in Chapter 1.

In this Chapter, a two-step technique to measure the lateral spatial spot size of a multi-photon laser scanning microscope to unprecedented accuracy is described. The first step consisted of scanning an in-focus specimen consisting of a thin aluminium coating deposited on a glass substrate, using the raster scan parameters usually employed to acquire an image. Even at modest laser intensities, this nano-ablation process left a permanent trace of the path of the scanning pulsed laser beam. The second step consisted of measuring the width of the ablated line in a scanning electron microscope (SEM). Analysis of the SEM image provided direct

measurement of the nano-ablated line-width to an accuracy of 20 nm, limited only by the resolution of the SEM, and from this measurement the spot size and resolution of the laser scanning microscope could be derived to similar accuracy. Measurements at a range of wavelengths used in multi-photon microscopy were perfomed in order to compare the results with theory, demonstrating the performance and accuracy of the technique. It is worth noting that the use of the scanning electron microscope to throw light on the performance of optical microscopes has a precedent: a test-plate produced by Norbert in 1885 proved, upon recent examination in an SEM, to have engraved lines 112.8 nm apart, beyond the resolution of the light microscope [66], [67], [115].

3.2 Theory

3.2.1 Relationship between lateral resolution and radius of optical focus

The theoretical lateral resolution was described in Chapter 1, where the relationship between theoretical resolution to the *NA* and wavelength of light was given by equation (1.2)

It is also given that the diffraction limited spot size, d_s (radius) is given by

$$d_s = \frac{4M^2 \lambda f}{\pi D}, \qquad \textbf{(3.1)}$$

where f is the focal length of the lens, D is the diameter of the entrance pupil and M^2 is the beam quality of the optical focus.

The numerical aperture was also defined in equation (1.1), this is further related to the diameter of the entrance pupil and the focal length by

$$NA = n\sin\theta \approx \frac{nD}{2f} \approx \frac{D}{2f}, \qquad \textbf{(3.2)}$$

Rearranging equation (3.2) gives,

$$\frac{f}{D} \approx \frac{1}{2N.A} \qquad \textbf{(3.3)}$$

Substituting equation (3.2) into equation (3.3) it can be seen that,

$$d_s = \frac{2M^2\lambda}{\pi N.A} \tag{3.4}$$

Assuming M^2=1 then d_s becomes,

$$d_s = \frac{0.637\lambda}{N.A} \approx \frac{0.61\lambda}{N.A} = r \tag{3.5}$$

Therefore, the beam radius at the focus of an objective lens is approximately equal to the resolution limit. Accurate measurement of the beam radius at the sample plane therefore provides a measure of the resolution of the microscope system.

3.2.2 Calculating the optical beam radius from the photo-ablated line width data for varying total pulse energy

Laser induced photo-ablation is the process where a focused laser beam of high intensity incident on a surface can remove material from that surface. This process is widely used in manufacturing applications. It is widely reported in the literature that laser ablation can also be used, under controlled conditions, to measure the radius of the laser beam used to photo-ablate a surface [116], [117]. Using this method, it is possible to correlate the width of the ablated region to the radius of the incident beam. This was first theoretically described and experimentally tested by Lui in 1982 [112].

To understand this process, single mode pulses with a Gaussian spatial and temporal profile are considered. The intensity distribution $I(r,t)$ is given by

$$I(r,t) = I_0 \exp\left(\frac{-r^2}{w^2}\right)\exp\left(\frac{-t^2}{\tau^2}\right), \tag{3.6}$$

Where, I_0 is the peak intensity, w and τ are the spatial and temporal radius respectively (at the 1/e intensity contour), r is the radial position and t is the time. It then follows that the energy fluence $E(r)$ is given by

$$E(r) = \int_{-\infty}^{\infty} I(r,t)dt = E_0 \exp\left(\frac{-r^2}{w^2}\right), \quad \textbf{(3.7)}$$

where, E_0 is the peak fluence at the centre of the beam. In the case of laser ablation the radius of the ablated zone is found to increase with the incident laser power. There is also a point below which ablation does not occur, known as the threshold fluence E_{th}. In addition the width of the ablated zone is also upper bound where the width stops increasing beyond the critical fluence E_c. The rate of growth of the ablated radius is consistent with a Gaussian beam profile given by equation (3.5), such that the following expressions for E_c and E_{th} as a function of the ablated radius at that fluence (r_c and r_{th}) can be expressed as

$$E(r_c) = E_0 \exp\left(\frac{-r_c^2}{w^2}\right) = E_c \quad \textbf{(3.8)}$$

$$E(r_{th}) = E_0 \exp\left(\frac{-r_{th}^2}{w^2}\right) = E_{th} \quad . \quad \textbf{(3.9)}$$

Therefore, the functional dependence of r_{th} and r_c on the respective energy fluence can be written as,

$$r_c^2 = w^2\left(\ln E_0 - \ln E_c\right) \quad \textbf{(3.10)}$$

$$r_{th}^2 = w^2\left(\ln E_0 - \ln E_{th}\right) \quad \textbf{(3.11)}$$

Thus, for a given energy fluence, E_0, provided that the energy is above the threshold and below the critical limit will generate an ablated region with a diameter D ($2r_0$). This is then given by the relationship of the same form of equation (3.10) and (3.11). Multiplying equation (3.11) by two to give in terms of ablated diameter instead of radius the expression can be written as,

$$D^2 = 2w^2\left(\ln E_0 - \ln E_{th}\right) \quad \textbf{(3.12)}$$

which is equivalent to

$$D^2 = 2w^2 \ln E_0 - 2w^2 \ln E_{th}. \quad \textbf{(3.13)}$$

Equation (3.13) is recognisable in the form of a straight line $y = mx + c$, where $y=D^2$, $x=ln(E_0)$ and the gradient $m = 2w^2$ and y-intercept $c = -2w^2 \ln E_{th}$. Setting $y=0$ it can be found that the x intercept corresponds to the threshold energy for the ablation process.

The beam radius can be determined by plotting the measured data in the form of equation 3.13, where the beam radius can be taken as the gradient of the best fitting straight line. This can be taken to be equivalent to the lateral spot size of the laser scanning microscope as described previously. A least-squares fitting method was applied to obtain the best fit with experimentally measured values.

3.2.3 Laser induced heating

It is well known that the high intensities produced by laser beams results in heating of the target material [118]. This is mathematically described by

$$T = \frac{P}{2\pi^{1/2} K w}, \quad \textbf{(3.14)}$$

where P is the power of the laser beam, K is the thermal conductivity of the material and w is the beam radius. The laser ablation process operates in different regimes depending upon the properties of the laser source applied. For high power CW laser sources and long pulse (nanosecond) lasers the process is mainly thermal. The material is heated to the liquid phase, then to a vapour phase resulting in removal of the material that the laser has interacted with. However, the time course involved in the laser or pulse interaction with the surface results in thermal expansion, beyond the confined area that the beam interacted with, resulting in a large heat affected zone (HAZ).

In the regime of ultra-short pulsed laser ablation, the laser pulse does not undergo a thermal phase and then a vapour phase as for longer pulses [119]. Instead the first phase is the creation of a plasma, which absorbs the pulse energy resulting in direct removal of material from the surface [120], [121]. This therefore means a reduction in the HAZ, resulting in a more controlled ablation process, which can be used to accurately determine the properties of the incident beam. This is the reason that ultra-short pulsed laser ablation is widely used in applications ranging from medical research to laser machining applications requiring high precision [77], [122–125].

In the case of ultra-short pulse ablation it is also important to consider the accumulation effect that will occur when a large number of pulses are incident on the sample. It has been observed experimentally, in the femtosecond regime, that the ablation threshold energy decreases with an increasing number of pulses at the sample [126]. However, there is a point where increasing the repetition rate no longer reduces the threshold energy and the threshold energy is constant whilst irradiating with more pulses at the sample. If the repetition rate is decreased then the threshold energy increases, there is not an upper bound limit in this case [114].

In addition to the properties of ultra-short pulsed laser ablation already discussed it is possible to also machine features that have dimensions that are below the diffraction limit [127]. Considering the relationship between the ablated region and the energy of the incident pulses given in equation (3.13), it can be shown that by accurately controlling the laser energy to just above a well defined threshold energy the dimension of the ablated feature will be below the limit imposed by the wavelength of light and the *NA* of the lens used to focus the beam [128]. Therefore, to achieve sub spot size crater formation the incident fluence must be controlled such that only the peak of the pulse has sufficient energy to ablate the material. The convention is such that if the incident pulse fluence is precisely controlled 2% above threshold then this will result in a crater width one tenth of the incident spot size [129]. This is shown schematically in Figure 3.1.

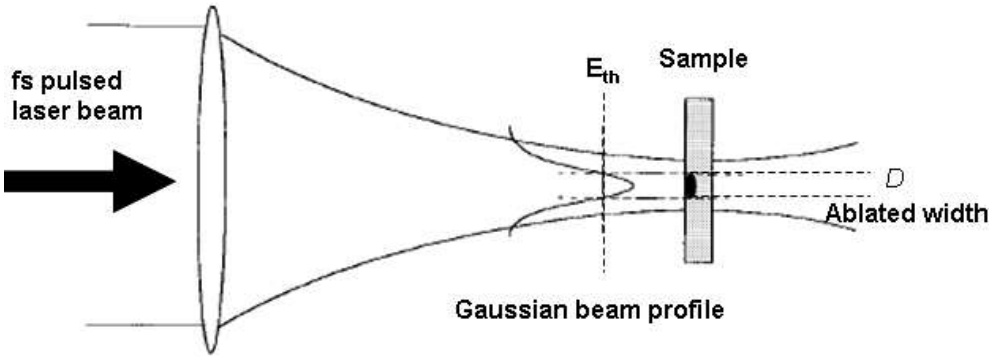

Figure 3.1- Schematic showing the control of the input pulse energy to just above the threshold energy to produce sub diffraction limited features via ultra-short pulsed laser ablation. Image reproduced from [113] **.**

3.2.4 Electron microscopy

Electron microscopy is an attractive technique to make measurements on a scale that optical microscopes are not capable of. There are a number of possible configurations for electron microscopy, the most common being transmission electron microscopy (TEM), where an image is formed by the transmitted accelerated electrons passing through the sample [130]. The electrons are produced by a filament (cathode), such that when a voltage difference, known as the accelerating potential, is applied between the cathode and the anode the electrons are accelerated and produce a beam travelling towards the anode [131]. In electron microscopes conventional lenses are not used and instead electromagnetic components acting as lenses are used to bring the electron beam to a focus at the sample. More recently the scanning electron microscope (SEM) has been employed which draws similarities from the raster scanning image formation technique used in LSM, as described and tested in Chapter 2 [132]. In this case the image is detected from back scattered electrons from the sample surface.

The resolution limit in electron microscopy stems from the size of an electron, which is much smaller than the wavelength of light used in optical microscopy and thus the inherent optical diffraction limit described in Chapter 1. The resolution is dependent on the size of the focus of the electron beam, also known as the probe size [132]. This is affected by the beam current, the brightness of the electron beam and any

aberrations present in the system [133], [134]. Thus resolutions on the order of picometers (pm) are theoretically possible [135]. The application of SEM to life science research is limited by the requirements for sample preparation, with specimens gold coated and working in vacuum means that only fixed samples can be imaged in this way.

3.3 Materials and Method

3.3.1 Material selection

To test the ablation process a range of samples were investigated in order to find a material, which under controlled experimental conditions, could prove reliable reproducible ablated lines suitable for a highly accurate measurement technique. A range of black ink and paint samples were initially investigated. The samples were prepared for microscopy using standard glass slides by applying a uniform thin coat of black enamel paint (Humbrol) or ink (marker pen) to the top surface of the slide. Enamel paint was selected as it is the most suitable paint used in applications where increasing temperatures are required. Therefore, the thermal HAZ, described previously, would theoretically have a reduced effect in enamel paints compared with matt paint. After the ink or paint was dry, lettering was carefully scribed on the surface with a fine sharp needle so that the ablated region could be identified and distinguished from other regions following the micromachining process.

The next stage of investigation used thin aluminium coatings on glass coverslips. Aluminium was selected for this study because of its low melting point and hence low damage threshold, and also the ready visibility of a metallic specimen in the SEM. Circular glass coverslips 10 mm in diameter were cleaned in concentrated sodium hydroxide, washed in tap water and then distilled water and dried before transfer to an Edwards coating unit equipped with standard rotary and diffusion pumps and a trap cooled with liquid nitrogen. Sodium hydroxide cleaning was carried out quickly to avoid detrimental effects to the surface of the glass. A fragment of aluminium foil approximately 5 mm square was wound around a tungsten wire positioned approximately 15 cm above the coverslips. When a vacuum of at least 10^{-5} Torr was attained, current was passed through the tungsten wire, sufficient to heat it to a yellow glow and the aluminium was evaporated on to the coverslips. A thickness monitor was not used, but coverslips were selected with a silvery appearance and an optical transmission of approximately 25%, judged by viewing the transmission of natural light through the coated coverslip. There was

unavoidable variation in film thickness according to position of the coverslips within the evaporator. The selection process was performed to ensure that the coverslips chosen were aluminised and free of dirt or debris before imaging. After 24 hours, scratches were made on the specimen using a fine sharp needle. This was performed under a stereo microscope, and irregular scratches made. This served two purposes, (i) to help with focusing the aluminised coverslip on the laser scanning microscope and, (ii) to assist with identifying nano-ablated regions during SEM.

3.3.2 Nano-ablation

To produce nano-ablated lines on the specimen, a standard MPLSM system to raster scan and provide focusing of the laser spot was used. A schematic diagram showing the layout of the system is presented in Figure 3.2.

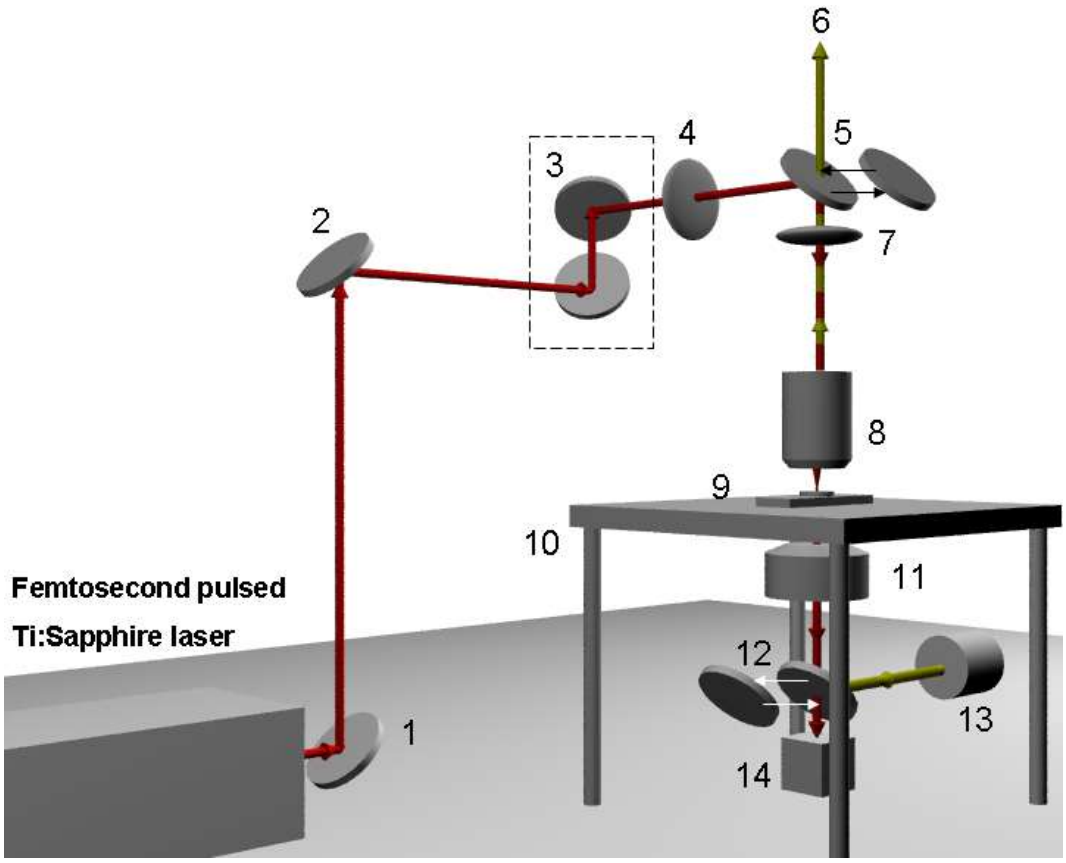

Figure 3.2-Laser scanning and brightfield microscope system. A 90 MHz repetition rate, femtosecond-pulsed near-infrared emitting Ti:Sapphire laser (Chameleon, Coherent) was coupled

using beam steering mirrors (1) and (2) into a laser scanning microscope. This comprised a Bio-Rad Radiance system equipped with computer-controlled scanning galvo mirrors (3) and a scan lens (4) and an upright Nikon Eclipse E600FN microscope. A spectral reflector (5) was used to direct the near-infrared Ti:Sapphire laser radiation through the tube lens (7) towards the objective lens (8), which brought the laser light to a focus on a specimen (9) on a mechanical stage (10). Alternatively, the reflector could be moved aside, to allow incoherent white light to pass from a halogen lamp (13), to transilluminate the specimen and form an image in the eyepieces (6). The same 20x/0.75 numerical aperture dry objective lens was used in both brightfield to bring the aluminised coverslip specimen into focus, and in the subsequent raster-scanning nano-ablation experiments with the Ti:Sapphire laser. The position of the specimen was adjusted using the X and Y manual controls on the sample stage. For IR transmission imaging, the light was collected by a substage condenser lens (11) and by displacing the mirror (12) directed towards a PMT detector (14). It was also possible to obtain IR reflection images, using an epi-reflection detector (not shown).

The laser scanning microscope consisted of a scan head (Radiance 2000MP, Bio-Rad) and an upright microscope (Eclipse E600FN, Nikon). The laser source for nano-ablation was a free-space-coupled Ti:Sapphire laser (Chameleon, Coherent), which was wavelength tunable between λ=720-900 nm, with pulse durations of less than 200 femtoseconds across the tuning range at a repetition rate of 90 MHz. The laser beam was deflected by galvanometer scanning mirrors and then via a scan lens into a microscope, where the radiation was focused onto the specimen with a 20x/0.75 numerical aperture dry objective lens (Nikon, Plan Fluor). The scanning software (LaserSharp 2000, Bio-Rad) was used to control the scan speed, optical zoom (from 1x to 10x) and the number of lines per scan. The average power at the sample plane was adjusted using an electro-optical modulator, which was controlled via the LaserSharp software, the power range in this study was from 10mW to 50mW.

Using the brightfield transmission imaging option available on the laser scanning microscope, the specimen was brought into focus, using the scratches, described in the sample preparation section, as a rough guide to focusing depth. In changing from the brightfield visible radiation to the near-infrared wavelength chosen for ablation, as was expected, the focal plane of the beam changed. To then focus the near-infrared radiation on the sample the transmission PMT was used to adjust the focus for each wavelength. This was done using low intensity near-infrared radiation at low digital zoom (zoom factor = 1) where the low intensity irradiation resulted in no alteration to the structure of the specimen.

To measure the beam radius with varying wavelength, a series of nano-ablated lines scanned at varying power (and thus total pulse energy) was produced for six wavelengths across the tuning range of the Ti:Sapphire laser. The wavelengths selected were λ=740nm, 760nm, 780nm, 800nm, 820nm and 850nm, as these are common wavelengths for MPLSM, matching the widely used fluorophores hydroxyl-coumarin, DAPI and GFP for biological imaging [136].

The power transmission through the 20x/0.75 N.A. air immersion objective lens was measured before nano-ablation experiments using a highly sensitive photo-detector (NOVA II, Ophir) for low power (1-10 mW) and a calorimetric power meter (407A, Spectra-Physics) for average powers greater than 10 mW. The average power was measured at the focus of the objective lens for each wavelength and for each power setting in the software (defined as % of laser power). The maximum average power used in this study was limited by the optical transmission of the laser scanning microscope at each wavelength, and the range of total pulse energies examined was commensurate with the pulse energies commonly used in MPLSM [122]. The calculated peak power range at the sample was varied between 5 and 35MW in the ablation experiments described.

3.3.3 Ablation scan settings

With the sample in focus, a single frame was scanned, so that the laser beam passed only once over each scanned line. To exceed the damage threshold of the specimen a 4x zoom and 64 x 64 line scan was used to perform all ablated raster patterns, with a pixel dwell time of 80 μs for single frame irradiation.

This system provided sufficient pulse energies to exceed the empirically determined nano-ablation threshold, as well as a low number of lines such that individual scan lines were spaced far enough apart to be easily identified and consequently analysed, although other configurations were possible. In this experiment, the nano-ablation process was a result of multiple pulses interacting with the substrate, on the order of

7000 pulses per pixel, where the number of pulses was calculated using the 80 μs pixel dwell time of the scan for the settings described previously.

3.3.4 Optical imaging of ablated specimens

To accurately measure the ablated line width, confocal transmission images were obtained for individual scanned raster tracks. The set-up shown in Figure 3.2 was reconfigured for confocal imaging by coupling the 488nm laser line of an Argon ion laser instead of the free- space coupled Ti:Sapphire laser. The Argon ion laser source was also controlled by the Radiance 2000 scanhead. The confocal configuration is presented schematically in Figure 3.3.

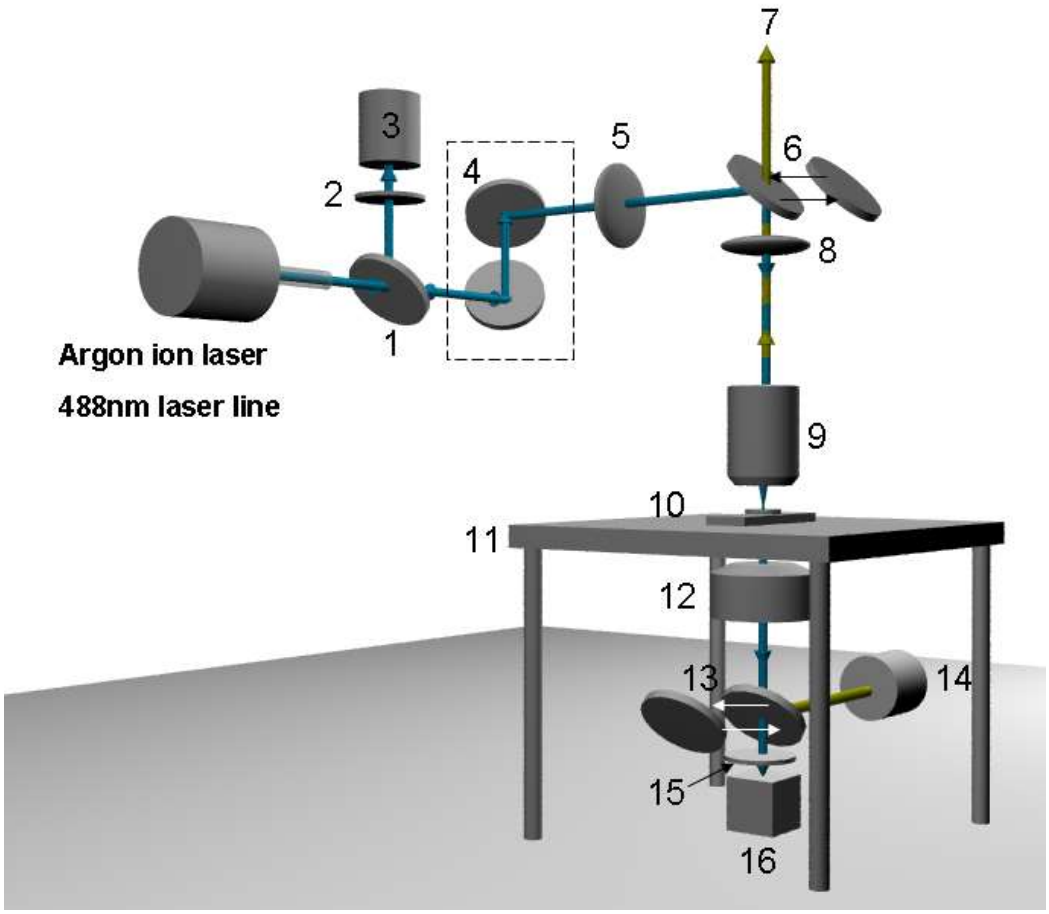

Figure 3.3- Optical imaging set up. The Bio-Rad system was configured after ablation experiments to allow for confocal transmission and reflection imaging. The 488nm Argon Ion laser line was fibre coupled to the laser scanhead (4) and directed to the objective lens (9) via the scan lens (5) and the tube lens (8). The sliding mirror (6) was used to change between laser scanning and viewing the sample in brightfield mode via the eyepiece (7). For confocal transmission detection the transmitted light was collected by the condenser lens and detected by the PMT (16). Reflection confocal imaging was detected by the PMT (3) using no filters in the beam path, thus detecting the signal reflected from the sample (10) via the mirror (1). The pinholes (2) and (15) were used for confocal detection in both transmission and reflection channels.

During ablation experiments the confocal configuration was used to check ablated rasters and to translate the stage to another suitable part of the aluminised coverslip for the next ablated raster. This allowed for an estimate of ablation quality to be determined prior to high resolution imaging after ablation. To provide high resolution optical images of the ablated regions a 60x/1.4 N.A. oil immersion objective lens was used for imaging. This provided an imaging field of view of 167 x 167 micron at 1x zoom and a theoretical resolution of 396nm from equation (1.2). The ablated coverslips described in section 3.3.1 were inverted such that the aluminium surface was below the glass coverslip. The coverslips were then secured using hard setting mountant (Vectashield, Vectorlabs) and left for 24hrs to set before imaging using the 60x/1.4 *NA* objective lens.

3.3.5 SEM imaging

3.3.5.1 Determining optimum SEM imaging platform and settings

To obtain the best possible images several SEM instruments were used to investigate the ablated specimens. The first SEM investigation used the FEI Sirion 200 field emission gun SEM. Images were acquired using an accelerating voltage of 5kV and a probe current of 100pA. At high accelerating potentials significant charging effects were observed.

To overcome charging effects the method of gold sputtering, routinely used in biological SEM imaging, was applied to reduce charging. Here, a thin coating of gold is applied to the specimen to ensure electrical conductivity across the full sample so that charge can be dissipated effectively. No sputtering facilities were available at the University of Strathclyde and so this was carried out at the University of Cambridge by Dr W.B. Amos with assistance by Dr J.N. Skepper. A coating of 5nm of Au was applied to the sample using a gold sputter coater (Quorum EmitechK557). SEM images were then acquired using the 5kV accelerating potential described previously.

The possibility of reducing the charging effects without the requirement of gold sputtering was investigated using the JEOL, JSM-6400 SEM (University of Glasgow). In this system, low accelerating voltages were used to image the sample where accelerating potentials from 0.5kV to 1 kV were investigated.

3.3.5.2 Routine SEM imaging method

After investigating and optimising the SEM imaging settings the JEOL, JSM-6400 was used for all SEM imaging. The aluminium coated glass coverslips were mounted on aluminium stubs using silver electro-dag paint (Agar Scientific) after ablation. A low accelerating potential of 0.5-0.8kV was used throughout the study, to minimise detrimental charging effects and also to provide high contrast images however, this was at the cost of reduced resolution relative to high voltage SEM systems. The manufacturer quoted systematic resolution for this type of instrument is 3.5 nm, however the use of such low acceleration voltages gave a measured resolution of 20nm or better. Therefore, the quoted resolution is 20 nm for the SEM images throughout this study, although improved resolution may be possible with an alternative SEM system or, where possible, using higher accelerating potentials. Low magnification (500-550x) and high magnification (9000x) SEM images were taken for analysis. The low magnification was used to locate the nano-ablated regions, and the high-magnification images were acquired for line-width analysis.

3.3.6 Image analysis

Measurements of the nano-ablated line-widths in the high magnification SEM images were made by taking the $1/e^2$ intensity profile of each line using ImageJ (NIH). The $1/e^2$ value was determined in accordance with Gaussian optics and as per the work of Liu [112]. For all images, n=20 intensity profiles were analysed and an average nano-ablated line-width measured, from which the beam radius and hence lateral resolution of the laser scanning microscope could be calculated with an accuracy of 20 nm, as described previously.

A least-squares fitting method was applied to obtain the best fit with experimentally measured values. From the gradient of this line, the beam radius could then be determined, and this was taken to be equivalent to the lateral resolution of the laser scanning microscope as outlined in section 3.2.1.

3.3.7 System comparison

To determine the efficacy of this technique, the ablation method for the aluminium specimen was repeated using a Leica SP5 system. To generate comparable ablated regions similar settings to the Bio-Rad system described in Section 3.3.4 were used as far as possible. For this system the air objective lens available was a 20x/0.7 N.A. and the minimum number of lines was a 16 line scan. The laser source was also a free-space coupled Ti:Sapphire laser (Chameleon, Coherent) in the same geometry shown in Figure 3.2. However the maximum power available from the Ti:Sapphire was 3W instead of 1.5 W used in the Bio-Rad system, thus providing higher pulse energies at the sample. After observing the ablated raster scans using 64 x 64 lines it was decided to use the lowest pixel scan of 16 x 16 lines which provided clearer tracks for the beam. A scan speed of 200 lines per second was used, resulting in a pixel dwell time of 312μs for 16 x 16 line scan and 78μs for a 64 x 64 line scan. The pixel dwell times at 64 lines was approximately matched to that used in the Bio-Rad system. However, for scans at 16 lines the dwell time was significantly longer. Confocal transmission imaging was performed after ablation, using the same 20x/0.7*NA* objective lens. SEM imaging using the same method to characterise the ablated rasters using the radiance system was also performed for irradiation at 730nm at varying powers controlled by the Leica SP5 software.

3.4 Results

3.4.1 System characterisation

The average output laser power of the Chameleon before entering the scan head is shown in Figure 3.4 for varying wavelength. The power values were measured across

the full tuning range of the Ti:Sapphire laser although only 6 wavelengths were used for ablation experiments. The wavelengths selected were 740nm, 760nm, 780nm, 800nm, 820nm and 850nm. The measured average output power of the system at the sample plane is shown in Figure 3.5 and Figure 3.6. Figure 3.5 shows the average output power at the objective mount without an objective lens in place. The average output power transmitted through the 20x/0.75 air objective for the range of wavelengths available is shown in 5. Measurements were made at the defined laser settings controlled by the laser2000 software defined as the percentage of laser power. The error in the average power measured is taken to be 2%.

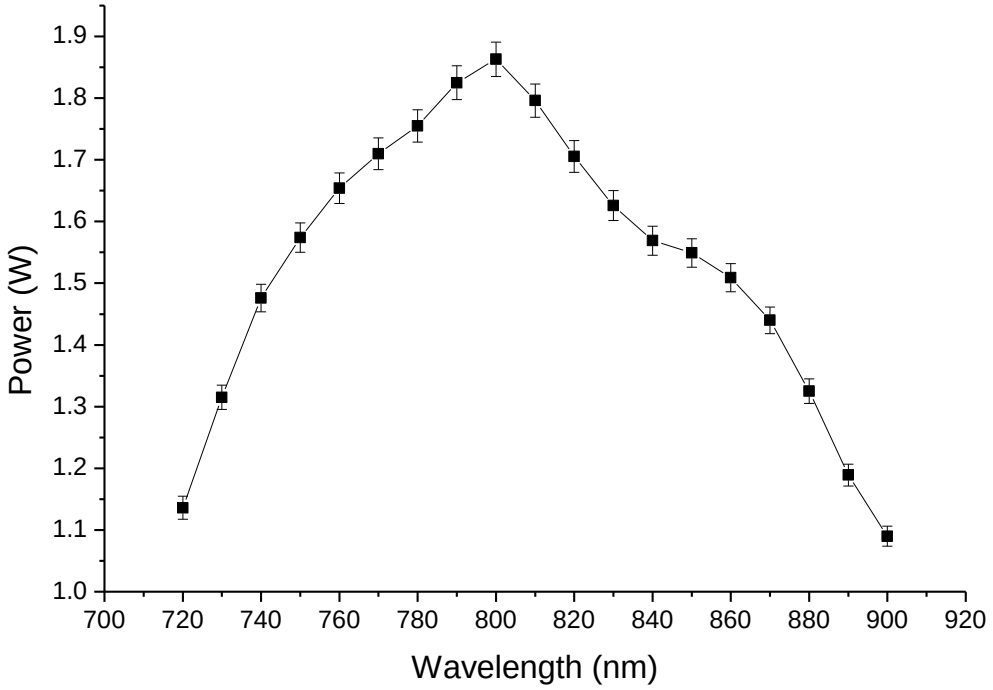

Figure 3.4- Maximum output power of the Chameleon laser across the full tuning range 720-900nm. Measurements were taken from the internal optical power metre in the Chameleon system. Power values are quoted with 2% standard error (manufacturers guide).

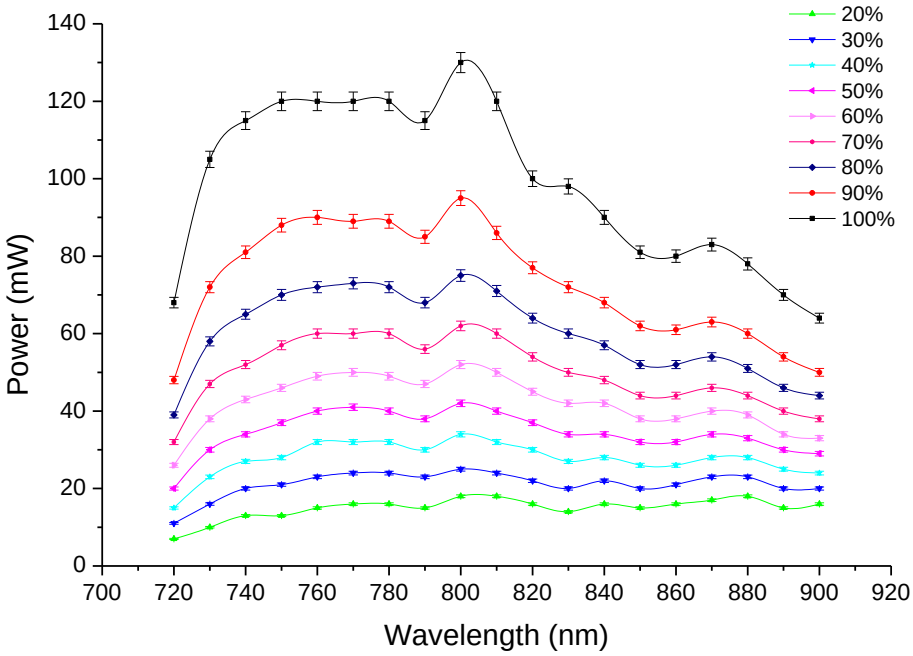

Figure 3.5- Average laser power transmitted through the Bio-Rad Radiance system and microscope without any objective lens. Power values are quoted with 2% standard error (manufacturers guide).

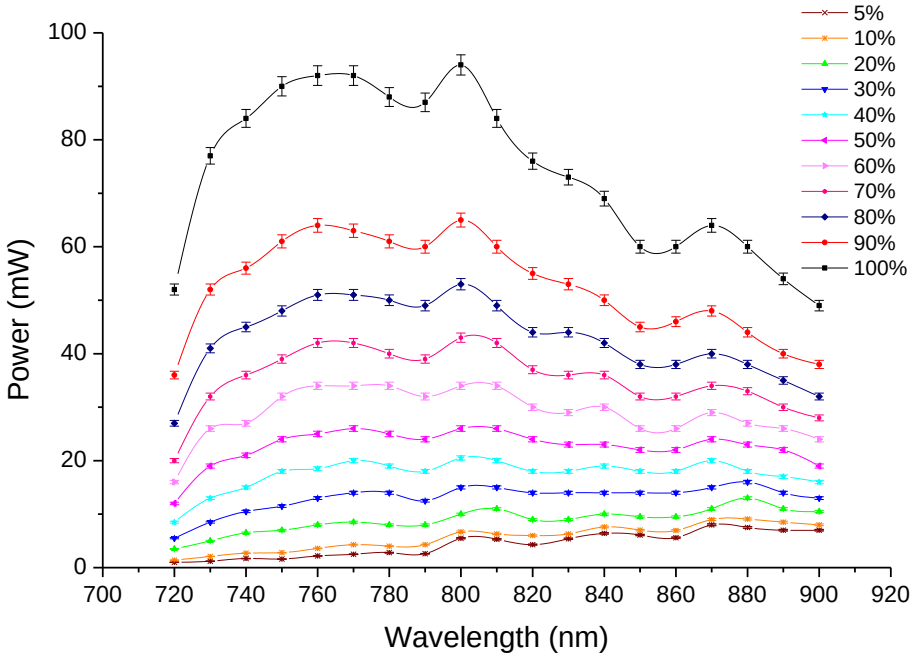

Figure 3.6- Average laser power transmitted through the Bio-Rad system and microscope with a 20x/0.75 N.A. objective lens. Power values are quoted with 2% standard error (manufacturers guide).

Prior to analysis of the ablated line widths, the measured average power at the sample after the 20x/0.75 N.A objective lens, shown in Figure 3.6, were converted into total pulse energy as outlined in the theory section. The calculated pulse energy is shown in Figure 3.7 for the corresponding power settings, defined by the Lasersharp2000 software, for each wavelength used in the ablation experiments.

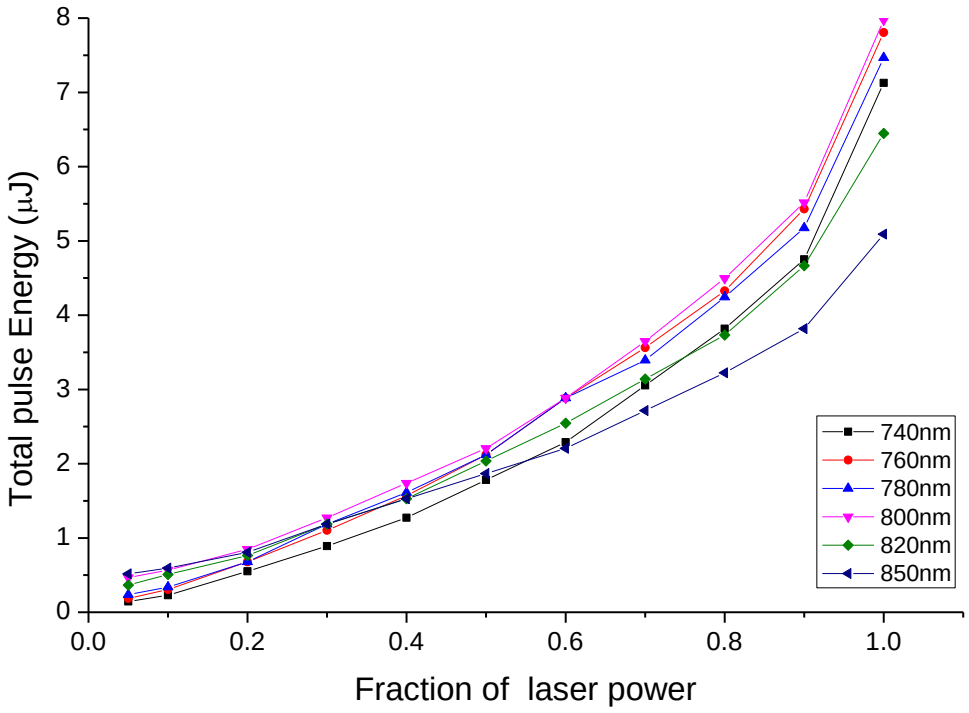

Figure 3.7- Calculated total pulse energies from measured average power values shown in Figure 3.6, corresponding to 7600 pulses incident on the sample for a pixel dwell time of 84µs.

It can be seen that the difference in pulse energies, across the wavelength range, for a given fraction of laser power is greatest when approaching the highest power settings.

The pulse duration at varying wavelength were measured at the output of the Ti:Sapphire laser before the beam was coupled to the microscope scanhead. The pulse check autocorrelator was used. It was not possible to measure the pulse duration using this autocorrelator at the sample plane. The pulse durations measured using a $sech^2$ fit to the autocorrelation are shown in Figure 3.8 across the full tuning wavelengths of the Ti:Sapphire laser.

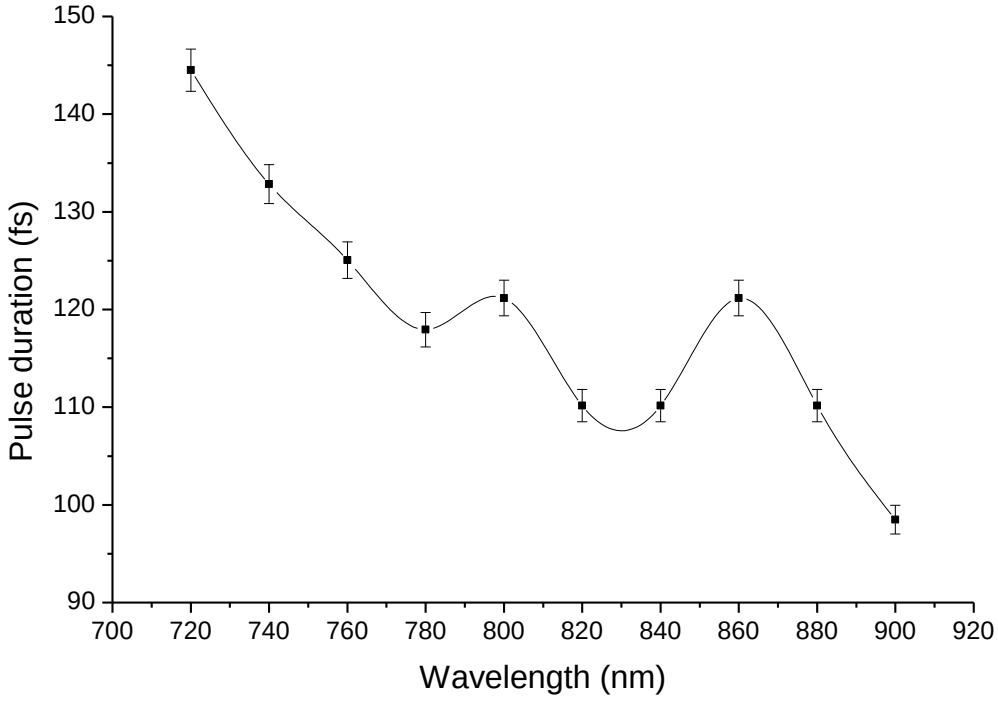

Figure 3.8- Measured pulse duration with varying wavelength over the tuning range of the Ti:Sapphire laser.

The spectrum of the laser output was also measured across the tuning range, using a spectrometer (USB2000+VIS-NIR, Ocean Optics) with a 1.5nm resolution (FWHM). The normalised spectra are shown in Figure 3.9.

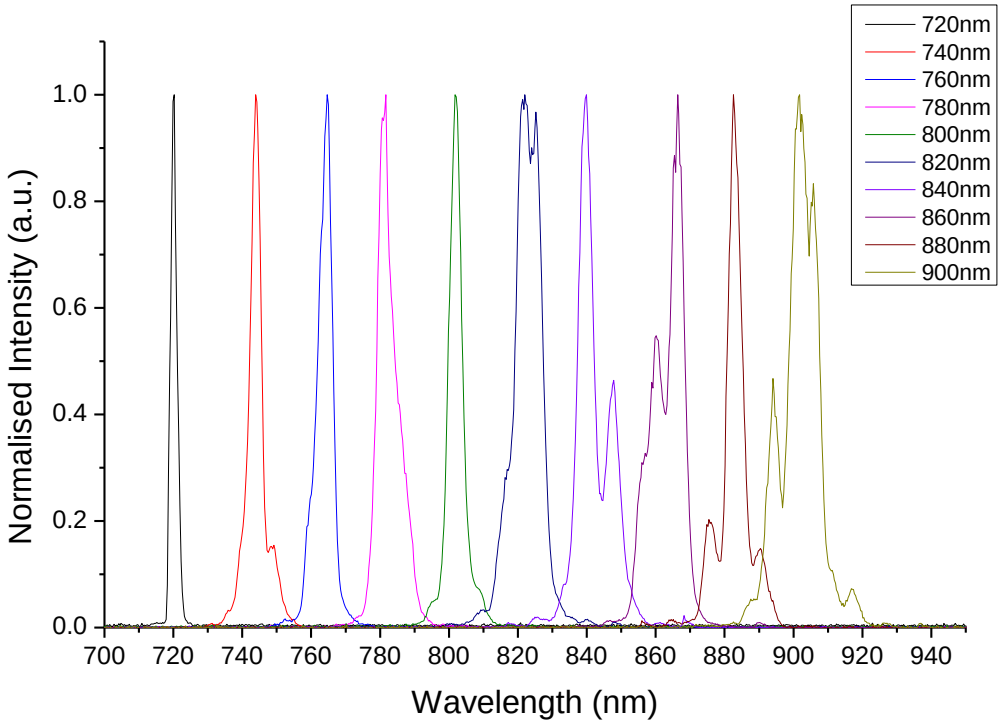

Figure 3.9- Wavelength spectra obtained over full tuning range.

3.4.2 Material Investigations

To determine the most appropriate material to use for optical focus characterisation a series of ablations were performed at 760nm with varying laser power at the sample plane. Figure 3.10 shows a reflection image at 488nm following ablation at 20% laser power (10mW) at 760 nm of a layer of ink. The image was taken at a zoom factor = 3 to show the full ablated region.

Figure 3.10-Ablation of an ink sample using a 20x/0.75 N.A. air objective at a power of 10mW at 760nm. The reflection confocal image was taken after ablation at 3x zoom using the 488nm laser.

It can be seen that the areas around the edges of the scan have melted more than in the centre of the scan. This is due to the turnaround time of the scanning

galvanometer mirrors in moving from one line of the raster scan to the next. There also appears to be a bubble of ink formed by the beam at the top left of the image. This is at the starting point of the ablation scan. At increasing power at the sample plane, it was found that the bubble and melting effects were more prominent resulting in little detail of the scan lines being visible in the reflection image. In comparison enamel paint samples were investigated. A series of reflection images, taken as described before, are shown in Figure 3.11.

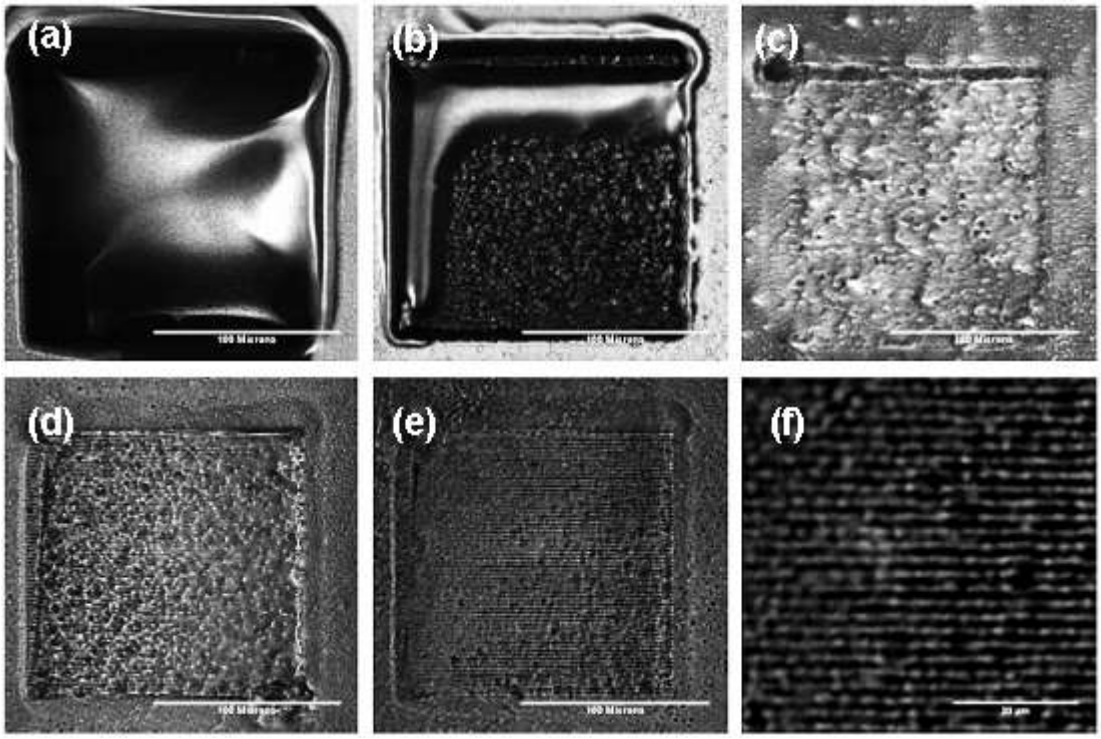

Figure 3.11- Confocal reflection images (λ=488nm) following ablation of enamel paint samples at 3x zoom. Ablation was performed with 760nm irradiation with power varying from (a) 51mW, (b) 34mW, (c) 25mW, (d)18mW, (e)13mW and(f) shows the ablated raster in image (e) at 10x zoom . Scale bar corresponds to 100µm.

It can be seen that the ablation of enamel paint at high powers Figure 3.11(a) and (b) resulted in complete melting over the ablated region, where no micromachined lines were observable. However, at lower powers, as shown in Figure 3.11(e) at 3x zoom and Figure 3.11(f) at 10x zoom, individual lines were observed. These samples were not stable enough to be suitable for this measurement technique described. Therefore,

the aluminium coating on a glass cover slide were used for all future experiments. Images of ablation of the aluminium surface are shown in the next section.

3.4.3 Optical Imaging

Transmission images of ablated rasters at varying powers of an aluminium sample are shown in Figure 3.12. These images were taken after remounting the sample for imaging with a 60x/1.4*NA* oil immersion objective lens.

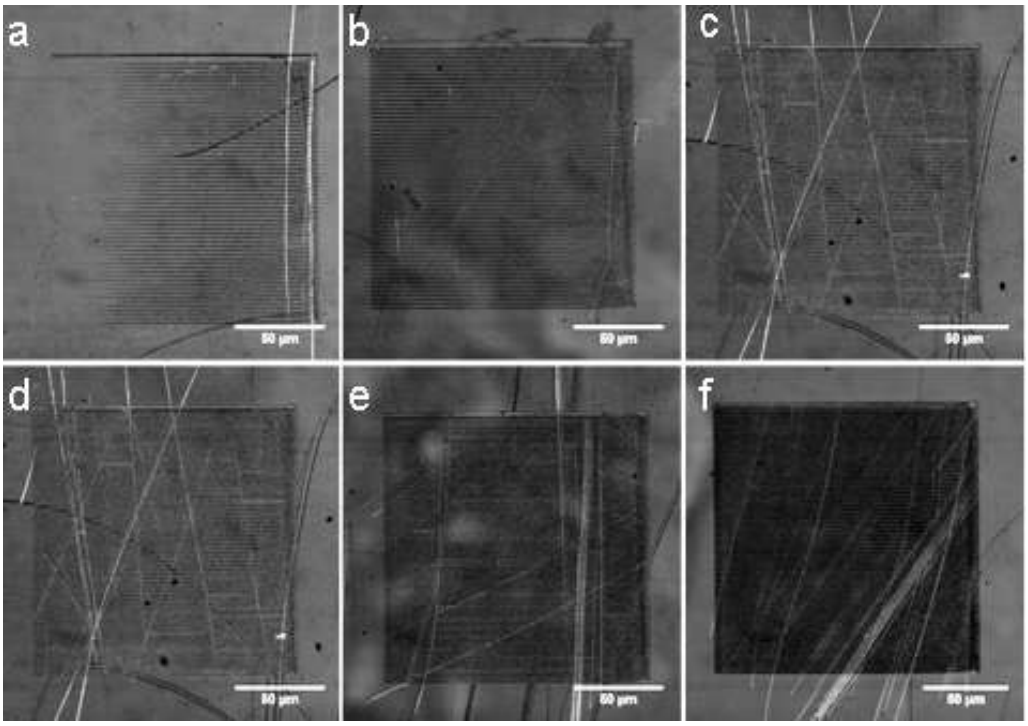

Figure 3.12- Ablated regions using 780nm irradiation at (a) 8mW, (b) 13mW, (c) 18mW, (d) 25mW, (e) 34mW and (f) 51mW laser power. Confocal transmission images were taken at 1x digital zoom using a 60x/1.4 *NA* oil immersion objective lens using 488nm irradiation. Scale bar corresponds to 50 µm.

To obtain accurate quantitative measurements of the dimensions of each ablated track, images of the regions shown in Figure 3.12 were taken at higher digital zoom (10x) providing a field of view of 19µm by 19µm. The theoretical lateral resolution was calculated using equation 3.1 to be 212nm, for the 1.4 *NA* objective for imaging at λ=488nm.

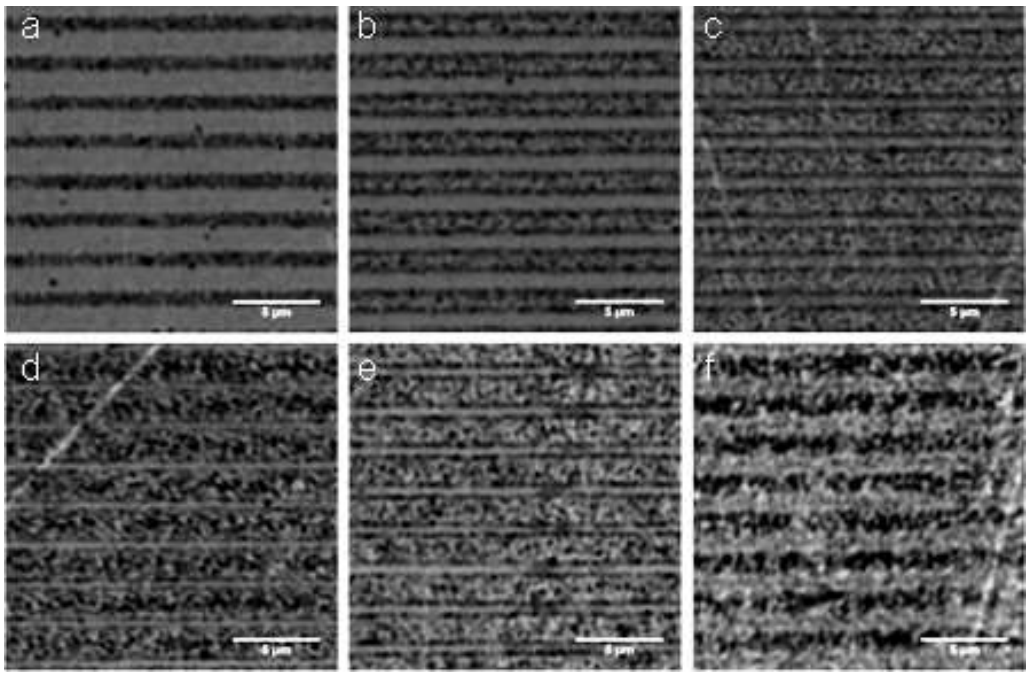

Figure 3.13- Ablated regions using 780nm irradiation at (a) 8mW, (b) 13mW, (c) 18mW, (d) 25mW, (e) 34mW and (f) 51mW laser power. Confocal transmission images were taken at 10x digital zoom using a 60x/1.4 *NA* oil immersion objective lens using 488nm irradiation. Scale bar corresponds to 5µm.

The measured widths performed using ImageJ on the images taken in Figure 3.13 for 780nm ablation is plotted in Figure 3.14. The data for images taken of ablated regions at wavelengths of 800nm, 820nm and 850nm are also plotted in Figure 3.14. Each linewidth measurement was the average of n=20 measurements across the imaged region. The error quoted is the standard deviation of the mean.

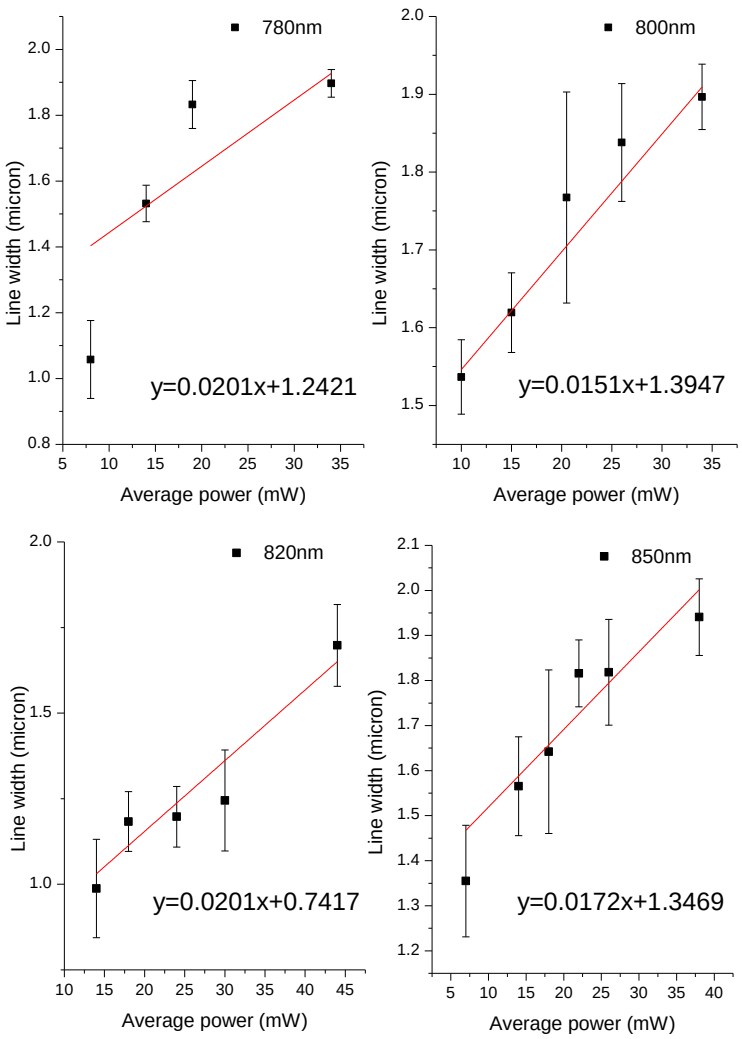

Figure 3.14- Measured ablated line width at the 1/e^2 intensity contour at varying excitation powers for (a) λ=780nm, (b) λ=800nm, (c) λ=820nm and (d) λ=850nm. Errors are the standard deviation in the mean for an n=20 at each wavelength.

It can be seen that the expected linear increase in ablated width with increasing average power at the sample was observed to an extent. However, significant deviations from this trend are shown in Figure 3.14(a) for 780nm laser irradiation. Converting the measured values into the form of the ablation equation (3.14), the corresponding semi-log plot of D^2 against the total pulse energy applied $ln(E_0)$ is shown in Figure 3.15. The least squares fitting method was applied to fit the experimentally measured ablated widths to obtain the beam radius at the sample plane. However, the experimental data does not fit well with ablation theory, this is

due to difficulties measuring the width of the ablated region from the optical images obtained (Figure 3.13).

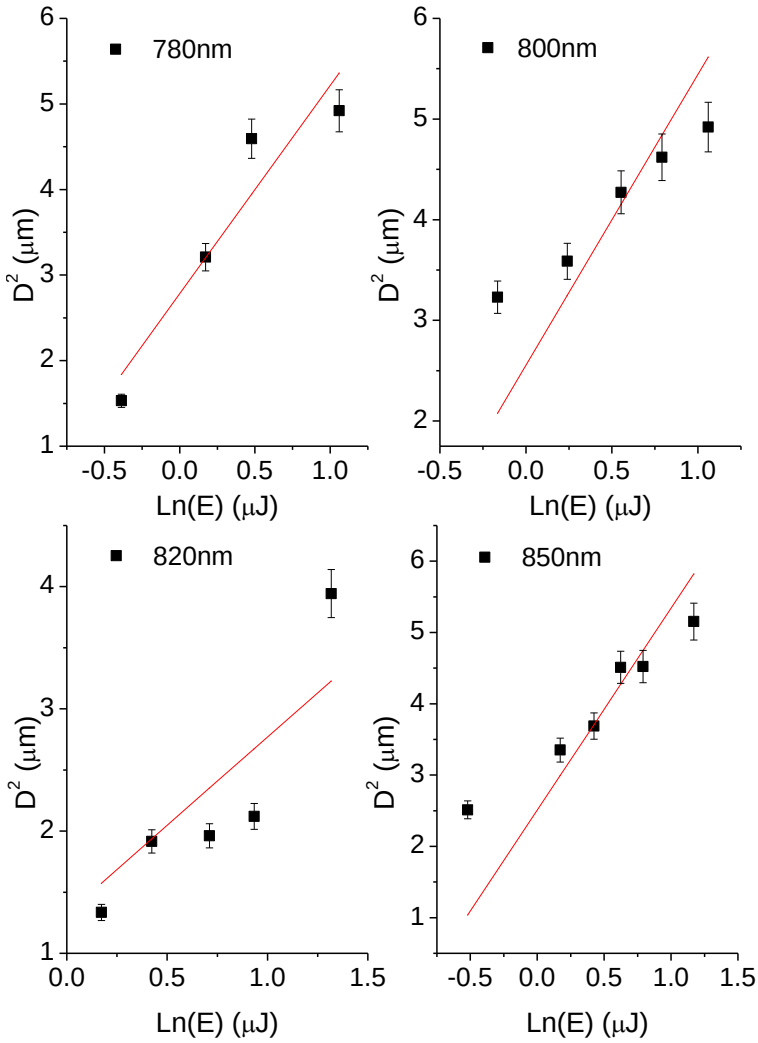

Figure 3.15- Theoretical fitting of data shown in figure 3. 14 in the form of ablation theory for (a) λ=780nm, (b) λ=800nm, (c) λ=820nm and (d) λ=850nm. Fitting was carried out using a least squares fitting of the ablation equation to the experimental data.

The least squares fitting allowed for absolute measurements of the beam radius for each wavelength investigated. The beam radii are plotted in Figure 3.16.

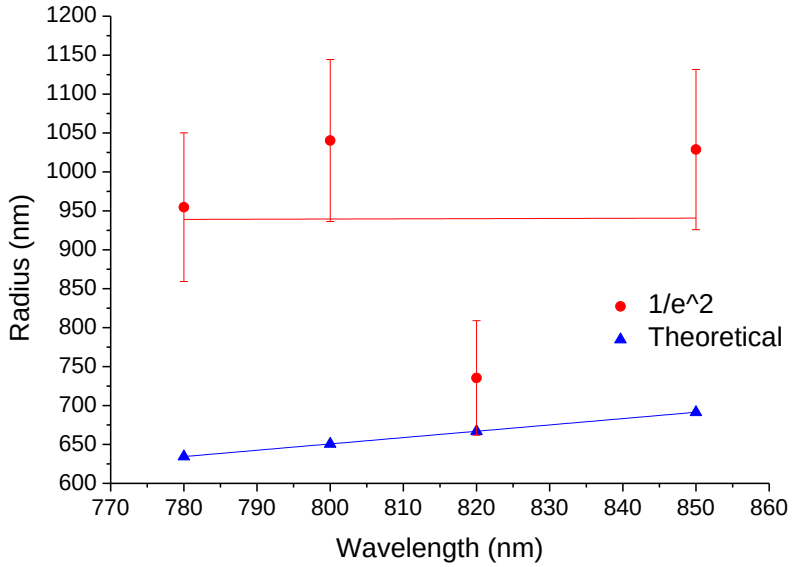

Figure 3.16- Beam radius measurement from the gradient of the theoretical fit in Figure 3.15 . The calculated beam radii for each wavelength are also plotted for measured and theoretical resolution limit.

Figure 3.16 shows that the measured spot size at the sample plane provided by the 20x/0.7NA objective lens is significantly larger than the theoretical resolution calculated by equation 3.1. However, it was also evident whilst performing confocal transmission images of the specimen that constraints by preparation and imaging from beneath the ablated region resulted in the imaging of what could be explained as debris at the bottom of the ablated scan line or perhaps even regions of the glass slide under the coating of aluminium that has been damaged by the beam. This introduces additional source of error that limit accurate measurements of the ablated line width and thus the beam radius. It was therefore necessary to investigate the ablated raster scans using a microscope beyond the resolution capabilities of laser scanning microscopy.

3.4.4 SEM imaging

Using the FEI Sirion 200 SEM to image ablated regions, there were significant and ultimately detrimental charging effects on the sample by the 5kV accelerating potential. This made it difficult to locate regions of interest as the charge build up was highest around regions where the aluminium coating was partially removed exposing the glass coverslip below. Two representative regions of ablation imaged

with these settings are shown in Figure 3.17. This region corresponds to a test ablation scan using a 60x/1.3 N.A. water immersion objective lens.

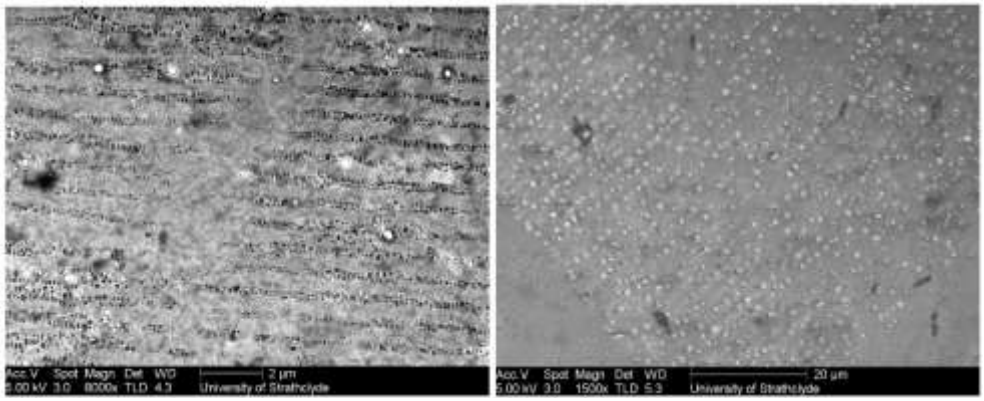

Figure 3.17-SEM images of ablated regions by a water immersion lens using FEI Sirion 200.

The ablated lines shown have a less uniform structure than expected from a standard raster scan. There were significant effects on the aluminium coating when using water immersion thus limiting the use of this objective. Therefore, there are no comparative images of other water ablation regions using other SEM techniques.

To minimise the charging effects observed using the FEI Sirion 200 instrument the samples were coated with a thin layer of gold and then re-imaged using the Cambridge SEM system. Example images are shown in Figure 3.18.

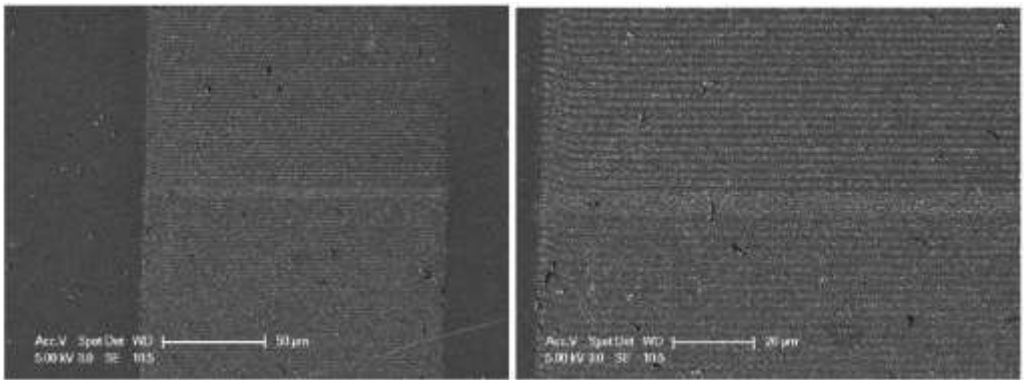

Figure 3.18-SEM images of an air ablated raster scan using university of Cambridge system with accelerating potential of 5kV at high and low zoom.

In Figure 3.18 a series of lines resulting from the ablation using the 20x/0.75 N.A. objective lens are shown. In the images lines are clearly visible, however, there is a

grainy structure of the lines suggesting that the ablation process has left significant amount of debris in the tracks. However, the initial problems of charging were solved by the gold coating applied enabling ablated regions to be imaged without charging artefacts.

It was found that whilst using accelerating voltages of up to 0.8kV, charging effects were minimised. Sample SEM images of an ablated raster scan with a 20x/0.75 N.A. objective lens are shown in Figure 3.19.

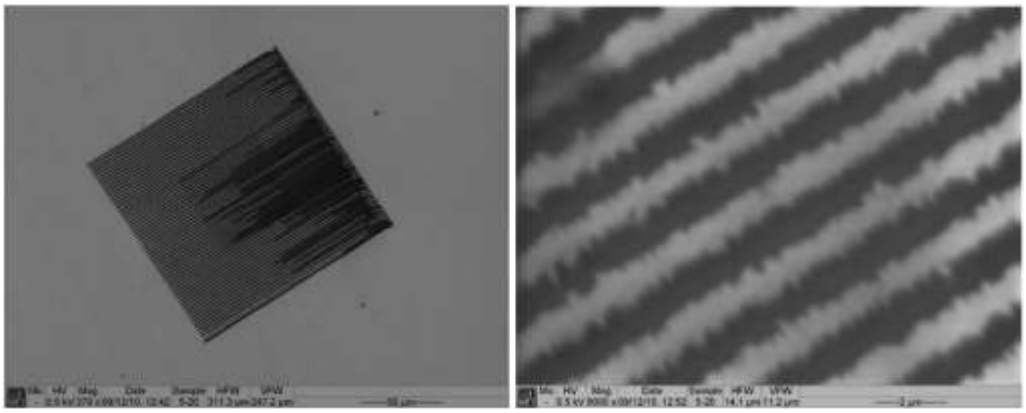

Figure 3.19-Sample SEM images obtained using the JEOL instrument, at 0.5 kV accelerating potential for an ablated raster at 51mW and 760nm irradiation. Image LHS shows the low magnification (370x) and RHS shows high magnification (8000x) over a region the same ablated raster.

In Figure 3.19, it can be seen that the SEM images of the ablated regions are of the best contrast of all three imaging platforms. All SEM images shown and analysed in the following section were imaged using this SEM platform at low accelerating potential.

3.4.5 SEM imaging of air ablated aluminium films

Using the method described, nano-ablated raster patterns were produced and SEM images obtained, with a resolution of 20 nm. Figure 3.20 shows a series of representative SEM images, with nano-ablation performed at a fixed wavelength of λ= 760 nm with increasing applied average power (and thus increasing total pulse energy).

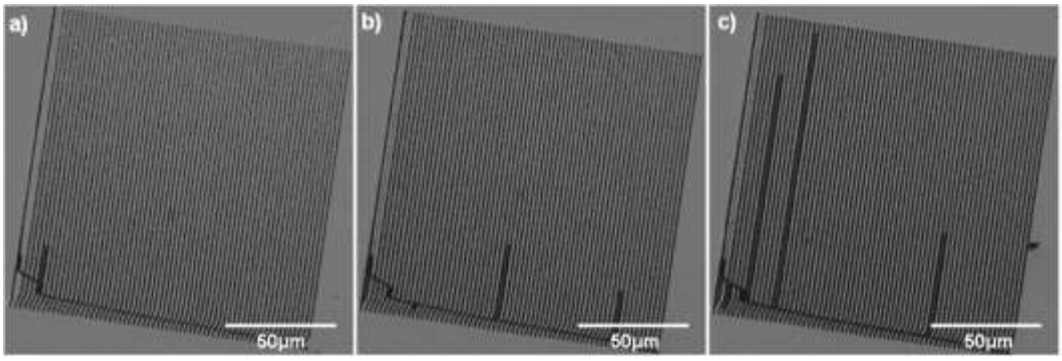

Figure 3.20- Single-frame nano-ablated raster scans taken with varying total pulse energy (a) 1.5 µJ, (b) 2.1 µJ and (c) 2.9 µJ applied to the specimen, at a fixed wavelength of λ=760nm were imaged using SEM at low magnification (550x). The energies used correspond to applied average power of (a) 18mW, (b) 25 mW and (c) 34 mW.

This increase in linewidth with increasing applied pulse energy was expected, because of the cumulative nature of the ablation process described previously, and with reference to the energy dependence of equation (7). The low magnification images show the overall condition of the nano-ablated raster from which an area representative of the nano-ablation process could be identified and a higher magnification image subsequently obtained. In each of these low magnification images, the beam flyback line is clearly visible. Some scan anomalies are also visible as thick black lines in Figure 3.20 (b) and (c): this further informed the choice of region for high-magnification SEM image acquisition.

Typical high magnification (9000x) SEM images are shown in Figure 3.21. The regions were nano-ablated by raster scanning at λ=760 nm with total pulse energy increasing from 0.7 µJ to 4.3 µJ, corresponding to applied average power of 8 mW to 51 mW. Similar data was obtained for each wavelength used over the operating range of the laser source.

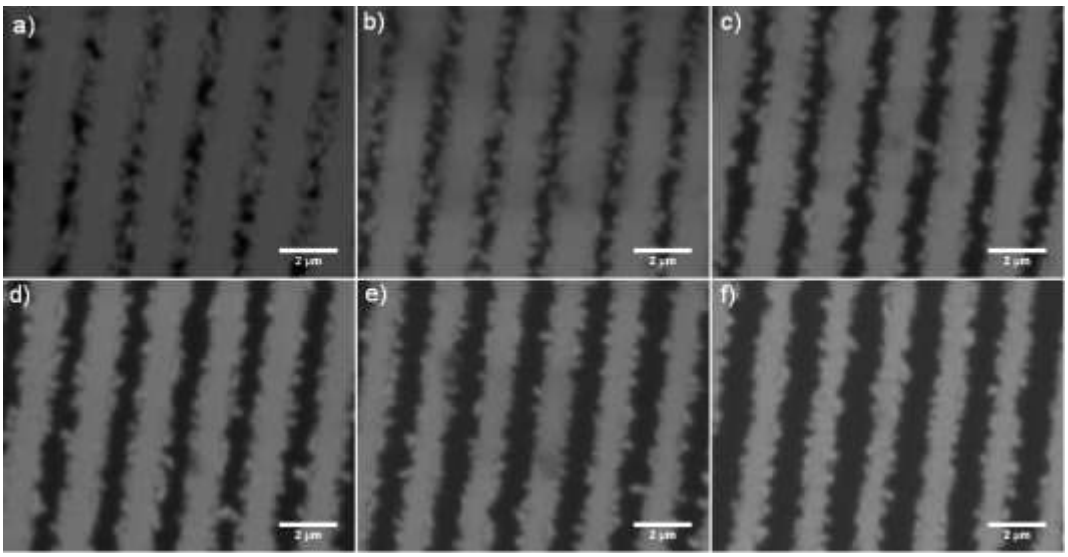

Figure 3.21- Single-frame nano-ablated raster scans taken with varying total pulse energy (a) 0.7 µJ, (b) 1.1 µJ , (c) 1.5 µJ, (d) 2.1 µJ, (e) 2.9 µJ and (f) 4.3 µJ applied to the specimen, at a fixed wavelength of λ=740nm were imaged using SEM at high magnification (9000x). The energies used correspond to applied average power of (a) 8 mW, (b) 13 mW, (c) 18 mW, (d) 25 mW, (e) 34 mW and (f) 51 mW.

It is evident from the high magnification images shown in Figure 3.21 that the nano-ablated zone at low pulse energies is less homogeneous than at high pulse energies. It is likely this is due to non-ablated aluminium remaining within the track. This contributed towards an increase in the error of the line-widths obtained following nano-ablation with low pulse energies, and therefore a similar increase in the error of the calculated lateral resolution.

The intensity profiles over one line in each image shown in Figure 3.21 is plotted in Figure 3.22, and shows the relative increase in ablated line width with increasing power. Measurements of the width of these intensity profiles were taken at the $1/e^2$ intensity. The average measured line width with increasing power over n=20 intensity profiles are plotted. This is plotted for each wavelength used in the ablation experiments. The results were consistent with a linear increase in nano-ablated line-width with increasing average power.

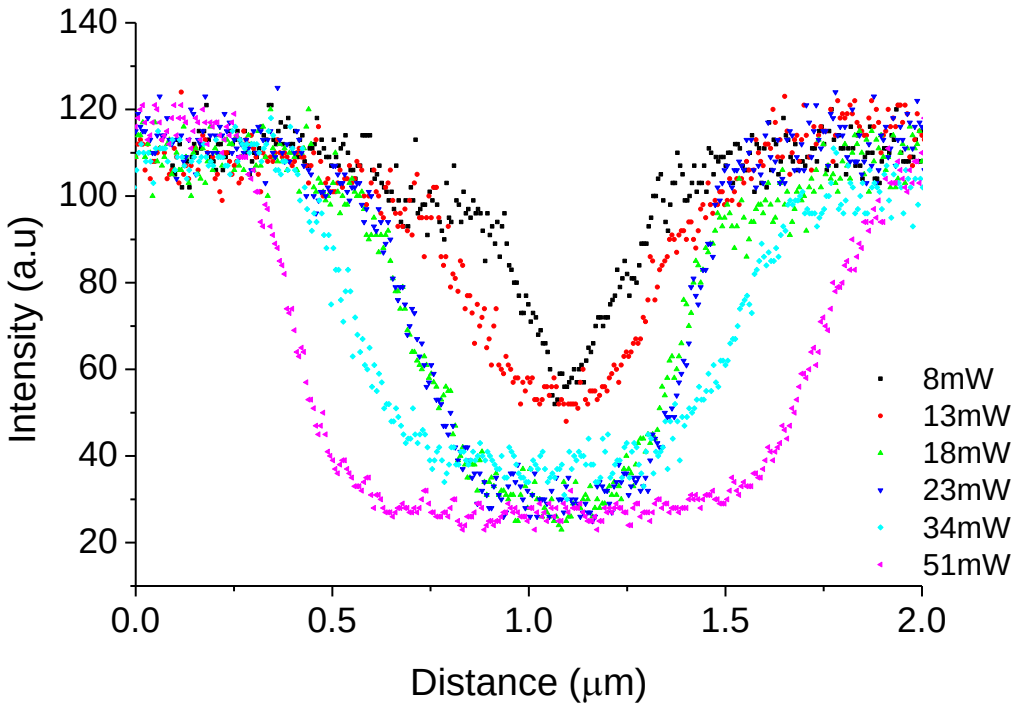

Figure 3.22- Intensity profile across one ablated line for increasing powers (from the images shown in Figure 3.21)

The average measured line width with increasing power over n=20 intensity profiles are plotted in Figure 3.23. This is plotted for each wavelength used in the ablation experiments. The results were consistent with a linear increase in nano-ablated line-width with increasing average power.

3.3.5 Image analysis

To obtain a value for the focused beam radius, the line-width data obtained from SEM image analysis was squared and plotted against the natural log of the incident pulse energy for each wavelength used in the nano-ablation process. This is presented in Figure 3.24, where the measurements are quoted with standard deviation in the mean. With the gradient of the line equivalent to $2w_0^2$, the value of the beam radius can then be determined from the best fit.

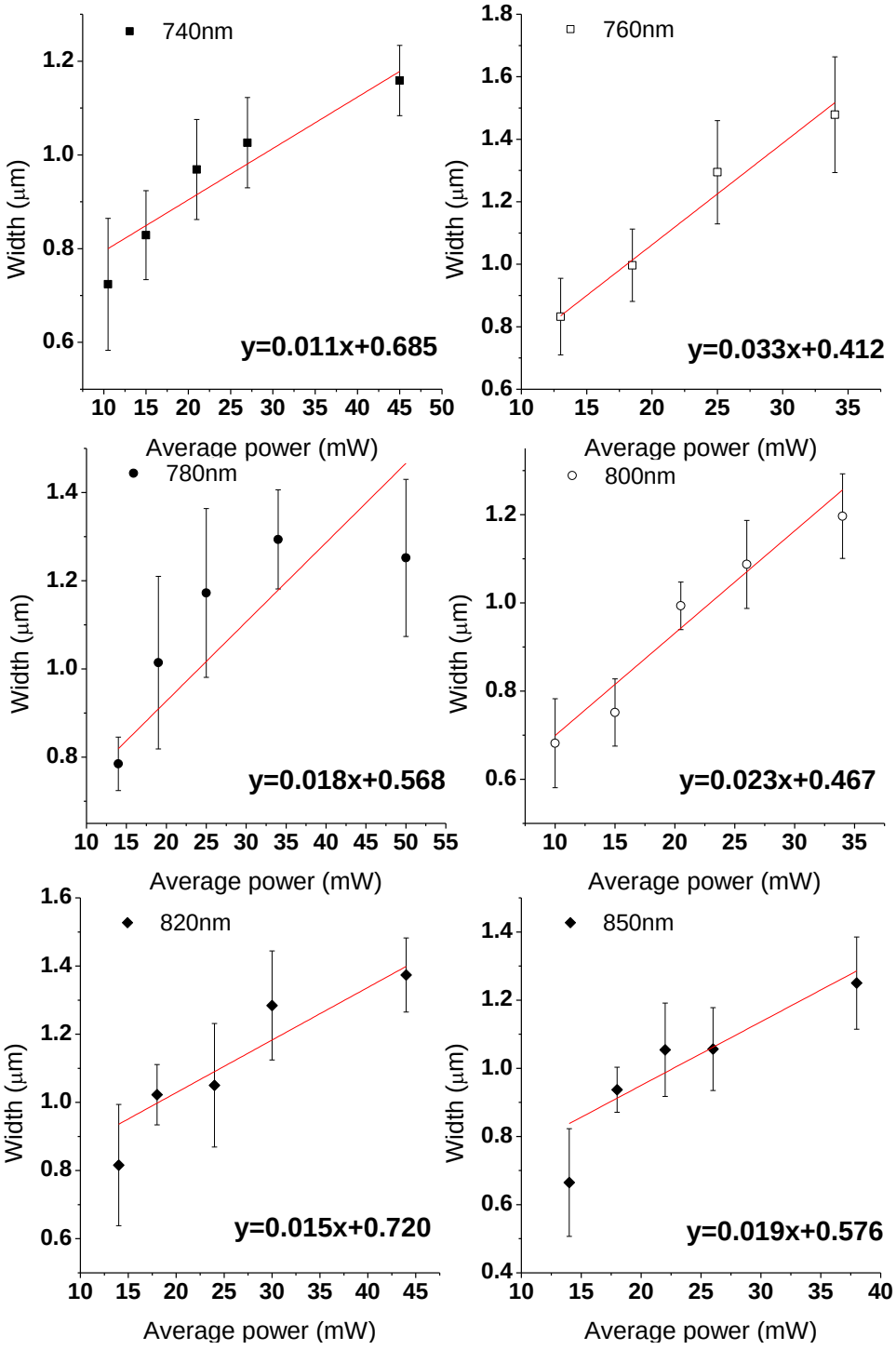

Figure 3.23- From the high-magnification SEM images, the line-width with varying average power was measured using ImageJ software for each wavelength used in the nano-ablation experiment. The measurements are quoted with standard deviation in the mean.

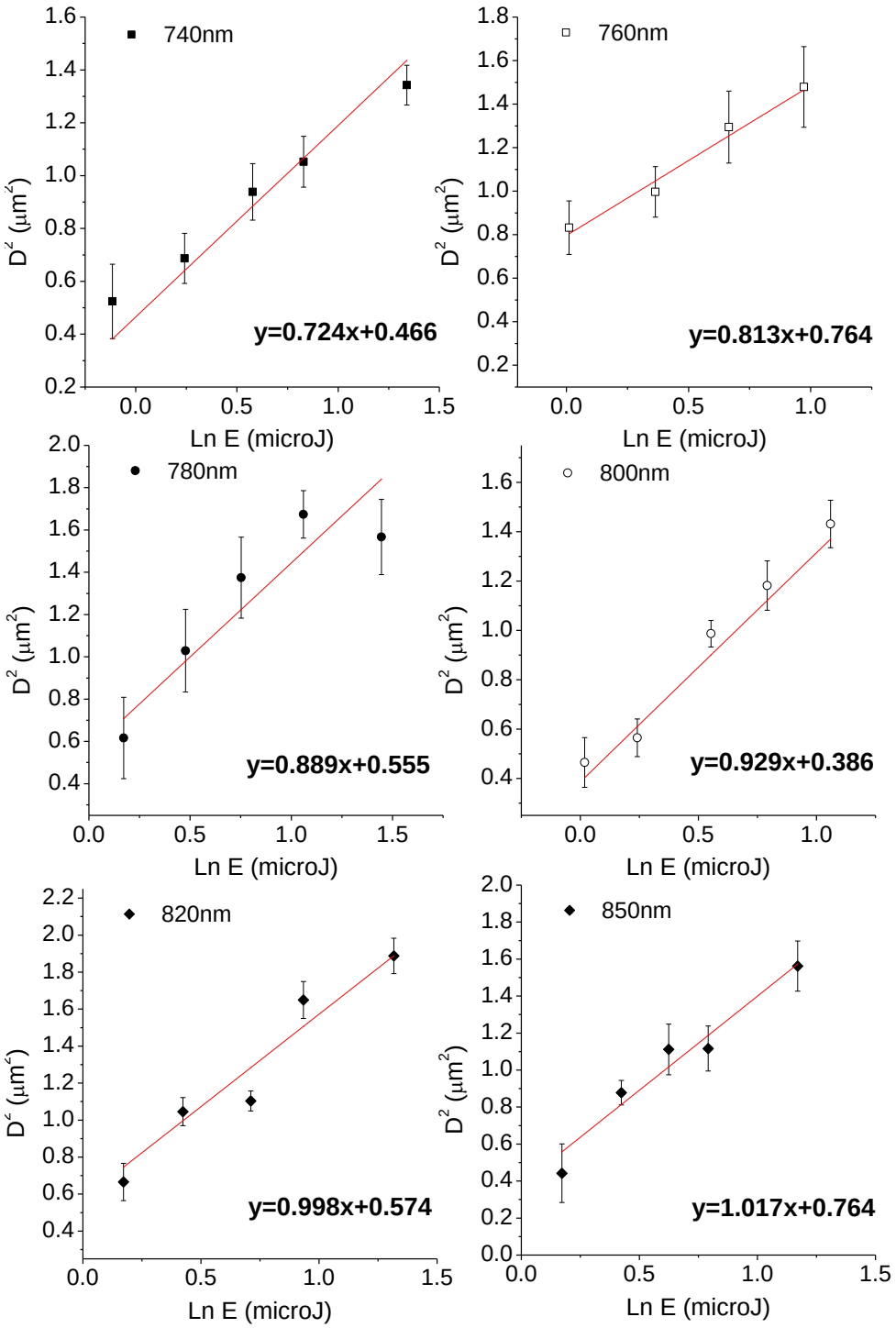

Figure 3.24- The square of the line-widths obtained for each wavelength with increasing average power are plotted against the natural log of the total pulse energy employed in the nano-ablation experiments. Mathematical fitting to experimental data was performed to obtain the best fit line and the gradient of the line, which, from Gaussian beam theory, was equal to $2w_0^2$, was used to calculate the beam radius and hence to determine the lateral spatial resolution of the laser scanning microscope. In this data, the error is the standard deviation in the mean.

The values of beam radius obtained from the gradients of the best fit line in Figure 3.24 are presented for each wavelength in Figure 3.25. For comparison, the theoretical resolution calculated from equation (1.2) for the 20x/0.75 N.A. dry objective lens used during the nano-ablation process at each wavelength is also shown in Figure 3.25. It can be seen that there is a reasonable agreement between experimental and theoretical data, with less than a 10% deviation from the values predicted using equation (1.2).

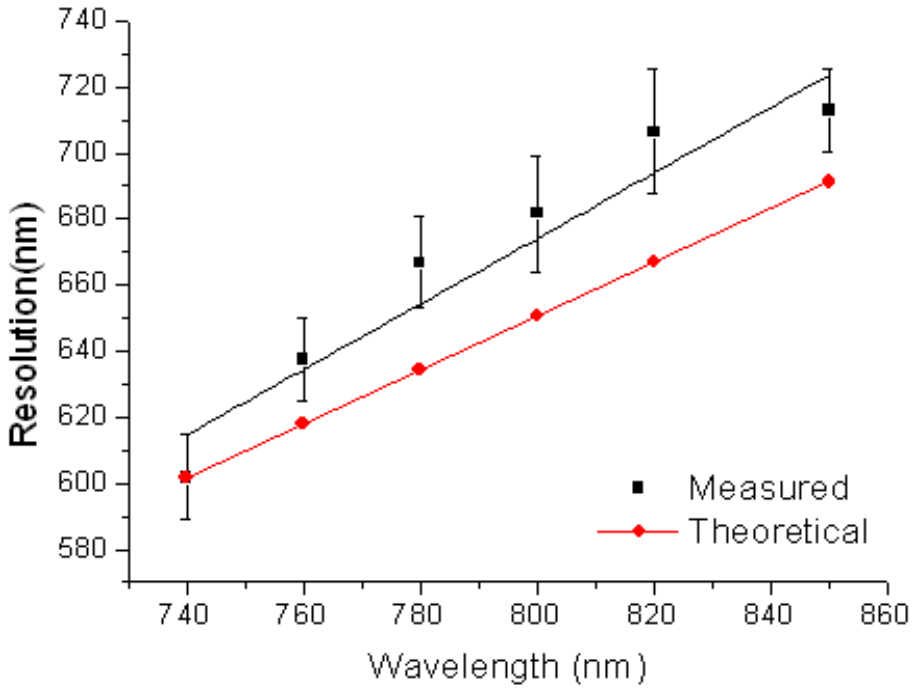

Figure 3.25- Lateral spatial resolution determined by analysis of SEM images of nano-ablated raster scans (squares). On the same scale is the theoretical lateral resolution given by equation (1) for the same numerical aperture and wavelengths used (circles). Good agreement between experimental and theoretical data was shown, with less than a 10% deviation from the values predicted using equation (1.2).

3.4.6 Comparison with ablation using the Leica SP5 system

To further test this method on another MPLSM platform the Leica SP5 was used to perform test ablation patterns on the aluminium surface. Confocal transmission images for a selected ablated rasters with 15mW excitation power at λ=730nm is shown in Figure 3.26.

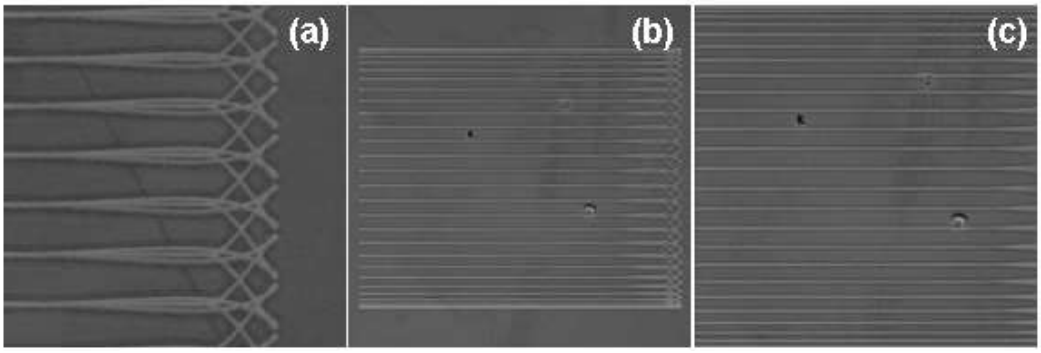

Figure 3.26- Confocal transmission images of ablated rasters at λ=730nm for (a) region showing flyback scan pattern, (b) region showing complete ablated raster at 3x zoom and (c) image of the scan lines that correspond to the image region at zoom=4x. Confocal transmission using the 488nm confocal laser line.

The image in Figure 3.26 (a) was taken at 10x zoom at the edge of the scan, this shows that the flyback pattern follows an unusual path relative to the Bio-Rad system. The image shown in Figure 3.26 (b) was taken at 3x zoom showing the full ablated region, from this image it is clear that the scan spacing is not uniform across the pattern, with the lines closer together at the top and bottom of the scan. Whereas, Figure 3.26 (c) was taken at 4x zoom, the same setting used to perform ablation, region corresponding to a 4x zoom image. It is clear that the unusual flyback lines in Figure 3.26 (a) do not contribute to the imaged region. However, this shows that there was significant overscan with this laser scanning system. It was found after discussions with service engineers that baffles in the beam path were not configured correctly and that these overscan effects would be eliminated with correct configuration. This problem would have been difficult to observe using existing measurement techniques that do not probe the scanning beam directly.

SEM images of representative raster patterns with increasing optical power and thus pulse energy are shown in Figure 3.27, using the same protocol as for the Radiance raster ablation. Low magnification images at 350x zoom are shown in Figure 3.27 (a-

c). Higher magnification images over a selected region are shown in Figure 3.27 (d-f).

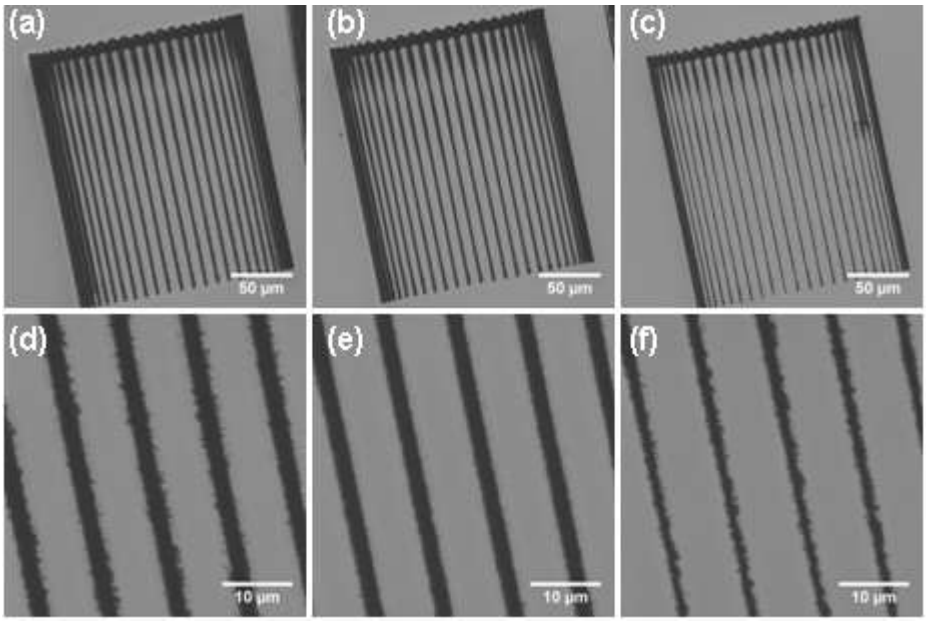

Figure 3.27- SEM images of ablated raster scans using the Leica SP5 system. Images (a-c) show low magnification images of ablated rasters at optical power (a) 10%, (b) 15% and (c) 20% laser power. Panes d-f are low magnification SEM images of the rasters shown in a-c respectively.

From the low magnification SEM images it can be seen that the expected trend of reducing ablated line width with reducing power was observed. The beam interaction was more noticeable at the flyback region where the beam slows (top) as well as the top and bottom of the scanned region where the line spacing is closer together (LHS and RHS on the SEM image). The 16x16 line scan produces more distinguishable and uniform straight lines than the 64 x 64 lines used in the Bio-Rad system (Figure 3.21) which would reduce the measurement errors. The lowest power ablation again produced less uniform lines than those in Figure 3.27 (d and e)

3.5 Discussion

This chapter has outlined the theory and testing of a novel measurement technique for use with multi-photon laser scanning microscopes. The effectiveness of this technique is proven in Figure 3.25, where a reasonable agreement was found between the measurements obtained and the theoretical resolution according to the Abbe-Rayleigh diffraction limit[66], [67]. This method offers improved accuracy because the scan line is swept rapidly, thus eliminating the effects of vibration at sub-kiloHertz frequencies, which often limits the precision of measurements with fluorescent beads or gold nanoparticles; however the main advantage comes from the use of the high-resolution SEM to measure the laser scanning microscope beam properties with 20nm resolution. This allows for nano-ablated line-widths to be measured more accurately and, assuming Gaussian optics, a beam radius can be determined. It would be interesting to perform the nano-ablation test with objectives within their design range of wavelengths, rather than those optimised for visible radiation but subsequently selected for high infra-red transmission.

The wavelength effects observed in Figure 3.25 indicate that the resolution of the system is lower than theoretically expected at longer wavelengths. This is likely due to under filling the back focal plane of the objective lens, which reduces the lateral resolution of the microscope [137]. It would be desirable to repeat these measurements at the shorter wavelengths used for confocal laser scanning microscopy, but the commonly-used lasers at these shorter wavelengths are continuous wave emitters with low average power, which was found to be insufficient to perform nano-ablation of aluminium. However, although other materials have been investigated, including gold, these proved much more difficult to nano-ablate. Alternative materials with low damage thresholds may be appropriate for similar measurement of confocal laser scanning microscopes. Alternatively, frequency doubling the Titanium Sapphire laser output would allow for access to shorter wavelengths, whilst fulfilling the required pulse energy to achieve ablation of the aluminium film. In view of renewed interest in regenerative amplifier lasers for

MPLSM [138], [139], the high pulse energies available from these systems may be suitable with the materials and methods used here [140]. The number of laser machining studies that use a regenerative amplifier type system far out-numbers those that use a high repetition rate source like the 90 MHz laser used in this study. This therefore would widen the number of materials suitable for ablation, such that a sample, such as silicon, which is more compatible with high voltage SEM systems, could be used to perform the type of measurements described in this chapter.

Although it was not the primary objective for this study, this method may well prove useful also in evaluating laser scanning microscopes, since it provides a permanent record of precise scan parameters such as line spacing, local velocity variations, the jitter due to bearing error in galvanometer-driven mirrors, errors such as bouncing at the end of each scan, or flyback errors. The true power of this technique as a general test was proven in the images taken for the Leica SP5 system, where the incorrect set-up of baffles on installation of the system was identified. It is particularly useful that the tests can be carried out in the laser scanning microscope without removing the scanning mechanism, as, for example, if deterioration in mechanical performance of the galvo drive mechanism over long periods of use is suspected. Although dry objective lenses were used in this study there is no reason why the same method could not apply for glycerol, oil or water immersion objective lenses, although some consideration for the compatibility of the specimen to be ablated with the immersion fluid may be required. In addition the cooling of the sample induced by using water or other liquids as an immersion material would change the line widths and ablation thresholds for the material; however the ablation width dependence on the power applied to the sample would still follow the same theoretical relationship.

This method used in combination with the technique described in chapter two is sufficient to adequately test the alignment, stability and resolution of any laser scanning microscope system. These techniques are more robust than current techniques which are far more subjective, which in turn reduces the quantification and calibration of the microscope.

3.6 Conclusion

This chapter has reported a novel approach to the measurement of the focal spot in laser scanning microscopy, which can be performed at laser powers currently used in biomedical microscopy. The results are precise and give absolute values broadly as expected from elementary diffraction theory. This approach is likely to be of value in the search for improved optical performance in the near-infrared. This technique may also prove of value in servicing and developing laser scanning instruments.

Chapter 4: Light-induced Ca^{2+} transients observed in widefield epi-fluorescence microscopy of excitable cells

4.1. Introduction

With innovations in photochemistry such as the development of fluorescent proteins and synthetic biomarkers [39], [41], and advances in light emitting diodes (LEDs) [5], [6], computers and electronic detectors specifically for imaging applications [141], epi-fluorescence microscopy techniques have become widely used in the study of live biological specimens to examine morphology and physiological processes. Except in experiments where photo-bleaching is deliberately induced (e.g. in order to measure the rate of recovery of fluorescence [142], [143]), the levels of light used in widefield epi-fluorescence microscopy are typically a few mW or sub-mW. At these levels, photo-bleaching is slow and it is widely assumed that under these experimental conditions, the incoherent light has no effect on the specimen.

It has been reported previously that laser scanning microscopy can induce physiological responses [144–146]. For example, Smith et al. [144], [145] demonstrated that ultra-short pulsed near-infrared lasers similar to those used in multi-photon imaging can evoke intracellular Ca^{2+} transients, while Knight et al. demonstrated that lower power continuous wave lasers usually employed in confocal microscopy may trigger transient responses and cell death [146]. However, it is not confocal or multi-photon imaging techniques that are most frequently employed in studying Ca^{2+} transients, but widefield epi-fluorescence microscopy.

This Chapter investigates the effect of sub-mW levels of widefield incoherent light on excitable cells, specifically to evaluate the possibility that variations in the level of intracellular Ca^{2+} in excitable cells might be induced as an artefact of the incoherent illumination that is being used to monitor the transient responses. In order to avoid any fluctuations in power of an arc lamp source, a microscope using a light emitting diode that was calibrated accurately at low power levels, was

constructed to provide good control over the dose of light applied to the biological specimen. This Chapter shows that higher powers of illumination increased the probability of occurrence of Ca^{2+} transients even in the sub-mW range normally used to measure such transients in epi-fluorescence work, suggesting that caution should be exercised when designing experiments and interpreting data.

4.2 Background Information

4.2.1 Ca^{2+} transients in smooth muscle cells

Ca^{2+} signalling has been an area of intense research for many decades. This is undoubtedly due to the prominence of Ca^{2+} in cellular processes ranging from cell contraction to apoptosis and necrosis [147]. Probing the underlying Ca^{2+} transients and signals gives an insight into the vast array of cellular functions. Studying Ca^{2+} signalling is of importance and in particular understanding the paradox that Ca^{2+} can act as a signal for both life and death [148]. There are consequently a range of protocols and techniques in place to study such ion channel processes. The main techniques applied are electrophysiology procedures [147] as well as chemical controls [149]. However, these techniques are invasive thus there is a drive to produce a technique that does not compromise the behaviour of the cells in an *ex vivo* environment.

Through many years of research in Ca^{2+} transients and signalling mechanisms it has been extensively noted that the transients can be very versatile [150]. Current opinion in this field defines Ca^{2+} transients through three domains, namely space, time and amplitude. Information is encoded in these three domains thus controlling the physiology of the cell. Within the spatial signalling domain, the Ca^{2+} release can occur at localised regions of the cell or globally over the entire cell. These can also generate Ca^{2+} waves that then signal to other cells in close proximity. These variations in Ca^{2+} are shown in Figure 4.1.

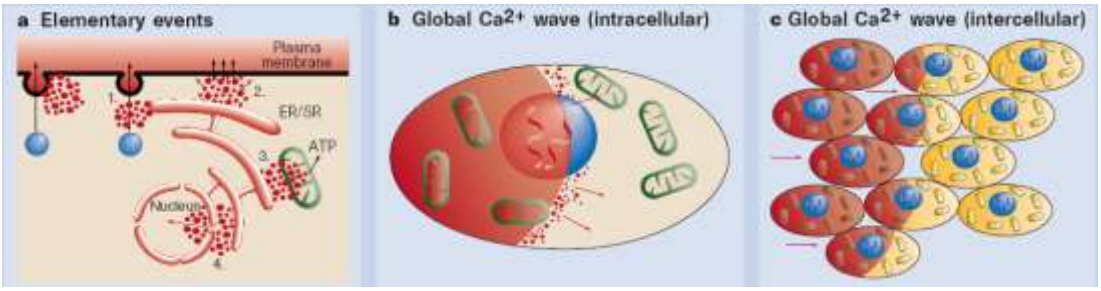

Figure 4.1- Spatial aspects of Ca^{2+} signalling. (a) shows a schematic representation of localised Ca^{2+} release from the internal stores (ER/SR), the mitochondria and the channels that span the plasma membrane, (b) shows the generation of a Ca^{2+} wave where a number of localised events combine to generate a global rise in Ca^{2+} and (c) shows the inter cellular Ca^{2+} wave transferring to neighbouring cells. Reproduced from [148]**.**

Changes in Ca^{2+} concentration are necessary for it to act as a signal. However, elevations in Ca^{2+} concentration over a long time scale can be damaging [151]. Therefore, Ca^{2+} signals that initiate a physiological process are usually in the form of brief transients, where there is a sharp rise and then decay back to the resting Ca^{2+} level. A typical Ca^{2+} transient, measured using a fluorescent Ca^{2+} indicator (described in more detail in Section 4.2.4), is shown in Figure 4.2.

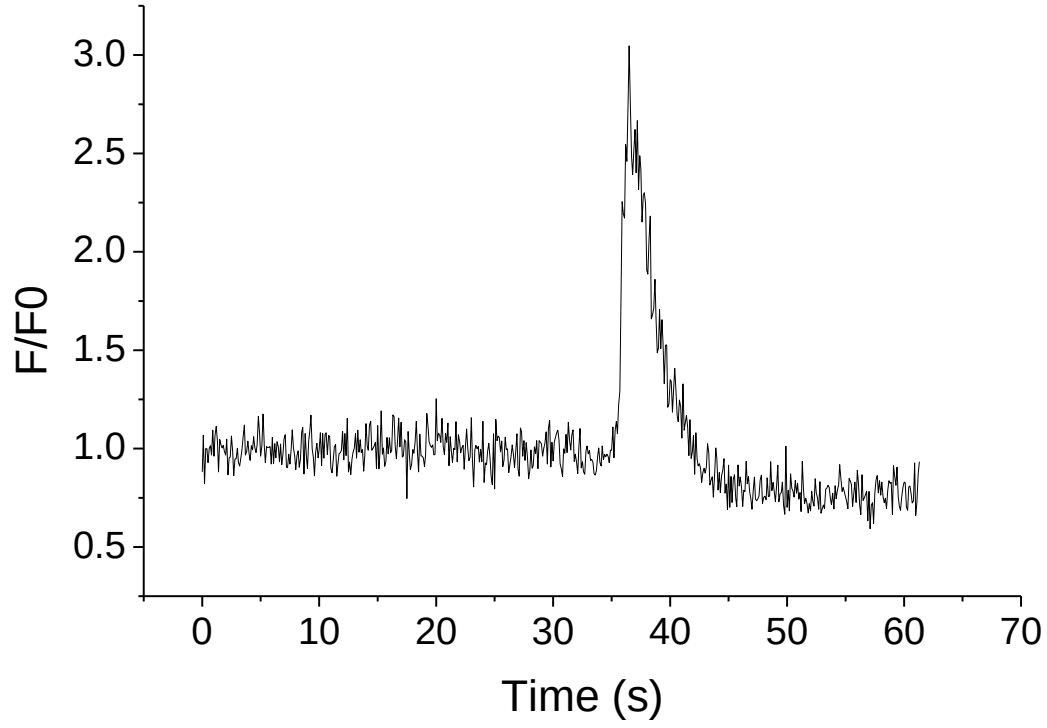

Figure 4.2- Ca^{2+} transient shown by fluorescence intensity variation over time relative to the baseline fluorescence level, showing a sharp rise in intensity and thus Ca^{2+} concentration followed by a decay in intensity.

Single transients can be used for one cell function, whereas a repetition of a single transient can signal for a completely different process [151]. This therefore results in a variation of the physiological output. It is thought that cells use frequency modulations in Ca^{2+} release from internal stores to vary the physiological output [151]. One example is that arteries can be made to dilate by increasing the frequency of Ca^{2+} sparks at the membrane surface [148]. The temporal signals can also be combined with amplitude to control the cellular response where, the concentration of Ca^{2+} can be varied to form a signal. However, this is not investigated to the same extent as temporal signalling due to low sensitivity in the instrumentation used which does not allow for small changes in Ca^{2+} concentration to be detected [151].

4.2.2 Stimulation of intra-cellular Ca^{2+} events

There are a number of techniques routinely used in biology research to study Ca^{2+} transients. What follows is a historical perspective of the development of techniques currently widely applied to probe the Ca^{2+} signalling in live cells. For clarity, I will group this into two main categories, namely electrophysiology techniques and chemical stimulation techniques.

Electrophysiology is the most prominent technique for studying ion channel behaviour. Since the early experiments by Luigi Galvani and Alessandro Volta on bio-electricity in the late 18^{th} century, many developments were made in biology developing the understanding that the membrane layer could be controlled by a voltage [152]. However, it was not until the 1930's when Hodgkin and Huxley used electrodes to make measurements of the membrane potential [153] . From this, the voltage clamp method and later the patch clamp methods were developed into the electrophysiology techniques used today [154–156]. The patch clamping technique is now widely used in biology, however to measure currents from the ion channels a tight seal has to be formed around the micropipette containing the electrode. Firstly, this reduces the channels studied as the voltage clamp is only possible for ion channels in close proximity to the membrane. Secondly, the methods involved could damage the cell membrane, thus compromising the behaviour of the ion channel

being studied. However, this technique has become a powerful tool in understanding biological processes and the nature of the diverse Ca^{2+} signalling processes. Without such developments a wide range of medical treatments would not be available today.

Electrophysiology is more widely used due to the high controllability using electrical stimulus, however the use of chemical stimulus is also of significant importance. In particular the use of a chemical to induce a known and relatively well understood process within a cell can provide an alternative route in establishing the roles of different ion channels. Chemicals are also used to block certain ion channels providing a way of determining the location and mechanisms of Ca^{2+} release in the cell.

4.2.3 Optical stimulation techniques

Inducing cellular Ca^{2+} transients using only an optical stimulus is a recent development in this field. This was first reported in 2001 in a study which used an intense laser source to induce Ca^{2+} rises in HeLa cancer cells [157]. This study used a multi-photon effect where tens of milliWatts of average power was focused below the cell membrane. This resulted in a Ca^{2+} transient which was detected using a Ca^{2+} indicating fluorescent probe. This investigation was later extended to other cell types and was later applied to induce beating of a cardiac myocyte in isolation as well as inducing oscillations within a group of cells [158]. Following these investigations a number of studies have been performed to examine the cellular mechanism responsible for photo-stimulated Ca^{2+} transients [145], [146], [157], [158].

4.2.4 Fluorescent Ca^{2+} indicators

Fluorescent indicators for measuring Ca^{2+} levels in live cells are of significant benefit to current ion channel studies using chemical and electrophysiological methods. For this study fluorescent Ca^{2+} indicators are also required. There are a number of fluorescence indicators for intra-cellular Ca^{2+} with varying spectral properties as well as specificity to location of intra-cellular Ca^{2+}.

4.2.5 Cell viability

When working with and imaging live cells there are many constraints to ensure that the cells are not damaged in a way that would alter the parameters under investigation. Therefore, it is of no surprise that this in itself is an intense area of research [53], [146]. With new imaging technologies there is an increased ability to image cellular components with high resolution and also with increased depth [159]. However, the technology required to do this can be potentially damaging to the sample of interest as described in Chapter 3. In 2001 it was reported by Tirlapur *et al* that near infra-red laser pulses can generate harmful levels of reactive oxygen species (ROS) inducing apoptosis in mammalian cells [54]. This type of light source is commonly used for two-photon imaging, a technique widely used for in-vivo imaging due to the deeper imaging depths from reduced scattering at long wavelengths [160]. Although the damage caused can be attributed to the high powers used in this application, later studies have shown that lower power levels using confocal imaging can also generate significant quantities of ROS [161]. This is of significant interest in this study as ROS has also been linked as a potential pathway for the generation of Ca^{2+} transients [162].

4.3 Methodology

4.3.1. Cell isolation

Colonic smooth muscle cells were selected for this study as they are robust cells which allow for imaging over extended periods of time without reduced cell viability. Male guinea pigs (500–700g) were sacrificed by cervical dislocation and immediate exsanguination in accordance with the Animal (Scientific Procedures) Act UK 1986. A segment of distal colon (~5 cm) was immediately removed and transferred to an oxygenated (95% O_2–5% CO_2) physiological saline solution of the following composition (mM): NaCl 118.4, $NaHCO_3$ 25, KCl 4.7, NaH_2PO_4 1.13,

$MgCl_2$ 1.3, $CaCl_2$ 2.7 and glucose 11 (pH 7.4). Following the removal of the mucosa from this tissue, single smooth muscle cells, from circular muscle, were isolated using a two-step enzymatic dissociation protocol [163], stored at 4 °C and used the same day. This procedure was carried out by Drs Marnie Olson, Susan Chalmers and Debbi MacMillan (Prof. John McCarron). All experiments and loading of cells with the fluorescent indicator Fluo-3AM were then conducted at room temperature (20±2 °C).

4.3.2 Loading with fluorescent proteins

Initially the Fluo-3 acetoxymethylester (Fluo-3 AM) in powdered form was dissolved in Dimethyl Sulfoxide (DMSO) to make a 1ml 10mM stock solution. It is imperative to use gloves whilst using this compound as DMSO penetrates the skin rapidly. The container was then covered in foil to prevent light exposure. The solution was mixed and left on a rocker at room temperature for 3 hours before use or freezing to ensure efficient mixing. The stock solution was then stored at -20°C between experiments. Freeze and thaw cycles were minimised as much as possible. When required, the Fluo-3AM stock solution was removed from the freezer and warmed slightly by hand. Initially 700 µL of dissociation medium without bovine serum albumin (BSA) was transferred into a glass vial. Into this 1 µL of 10 mM Fluo-3AM stock solution was added giving a working concentration of 10µM. The solution was then mixed to minimise clumps of fluorescent dye forming in the solution. Next, 300 µL of cells from one vial was added to the buffer solution containing the fluorescent dye. The container was then sealed and covered to avoid light exposure then placed on a rocker for 30 minutes prior to imaging to prevent sedimentation and to ensure effective loading of the dye to the cells.

Cells were loaded with the membrane-permeable dye, fluo-3 AM (10µm; Molecular Probes, Paisley, UK) for 30 minutes prior to the beginning of the experiment. The composition of the extracellular solution was (mM): Na glutamate 80, NaCl 40, tetraethylammonium chloride (TEA) 20, $MgCl_2$ 1.1, $CaCl_2$ 3, HEPES 10 and glucose 30 (pH 7.4 adjusted with NaOH 1M).

4.3.3 Epi-fluorescence microscopy

Initially, a standard epi-fluorescence microscope (Nikon Eclipse E600 with mercury arc lamp system) was used, but this proved difficult due to fluctuations in average power and so the microscope was modified to give better control over the illumination. The experimental layout used for this study is shown in Figure 4.3. Cells were placed in a recording chamber (1 ml) on the stage of an inverted fluorescence microscope (Olympus IX81). Instead of using the epi-fluorescence illumination system provided by the manufacturer, the system was adapted to couple in an external LED as the excitation source. The system is deliberately simple, providing the same excitation geometry as used in conventional epi-fluorescence microscopy, but with good control over the illumination power and improved detection to capture rapid changes in fluorescence. While the design of the microscope is intrinsically safe due to the low power of the LED light source, great care must be taken if considering using a similar design with more powerful sources such as arc lamps, as blindness could result. The use of safety interlocks in such a scenario is of importance and should be considered.

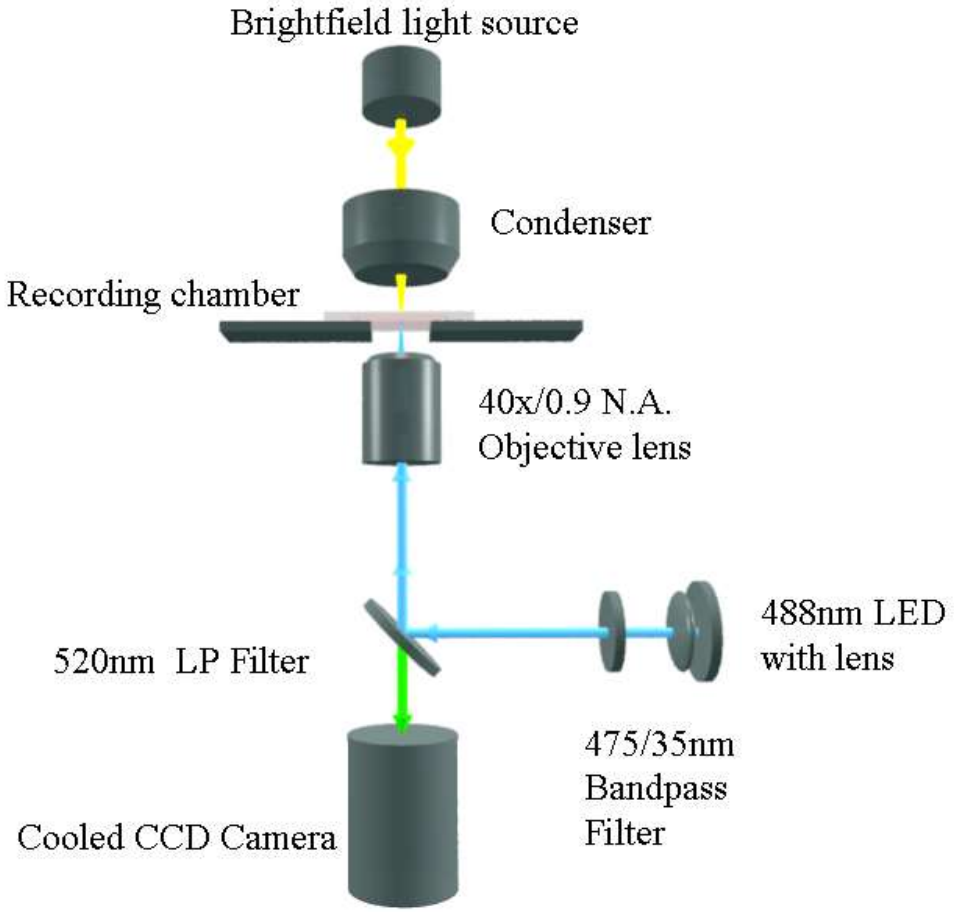

Figure 4.3- Schematic of widefield epi-fluorescence and brightfield transmission microscope system. Brightfield transmission was collected by the condenser lens and viewed through the eyepiece. White light illumination from the lamp was computer controlled via a flip mirror. The 488 nm LED excitation source was lensed and filtered externally from the inverted microscope to uniformly fill the field of view. Fluorescence was detected using a highly sensitive fast CCD camera with a 520nm LP filter in the detection path.

The LED (Luxeon Star K2, Lumileds Lighting) had a peak emission wavelength of 488 nm, collimated by single lens (LXHL-NX05, Lumileds), anti-reflection coated for the visible spectral region. An optical bandpass filter (FF01-475/35-25) was used to ensure that only 475 ± 35 nm output was used for excitation. The LED output power was controlled by a power supply (Iso-tech IPS303A), which provided a maximum current and voltage of 3 Amps and 30 Volts respectively, satisfying the maximum operational parameters suggested by the LED manufacturer.

A 40x/0.9 N.A. dry objective lens (UPlanSApo, Olympus) was used for all experiments providing a field of view of (0.316 mm x 0.316 mm) and a theoretical lateral resolution of 330 nm [17]. The spectral reflector used was a 520 nm long-

wave pass filter, reflecting the shorter wavelength excitation towards the specimen and the longer wavelength fluorescence to the detector. The LED filled the field of the objective uniformly with light to illuminate an area of 0.316 μm x 0.316 μm.

The light power and hence intensity delivered to the cells on the microscope stage was controlled by maintaining the LED at fixed voltage and altering the applied current. During this study, four power parameters were used as described in Table 1. The average power at the sample is quoted with a standard scale reading error. The light power was measured using a sensitive photodiode based power meter (Nova II, Ophir Optronics) for each current value applied to the LED. The lowest power of 30 μW was chosen because lower powers of illumination gave a fluorescence signal almost indistinguishable from the background intensity level. As a dry objective lens for the study, no immersion material was required for this measurement. The average power was measured before every imaging experiment to ensure the power at the sample did not vary between different experiments. All experiments were undertaken in a dark room environment to minimise light exposure to the sample and also to prevent leakage of room light into the camera.

Table 1- LED current correlated with power at sample, with scale reading uncertainty.

Current (A)	Power (μW)	Power per unit area (nW/μm2)
0.1	30 ± 0.5	0.30
0.2	70± 0.5	0.70
0.3	110± 0.5	1.10
0.4	150± 0.5	1.50

For capture of the images and video clips, a charge-coupled device (CCD) camera (I-PentaMAX:HQ, Princeton Instruments) was used at 10 fps. This system was computer controlled using WinFluor software [164] and the same software was used for image acquisition.

Before each imaging session, the CCD camera was pre-cooled to -20 °C for at least ten minutes to reduce dark noise levels. The alignment of the LED was also checked using a standard fluorescent test slide (*Convallaria* specimen, Leica).

To perform the experiment, a cell was brought into the field of view and into focus using brightfield transmission imaging at low power (sub-10 μW). Cells that appeared rounded or showed signs of blebbing or structural damage under brightfield illumination were excluded from this study. The same selection protocol is also used by electrophysiologists working on cells of this type.

With the cell in focus, the configuration was then switched to epi-fluorescence excitation and recording using the LED and fast CCD camera. Initially, the current was adjusted to 0.1 A (corresponding to the lowest light power, 30 μW) used in the experiment and a movie was recorded using the fast CCD camera for durations in excess of 60 seconds, during which time the fluorescence signal was recorded. After each movie, a different cell was selected. Cells were selected systematically by moving the recording chamber in one direction to ensure that the same cells were not re-exposed to the visible wavelength excitation source. This process was repeated at the power levels detailed in Table 1 for n=30 cells per power level.

The movie files generated were then analysed using the same software as for movie acquisition (WinFluor). Region of interest (ROI) analysis of the fluorescence signal intensity of the full or partial cell was performed over the duration of the movie. A Ca^{2+} localised response was defined as an increase in fluorescence signal intensity that exceeded 10% of the baseline, but which occurred over less than 10% of the cell body, while a global Ca^{2+} response was defined as a fluorescence signal intensity that exceeded 10% of the baseline level and occurred over more than 50% of the cell body. A null response was taken as a fluorescence signal intensity which did not vary by >10% from the baseline fluorescence level. To verify the significance of the results observed, $\chi 2$ testing was performed.

4.4 Results

To investigate the effects of low light intensity illumination during epi-fluorescence microscopy on the number of cells exhibiting Ca^{2+} responses, cells were loaded with the fluorescent Ca^{2+} indicator fluo-3 AM and exposed to varying illumination powers for at least 60 seconds. Ca^{2+} responses, measured as changes in fluorescence intensity were analysed and spatially categorised as described previously.

Few responses were observed at low incident powers. However, the number of cells exhibiting a Ca^{2+} response increased with increasing excitation powers. Cells exhibiting Ca^{2+} responses were subdivided into those exhibiting either a local or global Ca^{2+} rise. The number of cells exhibiting each response at incrementally increasing illumination power is illustrated in Figure 4.4. Cells that did not respond are not shown explicitly. The results are presented with a 5% error in detection of a fluorescence signal increase (local or global) and with a standard error for optical power. At 30 μW power, only a minority (10%) of cells exhibited Ca^{2+} responses. Of these, 7% exhibited a local response (2 of 30 cells) and 3% exhibited a global response (1 of 30 cells). At increasing excitation powers, the number of cells exhibiting Ca^{2+} responses increased to 60% and 43% at 110 μW and 150μW, respectively. At 110 μW, 36% of cells exhibited a local response (11 of 30 cells) and 23% of cells exhibited a global response (7 of 30 cells). Increasing the power to 150μW did not further increase the percentage of cells exhibiting either a local (33%; 10 of 30 cells) or global rise in Ca^{2+} (10%; 3 of 30 cells). An unexpected decrease in the number of Ca^{2+} responses at 150 μW in comparison to illumination at 110 μW was observed (as shown in Figure 4.4). However, from $\chi 2$ tests this was not statistically significant ($p>0.05$).

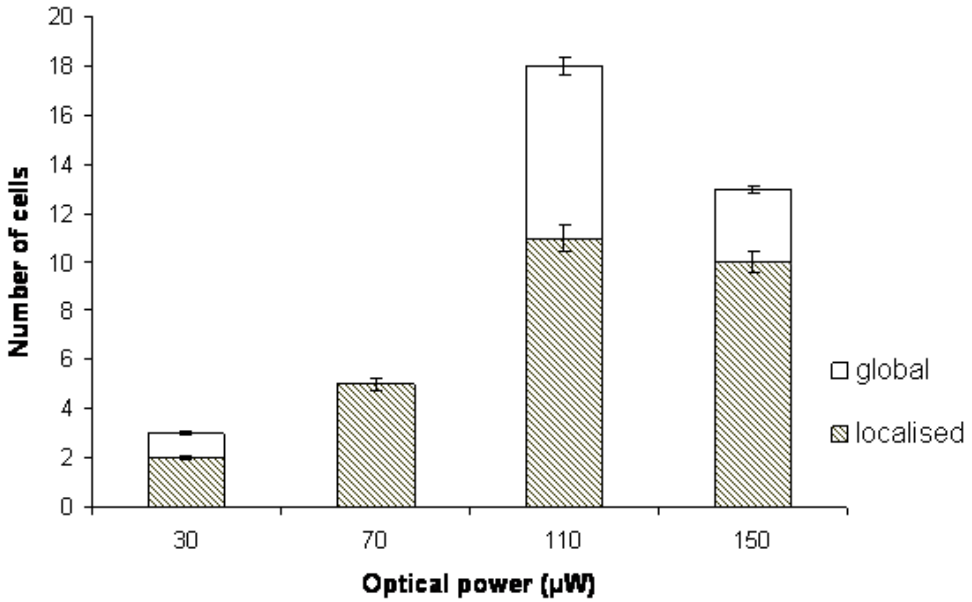

Figure 4.4- The number of cells exhibiting Ca^{2+} responses for n=30 cells are shown for each optical power setting. The responses are categorised as global or localized response. The data is expressed with a 5% error in detection for optical power.

Representative examples of localised and global Ca^{2+} responses at 150 μW power are illustrated in Figure 4.5. Figure 4.5 (a) shows a localised Ca^{2+} rise at t=16.4 seconds. In the same cell, a global Ca^{2+} transient was observed (Figure 4.5(b)) following the local response (t=36.8 seconds). The corresponding localised and global Ca^{2+} traces are illustrated in Figure 4.5(c).

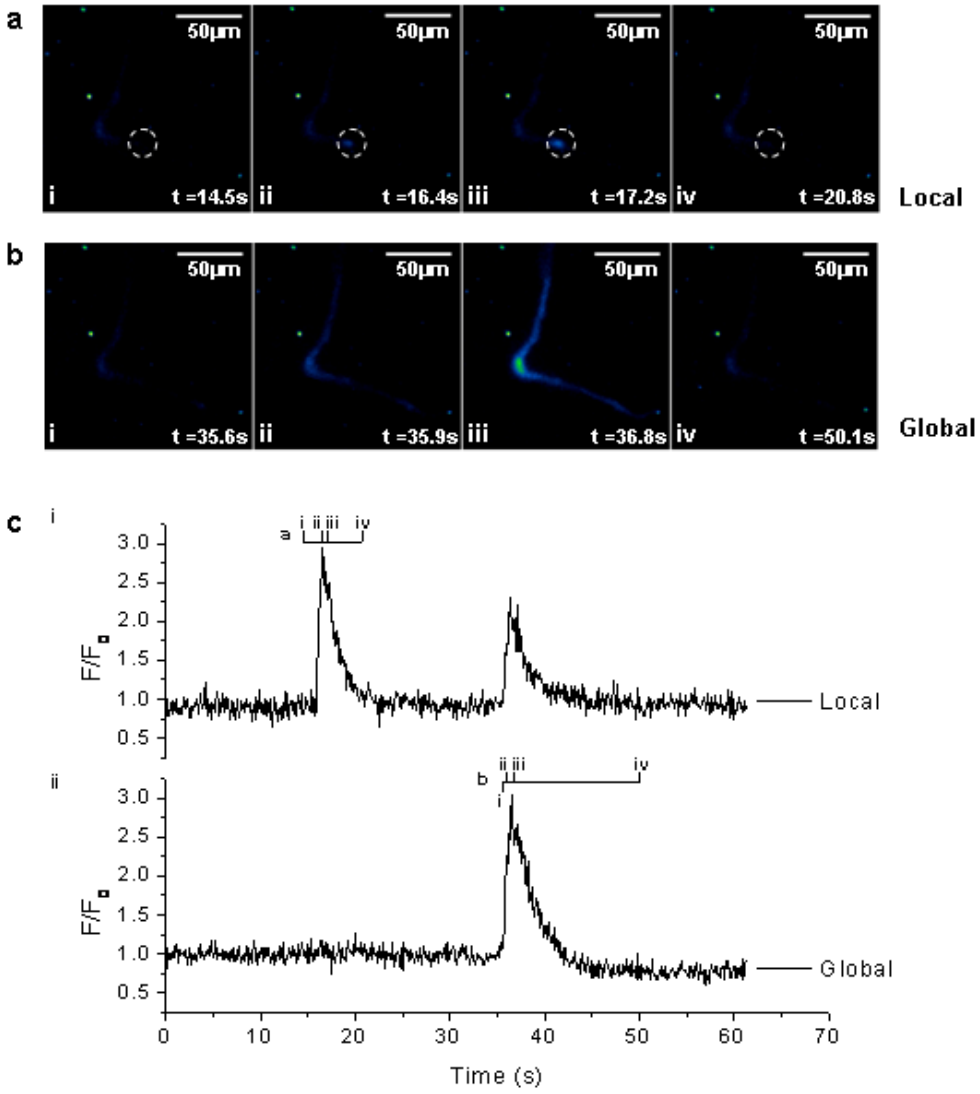

Figure 4.5-Extracted frames from a movie of an isolated smooth muscle cell with 150 µW of 488 nm irradiation. The progression of a localised Ca^{2+} transient is shown in Fig4.5(a) at time points i) 14.5 seconds, ii) 16.4 seconds, iii) 17.2 seconds and iv) 20.8 seconds. The region of interest is indicated by the broken circle. Fig 4.5 (b) Extracted frames of the same cell shown in Fig4.5(a) at a later time point. The progression of a global Ca^{2+} transient is shown over the following time points i) 35.6 seconds, ii) 35.9 seconds, iii) 36.8 seconds and iv) 50.1 seconds. Fig4.5 (c) Corresponding normalised fluorescence signal intensity profiles over the course of the acquisition period shown in Fig4.5 (a) and 4.5(b). 4.5(c)i shows the intensity measured in the region circled in Fig 4.5 (a) over time, and 4.5(c)ii shows the intensity of the full cell over time.

A representative frame from a video clip demonstrating a single global Ca^{2+} transient is shown in Figure 4.6 (Media 1). Here, for illustration purposes, the movie is truncated from t=0 seconds to t=80 seconds, where 30 µW average power was applied to the specimen, during which time the cell was brought into focus and centred on the field of view. At t=164 seconds, the average power applied to the specimen was increased from 30 µW to 70µW, and the power was again increased,

from 70 μW to 110 μW at t=271.2 seconds. The movie is shown together with the fluorescence signal intensity plot, where the signal is monitored at a single point, marked on the cell body (+). The movie capture rate of 10 Hz is indicated on the y-axis (10). At 30 μW and 70 μW powers, no apparent changes in fluorescence signal intensity were observed, relative to the proportional increase in background signal. However, at t=307.6 seconds (110 μW), a global Ca^{2+} transient was evoked, with several orders of magnitude increase in fluorescence signal that returned to baseline. A rise in intracellular Ca^{2+} concentration triggers cellular contraction (as shown in Media 1: see supplementary movie files) and can cause cell death. However, the ability of each cell to relax following contraction suggests that the powers of illumination used in this study, including higher powers, did not cause irreversible cell damage (n=30).

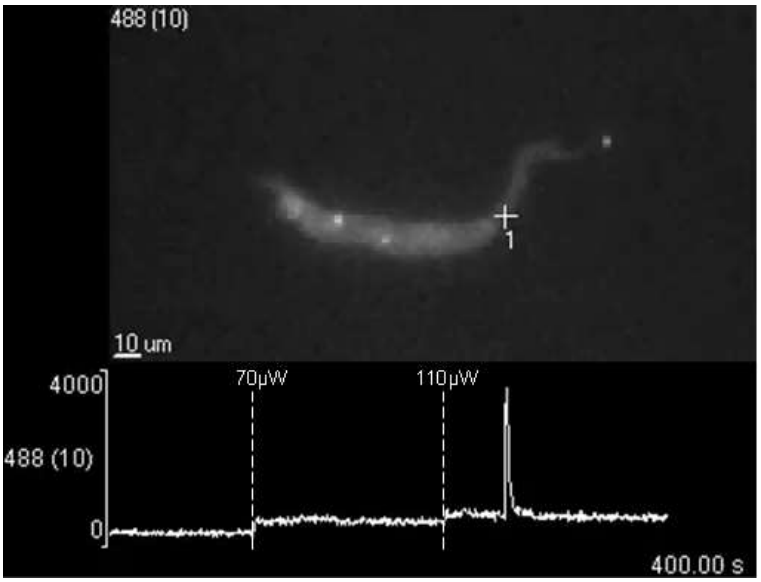

Figure 4.6-A global Ca^{2+} transient was observed after a step-wise increase in optical power (Media 1). The specimen was initially irradiated from t=0-80 seconds at 30μW (not shown). The 30 μW irradiation continued from t=80 seconds until t=164 seconds, when the average power was increased to 70 μW. The specimen was illuminated from t=164 seconds to t=271.2 seconds, and then the power was incremented to 110 μW for the remainder of the experiment. A global Ca^{2+} transient is observed with illumination of 110 μW average power at t=307.6 seconds. The selected frame shows the recovered cell at t=400.00 seconds. The measuring point (cross and '1') indicates a highlighted single point from which the fluorescence intensity over time data was plotted.

The representative images in Figure 4.7 illustrate contraction and recovery of a smooth muscle cell following a global rise in Ca^{2+}. Figure 4.7(a) shows a cell in which no Ca^{2+} responses were observed under 70 μW illumination. Increasing the

illumination power to 110 μW evoked a global rise in Ca^{2+} (Figure 4.7(b)) resulting in cellular contraction (Figure 4.7 (c)) and recovery (Figure 4.7 (d)). Again, no morphological changes were observed that would indicate cell damage.

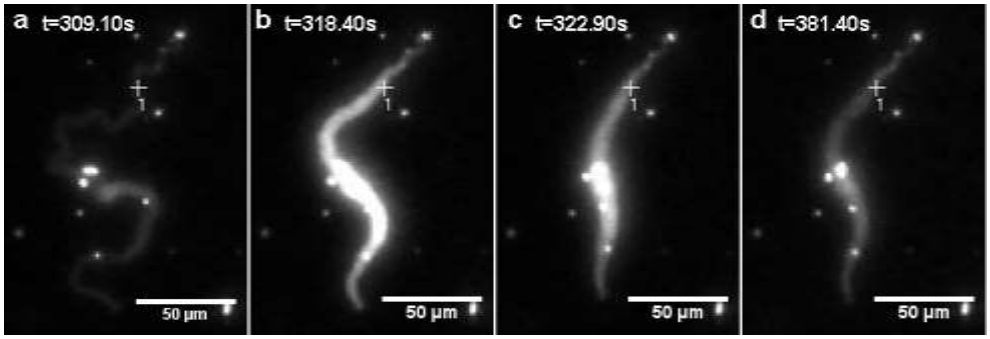

Figure 4.7-A global Ca^{2+} rise resulting in contraction of a single smooth muscle cell under epi-fluorescence excitation. Frames show (a) an unresponsive cell under 70 μW illumination at t=309.10 seconds, (b) a global Ca^{2+} rise under 110 μW illumination at t=318.40 seconds, (c) subsequent cell contraction at t=322.90 seconds followed by (d) recovery at t=381.40 seconds. The cross (+) and '1' indicates a highlighted single point from which it was possible to plot fluorescence intensity over time data (not shown).

4.5 Discussion

Intracellular Ca^{2+} is a ubiquitous second messenger controlling fundamental and diverse cellular processes, including cell division, growth and cell death and provides the major trigger for smooth muscle contraction. Here, the demonstration of an increase in the number of cells exhibiting Ca^{2+} responses at increasing excitation power of the light source, which is marked even in the sub-mW range. Thus, light-induced Ca^{2+} signalling may trigger alterations in numerous cell processes at power levels provided by standard, commercial epi-fluorescence microscopes. Caution should be exercised in interpreting data.

There has been little work to date on disturbances in cell physiology at the low powers of incoherent light used here. This is possibly because the mercury arc lamp used as a source in many epi-fluorescence studies shows marked fluctuations such as those observed by us in the experimental design process, making quantification of the type done here difficult [14]. The use of an LED as the excitation source overcomes this limitation and has allowed investigations with low powers of

incoherent light. However, it is also possible that in standard epi-fluorescence systems using an arc lamp as the excitation source, the average power at the specimen can be much greater than that used in this study. With a FITC cube to provide a similar excitation wavelength range in the Nikon microscope and arc lamp system initially investigated, the average power at the sample plane was measured to be 2.04 mW with no attenuation of the excitation source, and 529 μW for ND=4, 230 μW for ND=8 and 73.3 μW for ND=12. All of these powers exceed the lowest applied power in this study of 30 μW, further validating the choice of 30 μW for low power illumination. The observation of an increased number of Ca^{2+} transients occurring at higher average excitation power therefore suggests that regardless of the light source used, whether LED or arc lamp, in practical live cell physiological imaging the applied power should be kept as low as possible and the light source may require attenuation beyond the standard options provided on commercial instruments.

The underlying mechanism(s) mediating photo-induced Ca^{2+} signalling remain unclear [15]. However, the Ca^{2+} transients observed in this study are unlikely to be attributed to warming as a consequence of water absorption, as the temperature rise would be insignificant at the powers used in this study [166]. Neither can the presence of TEA alone explain these results. While any influence of TEA present in the extracellular solution bathing the cells on either the generation of Ca^{2+} transients or the sensitivity of the cells to light cannot be fully excluded, photo-induced Ca^{2+} signalling is observed in single cells and intact tissue in the absence of TEA or a photosensitising agent [8-10]. Nevertheless, caution should be advised when TEA is included in the bath solution.

Absorption of the visible light by a constituent of the cell, as demonstrated in motor end plates [17], the applied fluorochromes or coloured pigment [18] is more likely. Yet, light-induced effects are unlikely to be specific to the use of Fluo-3AM in this study because photo effects are also observed in cells stained with various fluorochromes, including Fluo-4AM [8-10]. Indeed, light-induced release of reactive oxygen species (ROS), associated with the interaction of light and the fluorochrome,

has been shown to evoke Ca^{2+} responses and cell death [10]. Although such chemically reactive molecules occur naturally in living cells, and have key roles in cell signalling and homeostasis [167], significant rises in ROS can be detrimental to normal cell function [20]. However, few studies of light-induced ROS with incoherent sources exist. The work of Dixit and Cyr [169] have used both arc lamps and laser systems for studying light-induced ROS, however the light intensities are expressed as percentages of the original source rather than in convenient S.I. units, and so relating their findings to the results outlined in this chapter is not possible, particularly given the fluctuations in arc lamp intensity described previously.

4.6 Conclusion

The present study demonstrates for the first time that low powers of incoherent light may evoke intracellular Ca^{2+} transients, with an increased probability of responses occurring at higher excitation powers. Thus, caution must be exercised in using epi-fluorescence for studies of live cell physiology, even at the mW and sub-mW optical powers commonly used. Even with an incoherent source not brought to a diffraction-limited focus at the specimen it would appear that light is more invasive than is generally thought.

Chapter 5: - Measurement of the focal length of miniature mirrors using reflection microscopy.

5.1 Introduction

The development of micron sized optical components is an area of interest for a wide range of applications, in particular in optical physics research [170–174]. These devices are generally characterised using non–optical microscopy techniques such as SEM and AFM, providing high resolution measurements of the device structure. However, these surface mapping techniques do not provide a direct characterisation of the optical performance of the device [170]. Accurate measurement of the focusing capabilities of an optical element is essential prior to conducting experiments with that element.

In recent years most attention has been paid to micro lens arrays and their possible applications [175]. However, the development of micron-scale lens elements are limited by refractive properties that limits the characteristics achievable, largely because of chromatic aberration [176]. As a result the lenses available on this scale are of relatively low *NA* [177]. In addition the relatively long focal length scales limits the applications possible [176]. Therefore alternative optical components such as the micron scale mirrors investigated using the technique described in this chapter are an attractive option for many applications, in particular for the case of quantum optical trapping arrays.

Current methods to characterise optical components use bulk optics, where the beam is observed in the far field, or near field and measurements made using CCD camera detectors and beam profilers [178]. However, these instruments have limited accuracy when investigating micron-scale optical elements. In recent years the application of optical microscopy to optical device characterisation has been employed more frequently [170], [175]. In particular, reflection and transmission confocal microscopy has been applied, due to the superior optical sectioning

capabilities of confocal microscopy as outlined in Chapter 1, providing relative measurements of the light intensity along the direction of propagation as well as surface mapping with the resolution of the optical microscope. Other techniques such as interferometers and digital holographic microscopy have also provided a means to measure the optical properties of micro devices [179].

The confocal reflection LSM techniques described to date have used the integrated confocal laser sources to visualise the optical element of interest [170], [175]. As described throughout the previous chapters, confocal microscopy requires a diffraction limited focal spot for scanning. However, this does not provide sufficient illumination conditions to achieve the full *NA* aperture of the optical element. Whereby, the surface is illuminated by point scanning in a raster pattern compared to collimated illumination to fill the full element as per the requirements to achieve the maximum *NA* of the element. This could result in an incomplete measurement of the element scale and performance. In addition transferring the confocal data, under collimated illumination conditions, to an absolute measurement of the intensity profile about the focal plane a number of assumptions are made in particular in the regime where diffraction effects are important.

This chapter presents a modified reflection confocal microscope technique to measure the full capabilities of micron scale mirrors. Measurements of the optical performance of micron-scale parabolic and Fresnel mirrors are presented. It is hoped that the combination of accurate measurement techniques, post fabrication, will inform the design of these micro mirror arrays, towards a possible platform for experimentally observing resolved interactions between individually trapped atoms for the first time.

5.2 Theory

Mirrors operate on the principle of reflection, whereby when light illuminates the surface at normal incidence part of the energy is reflected back in the direction of the source of the rays. The amount of light reflected back will depend upon the properties of the material. There are a large number of options for coatings to provide

effective reflection at varying wavelengths, ranging from metal surfaces to dielectric coatings [180]. In addition there are a number of different categories of reflectors ranging from plane mirrors and spherical mirrors to diffractive elements. In this section the theory of parabolic mirrors and Fresnel mirrors will be presented using paraxial approximations.

5.2.1. Parabolic reflectors

Parabolic reflectors are a type of aspherical (curved) mirror. By definition a parabola is a series of points in a plane that are equidistant from a line, the directrix, and the point known as the focus (F) [181]. The directrix is defined as a line perpendicular to the axis of symmetry of the parabola. A schematic of the geometry of a parabolic reflector is shown in Figure 5.1.

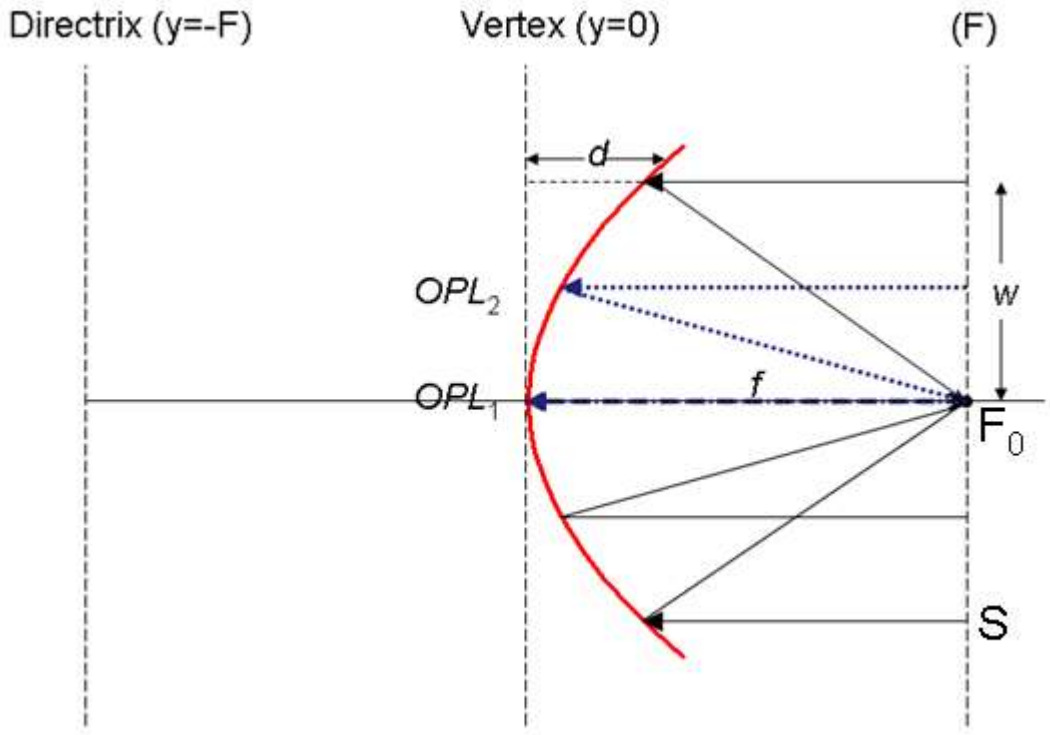

Figure 5.1- Parabolic mirror showing the focus at plane F a distance f from the surface of the parabola. OPL_1 corresponds to the path the ray takes travelling from F to the surface and then back to the focus (2f). OPL_2 is the optical path length for a ray that travels from F at a distance w (S) on the x axis from the centre of the parabola, to the mirror surface and then to the focus (Fo).

The equation for a parabola in 2D is given by the following geometric relationship in Cartesian coordinates,

$$y^2 = 4ax, \quad \textbf{(15)}$$

Where *a* is the distance from the surface to the focus on axis.

According to Fermat's principle, any ray travelling from point S to point F_0, as shown in Figure 5.1, must traverse an optical path length that is stationary with respect to variations of that path [180]. Therefore, all rays travelling from S to F_0 must have an equal optical path length. Considering Fermat's principle with the geometry of a parabolic surface the optical path lengths (OPL_1 *and* OPL_2 shown in Figure 5.1) are given by,

$$OPL_1 = 2f, \text{ and } OPL_2 = (f-d) + \sqrt{(f-d)+w^2} \quad \textbf{(16), (17)}$$

where *f* is the focal length, *d* is the depth of the mirror and *w* is the radius as labelled in Figure 5.1. Given that OPL_1=OPL_2 it is possible to show that the focal length of a parabolic mirror is given by,

$$f = \frac{w^2}{4d} \quad \textbf{(18)}$$

Parabolic mirrors are ideal focusing devices, because under collimated illumination they can focus a parallel beam to a point without any aberration effects. However, this is only true for alignment of the incoming beam parallel with the optical axis, and as a result the performance is strongly dependent on alignment. However, with current fabrication techniques devices can be manufactured with high *NA*, without the limitations imposed upon micro lens arrays [171], [176].

5.2.2. Fresnel zone plate reflectors

The theory of Fresnel zone plates is well covered in the literature [180], but will be briefly reviewed here. The theory of Fresnel diffraction from a circular aperture shows that the successive Fresnel zones will cancel out [182] . Therefore, by removing either all the odd or even zones will result in constructive interference and therefore an increase in irradiance at the point where the waves combine. It is therefore possible to produce a screen which alters the light incident upon it, either in amplitude or phase, by filtering the light only through every odd or even half period zone. The zone plate geometry is shown in Figure 5.2a and b for odd and even zones respectively. The width of the zones reduces the further from the centre of the plate by a factor of the root of the integer [182].

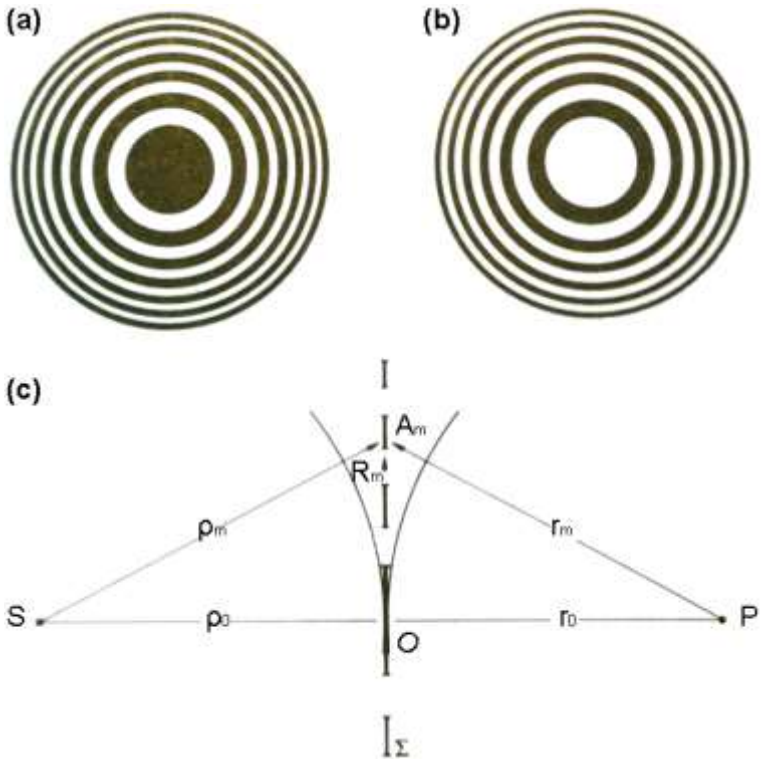

Figure 5.2- Zone plate a) blocking all odd zones, b) blocking all even zones and c) the optical paths from a source to the focus point, reproduced from [182]**.**

To calculate the radii of the zones, R_m marked at the outer edge of the zone A_m, the geometry of the zone plate shown in Figure 2c is considered. It then follows from the definition of a zone plate that a ray that travels S-A_m-P must arrive out of phase by $m\lambda/2$ with a ray that follows the path S-*O*-P.

$$(\rho_m + r_m) - (\rho_0 + r_0) = \frac{m\lambda}{2} \quad \textbf{(19)}$$

Where,

$$\rho_m = \left(R_m^2 + \rho_0^2\right)^{\frac{1}{2}}, \text{ and } r_m = \left(R_m^2 + r_0^2\right)^{\frac{1}{2}}. \quad \textbf{(20)}$$

After binomial expansion of the expressions stated in equation (20), and assuming that R_m is comparatively small. Only the first two terms are retained,

$$\rho_m = \rho_0 + \frac{R_m^2}{2\rho_0}, \text{ and } r_m = r_0 + \frac{R_m^2}{2r_0}. \quad \textbf{(21), (22)}$$

Substituting these relationships into equation (19), we obtain

$$\left(\frac{1}{\rho_0} + \frac{1}{r_0}\right) = \frac{m\lambda}{R_m^2}, \quad \textbf{(23)}$$

In the case where the illumination source is at a distance approaching infinity $(\rho_0 \to \infty)$ from the zone plate, the relationship shown in equation (9) simplifies to

$$R_m^2 = mr_0\lambda, \quad \textbf{(24)}$$

which is in the form of the thin lens equation and it therefore follows that the primary focal length is given by,

$$f_1 = \frac{R_m^2}{m\lambda}. \quad \textbf{(25)}$$

The primary focus, at point P, corresponds to the principal maximum in the irradiance distribution. Under collimated illumination in a standard zone plate, the focus at point P, has a conjugate focus at point S. This is shown schematically in Figure 5.3. In this chapter we are dealing with a Fresnel mirror, which is designed to reflect the light back to point S under collimated illumination. In this case the light will be reflected to point S, with a virtual focus on the opposite side of the surface at point P.

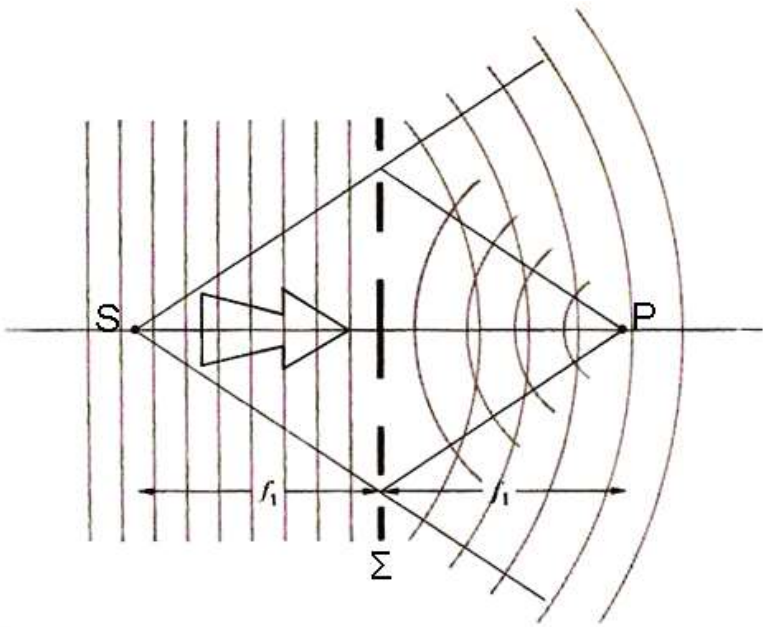

Figure 5.3- Fresnel zone plate showing two conjugate focii reproduced from [182]**.**

Fresnel zone plates are extremely versatile and can be used to produce reliable optical components on very small as well as very large dimensions, with reproducible and reliable manufacturing techniques. In addition, by altering the properties of the material and by using reflective coatings, Fresnel zone plates can act as a lens or a mirror.

5.3 Methodology

5.3.1 Mirror design and fabrication

5.3.1.1 Parabolic mirrors

Parabolic mirrors were designed in collaboration between Prof. Erling Riis and Dr Paul Griffin at the University of Strathclyde with David Cox of ATI at the University of Surrey. The parabolic mirrors were designed using the geometric relationship for a parabola as outlined in section 5.2.1. This allowed for varying diameters and focal lengths to be produced by varying the depth of the parabolic surface. Mirrors were fabricated using focussed ion beam milling (FIBM) on a silicon substrate. The parameters of the ion beam could be sufficiently controlled to produce smooth

surfaces (~1nm surface roughness across the mirror). Representative SEM images of initial parabolic mirrors are shown in Figure 5.4. After initial investigations of these mirrors, it was decided that after FIBM the mirrors would be coated with gold to improve the reflectivity of the surface and therefore improve the efficiency of the mirror.

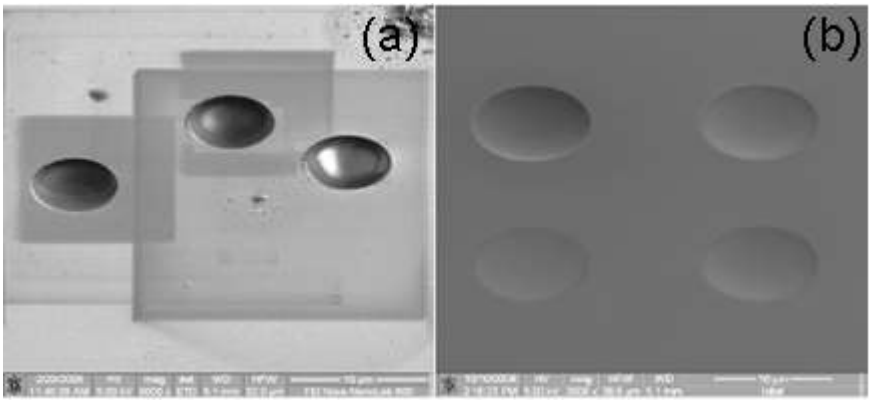

Figure 5.4- SEM images of sample parabolic mirrors produced using the focussed ion beam milling technique. (a) shows 3 mirrors of varying depths, the square regions surrounding show the regions scanned during FIBM. (b) shows the optimised manufacturing procedure of a grid of micro mirrors with varying focal lengths. These mirrors were fabricated and imaged by David Cox (University of Surrey).

An array of parabolic mirrors were investigated in this study. This grid consisted of mirrors with diameters of 5, 10 and 20 μm. There were five 5 μm diameter mirrors designed with focal lengths of 3, 5, 7.5, 10 and 15 μm, four 10 μm diameter mirrors with 7,10,15 and 20 μm focal lengths and finally 20 μm diameter mirrors with 10,15,20 and 30 μm focal lengths.

5.3.1.2 Fresnel mirrors

Fresnel mirrors of varying designs were fabricated using electron beam lithography by Kelvin Nanotechnology (KNT) at the James Watt Nanofabrication Centre. These were based on detailed designs created by Prof. E. Riis and Dr P. Griffin at the University of Strathclyde. To improve the efficiency of the mirrors the unwanted zero order reflection from the plate was minimised by etching each subsequent region to a depth of λ/4, resulting in λ/2 path length difference and thus destructive

interference. The efficiency of the mirror is improved accordingly, as light cannot be reflected straight back and instead will be diffracted into the focus.

The mirrors were fabricated on a 4 inch wafer silicon substrate. The substrate was covered in an electron beam resist prior to loading into the electron lithography beam writer. The resist was then exposed to the electron beam, such that the designed etch patterns were then written over the 4 inch wafer – taking approximately 25 hours of machine time. Post electron beam exposure the sample was then removed and the patterns developed. The sample is then dry etched and coated in metal to make the patterns reflective. In this case the reflective coating of 3nm NiCr and 100nm Au was applied to the silicon substrate. The etch depth was then measured by KNT using an atomic force microscope (AFM) to be 150 nm deep. This is accurate within 2nm of the designed depth of 148 nm, to satisfy the $\lambda/4$ requirements described previously.

Two main designs were fabricated using this technique. The first was a 10 x10 array of 200μm diameter mirrors designed for operation in air at λ=589nm. The diameter of the Fresnel zones and the focal length were designed to achieve a theoretical *NA* of 0.7. The second was based on this previous design, but where the 200μm diameter mirror was divided into four parts and separated by varying spacings to produce four focii. Mirrors with separations of 5, 10, 15, 20, 30 and 40μm were characterised using the technique presented. SEM images of representative mirrors for both designs are shown in Figure 5.5. A region of the 10x10 fresnel array is shown in Figure 5.5a, with a higher magnification image of the etched zones shown in 5b. The split Fresnel mirror is shown Figure 5.5c, with a high magnification image of the mirror shown in Figure 5.5d.

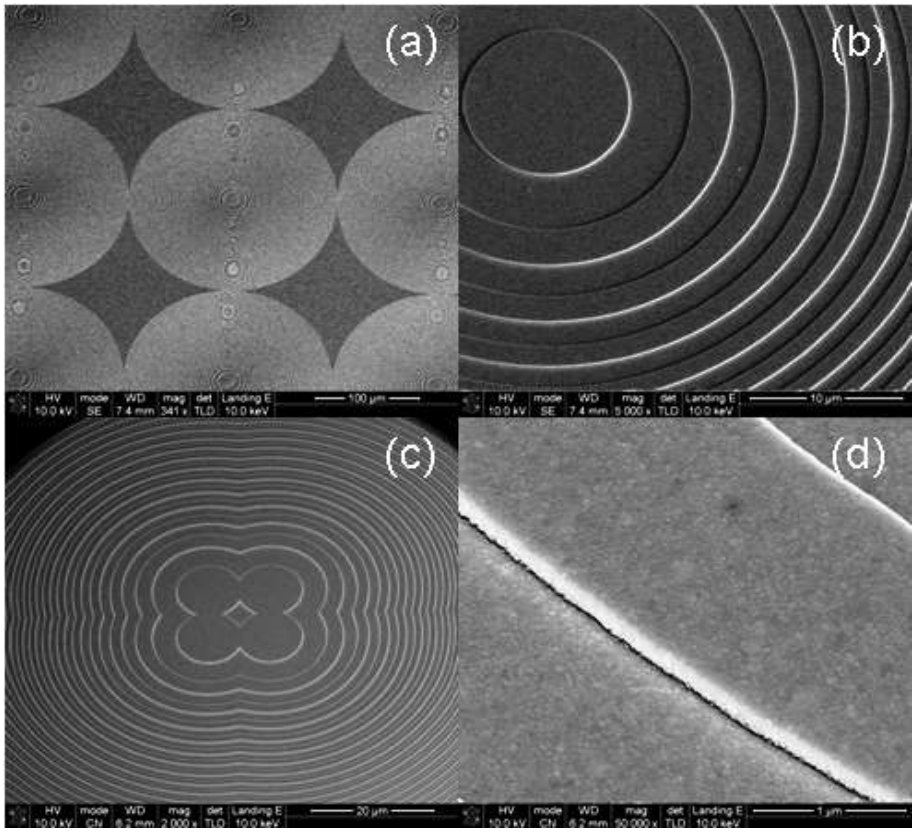

Figure 5.5- SEM images of Fresnel mirrors 10 x10 array at a) low zoom (340x) and b) high zoom (5000x). SEM images of a quadrant separated mirror at c) low zoom (2000x) and d) high zoom (50,000x) showing a single groove on the surface with an AFM measured etch depth of 150nm. SEM images courtesy of KNT.

5.3.2 Modified confocal reflection microscopy

To characterise the mirrors a mount was required to modify the objective lens on the existing LSM platform. Confocal microscopes generate an image by scanning a focused laser beam across the sample, to get the maximum *NA* of the micron scale mirror the illumination conditions required are different from confocal imaging. It is therefore necessary to illuminate the full mirror with a collimated beam. This is made possible, with the mount described in Figure 5.6.

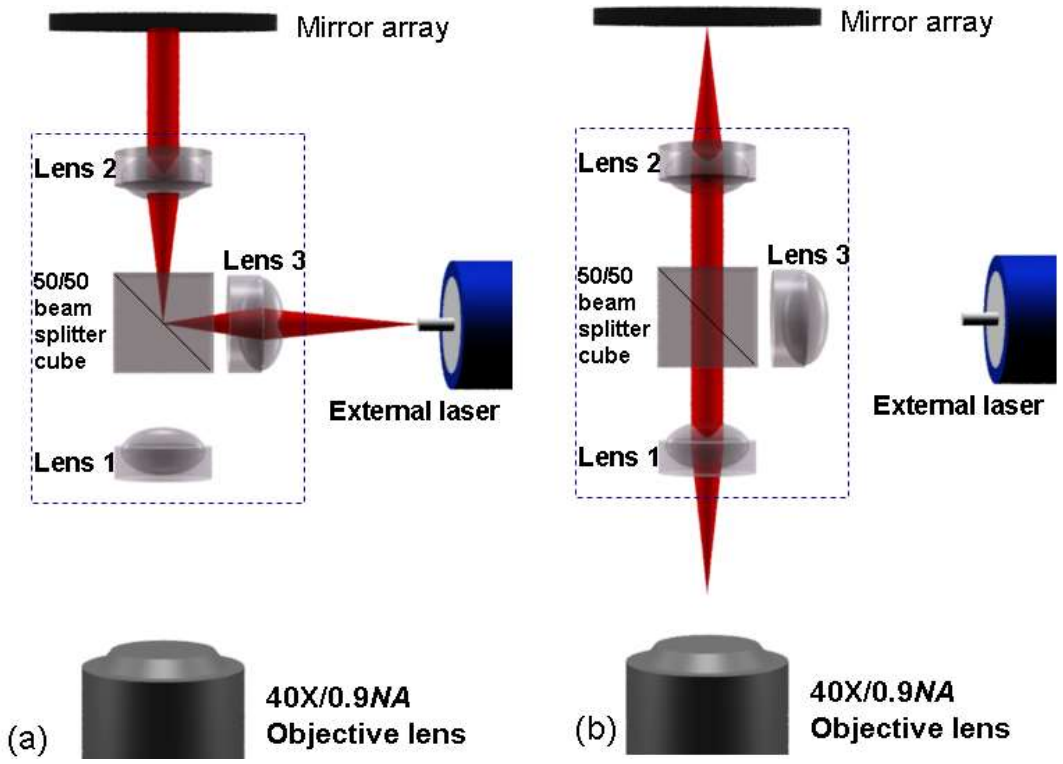

Figure 5.6- a) Objective lens mount under collimated illumination conditions with external laser beam and b) Reflection 'confocal' beam path through the objective mount. Lens 1 and 2 are moulded aspheric lenses f=1.2mm, N.A=0.4.

The mount was built by the mechanical workshop in the Department of Physics and was designed by Dr P Griffin and Prof Erling Riis. This mount consisted of two identical aspheric lenses (Lens 1 and Lens 2 in the Figure 5.6), with a focal length f=1.2mm and *NA* 0.4. A 50/50 beam splitting cube was placed between the two lenses to reflect the incoming light from the external laser as well as to allow for reflection detection. This mount acts as a 1:1 imaging relay system. The external

laser source (two sources were used in this study) was then coupled by a side mounted lens. The parabolic mirrors design is not wavelength dependent and a λ=658nm laser diode (HL6503MG, Hitachi) was used to provide collimated illumination. The Fresnel mirrors are strongly wavelength dependent as shown in equation 25, a yellow laser diode operating at λ=589nm (Spartan series, Dragon lasers) was used for collimated illumination. Both lasers provided 50mW output power at their respective wavelength.

For image detection the confocal microscope system, Olympus FV1000 scanhead and IX81 inverted microscope was set up to record the reflected beam using the configuration outlined in Figure 5.7. This allowed for confocal detection of the reflected light from the external, collimated beam, by using the motorized z control of the objective lens in combination with the confocal detection on the de-scanned internal PMT with the confocal pinhole. This detection set-up was used to provide optical sectioning as for conventional confocal microscopy to produce a 3D data set (z-stack). However, in this case the laser source was not confocal as we used collimated illumination and not a focused point. In addition the beam is not scanning for the collimated illumination case. However, to accurately determine the surface of the mirror, confocal illumination and detection was employed. With the only difference that the scanned beam passes through the custom made optical point prior to imaging the sample. For confocal imaging the set-up shown in Figure 5.8 was used to probe the surface of the micro-mirror array. The internal confocal lasers, (Melles Griot) were used for imaging and the external (collimated illumination) beam was blocked. The confocal lasers were software controlled and used to generate a z stack over the same settings as the collimated z stack. The wavelength was selected to be as close to the two external laser sources described previously. This was to reduce the effects of chromatic aberration of the optical elements as well as in the case of the Fresnel lens to negate any wavelength dependent variations in performance of the micro-mirror.

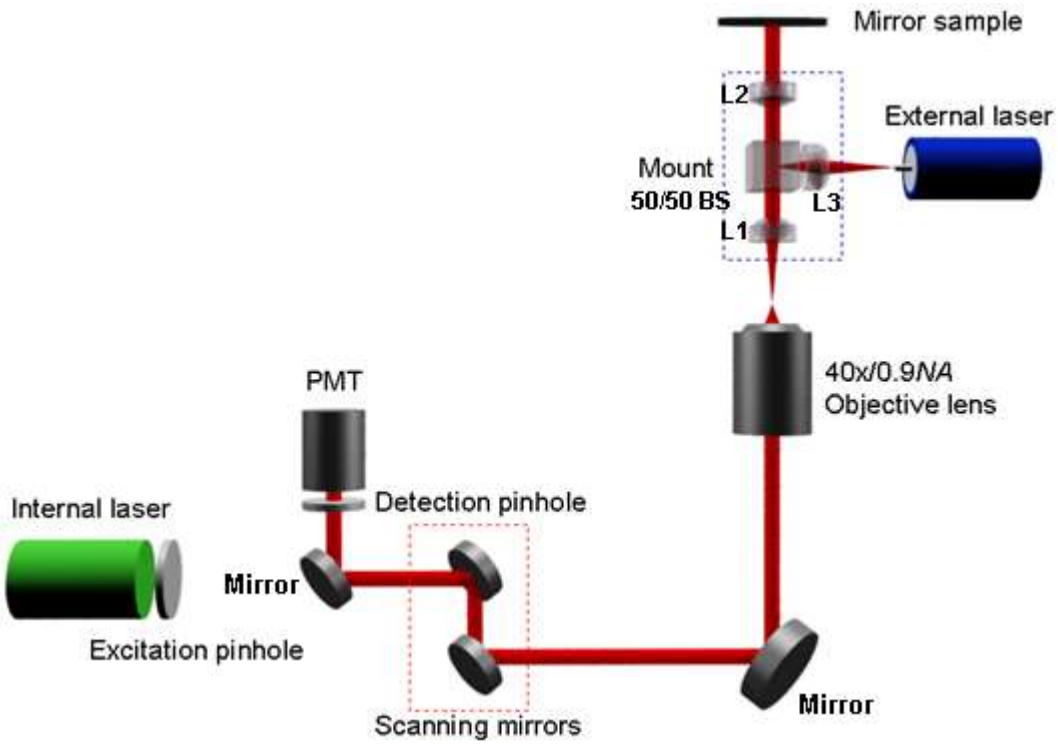

Figure 5.7- Configuration of the microscope for confocal reflection imaging with collimated illumination as shown in Figure 5.6. The external laser source is set up to uniformly illuminate the sample. Reflected light from the mirror array is collected by the objective lens and de-scanned by the scanning mirrors to acquire a reflection image on the PMT. The confocal pinhole was used to optically section the reflected light to correspond to the plane of focus. The objective lens z-position was then varied using the software controlled motorised stage to acquire a stack of reflection images.

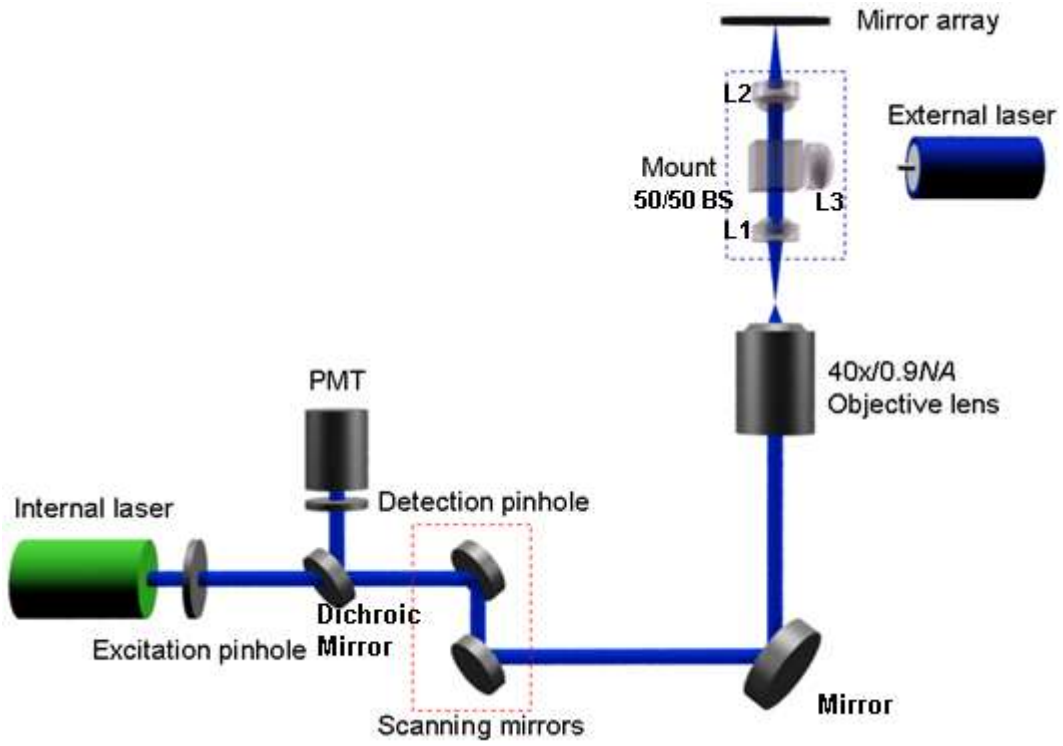

Figure 5.8- Configuration of the microscope for confocal reflection imaging with confocal illumination. The internal laser source was set to scan the surface of the sample. Reflected light from the mirror array is collected by the objective lens and de-scanned by the scanning mirrors to acquire a reflection image on the PMT. The confocal pinhole was used to optically section the reflected light to correspond to the plane of focus. The objective lens z-position was then varied using the software controlled motorised stage to acquire a stack of reflection images.

During Z-stack acquisition, using both collimated and confocal illumination, the PMT gain was selected to obtain images below saturation close to the focus which is of higher intensity as well as at regions far from the focus at lower intensity. As a result three sets of data were taken for each mirror across the same image volume.

5.4 Results

5.4.1 Parabolic mirrors

Confocal images of the reflected beam from micron scale parabolic mirrors were used to measure the focal plane of each mirror as well as the effective *NA.* To assess the axial propagation of the beam on reflection a series of XY images were taken (slices) at known axial intervals to produce a 3D data set of the beam characteristics (Z stack). Three z stacks of each parabolic mirror was obtained two different levels of PMT gain in order to observe both the near field (around the focal plane) as well as further from the plane of focus, where detector sensitivity and saturation issues did not allow for all data to be taken at the same PMT setting. XZ snapshots of the stack series taken for the 20μm, f=10μm mirror are shown in Figure 5.9. The three stacks taken, confocal, collimate high gain and collimated low gain were obtained for each mirror investigated.

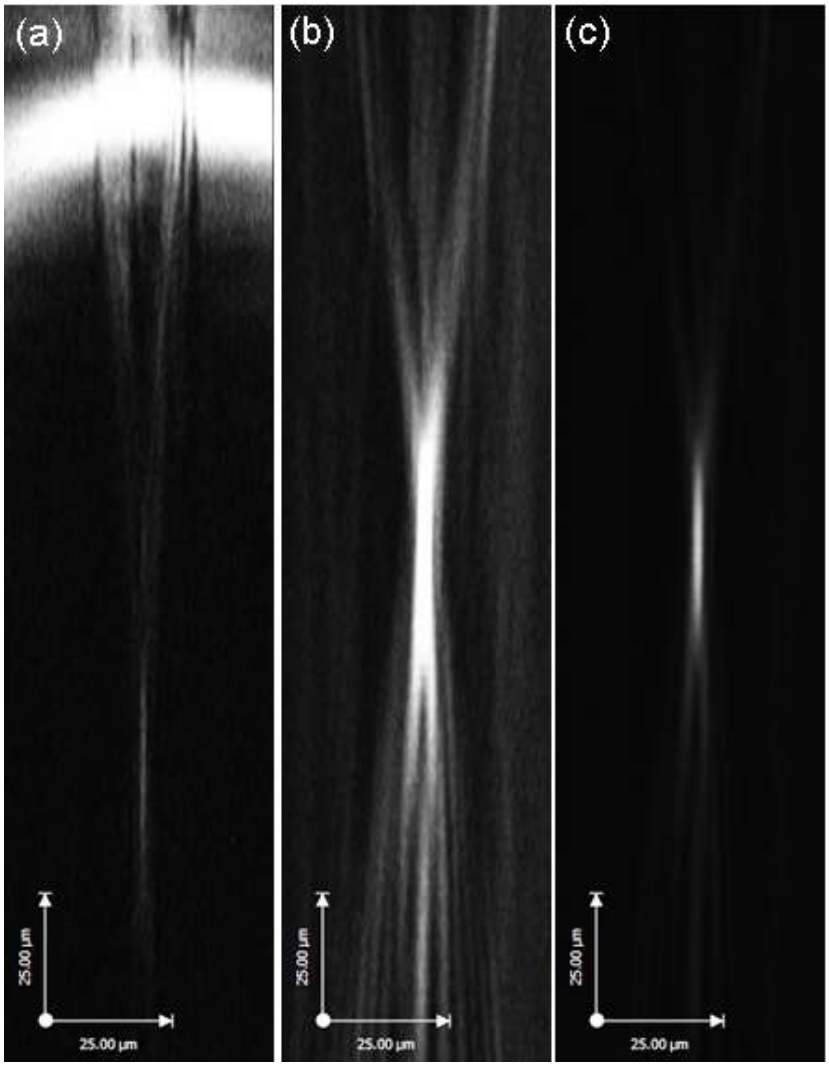

Figure 5.9- Z stacks for the 20 µm parabolic mirror designed to provide a focal length f=10µm, (a) confocal stack, (b) collimated high gain and (c) collimated low gain.

The XZ snapshot in Figure 5.9a shows the mirror using confocal illumination which was used to determine the surface of the mirror. It is evident that the surface appears to be thicker than the expected dimensions and therefore introduces an error into determining the surface accurately of the order of ±2µm. The surface was taken as the centre of the bright band. All XZ profiles of all mirrors were then analysed using this method. The determined surface was then used as the reference point to measure the focal length of each mirror.

XZ snapshots corresponding to the low gain collimated illumination are shown in Figure 5.10. The focal lengths ranging from f=10µm to f=30 µm are presented. The pre-determined surfaces are marked by the white dashed line.

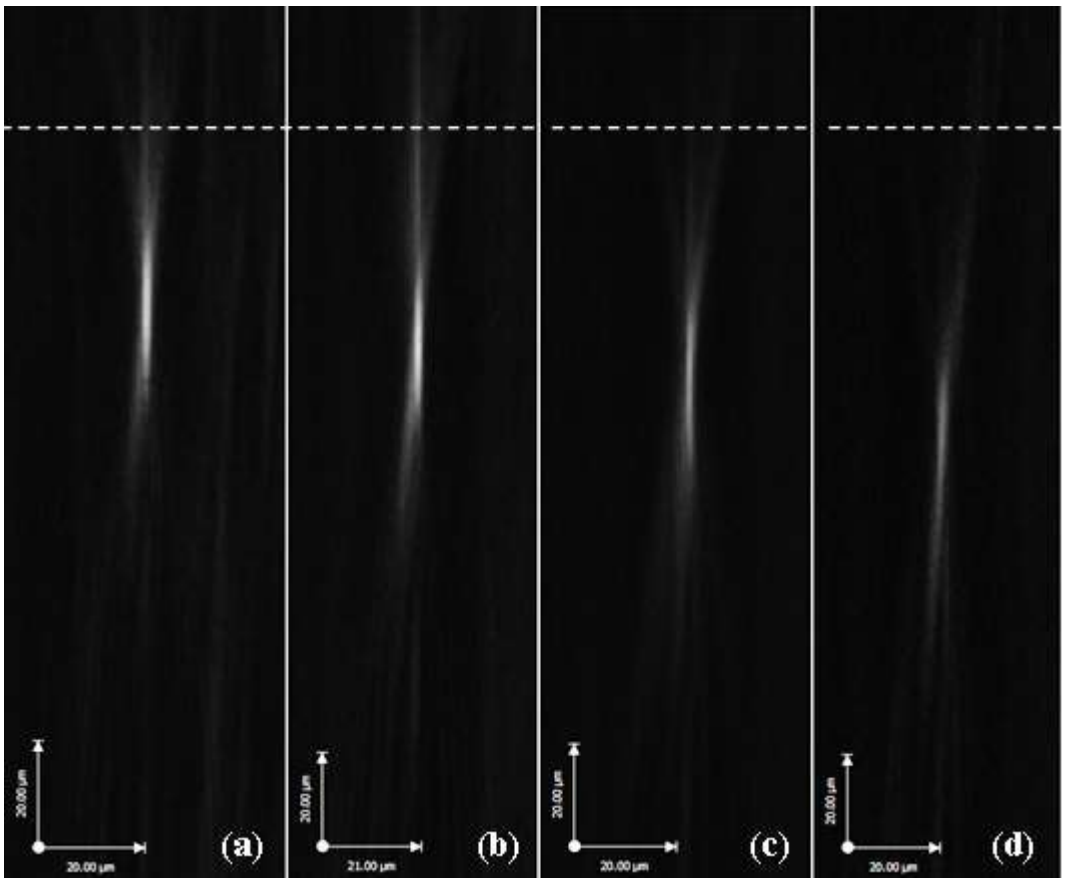

Figure 5.10- Low gain z stacks showing the focal length variation of the 20µm mirrors with designed focal lengths (a) 10µm, (b) 15µm, (c) 20µm and (d) 30µm.

Using this data it was then possible to measure the focal length of each 20 µm diameter parabolic mirror. This data is presented in Figure 5.11.

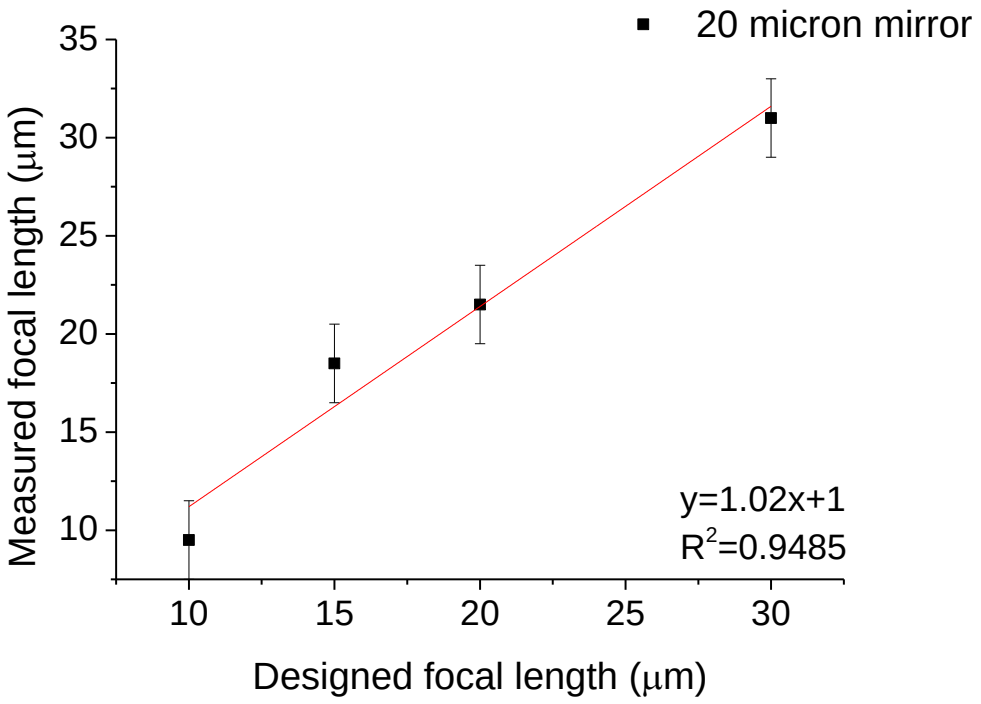

Figure 5.11- Measured focal length against designed focal length for the 20 μm diameter parabolic mirrors, data is shown with a 2micron error in determining the surface postion.

This analysis technique was then repeated for the low gain collimated Z-stacks for the 10 μm diameter mirrors shown in Figure 5.12 and for the 5 μm diameter mirrors shown in Figure 5.13. The measured focal lengths are presented in Figure 5.14.

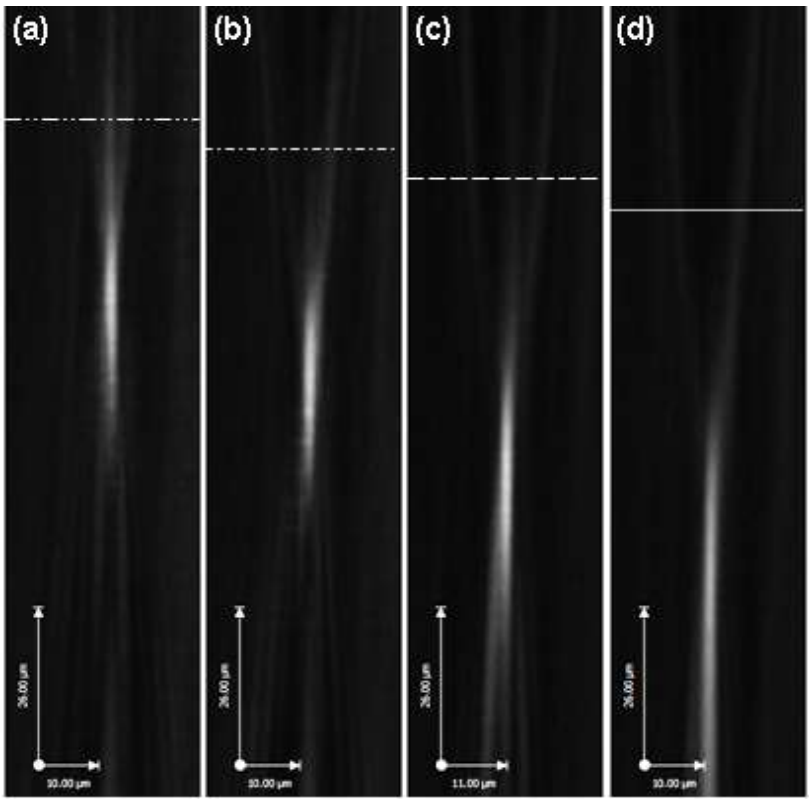

Figure 5.12- Low gain z stacks showing the focal length variation of the 10µm mirrors with designed focal lengths (a) 7µm, (b) 10µm, (c) 15 µm and (d) 20µm.

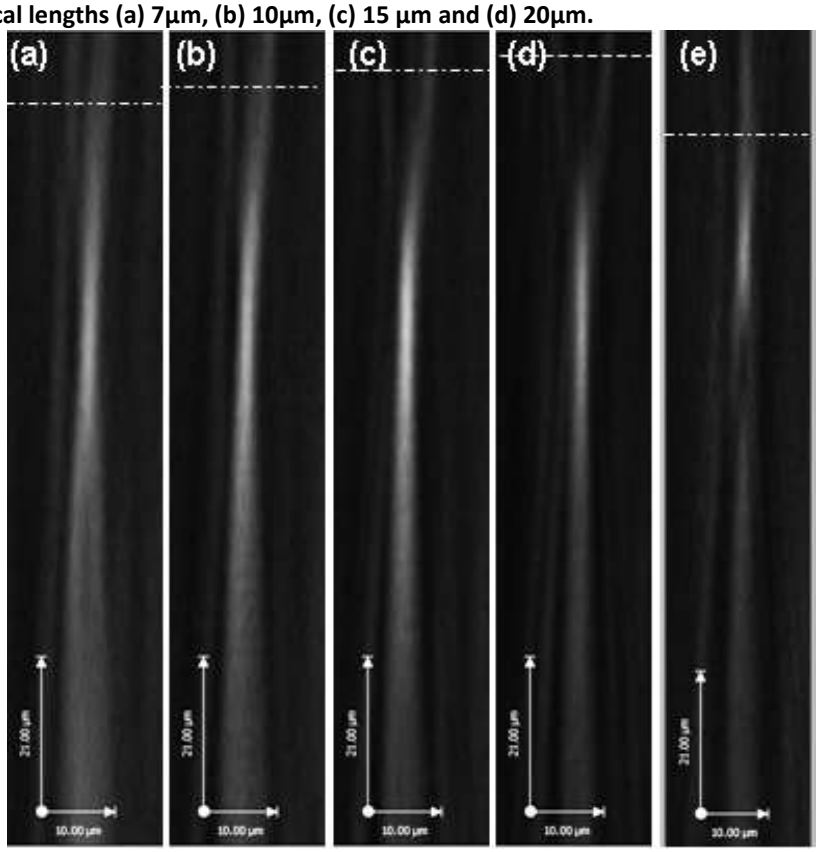

Figure 5.13- Low gain z stacks showing the focal length variation of the 5µm mirrors with designed focal lengths (a) 15µm, (b) 10µm, (c) 7.5 µm and (d) 5 µm and (e) 3 µm.

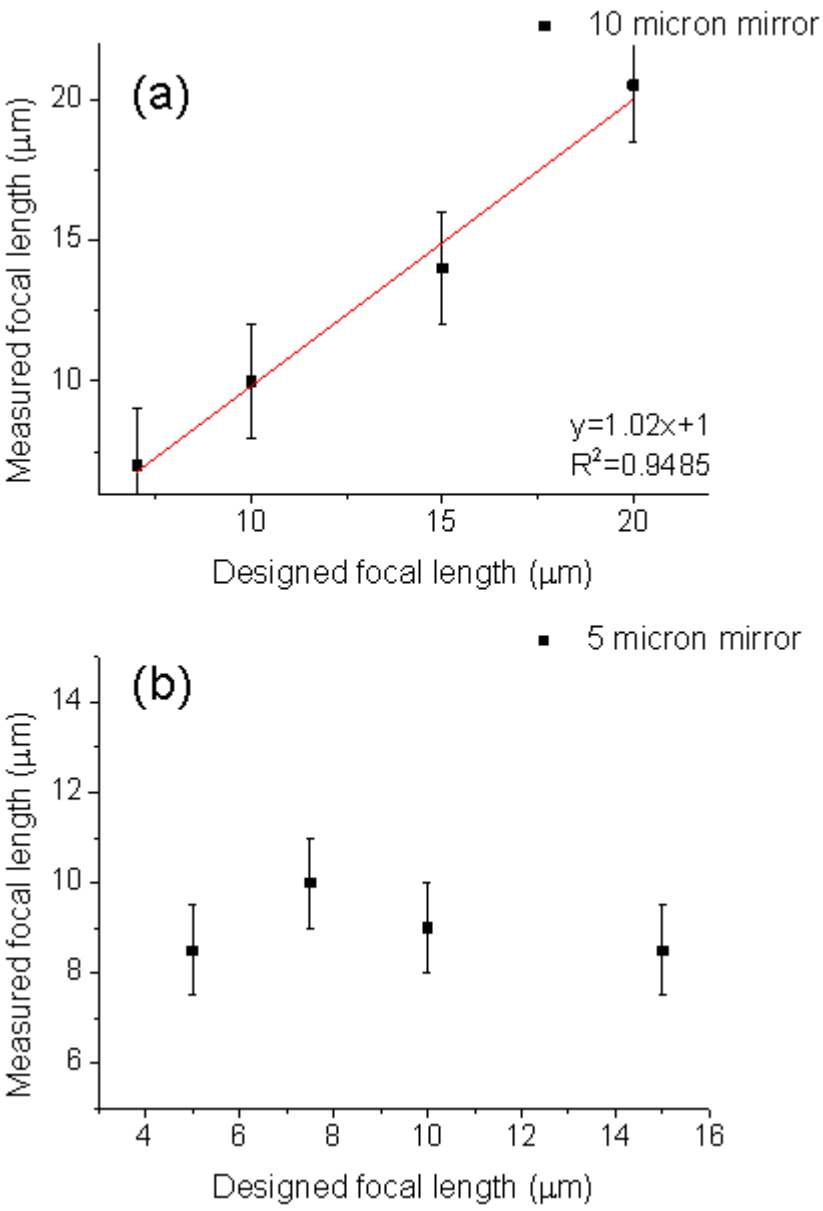

Figure 5.14- Measured focal length against designed focal length for the (a) 10 µm and (b) 5 µm diameter parabolic mirrors.

From the measured focal lengths versus designed focal lengths the 10micron and 20 micron mirrors, fit reasonably well with the designed values. However, the 5 micron case doesn't follow the same trend, suggesting that diffraction effects at this dimension of mirror are more pronounced than the other cases.

It was also possible to measure the beam waist at the focus of the parabolic mirror. This was measured by determining the 1/e^2 width of the intensity profile at the

focus by fitting the experimental data with a Gaussian profile. The focal plane was determined by the intensity maximum on the z axis. The measured beam waists from the collimated z-stack data for each mirror are plotted in Figure 5.15

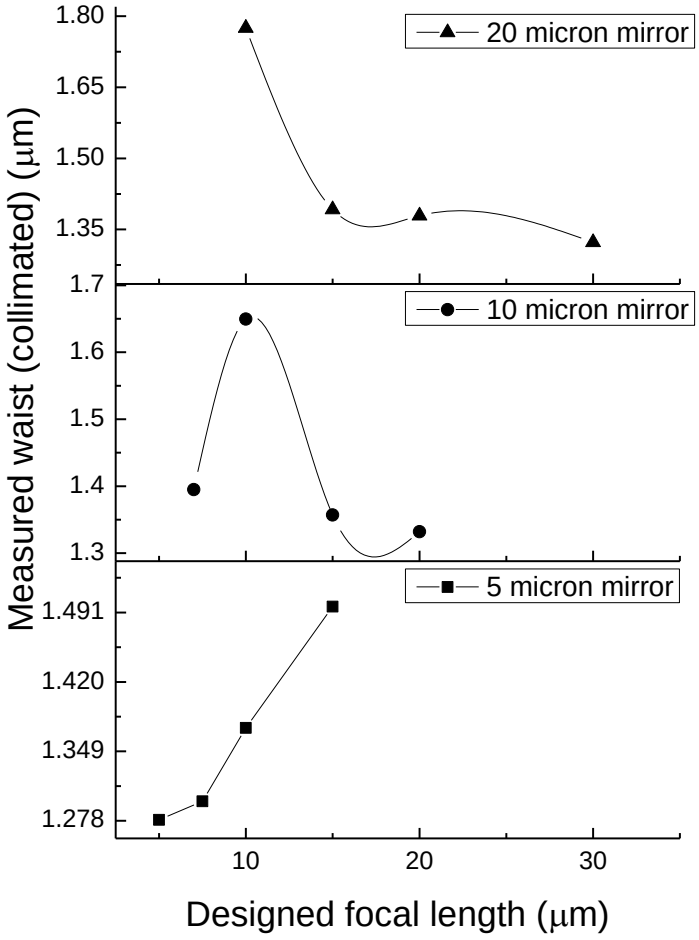

Figure 5.15- Measured beam radii from collimated illumination z stack data for the 5, 10 and 20μm diameter mirrors.

The confocal reflection z-stacks were also used to obtain the measured beam radii by applying a Gaussian fit. The extracted beam radii are plotted in Figure 5.16.

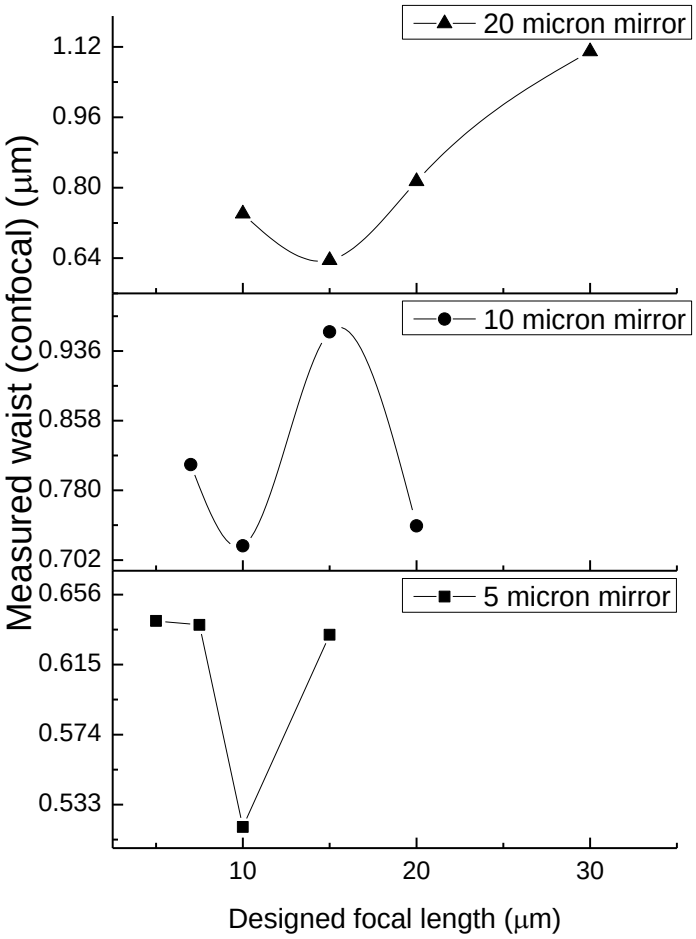

Figure 5.16- Measured beam radii from confocal illumination z stack data for the 5, 10 and 20μm diameter mirrors.

The comparison between the measured beam width for collimated and confocal illumination is presented in Figure 5.17. It can be seen that the measured beam waist by confocal illumination is approximately half of the measurement made using collimated illumination. This highlights that there must be a limitation in the collimated illumination mount which does not allow for the beam waist to be measured accurately. However, the confocal illumination conditions mean that this also is not an accurate measurement as the illumination source is scanned point by point over the mirror which does not fulfil the illumination conditions required to assess the true performance of the parabolic mirror.

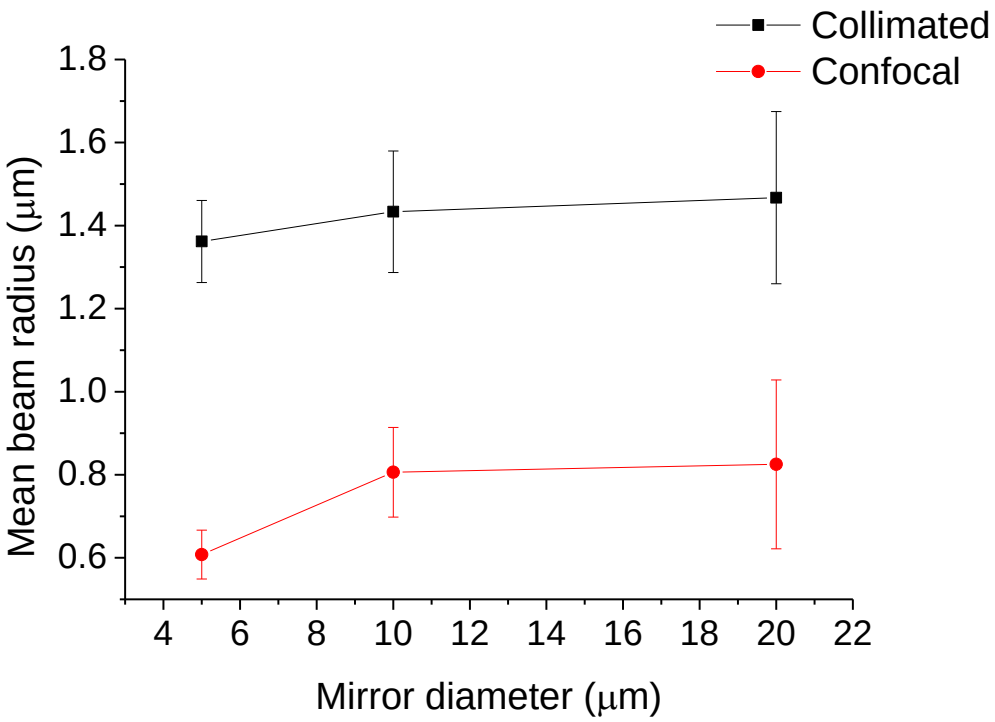

Figure 5.17- Mean beam radii for each diameter of mirror for confocal and collimated illumination. Values are quoted with the calculated standard deviation in the mean.

The experimental data acquired was also compared with theoretical simulation by Dr P Griffin, using a Fourier optics based simulation. A comparison of the simulated beam characteristics with the experimental results for the 20 μm diameter mirror with a focal length of f= 30 μm is shown in Figure 5.18. The measured data corresponds to the XZ snapshot shown in Figure 5.10(d), where the data has been radially averaged to compensate for the slight misalignment of the beam. The zero point on the z-axis corresponds to the surface of the mirror.

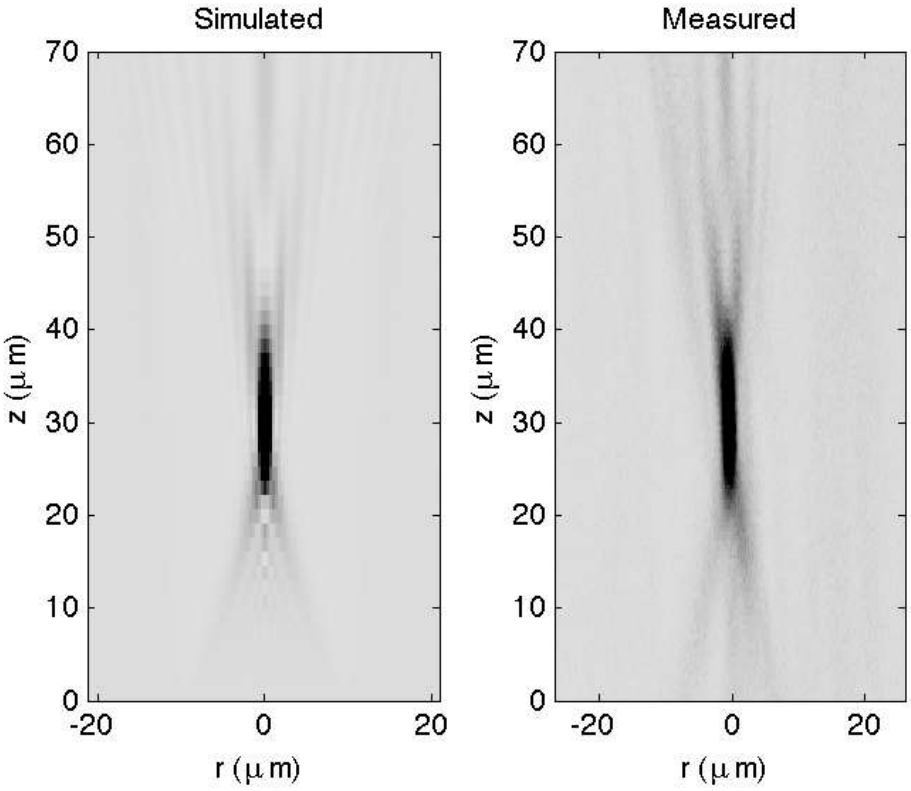

Figure 5.18-a) Simulated and b) experimentally measured (radially averaged) data for the collimated illumination of the 20µm mirror with a focal length f=30µm. Simulation comparison was carried out by Dr P. Griffin.

5.4.2 Fresnel mirrors

XZ snapshots of the 200 μm diameter Fresnel mirror are shown in Figure 5.19. The surface of the mirror was determined with reflection confocal microscopy as with the parabolic mirrors (Figure 5.19(a)). It can be seen with comparison to the high and low gain collimated illumination that the surface is located in the middle between two foci. This corresponds to the real focus in front of the surface of the mirror (LHS) and the focus behind the surface comes from the partially transmitted rays. This was previously described in Figure 5.3.

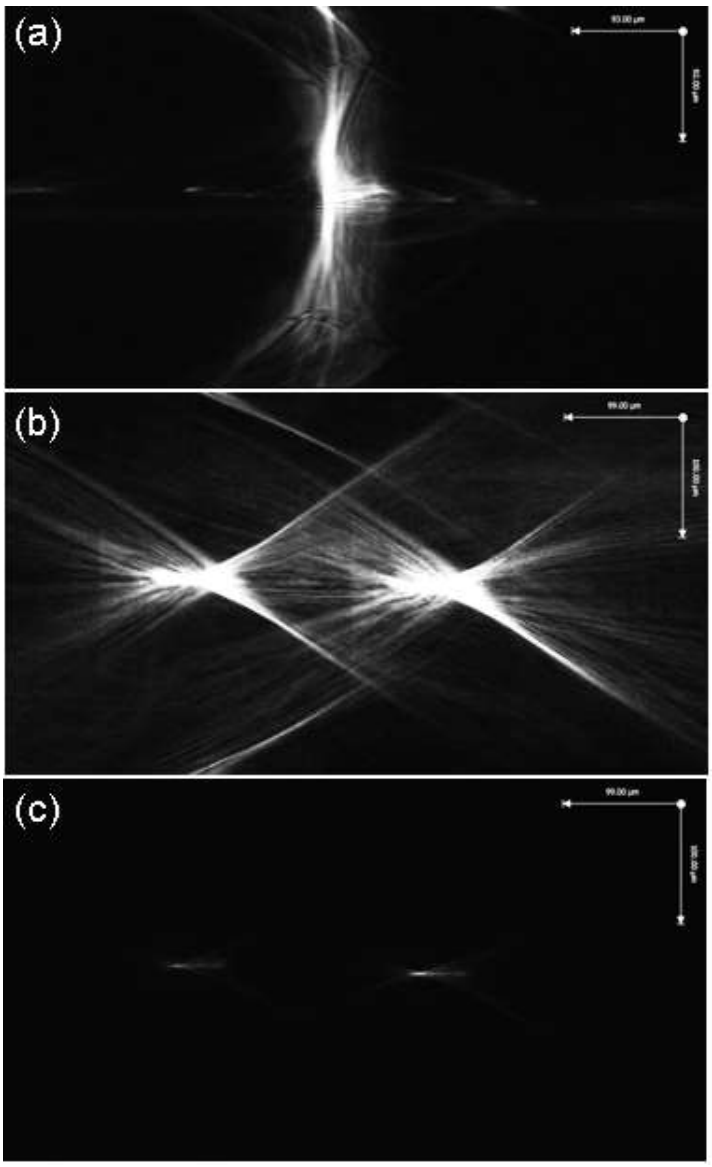

Figure 5.19- Fresnel 200µm mirror a) confocal, b) high gain collimated and c) low gain collimated XZ snapshot. Scale axis corresponds to 100µm.

The collimated illumination z-stack at low gain, shown in Figure 5.19(c), was then used to determine the focal length, beam diameter and *NA* of the mirror. The focal length was measured as f=138 µm. However, the focal length expected for the mirrors was f=100 µm which would have corresponded to a *NA* of 0.7. The beam diameter was measured as 1.4 µm from the collimated z-stack data.

XZ profiles of the quadrant Fresnel mirrors are presented in Figure 5.20 and Figure 5.21 for a separation of 5 µm and 40 µm respectively.

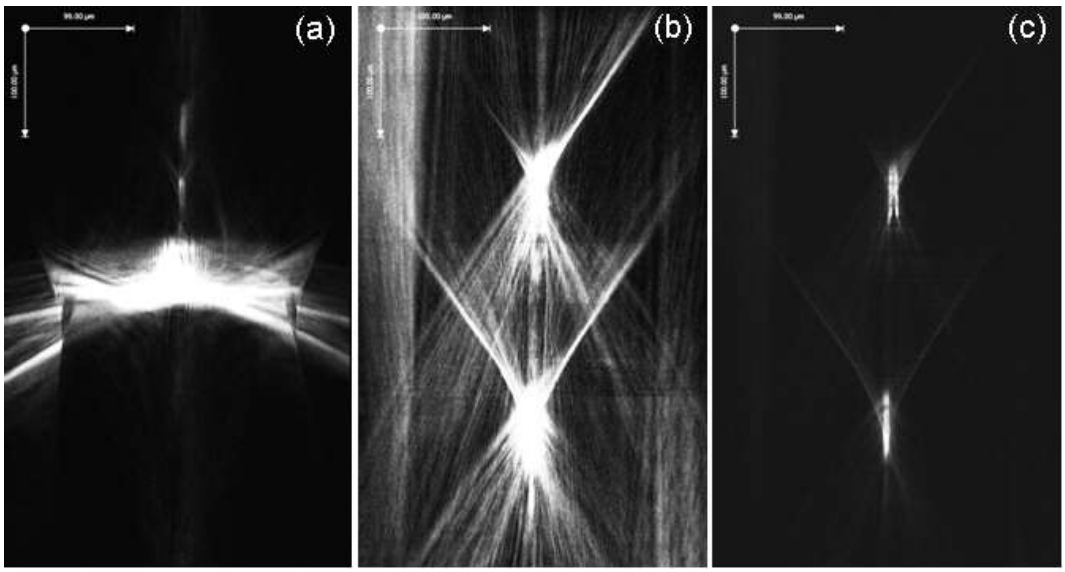

Figure 5.20- XZ profiles of quadrant Fresnel mirrors separated by 5µm, a) confocal, b) collimated high gain and c) collimated medium gain. Scale axis corresponds to 100µm.

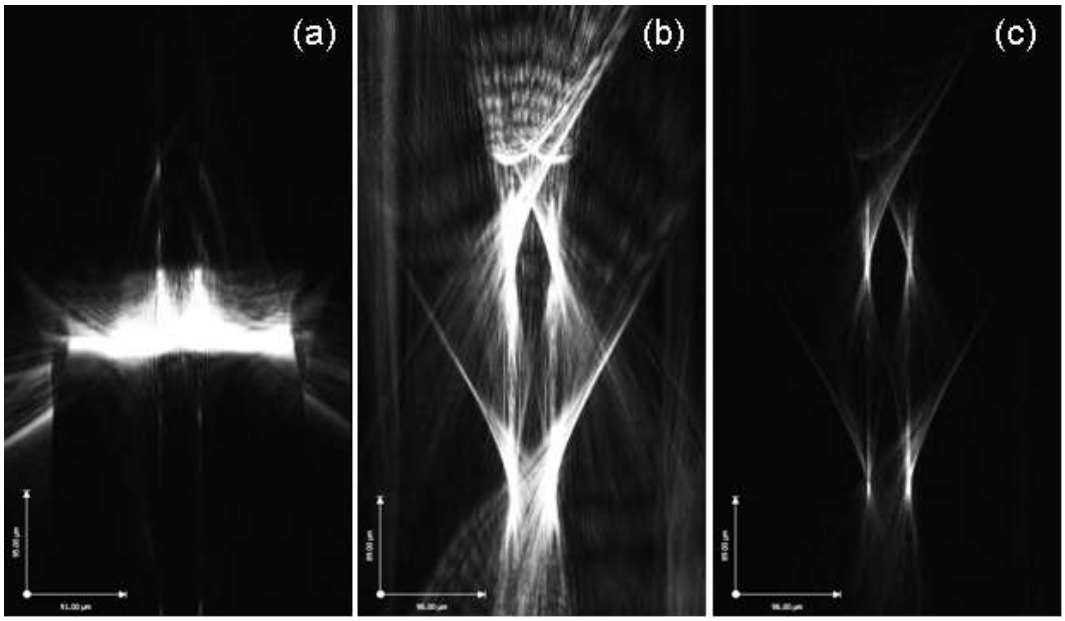

Figure 5.21- XZ profiles of quadrant Fresnel mirrors separated by 40µm, (a) confocal, (b) collimated high gain and (c) collimated low gain. Scale axis corresponds to 100µm.

The individual foci at the focal plane (defined by maximum intensity in the z axis) are shown in Figure 5.22.

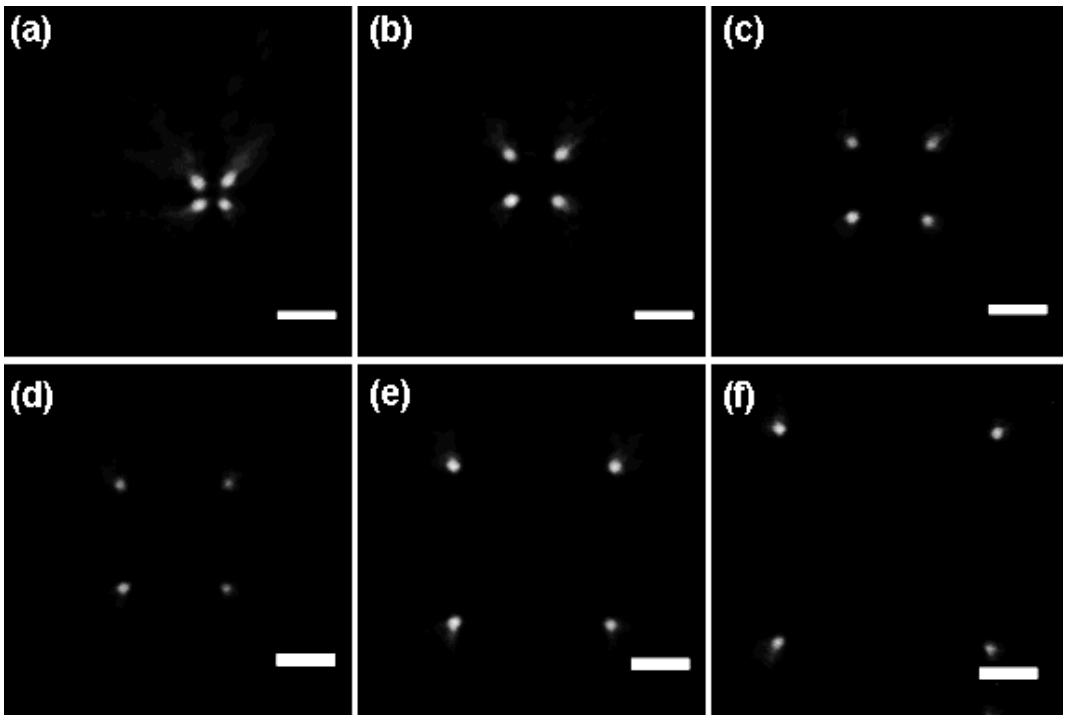

Figure 5.22- Images at the focus (intensity maximum) for the separated Fresnel zones at separation a) d=5µm, b) d=10µm, c) d=15µm, d) d=20µm, e) d=30µm and e) d=40µm. Scale bars correspond to 10µm.

It was then possible to measure the separations between the four foci at the focal plane. The measured separations against the designed separations are plotted in Figure 5.23.

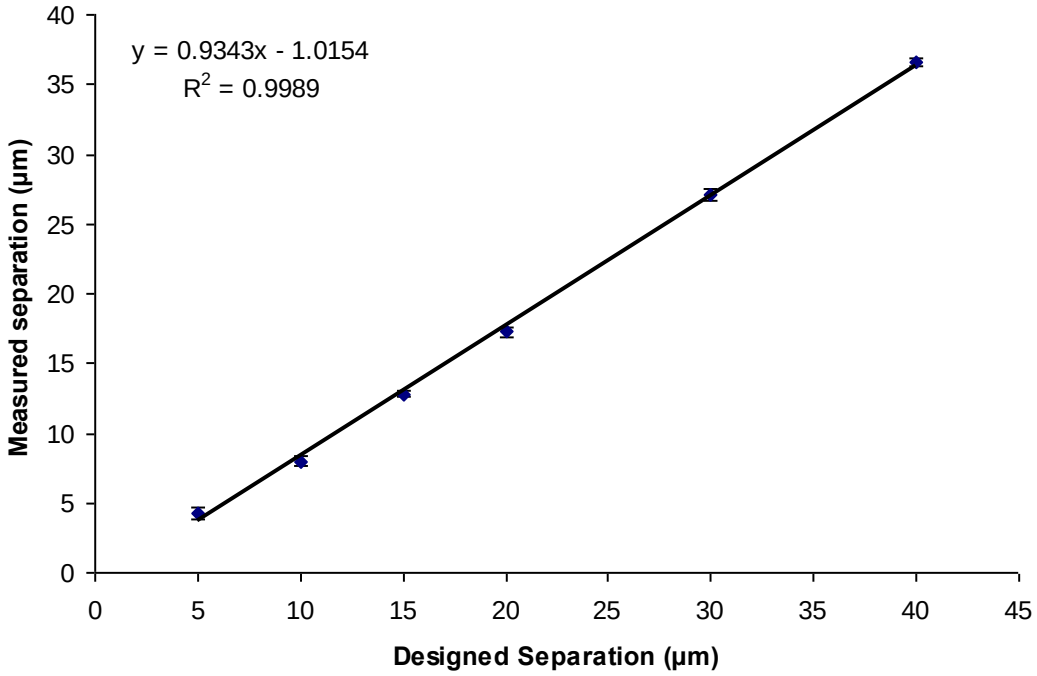

Figure 5.23- Measured separation (y axis) of the four foci against the designed separation for the d=5,10,15,20,30 and 40 µm mirrors (x axis). Data plotted with standard deviation in the mean measured separations.

It can be seen that the measured separation are not in complete agreement with the designed separation. Whereby, the gradient of the straight line fit should be equal to 1. The measured focal length, *NA* and beam diameter were measured to be in agreement with the single focus Fresnel mirror. The mirrors designed to have separations below 20µm were found to converge from an increasing separation to the measured separation at the focal plane, whereas at higher separations the individual foci were found not to converge. This makes it difficult to determine the absolute focal point separation as this was found to vary in the z axis of propagation. This is shown clearly in 3D reconstruction of the low gain z-stacks (collimated illumination) shown in Figure 5.24. Where the low separations, (a) d=5 µm and (b) d=10 µm converge. Whereas, the foci at (c) d=40 µm separation maintain a fixed separation across the axis of propagation.

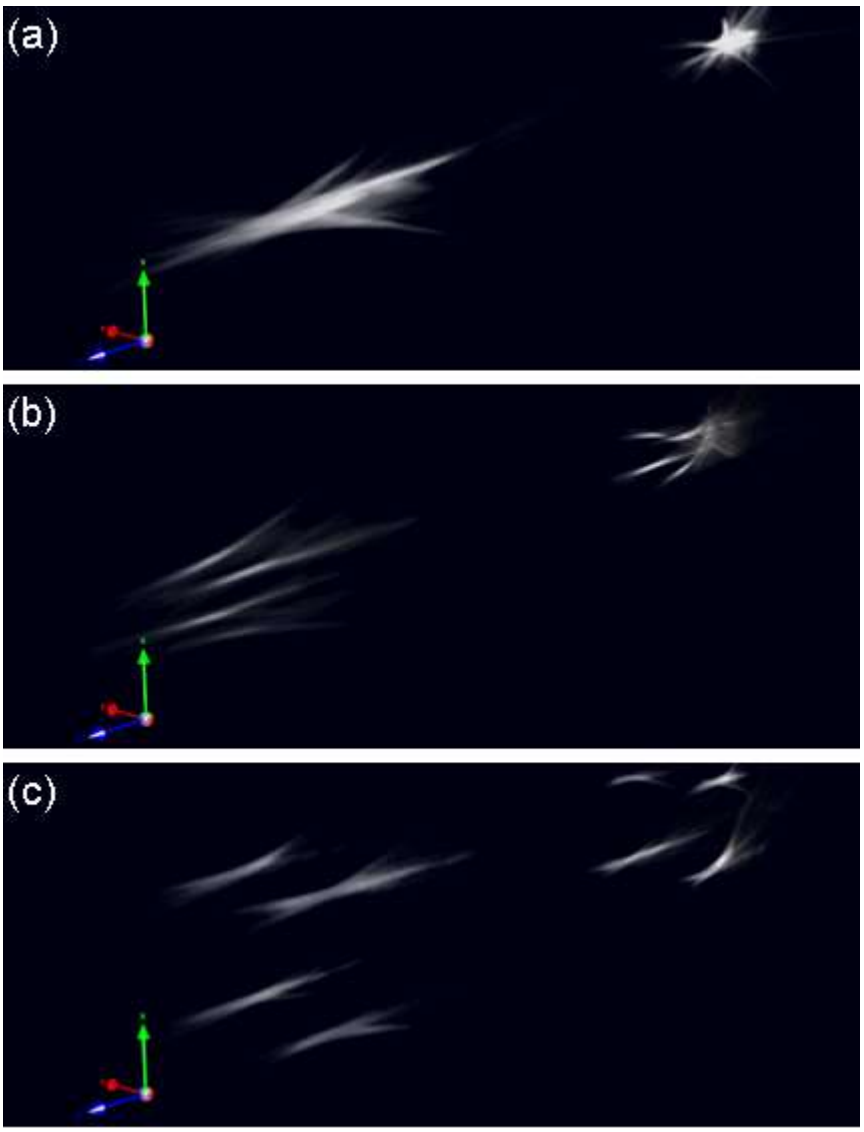

Figure 5.24- 3D reconstruction of z stack data of (a) quadrant separation d=5µm, (b) quadrant separation d=10µm and (c) quadrant separation d=40µm. Image reconstruction using Volocity software.

5.5 Discussion

The technique outlined in this chapter was applied to measure the characteristics of micron scale optical components of varying dimensions and structures. The results provided details on the optical capabilities of these devices that cannot be determined using alternative techniques such as AFM and SEM microscopy, as well as bulk optics techniques applied to measure beam profiles of larger dimension optical components.

The largest parabolic mirrors, 20 micron in diameter, characterised using this technique were found to fit well with the designed parameters. However, at the smaller dimensions, 5 micron and 10 micron, the measured focal lengths were found to differ significantly. In addition to this theoretical simulations of the expected characteristics of the mirrors also have only provided an agreement with the 20 micron diameter mirrors. However, this is so far not expected to be due to errors in the measurement technique, where the modelling of structures less than 20 microns requires full analysis, where in this study the theoretical models use the paraxial approximation as well as negating higher order terms. In particular for the lowest diameter mirrors (5μm), modelling the light propagation requires solving Maxwell equations in full taking into account scattering from wavelength-scale particles. Therefore, the full behaviour of the devices is not theoretically understood at this time. This will be the feature of future simulations within the Optics group at the Department of Physics, University of Strathclyde.

Two types of Fresnel mirrors were studied using the method presented in this chapter. Representative z- stacks for the 10x10 grid array did not give a measured focal length of 100 micron to achieve the expected 0.7 N.A. It is expected that the relatively low N.A of the lenses in the designed objective lens mount does limit the measurements taken. It is unlikely that errors from the manufacturing process would cause the focus capabilities to be this far from theoretically expected as the manufacturing tolerances are on the nm scale.

It is important to measure the N.A. and thus focusing capabilities of the mirrors for the application of optical trapping, which generally requires high collection efficiency providing the forces required for optical trapping. However, there are limitations to the technique described in this chapter. The low N.A lenses used in the mount ultimately limits the resolution of the images obtained, which as described in Chapter 1, will then reduce the accuracy and precision of the quantitative measurements possible. It is likely that this is why all measured beam waists were found to be 1.4 μm.

5.6 Conclusion

Techniques to measure the optical properties of a range of micrometer scale optical components were reported in this chapter. The design of a modified objective lens was described with reference to the requirements of collimated illumination with reflection confocal detection. Detailed imaging was performed in order to obtain non-destructive quantitative measurements and testing of the optical component. The experimentally recorded focusing capabilities of the mirrors were measured and compared with the designed parameters.

Chapter 6: Conclusion

The work presented in this thesis has investigated the implications of calibration and quantitative analysis on the measurements that can be made post image acquisition in all applications of microscopy. This has been made possible by the development of two techniques that can be used to assess the microscope, and then by performing two applications requiring accurate microscopy analysis and modifications to the imaging approach to improve the data acquisition.

6.1 Review

The general background of optical microscopy techniques were outlined in Chapter 1, followed by a review of the properties of the system which requires adequate consideration prior to imaging. Details of some current methods used to test microscope systems were also outlined in this chapter.

The first technique developed in this thesis, reported in Chapter 2, was an improved and quantitative method of determining the stability of the laser scanning mechanism *in situ*. This has direct impact on the work presented in Chapters 3 and 5, which also used laser scanning mechanisms to acquire quantitative data. The technique described uses an external camera to image the raster scan across the image acquisition path at the sample plane. Simple image analysis techniques using freely accessible software were used to assess the scanning performance. This allowed for a point by point assessment of scan shifts over time for a continuously scanning raster pattern for a period of 8 minutes. Accurate measurements of scan drift and mirror wobble on the x and y scanning galvanometer mirrors were observed and measured using this method for a commercial system. This technique proves to be a valuable tool in assessing imaging errors associated with scanning galvanometer mirrors, these effects are rarely investigated in LSM applications, with only specimen stage drift routinely measured. Having an accurate technique to measure these properties of the scan could potentially be useful in super resolution techniques like STED

which use scanning image acquisition. The measurements for this commercial system showed drifts of up to a micron in the relatively short (8 minute) scan time.

The second method described in this work, in Chapter 3, is an improved method of determining the beam radius at the focus of an objective lens in a LSM imaging platform. This two part technique firstly recorded a permanent trace of the laser beam, via laser ablation, on the route taken to acquire an image. The trace was then imaged using an SEM, providing high resolution images of the ablated surface. The image analysis tools used in Chapter 2 were again applied to accurately measure the dimensions of the trace of the laser beam with 25nm resolution. Combining these measurements with ablation theory an accurate beam radius of the incident beam can be determined. This provides a robust method of assessing if the objective lens in use is achieving close to the diffraction limited spot size at the focus, which in turn will impact the resolution of the images acquired. This is an essential prerequisite to performing effective quantitative data from microscopic imaging. Current techniques for assessing the resolution of the microscope system can be subjective and are often difficult due to photo-damage and motion of the sample.

The second part of this thesis investigated the implications of accurate measurements in microscopy to measurements in two specific applications. The first application was discussed in Chapter 4, where the impact on the light dose applied on the behaviour of the sample was investigated. A modified epi-fluorescence microscope was used to accurately control the excitation dose, whilst monitoring the generation of physiological processes in live smooth muscle cells by monitoring Ca^{2+} levels in the cell. The power at the sample plane was titrated to determine whether the illumination was a controlling factor in the Ca^{2+} transients observed. This study showed for the specific case of Ca^{2+} imaging of Fluo-3AM labelled smooth muscle cells that the number of physiological processes observed increased with increasing light dose. The doses used were significantly lower than commercial systems using arc lamp excitation sources. This study showed that the dose of light in epi-fluorescence microscopy has a marked impact on the behaviour of the sample, where

prior to this study the impact of epi illumination light sources were assumed to have no effect on the behaviour of the specimen.

Finally, in Chapter 5, the application of a modified confocal reflection microscopy to the characterisation of micron scale optical elements was described. Characterising the optical focus obtained by this scale of optical component was not possible by current methods used for larger optical elements. Therefore, a microscopic technique was required. The sectioning capabilities of a confocal system are particularly advantageous for this application, such that the axial propagation of the focused beam produced by the element of interest can be imaged on a plane by plane basis. However, the confocal microscope does not provide the required collimated illumination required to fully characterise the optical performance of the element. To overcome this issue a specially designed mount was used which could be placed on top of the objective lens fulfilling the requirements of collimated illumination with confocal detection. This method was applied to measure focal lengths and diameters of focussed ion-beam milled mirrors of micron dimensions.

6.2 Future work

The technique described in Chapter 2 allowed for accurate measurement of the scanning mirror error over time. The image analysis tools applied were not specifically designed for this type of repeat measurement. Only a sample of the full scan was measured and reported in Chapter 2 as a result. It would therefore be advantageous to develop a plug-in capable of handling the input images which could be used to make systematic measurements on scan line spatial variations. This would allow for an assessment of the full scan area, with less time taken to perform the analysis manually. This type of analysis tool would make it easier to monitor and correct for the scanning variations on the images obtained over time course imaging. This would then potentially improve the accuracy of measurements which require points to be accurately tracked over time and would reduce movement artefacts which are only due to scan inconsistencies and not movement of the sample or internal components of a fixed sample over time.

The method presented and tested in Chapter 3 provided an accurate measurement of the optical focus for an air objective lens. However, this technique at present is limited to multi-photon LSM systems, where the laser sources have sufficient pulse energy to perform ablation. It would be interesting to investigate other possible materials which could be suitable for performing this type of measurement in CLSM systems, which use low power CW laser sources. It is possible that engineered films which deform under low power illumination could be used for these measurements. However, the controllability of the process in order to accurately relate the deformation of the sample to the optical focus of the incident laser beam would need to be investigated further. In addition the suitability of the material to SEM imaging would need to be considered. Further to this, only a few objective lenses were evaluated in this study: air, water and oil-compatible specimens would be required to make this method widely accessible.

The investigation into light induced effects in Ca^{2+} imaging experiments reported in Chapter 4 provided initial insight into the effects of light dose in epi-fluorescence microscopy. However, there are a number of other parameters that would be useful to investigate the possible mechanisms of these light induced effects. It is not thought that that the light-induced Ca^{2+} transients are limited to the application of Fluo-3AM, and thus investigating other Ca^{2+} fluorescent probes would be useful. In addition, varying the concentration of the probe would provide further insight into whether the observations are due to light interaction with the fluorophore or with another constituent of the cell. An alternative approach would be to block specific ion channels and to investigate the corresponding numbers of cells exhibiting a response under these conditions. With these conditions satisfied, it may also be interesting to apply incoherent light to intact tissue loaded with Ca^{2+} indicators. If similar Ca^{2+} responses are shown and can be controlled, this opens up potential opportunities for therapeutic devices.

The results obtained for the optical characterisation of the micron scale elements, were limited by the modifications applied to the system. The mount used in this study used a lens relay with *NA* lower than that of the objective lens used for

imaging. It would therefore be necessary to modify and optimise the mount to achieve higher *NA* and thus to improve the measurements made by this technique. Unfortunately commercially available lenses with higher *NA* also suffer from greater chromatic aberrations, which would impact significantly on the measurement technique, but advances in manufacture may make this possible in the future.

References

[1] R. Hooke, *Micrographia, or, Some physiological descriptions of minute bodies made by magnifying glasses, with observations and inquiries thereupon: by Robert Hooke*. London: Royal Society, 1664.

[2] H. Zou, L. M. Lifshitz, R. a Tuft, K. E. Fogarty, and J. J. Singer, "Imaging Ca(2+) entering the cytoplasm through a single opening of a plasma membrane cation channel.," *The Journal of general physiology*, vol. 114, no. 4, pp. 575–88, Oct. 1999.

[3] J. R. Swedlow and M. Platani, "Live cell imaging using wide-field microscopy and deconvolution," *Cell structure and function*, vol. 341, pp. 335–341, 2002.

[4] S. Reichinnek, A. von Kameke, A. M. Hagenston, E. Freitag, F. C. Roth, H. Bading, M. T. Hasan, A. Draguhn, and M. Both, "Reliable optical detection of coherent neuronal activity in fast oscillating networks in vitro.," *NeuroImage*, vol. 60, no. 1, pp. 139–52, Mar. 2012.

[5] R. W. Cole and J. N. Turner, "Light-emitting diodes are better illumination sources for biological microscopy than conventional sources," *Microscopy and Microanalysis*, vol. 14, no. 3, pp. 243–250, Jun. 2008.

[6] V. Murthy, T. F. Sato, D. F. Albeanu, E. Soucy, and M. Meister, "LED Arrays as Cost Effective and Efficient Light Sources for Widefield Microscopy," *PLoS ONE*, vol. 3, no. 5, p. e2146, Jan. 2008.

[7] W. Amos and J. White, "Use of confocal imaging in the study of biological structures," *Applied optics*, vol. 26, no. 16, pp. 3239–43, Aug. 1987.

[8] W. Amos, "How the Confocal Laser Scanning Microscope entered Biological Research," *Biology of the Cell*, vol. 95, no. 6, pp. 335–342, Sep. 2003.

[9] W. Denk, J. Strickler, and W. W. Webb, "Two-photon laser scanning fluorescence microscopy," *Science*, vol. 52, no. 13 Suppl, pp. 1778–9, Oct. 1990.

[10] P. F. Curley, a. I. Ferguson, J. G. White, and W. B. Amos, "Application of a femtosecond self-sustaining mode-locked Ti:sapphire laser to the field of laser scanning confocal microscopy," *Optical and Quantum Electronics*, vol. 24, no. 8, pp. 851–859, Aug. 1992.

[11] S. Inoue, “Foundations of Confocal Scanned Imaging in Light Microscopy,” in *Handbook of Biological Confocal Microscopy*, J.B. Pawley, Ed. New York: Springer, 2006, pp. 1–19.

[12] A. R. Hibbs, G. MacDonald, and K. Garsha, “Practical Confocal Microscopy,” in *Handbook of Biological Confocal Microscopy*, Third edit., J. B. Pawley, Ed. New York: Springer, 2006, pp. 650–671.

[13] G. Cox and C. J. R. Sheppard, “Practical limits of resolution in confocal and non-linear microscopy.,” *Microscopy research and technique*, vol. 63, no. 1, pp. 18–22, Jan. 2004.

[14] R. Juskaitis, “Measuring the Real Point Spread Function of High Numerical Aperture Microscope Objective Lenses,” in *Handbook of Biological Confocal Microscopy*, J.B. Pawley, Ed. New York: Springer, 2006, pp. 239–250.

[15] D. W. Piston, “The impact of technology on light microscopy,” *Nature Cell Biology*, vol. 11, no. S1, pp. S23–S24, 2009.

[16] H. Keller, “Objective lenses for confocal microscopy,” in *Handbook of Biological Confocal Microscopy*, Third edit., J.B. Pawley, Ed. New York: Springer, 2006, pp. 145–161.

[17] S. Inoue, “Foundations of Confocal Scanned Imaging in Light Microscopy,” in *Handbook of biological confocal microscopy*, 2006, pp. 1–19.

[18] A. Kohler, “New method of illumination for photomicrographical Purposes,” *Journal of the Royal Microscopical Society*, vol. 14, pp. 261–262, 1894.

[19] A. Nolte, J. Pawley, and L. Horing, “Non-laser light sources for three-dimensional microscopy,” in *Handbook of Biological Confocal Microscopy*, 2006, pp. 126–144.

[20] G. G. Stokes, “On the Change of Refrangibility of Light,” *Philosophical Transactions of the Royal Society of London*, vol. 142, pp. 463–562, Jan. 1852.

[21] G. Stokes, “On the Change of Refrangibility of Light.--No. II,” *Philosophical Transactions of the Royal Society of*, vol. 143, no. Ii, pp. 385–396, 1853.

[22] T. Ehrig, D. O’Kane, and F. Prendergast, “Green-fluorescent protein mutants with altered fluorescence excitation spectra,” *FEBS letters*, vol. 367, pp. 163–166, 1995.

[23] F. Perrin, “La fluorescence des solution, induction moleculaire polarisatron et duree d’emission photochemie,” *Annalen der Physik (France)*, vol. 12, pp. 169–275, 1929.

[24] A. Jablonski, “Efficiency of Anti-Stokes Fluorescence in Dyes,” *Nature*, vol. 131, pp. 839–840, 1933.

[25] M. Kasha, “From Jablonski to femtoseconds. Evolution of molecular photophysics,” in *Acta Physica Polonica-Series A General*, 1999, vol. 95, pp. 15–36.

[26] A. Diaspro, Ed., *Confocal and two-photon microscopy*. New York: Wiley-Liss, 2002.

[27] B. Herman, *Fluorescence Microscopy*,Oxford, Bios Scientific. 1998.

[28] D. Magde, R. Wong, and P. G. Seybold, “Fluorescence quantum yields and their relation to lifetimes of rhodamine 6G and fluorescein in nine solvents: improved absolute standards for quantum yields.,” *Photochemistry and photobiology*, vol. 75, no. 4, pp. 327–34, Apr. 2002.

[29] R. Y. Tsien, L. Ernst, and A. Waggoner, “Fluorophores for Confocal Microscopy : Photophysics and Photochemistry,” in *Handbook of Biological Confocal Microscopy*, J. B. Pawley, Ed. New York: Springer, 2006, pp. 338–352.

[30] C. Vonesch, F. Aguet, and J. Vonesch, “The colored revolution of bioimaging,” *IEEE Signal Processing*, pp. 20–31, 2006.

[31] H. Schneckenburger, M. Wagner, P. Weber, W. S. L. Strauss, and R. Sailer, “Autofluorescence lifetime imaging of cultivated cells using a UV picosecond laser diode.,” *Journal of fluorescence*, vol. 14, no. 5, pp. 649–54, Sep. 2004.

[32] M. Elleder and J. Borovanský, “Autofluorescence of melanins induced by ultraviolet radiation and near ultraviolet light. A histochemical and biochemical study.,” *The Histochemical journal*, vol. 33, no. 5, pp. 273–81, May 2001.

[33] O. Heimstädt, “Das fluoreszenzmikroskop,” *Z Wiss Mikrosk*, vol. 28, pp. 330–337, 1911.

[34] A. H. Coons, H. J. Creech, and R. N. Jones, “Immunological properties of an antibody containing a fluorescent group,” *Proceedings Of The Society For Experimental Biology And Medicine*, vol. 47, no. 2, pp. 200–202, 1941.

[35] A. . Coons, H. . Creech, R. N. Jones, and E. Berliner, “The Demonstration of Pneumococcal Antigen in Tissues by the Use of Fluorescent Antibody,” *The Journal of Immunology*, vol. 45, pp. 159–170, 1942.

[36] O. Shimomura, F. Johnson, and Y. Saiga, “Extraction, purification and properties of aequorin, a bioluminescent protein from the luminous

hydromedusan, Aequorea," *Journal of cellular and*, vol. 1353, no. 165, pp. 223–239, 1962.

[37] M. Chalfie, Y. Tu, G. Euskirchen, W. Ward, and D. Prasher, "Green fluorescent protein as a marker for gene expression," *Science*, vol. 263, pp. 802–805, 1994.

[38] R. Heim, D. Prasher, and R. Tsien, "Wavelength mutations and posttranslational autoxidation of green fluorescent protein," in *Proceedings of the National Academy of Sciences of the USA*, 1994, pp. 12501–12504.

[39] J. Zhang, R. E. Campbell, A. Y. Ting, and R. Y. Tsien, "Creating new fluorescent probes for cell biology," *Nature Reviews Molecular Cell Biology*, vol. 3, no. 12, pp. 906–918, Dec. 2002.

[40] R. Heim, A. Cubitt, and R. Tsien, "Improved green fluorescence," *Nature*, vol. 373, pp. 663–664, 1995.

[41] N. C. Shaner, P. A. Steinbach, and R. Y. Tsien, "A guide to choosing fluorescent proteins," *Nature Methods*, vol. 2, no. 12, p. 905, 2005.

[42] R. Tsien, "New calcium indicators and buffers with high selectivity against magnesium and protons: design, synthesis, and properties of prototype structures," *Biochemistry*, vol. 19, pp. 2396–2404, 1980.

[43] F. Roberts and J. Z. Young, "The flying-spot microscope," *Proceedings of the IEE-Part IIIA:*, vol. 67, no. 6, pp. 673–5, Dec. 1952.

[44] M. Minsky, "Memoir on inventing the confocal scanning microscope," *Scanning*, vol. 10, no. 1 988, pp. 128–138, 1988.

[45] C. Sheppard and R. Kompfner, "Resonant scanning optical microscope," *Applied optics*, vol. 17, no. 18, pp. 2879–2882, Sep. 1978.

[46] J. White and W. . Amos, "Confocal microscopy comes of age," *Nature*, vol. 328, pp. 183–184, 1987.

[47] C. J. R. Sheppard and T. Wilson, "Reciprocity and equivalence in scanning microscopes," *Journal of the Optical Society of America A*, vol. 3, no. 5, p. 755, May 1986.

[48] C. J. R. Sheppard, "Scanning optical microscope," *Electronics and Power*, no. February, pp. 166–172, 1990.

[49] E. H. K. Stelzer, "The Intermediate Optical System of Laser-Scanning Confocal Microscopes," in *Handbook of Biological Confocal Microscopy*, 2006, pp. 207–220.

[50] M. Göppert-Mayer, “Elementary processes with two quantum transitions,” *Annalen der Physik*, vol. 18, no. 7–8, pp. 466–479, Aug. 2009.

[51] W. Denk, D. W. Piston, and W. W. Webb, “Multi-Photon Molecular Excitation in Laser-Scanning Microscopy,” *Handbook of Biological Confocal Microscopy*, pp. 535–549, 2006.

[52] W. Denk, J. H. Strickler, and W. W. Webb, “Two-photon laser scanning fluorescence microscopy,” *Science*, vol. 248, no. 4951, p. 73, Sep. 1990.

[53] J. M. Squirrell, D. L. Wokosin, J. G. White, and B. D. Bavister, “Long-term two-photon fluorescence imaging of mammalian embryos without compromising viability,” *Nature Biotechnology*, vol. 17, no. 8, pp. 763–767, Aug. 1999.

[54] U. K. Tirlapur, K. König, C. Peuckert, R. Krieg, and K. J. Halbhuber, “Femtosecond near-infrared laser pulses elicit generation of reactive oxygen species in mammalian cells leading to apoptosis-like death.,” *Experimental cell research*, vol. 263, no. 1, pp. 88–97, Feb. 2001.

[55] K. König, T. W. Becker, P. Fischer, I. Riemann, and K. J. Halbhuber, “Pulse-length dependence of cellular response to intense near-infrared laser pulses in multiphoton microscopes.,” *Optics letters*, vol. 24, no. 2, pp. 113–5, Jan. 1999.

[56] T. H. Maiman, “Stimulated Optical Radiation in Ruby,” *Nature*, vol. 187, no. 4736, pp. 493–494, Aug. 1960.

[57] F. Helmchen and W. Denk, “Deep tissue two-photon microscopy,”*Nature Methods*, vol. 2, no. 12, pp932-940, 2005.

[58] P. F. Curley and A.I. Ferguson, “Actively mode-locked Ti:sapphire laser producing transform-limited pulses of 150-fs duration.,” *Optics letters*, vol. 16, no. 13, pp. 1016–8, Jul. 1991.

[59] L. Schermelleh, R. Heintzmann, and H. Leonhardt, “A guide to super-resolution fluorescence microscopy.,” *The Journal of cell biology*, vol. 190, no. 2, pp. 165–75, Jul. 2010.

[60] S. W. Hell and J. Wichmann, “Breaking the diffraction resolution limit by stimulated emission: stimulated-emission-depletion fluorescence microscopy.,” *Optics letters*, vol. 19, no. 11, pp. 780–2, Jun. 1994.

[61] T. a Klar, S. Jakobs, M. Dyba, a Egner, and S. W. Hell, “Fluorescence microscopy with diffraction resolution barrier broken by stimulated emission.,” *Proceedings of the National Academy of Sciences of the United States of America*, vol. 97, no. 15, pp. 8206–10, Jul. 2000.

[62] G. Donnert, J. Keller, R. Medda, M. A. Andrei, S. O. Rizzoli, R. Lu, R. Jahn, C. Eggeling, and S. W. Hell, “Macromolecular-scale resolution in biological,” 2006.

[63] M. Studencka, A. Konzer, G. Moneron, D. Wenzel, L. Opitz, G. Salinas-Riester, C. Bedet, M. Krüger, S. W. Hell, J. R. Wisniewski, H. Schmidt, F. Palladino, E. Schulze, and M. Jedrusik-Bode, “Novel roles of Caenorhabditis elegans heterochromatin protein HP1 and linker histone in the regulation of innate immune gene expression.,” *Molecular and cellular biology*, vol. 32, no. 2, pp. 251–65, Jan. 2012.

[64] S. Berning, K. I. Willig, H. Steffens, P. Dibaj, and S. W. Hell, “Nanoscopy in a Living Mouse Brain,” *Nature*, vol. 335, no. February, p. 2012, 2012.

[65] T. J. Fellers and M. W. Davidson, “Introduction to Micrometry,” *Nikon microscopy primer*. [Online]. Available: http://www.microscopyu.com/articles/formulas/measurements.html. [Accessed: 08-Aug-2012].

[66] R. W. Ditchburn, *Light*. New York: Dover Publications Inc., 1991, p. 228.

[67] E. Abbe, “A note on the proper definition of the amplifying power of a lens system.,” *Journal of the Royal Microscopical Society*, vol. 4, pp. 348–351, 1884.

[68] P. Cheng, “The Contrast Formation in Optical Microscopy,” in *Handbook of Biological Confocal Microscopy*, J.B. Pawley, Ed. New York: Springer, 2006, pp. 162–206.

[69] E. Stelzer, “Contrast, resolution, pixelation, dynamic range and signal-to-noise ratio: fundamental limits to resolution in fluorescence light microscopy,” *Journal of Microscopy*, vol. 189, no. 1, pp. 15–24, Jan. 1998.

[70] C. L. Curl, C. J. Bellair, T. Harris, B. E. Allman, P. J. Harris, A. G. Stewart, A. Roberts, K. a Nugent, and L. M. D. Delbridge, “Refractive index measurement in viable cells using quantitative phase-amplitude microscopy and confocal microscopy.,” *Cytometry. Part A : the journal of the International Society for Analytical Cytology*, vol. 65, no. 1, pp. 88–92, May 2005.

[71] A. Rose, “Television Pickup Tubes and the Problem of Vision,” in *Advances in Electronics and Electron Physics: Volume 1*, Elsevier, 1948.

[72] J.B. Pawley, “Fundamental limits in Confocal Microscopy,” in *Handbook of Biological Confocal Microscopy*, Third edit., J.B. Pawley, Ed. New York: Springer, 2006, pp. 20–42.

[73] D. Wright, SJ; Wright, “Introduction to confocal microscopy,” in *Methods in cell biology*, Vol 70., B. Matsamoto, Ed. San Diego, California: Elsevier, 2002.

[74] J. B. Pawley, “Points , Pixels , and Gray Levels : Digitizing Image Data,” in *Handbook of Biological Confocal Microscopy*, 2006, pp. 59–79.

[75] D. G. Grier, “A revolution in optical manipulation.,” *Nature*, vol. 424, no. 6950, pp. 810–6, Aug. 2003.

[76] J. Guck, S. Schinkinger, B. Lincoln, F. Wottawah, S. Ebert, M. Romeyke, D. Lenz, H. M. Erickson, R. Ananthakrishnan, D. Mitchell, J. Käs, S. Ulvick, and C. Bilby, “Optical deformability as an inherent cell marker for testing malignant transformation and metastatic competence.,” *Biophysical journal*, vol. 88, no. 5, pp. 3689–98, May 2005.

[77] K. Konig, H. Liang, M. Berns, and B. J. Tromberg, “Cell damage by near-IR microbeams,” *Nature*, vol. 377, pp. 20–21, 1995.

[78] D. L. Wokosin, “Characterisation of excitation mode and dose for laser scanning microscopy,” University of Strathclyde, 2004.

[79] V. Centonze and J. B. Pawley, “Tutorial on practical confocal microscopy and use of the confocal test specimen,” in *Handbook of biological confocal microscopy*, Third edit., J.B . Pawley, Ed. New York: Springer, 2006, pp. 627–649.

[80] R. M. Zucker and O. T. Price, “Practical confocal microscopy and the evaluation of system performance.,” *Methods (San Diego, Calif.)*, vol. 18, no. 4, pp. 447–58, Aug. 1999.

[81] R. M. Zucker and O. Price, “Evaluation of confocal microscopy system performance.,” *Cytometry*, vol. 44, no. 4, pp. 273–94, Aug. 2001.

[82] C. Geisler, T. Hotz, A. Schönle, S. W. Hell, A. Munk, and A. Egner, “Drift estimation for single marker switching based imaging schemes.,” *Optics express*, vol. 20, no. 7, pp. 7274–89, Mar. 2012.

[83] R. M. Zucker, “Evaluation of confocal microscopy system performance.,” *Methods in molecular biology (Clifton, N.J.)*, vol. 319, pp. 77–135, Jan. 2006.

[84] J. M. Lerner and R. M. Zucker, “Calibration and validation of confocal spectral imaging systems.,” *Cytometry. Part A : the journal of the International Society for Analytical Cytology*, vol. 62, no. 1, pp. 8–34, Nov. 2004.

[85] J. Reitdorf and E. H. . Stelzer, “Special Optical Elements,” in *Handbook of Biological Confocal Microscopy*, Third edit., J. B. Pawley, Ed. New York: Springer, 2006, pp. 43–58.

[86] S. Singhrao, P. Thomas, and J. Wood, “Huntingtin protein colocalizes with lesions of neurodegenerative diseases: an investigation in Huntington’s, Alzheimer's, and Pick's diseases,” *Experimental Neurology*, vol. 150, no. 2, pp. 213–22, Apr. 1998.

[87] E. Lachmanovich, D. E. Shvartsman, Y. Malka, C. Botvin, Y. I. Henis, and a M. Weiss, “Co-localization analysis of complex formation among membrane proteins by computerized fluorescence microscopy: application to immunofluorescence co-patching studies.,” *Journal of microscopy*, vol. 212, no. Pt 2, pp. 122–31, Nov. 2003.

[88] J. Gelles and B. Schnapp, “Tracking kinesin-driven movements with nanometre-scale precision,” *Nature*, vol. 331, pp. 450–453, 1988.

[89] R. P. Aylward, “The Advances & Technologies Of Galvanometer-based Optical Scanners,” in *SPIE Conference on Optical Scanning: Design and Application*, 1999, vol. 3787, no. July, pp. 158–164.

[90] Cambridge Technology, “Technology Report Choosing the Right Galvanometer and Servo for the Job,” *Cambridge Technology Report*, pp. 1–5. accessed online http://www.camtech.com/index.php?option=com_content&view=article&id=112&Itemid=107. 08/09/12

[91] J. Montagu, “Galvanometric and Resonant scanners,” in *Handbook of optical and laser scanning*, 2nd ed., G. F. Marshall and G. E. Stutz, Eds. Boca Raton: CRC press Taylor and Francis, 2011, pp. 339–448.

[92] J. Rietdorf and E. H. K. Stelzer, “Special Optical Elements,” in *Handbook of Biological Confocal Microscopy*, Third edit., J.B. Pawley, Ed. New York: Springer, 2006, pp. 43–58.

[93] C. L. Hoy, N. J. Durr, and A. Ben-Yakar, “Fast-updating and nonrepeating Lissajous image reconstruction method for capturing increased dynamic information.,” *Applied optics*, vol. 50, no. 16, pp. 2376–82, Jun. 2011.

[94] M. Kraus, B. Potsaid, and M. Mayer, “Motion correction in optical coherence tomography volumes on a per A-scan basis using orthogonal scan patterns,” *Biomedical Optics*, vol. 3, no. 6, pp. 457–463, 2012.

[95] A. Miyawaki, “Proteins on the move: insights gained from fluorescent protein technologies.,” *Nature reviews. Molecular cell biology*, vol. 12, no. 10, pp. 656–68, Oct. 2011.

[96] F. Helmchen, M. S. Fee, D. W. Tank, and W. Denk, “A miniature head-mounted two-photon microscope. high-resolution brain imaging in freely moving animals.,” *Neuron*, vol. 31, no. 6, pp. 903–12, Sep. 2001.

[97] K. H. Koh, T. Kobayashi, and C. Lee, “A 2-D MEMS scanning mirror based on dynamic mixed mode excitation of a piezoelectric PZT thin film S-shaped actuator.,” *Optics express*, vol. 19, no. 15, pp. 13812–24, Jul. 2011.

[98] M. D. Jacobs, P. J. Donaldson, M. B. Cannell, and C. Soeller, “Resolving morphology and antibody labeling over large distances in tissue sections.,” *Microscopy research and technique*, vol. 62, no. 1, pp. 83–91, Sep. 2003.

[99] P. Xi and Y. Liu, “Scanning and Image Reconstruction Techniques in Confocal Laser Scanning Microscopy,” in *Laser Scanning, Theory and Applications*, 1995, pp. 523–542.

[100] J. Pawley, “LVSEM for high resolution topographic and density contrast imaging,” in *Advances in Electronics and Electron Physics*, Vol.83 ed., vol. 83, Elsevier, 1992, pp. 203–274.

[101] K. S. Giboney, S. T. Allen, M. J. W. Rodwell, and J. E. Bowers, “Picosecond measurements by free-running electro-optic sampling,” *Photonics Technology Letters, IEEE*, vol. 6, no. 11, pp. 1353–1355, 1994.

[102] J. Hancock, “Jitter- Understanding it, Measuring It , Eliminating It Part 1 : Jitter Fundamentals,” *High Frequency Electronics*, no. April, pp. 44–50, 2004.

[103] M. Muellller and R. Stephens, “Total Jitter Measurement at Low Probability Levels, Using the Optimized BERT Scan Method,” *Design and Test for Multiple Gbps Communication Devices and Systems*, p. 379, 2005.

[104] A. R. Hibbs, G. Macdonald, and K. Garsha, “Practical Confocal Microscopy,” in *Handbook of Biological Confocal Microscopy*, Third edit., J. B. Pawley, Ed. New York: Springer, 2006, pp. 650–671.

[105] B. Rohr, “Testing high-performance galvanometer-based optical scanners,” *Proceedings of SPIE*, vol. 2383, pp. 460–467, 1995.

[106] V. Duma, K. Lee, and P. Meemon, “Experimental investigations of the scanning functions of galvanometer-based scanners with applications in OCT,” *Applied Optics*, vol. 50, no. 29, pp. 5735–5749, 2011.

[107] J. Xie, S. Huang, Z. Duan, Y. Shi, and S. Wen, “Correction of the image distortion for laser galvanometric scanning system,” *Optics & Laser Technology*, vol. 37, pp. 305–311, 2005.

[108] R. Oldenbourg, H. Terada, R. Tiberio, and S. Inoué, “Image sharpness and contrast transfer in coherent confocal microscopy.,” *Journal of microscopy*, vol. 172, no. Pt 1, pp. 31–9, Oct. 1993.

[109] E. Betzig, G. H. Patterson, R. Sougrat, O. W. Lindwasser, S. Olenych, J. S. Bonifacino, M. W. Davidson, J. Lippincott-Schwartz, and H. F. Hess, “Imaging intracellular fluorescent proteins at nanometer resolution.,” *Science (New York, N.Y.)*, vol. 313, no. 5793, pp. 1642–5, Sep. 2006.

[110] M. Gordon and T. Ha, “Single-molecule high-resolution imaging with photobleaching,” *Proceedings of the National*, vol. 2004, pp. 15–18, 2004.

[111] A. Siegman, “How to (maybe) measure laser beam quality,” in *Diode Pumped Solid State Lasers: Applications and Issues*, 1998, vol. d, no. October 1997, pp. 1–18.

[112] J. M. Liu, “Simple technique for measurements of pulsed Gaussian-beam spot sizes.,” *Optics letters*, vol. 7, no. 5, pp. 196–8, May 1982.

[113] X. Liu, D. Du, and G. Mourou, “Laser ablation and micromachining with ultrashort laser pulses,” *IEEE Journal of Quantum Electronics*, vol. 33, no. 10, pp. 1706–1716, 1997.

[114] B. Tan, a. Dalili, and K. Venkatakrishnan, “High repetition rate femtosecond laser nano-machining of thin films,” *Applied Physics A*, vol. 95, no. 2, pp. 537–545, Nov. 2008.

[115] Turner G.L.E and Bradbury, “An electron microscopical examination of Norbert’s finest test-plate of twenty bands,” *Journal of the Royal Microscopical Society*, vol. 85, no. 4, pp. 435–447, 1966.

[116] D. Day and M. Gu, “Microchannel fabrication in PMMA based on localized heating by nanojoule high repetition rate femtosecond pulses.,” *Optics express*, vol. 13, no. 16, pp. 5939–46, Aug. 2005.

[117] D. E. Roberts, a. du Plessis, and L. R. Botha, “Femtosecond laser ablation of silver foil with single and double pulses,” *Applied Surface Science*, vol. 256, no. 6, pp. 1784–1792, Jan. 2010.

[118] M. Lax, “Temperature rise induced by a laser beam,” *Journal of Applied Physics*, vol. 48, no. 9, p. 3919, 1977.

[119] B. N. Chichkov, C. Momma, S. Nolte, F. Von Alvensleben, and A. Tu, “Femtosecond , picosecond and nanosecond laser ablation of solids,” *Applied Physics A: Materials Science & Processing*, vol. 115, pp. 109–115, 1996.

[120] T. Itina, “Modeling of metal ablation induced by ultrashort laser pulses,” *Thin Solid Films*, vol. 453–454, pp. 513–517, Apr. 2004.

[121] E. Gamaly, A. Rode, and B. Luther-Davies, “Ultrafast ablation with high-pulse-rate lasers. Part I: Theoretical considerations,” *Journal of Applied Physics*, vol. 85, no. 8, p. 4213, 1999.

[122] K. Konig, I. Riemann, F. Stracke, and R. Leharzic, “Nanoprocessing with nanojoule near-infrared femtosecond laser pulses,” *Medical Laser Application*, vol. 20, no. 3, pp. 169–184, Oct. 2005.

[123] A. Serafetinides, M. Makropoulou, C. Skordoulis, and A. Kar, “Ultra-short pulsed laser ablation of polymers,” *Applied Surface Science*, vol. 180, no. 1–2, pp. 42–56, 2001.

[124] A. Rode, B. Luther-Davies, and E. Gamaly, “Ultrafast ablation with high-pulse-rate lasers. Part II: Experiments on laser deposition of amorphous carbon films,” *Journal of Applied Physics*, vol. 85, no. 8, p. 4222, 1999.

[125] D. Day and M. Gu, “Femtosecond fabricated surfaces for cell biology,” *Journal of Optics*, vol. 12, no. 8, p. 084005, Aug. 2010.

[126] A. Ancona, F. Röser, K. Rademaker, J. Limpert, S. Nolte, and A. Tünnermann, “High speed laser drilling of metals using a high repetition rate, high average power ultrafast fiber CPA system.,” *Optics express*, vol. 16, no. 12, pp. 8958–68, Jun. 2008.

[127] S. Kawata, H. B. Sun, T. Tanaka, and K. Takada, “Finer features for functional microdevices.,” *Nature*, vol. 412, no. 6848, pp. 697–8, Aug. 2001.

[128] F. Korte, S. Adams, a Egbert, C. Fallnich, a Ostendorf, S. Nolte, M. Will, J. P. Ruske, B. Chichkov, and a Tuennermann, “Sub-diffraction limited structuring of solid targets with femtosecond laser pulses.,” *Optics express*, vol. 7, no. 2, pp. 41–9, Jul. 2000.

[129] K. Venkatakrishnan, “Sub-micron ablation of metallic thin film by femtosecond pulse laser,” *Optics & Laser Technology*, vol. 34, no. 7, pp. 575–578, Oct. 2002.

[130] D. Mcmullan, “The Early Development of the Scanning Electron Microscope,” no. 1928, pp. 1–25, 2008.

[131] P. D. Nellist, “Scanning Transmission Electron Microscopy,” in *Science of Microscopy*, P. . Hawkes and J. C. . Spence, Eds. New York, NY: Springer New York, 2007, pp. 65–132.

[132] J. B. Pawley, “LVSEM for Biology,” in *Biological Low-Voltage Scanning Electron Microscopy*, no. 1992, H. Schatten and J.B . Pawley, Eds. New York: Springer, 2008, pp. 27–106.

[133] D. C. Joy, “Noise and Its Effects on the Low-Voltage SEM,” in *Biological Low-Voltage Scanning Electron Microscopy*, H. Schatten and J. Pawley, Eds. New York: Springer, 2008.

[134] D. C. Joy, “The Aberration-Corrected SEM,” in *Biological Low-Voltage Scanning Electron Microscopy*, H. Schatten and J.B . Pawley, Eds. New York: Springer, 2008, pp. 107–127.

[135] J. Ximen, Z. Shao, and P. Lin, “Theoretical calculation of probe size of low-voltage scanning electron microscopes,” *Journal of Microscopy*, vol. 170, no. Section 3, pp. 5–10, 1993.

[136] W. R. Zipfel, R. M. Williams, R. Christie, A. Y. Nikitin, B. T. Hyman, and W. W. Webb, “Live tissue intrinsic emission microscopy using multiphoton-excited native fluorescence and second harmonic generation.,” *Proceedings of the National Academy of Sciences of the United States of America*, vol. 100, no. 12, pp. 7075–80, Jun. 2003.

[137] M. Muller, J. Schmidt, S. L. Mironov, and D. W. Richter, “Construction and performance of a custom-built two-photon laser scanning system,” *Journal of Physics D: Applied Physics*, vol. 36, no. 14, pp. 1747–1757, Jul. 2003.

[138] W. Mittmann, D. J. Wallace, U. Czubayko, J. T. Herb, A. T. Schaefer, L. L. Looger, W. Denk, and J. N. D. Kerr, “Two-photon calcium imaging of evoked activity from L5 somatosensory neurons in vivo,” *Nat Neurosci*, vol. 14, no. 8, pp. 1089–1093, Aug. 2011.

[139] C. Wang, L. Qiao, F. He, Y. Cheng, and Z. Xu, “Extension of imaging depth in two-photon fluorescence microscopy using a long-wavelength high-pulse-energy femtosecond laser source.,” *Journal of microscopy*, vol. 243, no. 2, pp. 179–83, Aug. 2011.

[140] F. Liang, R. Vallée, D. Gingras, and S. L. Chin, “Role of ablation and incubation processes on surface nanograting formation,” *Optical Materials Express*, vol. 1, no. 7, p. 1244, Oct. 2011.

[141] V. Ntziachristos, “Going deeper than microscopy: the optical imaging frontier in biology,” *Nature methods*, vol. 7, no. 8, pp. 603–614, Aug. 2010.

[142] J. White and E. Stelzer, “Photobleaching GFP reveals protein dynamics inside live cells,” *Trends in cell biology*, vol. 9, no. 2, pp. 61–65, 1999.

[143] J. Lippincott-Schwartz, E. Snapp, and A. Kenworthy, “Studying protein dynamics in living cells,” *Nature Reviews Molecular Cell Biology*, vol. 2, no. 6, pp. 444–456, 2001.

[144] S. Iwanaga, N. Smith, K. Fujita, and S. Kawata, “Slow Ca 2+ wave stimulation using low repetition rate femtosecond pulsed irradiation,” *Optics Express*, vol. 14, no. 2, pp. 717–725, 2006.

[145] N. I. Smith, S. Iwanaga, T. Beppu, K. Fujita, O. Nakamura, and S. Kawata, “Photostimulation of two types of Ca 2 + waves in rat pheochromocytoma PC12 cells by ultrashort pulsed near-infrared laser irradiation,” *Laser Physics letters*, vol. 3, pp. 154–161, 2006.

[146] M. M. Knight, S. R. Roberts, D. A. Lee, and D. L. Bader, “Live cell imaging using confocal microscopy induces intracellular calcium transients and cell death,” *American Journal of Physiology- Cell Physiology*, vol. 284, no. 4, p. C1083, Feb. 2003.

[147] J. G. McCarron, S. Chalmers, K. N. Bradley, D. MacMillan, and T. C. Muir, “Ca2+ microdomains in smooth muscle.,” *Cell calcium*, vol. 40, no. 5–6, pp. 461–93, 2006.

[148] M. J. Berridge, M. D. Bootman, and P. Lipp, “Calcium--a life and death signal.,” *Nature*, vol. 395, no. 6703, pp. 645–8, Oct. 1998.

[149] D. Macmillan and J. G. McCarron, “The phospholipase C inhibitor U-73122 inhibits Ca(2+) release from the intracellular sarcoplasmic reticulum Ca(2+) store by inhibiting Ca(2+) pumps in smooth muscle.,” *British journal of pharmacology*, vol. 160, no. 6, pp. 1295–301, Jul. 2010.

[150] M. Berridge and P. Lipp, “The versatility and universality of calcium signalling,” *Nature Reviews Molecular Cell*, vol. 1, no. October, 2000.

[151] M. D. Bootman, M. J. Berridge, and P. Lipp, “Cooking with calcium: the recipes for composing global signals from elementary events.,” *Cell*, vol. 91, no. 3, pp. 367–73, Oct. 1997.

[152] A. Verkhratsky, O. a Krishtal, and O. H. Petersen, “From Galvani to patch clamp: the development of electrophysiology.,” *Pflügers Archiv : European journal of physiology*, vol. 453, no. 3, pp. 233–47, Dec. 2006.

[153] A. Huxley, “Hodgkin and the action potential 1935–1952,” *The Journal of Physiology*, no. 2002, pp. 1–2, 2002.

[154] R. Chow, L. von Rüden, and E. Neher, “Delay in vesicle fusion revealed by electrochemical monitoring of single secretory events in adrenal chromaffin cells,” *Nature*, vol. 356, pp. 60–63, 1992.

[155] G. Stuart, H. Dodt, and B. Sakmann, “Patch-clamp recordings from the soma and dendrites of neurons in brain slices using infrared video microscopy,” *Pflügers Archiv European Journal of …*, vol. 423, pp. 511–518, 1993.

[156] M. Bebarova, “Advances in patch clamp technique: towards higher quality and quantity,” *GENERAL PHYSIOLOGY AND BIOPHYSICS*, vol. 31, no. 2, pp. 131–140, Jun. 2012.

[157] N. I. Smith, K. Fujita, T. Kaneko, K. Katoh, O. Nakamura, S. Kawata, and T. Takamatsu, “Generation of calcium waves in living cells by pulsed-laser-induced photodisruption,” *Applied Physics Letters*, vol. 79, no. 8, p. 1208, 2001.

[158] N. I. Smith, Y. Kumamoto, S. Iwanaga, J. Ando, K. Fujita, and S. Kawata, “A femtosecond laser pacemaker for heart muscle cells.,” *Optics express*, vol. 16, no. 12, pp. 8604–16, Jun. 2008.

[159] J. M. Girkin and G. McConnell, “Advances in laser sources for confocal and multiphoton microscopy.,” *Microscopy research and technique*, vol. 67, no. 1, pp. 8–14, May 2005.

[160] W. Denk, “Two-photon laser scanning fluorescence microscopy,” *Science*, vol. 52, no. 13 Suppl, pp. 1778–9, Oct. 1990.

[161] Y. Yan, J. Liu, C. Wei, K. Li, W. Xie, Y. Wang, and H. Cheng, “Bidirectional regulation of Ca2+ sparks by mitochondria-derived reactive oxygen species in cardiac myocytes.,” *Cardiovascular research*, vol. 77, no. 2, pp. 432–41, Jan. 2008.

[162] J. Jacobson and M. R. Duchen, “Mitochondrial oxidative stress and cell death in astrocytes--requirement for stored Ca2+ and sustained opening of the permeability transition pore.,” *Journal of cell science*, vol. 115, no. Pt 6, pp. 1175–88, Mar. 2002.

[163] J. G. Mccarron and T. C. Muir, “Mitochondrial regulation of the cytosolic Ca2+ concentration and the Ins P3 -sensitive Ca2+ store in guinea-pig colonic smooth muscle,” *Journal of physiology*, vol. 516.1, pp. 149–161, 1999.

[164] J. Dempster, D. Wokosin, K. McCloskey, J. Girkin, and A. Gurney, “WinFluor-An integrated system for the simultaneous recording of cell fluorescence images and electrophysiological signals on a single computer system,” *British Journal of Pharmacology*, vol. 137, pp. 146–146, 2002.

[165] R. Lavi, A. Shainberg, H. Friedmann, V. Shneyvays, O. Rickover, M. Eichler, D. Kaplan, and R. Lubart, “Low energy visible light induces reactive oxygen species generation and stimulates an increase of intracellular calcium concentration in cardiac cells,” *Journal of Biological Chemistry*, vol. 278, no. 42, p. 40917, Oct. 2003.

[166] A. Schönle and S. W. Hell, “Heating by absorption in the focus of an objective lens,” *Optics letters*, vol. 23, no. 5, pp. 325–327, 1998.

[167] Y. J. Suzuki and G. D. Ford, “Redox regulation of signal transduction in cardiac and smooth muscle,” *Journal of molecular and cellular cardiology*, vol. 31, no. 2, pp. 345–353, 1999.

[168] R. Lubart, H. Friedmann, and R. onit Lavie, “Photobiostimulation as a function of different wavelengths,” *Laser Therapy*, vol. 12, pp. 38–41, 2000.

[169] R. Dixit and R. Cyr, “Cell damage and reactive oxygen species production induced by fluorescence microscopy: effect on mitosis and guidelines for non-invasive fluorescence microscopy,” *The Plant Journal*, vol. 36, no. 2, pp. 280–290, Oct. 2003.

[170] J. M. Girkin, E. Gu, C. Griffin, H. W. Choi, M. D. Dawson, and G. McConnell, “Use of confocal and multiphoton microscopy for the evaluation of micro-optical components and emitters.,” *Microscopy research and technique*, vol. 64, no. 4, pp. 293–6, Jul. 2004.

[171] M. Lieb and a Meixner, “A high numerical aperture parabolic mirror as imaging device for confocal microscopy.,” *Optics express*, vol. 8, no. 7, pp. 458–74, Mar. 2001.

[172] E. Schonbrun, C. Rinzler, and K. B. Crozier, “Microfabricated water immersion zone plate optical tweezer,” *Applied Physics Letters*, vol. 92, no. 7, p. 071112, 2008.

[173] A. Lengwenus, J. Kruse, and M. Volk, “Coherent manipulation of atomic qubits in optical micropotentials,” *Applied Physics B: Lasers …*, pp. 1–8, 2007.

[174] A. Jechow, E. W. Streed, B. G. Norton, M. J. Petrasiunas, and D. Kielpinski, “Wavelength-scale imaging of trapped ions using a phase Fresnel lens.,” *Optics letters*, vol. 36, no. 8, pp. 1371–3, Apr. 2011.

[175] E. Gu, H. W. Choi, C. Liu, C. Griffin, J. M. Girkin, I. M. Watson, M. D. Dawson, G. McConnell, and a. M. Gurney, “Reflection/transmission confocal microscopy characterization of single-crystal diamond microlens arrays,” *Applied Physics Letters*, vol. 84, no. 15, p. 2754, 2004.

[176] H. Ottevaere, R. Cox, H. P. Herzig, T. Miyashita, K. Naessens, M. Taghizadeh, R. Völkel, H. J. Woo, and H. Thienpont, “Comparing glass and plastic refractive microlenses fabricated with different technologies,” *Journal of Optics A: Pure and Applied Optics*, vol. 8, no. 7, pp. S407–S429, Jul. 2006.

[177] P. F. Griffin, J. Harris, G. Mcconnell, A. S. Arnold, D. Cox, and E. Riis, “Investigation of Micrometre Scale Parabolic Mirrors for use as Single Atom Quantum Registers,” vol. 2754, no. 2004, p. 4244, 2009.

[178] A. Siegman, “Defining, measuring, and optimizing laser beam quality,” *Proc. SPIE*, vol. V, pp. 2–12, 1993.

[179] U. P. Kumar, N. K. Mohan, and M. P. Kothiyal, “Characterization of micro-lenses based on single interferogram analysis using Hilbert transformation,” *Optics Communications*, vol. 284, no. 21, pp. 5084–5092, Oct. 2011.

[180] E. Hecht, *Optics*, Fourth edi. San Francisco: Addison Wesley, 2002.

[181] M. M. Gow, *A course in pure mathematics*. Oxford: Elsevier, 1994, pp. 300–305.

[182] E. Hecht, “Diffraction,” in *Optics*, 4th editio., San Francisco: Addison Wesley, 2002, pp. 443–518.